5-2013

Creep, Fatigue and Creep-Fatigue Interactions in Modified 9% Cr - 1% Mo (P91) Steels

Valliappa Kalyanasundaram
University of Arkansas, Fayetteville

CREEP, FATIGUE AND CREEP-FATIGUE INTERACTIONS IN MODIFIED 9% Cr – 1% Mo (P91) STEELS

CREEP, FATIGUE AND CREEP-FATIGUE INTERACTIONS IN MODIFIED 9% Cr – 1% Mo (P91) STEELS

A dissertation submitted in partial fulfillment
of the requirements for the degree of
Doctor of Philosophy in Mechanical Engineering

By

Valliappa Kalyanasundaram
Madurai Kamaraj University
Bachelor of Engineering in Mechanical Engineering, 2004
University of Arkansas
Master of Science in Mechanical Engineering, 2008

May 2013
University of Arkansas

ABSTRACT

Grade P91 steel, from the class of advanced high-chrome ferritic steels, is one of the preferred materials for many elevated temperature structural components. Creep-fatigue (C-F) interactions, along with oxidation, can accelerate the kinetics of damage accumulation and consequently reduce such components' life. Hence, reliable C-F test data is required for meticulous consideration of C-F interactions and oxidation, which in turn is vital for sound design practices. It is also imperative to develop analytical constitutive models that can simulate and predict material response under various long-term in-service conditions using experimental data from short-term laboratory experiments. Consequently, the major objectives of the proposed research are to characterize the creep, fatigue and C-F behavior of grade P91 steels at 625°C and develop robust constitutive models for simulating/predicting their microstructural response under different loading conditions.

This work will utilize experimental data from 16 laboratories worldwide that conducted tests (creep, fatigue and C-F) on grade P91 steel at 625°C in a round-robin (RR) program. Along with 7 creep deformation and rupture tests, 32 pure fatigue and 46 C-F tests from the RR are considered in this work. A phenomenological constitutive model formulated in this work needs *just* five fitting parameters to simulate/predict the monotonic, pure fatigue and C-F behavior of grade P91 at 625°C. A modified version of an existing constitutive model is also presented for particularly simulating its isothermal creep deformation and rupture behavior.

Experimental results indicate that specimen C-F lives, as measured by the 2% load drop criterion, seem to decrease with increasing strain ranges and increasing hold times at 625°C.

Metallographic assessment of the tested specimens shows that the damage mode in both pure fatigue and 600 seconds hold time cyclic tests is predominantly transgranular fatigue with some presence of oxidation spikes. The damage mode in 1800 second hold time cyclic tests is an interaction of transgranular fatigue with dominant oxide spikes and creep cavitation. Other experimental results including the statistical analysis and inter- and intra-laboratory variability in the C-F lifetimes are provided in the text. Scatter factor for any of creep, monotonic, pure fatigue and C-F simulations is shown to be at a maximum of ~ 1.3, in comparison to > 5 expected for a RR. Moreover, the microstructural variability between nominally homogeneous specimens can be inherently accounted by the formulated constitutive model.

This dissertation is approved for recommendation to the Graduate Council.

Dissertation Director:

_____

Ashok Saxena, Ph.D.

Dissertation Committee:

_____

Rick J. Couvillion, Ph.D., P.E.

_____

Stuart R. Holdsworth, Ph.D.

_____

Douglas E. Spearot, Ph.D.

_____

Min Zou, Ph.D.

DISSERTATION DUPLICATION RELEASE

I hereby authorize the University of Arkansas Libraries to duplicate this dissertation when needed for research and/or scholarship.

Agreed _____
Valliappa Kalyanasundaram

Refused _____
Valliappa Kalyanasundaram

ACKNOWLEDGMENTS

First and foremost, I would like to express my grateful thanks to the Almighty for his eternal blessings in all of my sensible career endeavors and successes. I am really proud to have Mrs. K. Pitchammai and Mr. C. Kalyanasundaram as my Parents, who have been strong pillars of endless love and inspirational support for me at all times. "*Thank you*" should be an understatement for their utmost generosity, compliant deeds and sacrifices and I will remain everlastingly indebted to them in this birth. I also acknowledge the warmth love extended to me by my sisters, brother-in-laws and to all others in my family. All of my friends and acquaintances have directly or indirectly assisted me in numerous ways during the course of this accomplishment and I thank them all for giving me the moral support and love beyond my imagination.

From the bottom of my heart, I am eager to express my heartfelt gratitude and admiration to few wonderful people who have immensely helped me in my academic dissertation journey. In this regard, this work would not have seen the light of the day without the unconditional and unswerving support of my advisor, Dr. Ashok Saxena. His tremendous zeal, creative insight and problem solving skills have always inspired me to greater heights and I cherish this invaluable opportunity to learn from him. My competence as a scientific researcher has also significantly improved under his supervision, for which I am forever thankful. Besides academic themes, I am deeply touched by the love extended to me and my colleagues by him and Mrs. Madhu Saxena during social gatherings for which I am forever grateful. I would also like to sincerely thank my reading committee members, Dr. Rick J. Couvillion, Dr. Stuart R. Holdsworth, Dr. Douglas E. Spearot and Dr. Min Zou for their invaluable time, comments and suggestions during the course of this work. In particular, I take this

instance to thank Dr. Holdsworth and Dr. Edoardo Mazza once again for offering me an opportunity to directly work with them for 26 weeks at EMPA, Dübendorf, Switzerland.

Much appreciation should be extended to all of my former and current colleagues and peers for their consistent help during the course of this work. In this context, Sau Wee Koh, Jeff Evans, Rahul Rajgarhia and Santosh Narasimhachary at the Mechanical Properties and Research Laboratory (MPRL) deserve a special mention and I greatly enjoyed working with them on various aspects of materials science research. I also thank Rodolfo Montelongo for spending quality time assisting me in my research during his summer research program in 2010. The fruitful discussions I had with my mentors and colleagues at EMPA are also acknowledged. My special thanks go to Dr. Sunder, Girish and other staff at BiSS, India for all their help and support in maintaining the efficient functioning of testing equipments at MPRL.

I also sincerely appreciate the boundless support and encouragement of a dedicated team of staff at the University of Arkansas (UA), especially at the Engineering Research Center (ENRC), without whom this endeavor would have been much more tedious. The accomplishments I have achieved during the doctoral program would not have been readily possible without the technical support of Jeff Knox and his quick assistance in short notice during critical times. Technical assistance offered by Jeff Mincy and Jeff Metz, Struers in metallographic specimen preparation and related analysis is also greatly appreciated. Timely administrative assistance offered by Kathy Jones and Kristy Fink at the College of Engineering and all the Mechanical Engineering staff at UA is also acknowledged. Special mention also goes to Mike and June Brosius, Eric denBoer and Genevie Payne for keeping ENRC a lively place to do scientific research. Finally to all those who have

assisted me throughout this undertaking and not been explicitly mentioned herein, I sincerely thank each and every one of you!

I gratefully acknowledge Electric Power Research Institute, Charlotte, USA for offering the test material investigated in this work. I also thank all the ASTM E2714-09 round-robin participants for contributing most of the experimental test data utilized in this dissertation work. Financial support from the Irma F. and Raymond C. Giffels' Chair in Engineering and the Sam Walton Fellowship Foundation is also profoundly appreciated.

"Families are the compass that guides us. They are the inspiration to reach great heights, and our comfort when we occasionally falter."

Brad Henry

Dedicated to my Parents and Family

for their boundless support and love

TABLE OF CONTENTS

LIST OF TABLES

LIST OF FIGURES

LIST OF SYMBOLS

A_0	Initial cross-sectional area
Ac_1	Temperature above which austenite begins to form from ferrite
A_n	Constant in Norton's creep power-law
A_t	Norton's power-law creep coefficient
A_{orig}	Original cross-sectional area in the specimen gage length
A_{red}	Reduced cross-sectional area
A_{unif}	Uniform cross-sectional area obtained by using d_{unif}
A, a, b, c, f	Model indices for the newly proposed constitutive model
a, c	Lattice parameters
C	Material constant
d	Average particle size at time t
d_0	Average particle size at time $t = 0$
d_{unif}	Uniform diameter
E	Material's elastic modulus
F	External mechanical load
G	Shear modulus
HCF	High cycle fatigue
k	Particle growth rate
k_B	Boltzmann's constant
k'	Material constant
LCF	Low cycle fatigue
m	Fitting constant

M_f	Temperature at which austenite fully transforms to martensite
M_s	Temperature at which austenite starts to transform to martensite
n	Norton's power-law creep exponent
n_d	Number of data points
N	Number of loading cycles
$N_{2\%}$	Number of loading cycles for 2% load drop
p	Internal pressure
Q	Activation energy
R	Stress ratio
R^2	Coefficient of regression
R_1, R_2	Two roots of the second-derivative of the proposed constitutive model
t	Time
t_h	Duration of stress- or strain- hold within a loading cycle
t_r	Expected creep rupture time
t_ε	Time to given engineering creep strain
t^*	Actual creep rupture time
T	Absolute temperature
T_c	Temperature in °C
T_m	Absolute melting temperature
Z	Scatter factor
σ	Engineering axial stress
σ_0	Initial axial stress
$\sigma_{0.1\%\varepsilon}$	Stress at 0.1% total strain

σ_a	Stress amplitude (cyclic)
σ_{eq}	Equivalent stress
σ_{exp}	Experimental stress
σ_m	Mean stress (cyclic)
σ_{max}	Peak tensile stress (cyclic)
σ_{min}	Peak compressive stress (cyclic)
σ_{pred}	Predicted stress
σ_{relax}	Degree of stress relaxation during cyclic hold
σ_C	Cyclic compressive stress
σ_T	Cyclic tensile stress
$\Delta\sigma$	Stress range
ε	Engineering axial strain
ε_1	ε_t at time $t = 1$ hour
ε_{creep}	Cyclic creep strain
ε^{el}	Instantaneous elastic creep strain
ε_{in}	Total accumulated inelastic strain
ε_{ru}	Uniform strain at creep rupture
ε_t	Engineering creep strain at time t
ε_{tot}	Total inelastic strain
ε_C	Peak compressive strain (cyclic)
ε_{PL}	Proportional limit strain
ε_T	Peak tensile strain (cyclic)
ε_{UTS}	Strain at ultimate tensile strength
ε^*	Creep rupture strain

$\dot{\varepsilon}$	Nominal strain-rate
$\dot{\varepsilon}^{\mathrm{cr}}$	Creep rate
$\dot{\varepsilon}_{\mathrm{min}}^{\mathrm{cr}}$	Minimum or steady-state creep rate
$\Delta\varepsilon$	Strain range
β, p, C	Modified LCSP model fitting parameters
$\left\|\vec{b}\right\|$	Magnitude of Burgers vector
ω	Angular velocity
γ	Austenite
α	Ferrite
δ-ferrite	Deleterious phase in grade P91 steel
ρ_{n}	Number density of particles

LIST OF ABBREVIATIONS

ASME	American Society of Mechanical Engineers
ASTM	American Society for Testing and Materials
BCC	Body centered cubic crystal structure
BCT	Body centered tetragonal crystal structure
BiSS	Bangalore Integrated System Solutions
C-F	Creep-fatigue
CCT	Continuous cooling transformation
CIZ	Crystallographically imperfect zone
CL	Compressive loading
CPZ	Crystallographically perfect zone
CRIEPI	Central Research Institute of Electric Power Industry
CUL	Compressive unloading
DD	Dislocation dynamics
DSLR	Digital single-lens reflex
EMPA	Eidgenössische Materialprüfungs- und Forschungsanstalt (Swiss Federal Laboratories for Materials Science and Technology)
EPRI	Electric Power Research Institute
FCC	Face centered cubic crystal structure
GB	Grain boundary
HCP	Hexagonal close packed crystal structure
IEA	International Energy Agency
LCSP	Logarithmic creep strain prediction
LMFBR	Liquid metal fast breeder reactor

LMP	Larson Miller parameter
LSW	Lifshitz, Slyozov and Wagner
LVDT	Linear variable differential transformer
MD	Molecular dynamics
NIMS	National Institute for Materials Science
ORNL	Oak Ridge National Laboratory
P/T	Prefix that denotes piping or tubing application
PAG	Prior austenitic grain
PL	Proportional limit
RMS	Root mean square
RR	Round-robin
SLT	Second law of thermodynamics
TEM	Transmission electron microscopy
TH	Tensile hold
TL	Tensile loading
TTP	Time-temperature parameter
TUL	Tensile unloading
UA	University of Arkansas
USC	Ultra-supercritical
UTS	Ultimate tensile strength
YS	Yield strength

Chapter 1: INTRODUCTION

1.1. Background and motivation for research

Sustained efforts of environmentalists and proponents of continued ecosystem balance have created increasing awareness among world citizens to contribute less towards global warming and more towards "greener" practices. Due to lack of other large-scale viable options yet, electricity generation has rather ironically become more dependent on non-renewable resources – fossil fuels like coal, natural gas or oil shale – to cater the increasing global energy demand. As per the estimates of International Energy Agency (IEA) in 2011, fossil fuels will account for 75% of the global energy market by 2035 [**1**]. It is further stated that the usage of coal specifically is expected to increase by a staggering 65% in 2035 from utilization levels in 2011. If realized so, coal will gradually overtake oil as the largest fuel in the global energy mix in a decade or two. Considering that coal-fired steam power plants already produce ~ 40% of the world electricity needs, it thus becomes clearly evident that coal will play an integral role in the global power production for years to come.

It is well known that coal, when burnt, emits carbon dioxide (CO_2) – a greenhouse gas considered to contribute significantly to global warming – and other equally harmful particulate matter. In order to ensure efficient utilization of coal reserves with minimized environmental pollution, coal-fired steam power plants should therefore be operated at maximum thermal efficiencies with consistent impetus on further improvement(s). From earlier attempts, the impact that an improvement in the operating efficiencies of power plants will have on reducing their contribution to global pollution levels is well documented (*cf.* section 1.3 for a quantitative discussion) [**2**, **3**].

The maximum working pressure and temperature in the steam cycle are the critical factors that largely determine the thermal efficiency of steam based systems, as they help reduce heat transfer losses. Hence, there has been a global effort to increase the maximum service steam pressure and temperature in an effort to improve the net operating efficiencies of coal-fired steam power plants (see Figure 1.1) [**4**]. The chief limiting concern in this endeavor is the lack of superior materials – inherently limited by their mechanical properties – for fabricating elevated temperature components in such facilities [**5**]. So, it can be generally interpreted that improvement of existing materials and/or development of new materials will not only improve the thermal efficiencies of fossil-fired steam power plants, but also concurrently help reduce environmental pollution [**6**, **7**, **8**, **9**].

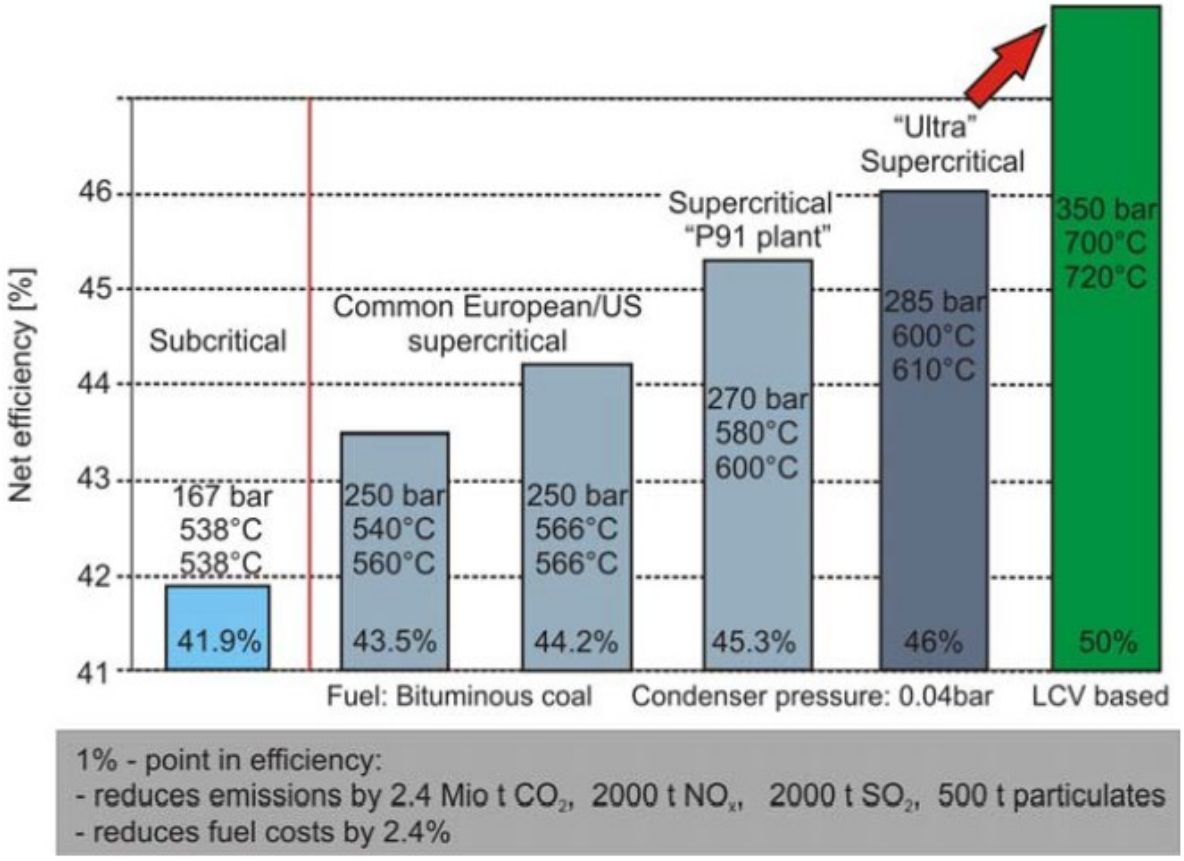

Figure 1.1. Improvement in net efficiency as a function of steam pressure and temperature in coal-fired steam power plants [4].

Of all the materials considered for structural applications in power plants, steels – iron based alloys containing few alloying elements, primarily carbon – remain the primary choice since they have been employed and studied extensively for the last few centuries, and are relatively inexpensive. Due to increased global research activities in alloy development over the years, steels with improved mechanical properties have been progressively developed to operate structural components at ever increasing temperatures and stresses or steam conditions [**9**, **10**, **11**, **12**, **13**]. This global effort has been much more pronounced in advanced steam power plants with particular focus on improved elevated temperature properties (see Figure 1.2) [**14**, **15**, **16**, **17**, **18**, **19**, **20**, **21**].

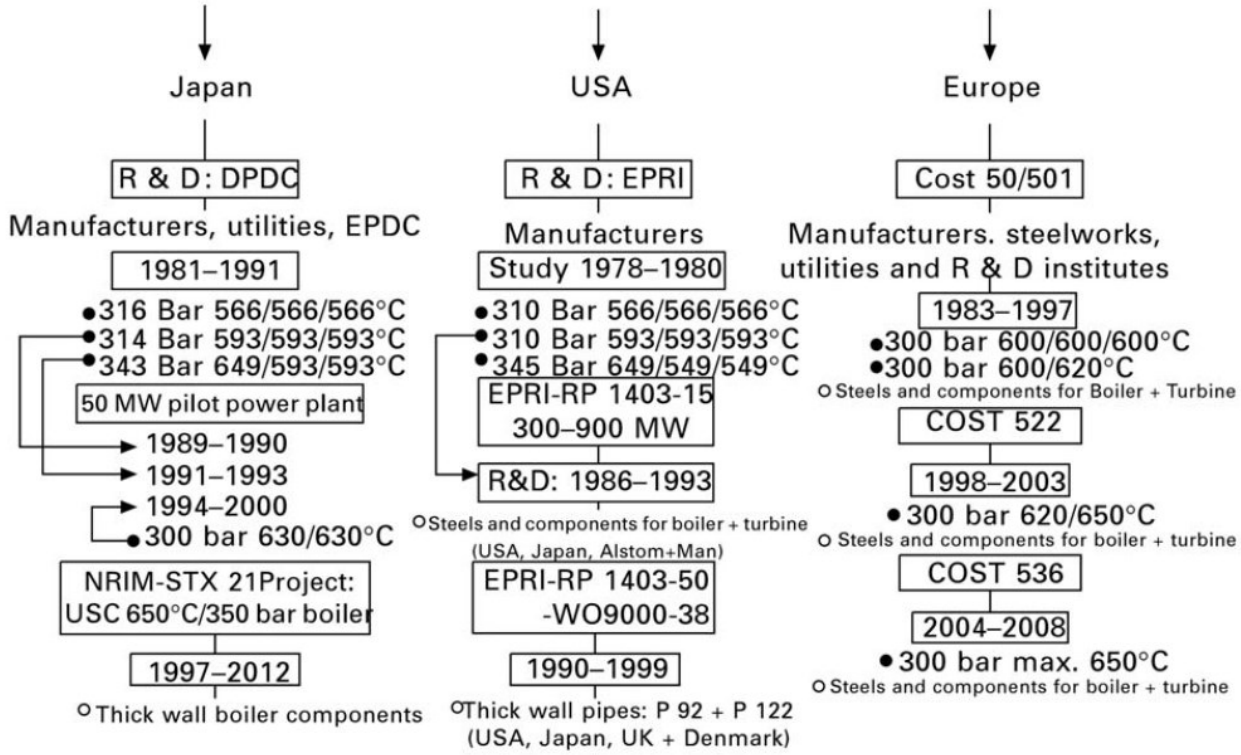

Figure 1.2. Overview of global research activities towards development of steels for advanced steam power plant components [21].

Among the class of steels, high-chrome – containing 9-12% chromium (Cr) content – martensitic/ferritic steels have made it possible to run ultra-supercritical (USC) steam power plants

that typically operate up to 630°C and 300 bar [**22**, **23**, **24**, **25**, **26**, **27**, **28**, **29**, **30**]. Of particular interest to this work is grade tempered martensitic steel that nominally contains 9% Cr, 1% molybdenum (Mo) and 0.2% vanadium (V) and is designated by the American Society for Testing and Materials (ASTM) as grade T91/P91 steel. The prefixes in this designation correspond to tubing and piping applications, respectively. This material is commonly employed for fabricating structural components such as steam headers, superheater and reheater tubes in USC power plants. Such components typically operate at high steam pressures and temperatures under a combination of cyclic (startup and shutdown) loading conditions with hold periods – lasting as much as a month – of sustained stress.

When metallic structural components are subjected to sustained or cyclic mechanical loading at ambient temperatures, they undergo elastic/inelastic or fatigue deformation, respectively. But when their operating temperature increases (typically greater than 40% of the absolute melting temperature T_{m}), the primary deformation and damage mode becomes creep or creep-fatigue (C-F), respectively. Thus, creep, fatigue and C-F behavior of high temperature structural components is an important design concern. As grade P91 steel is one of the preferred materials for such applications, it thus becomes imperative to understand the role and effects of each of these distinct deformation modes during its elevated temperature operation. In this context, few researchers have investigated the deformation response of grade P91 steel under different elevated temperatures – discussed in detail in Chapter 4 – mostly ranging between 450°C and 600°C. In an effort to increase the thermal (and net) efficiency of USC power plants as discussed earlier, it is desired to increase the maximum operating temperature of these steels up to 625-650°C. Hence, one of the goals of this work is to characterize the creep, fatigue and C-F interactions in this class of steels at the critical temperature, 625°C, and to achieve a thorough understanding of the deformation mechanisms involved.

But to achieve this, it requires extensive amounts of time and laboratory test data under various loading conditions. Since such experiments also require considerable test resources, it is advantageous to utilize the resources in several laboratories. Hence this work will utilize data from 16 laboratories worldwide that conducted tests (creep, fatigue and C-F) on grade P91 steel at 625°C in a round-robin (RR) program for evaluating the recently developed ASTM E2714-09 [**31**] standard on C-F testing. The results of this RR were primarily used to formulate a definitive precision and bias statement for supporting this test standard. This RR also allowed the assessment of the intra- and inter-laboratory variability in the C-F test data generated while following the guidelines recommended in the test standard. Therefore, the overall program led by the University of Arkansas was designed to meet several objectives that range from studying deformation mechanisms in grade P91 steel to contributing to C-F test standard development. The specimens tested by the various RR participants were sent to the University of Arkansas after testing for microscopic investigation of the influence of the different elevated temperature deformation and damage accumulation mechanisms on C-F lifetime.

Laboratory specimens, contrary to components in-service, are mostly tested under accelerated loading conditions to expedite the rate of deformation and specimen failure within realistic cost- and time-bounds. Predictive constitutive modeling thus plays a pivotal role in characterizing a material's response under long-term in-service conditions, with required input(s) from short-term laboratory test data. Therefore, this work will also involve the development of analytical constitutive models that can robustly predict the deformation response of grade P91 steel using the RR test data, if existing models do not perform satisfactorily. Appropriate scientific consideration is also accordingly provided therein to clearly distinguish the need for developing a better constitutive model in this regard.

1.2. Research objectives

The objectives of this dissertation work can thus be briefly summarized as follows:

1. Characterize the creep, fatigue and C-F interactions in grade P91 steel at 625°C. This task has been accomplished by collaboratively working with 15 other laboratories that have performed the required testing. As part of their RR participation, the University of Arkansas have contributed their creep deformation and rupture data and monotonic tensile test data. All other test data were sent to the University of Arkansas for analysis.
2. Understand the deformation and damage accumulation mechanisms under sustained and cyclic loading conditions. The participants of the RR program provided their tested samples to the University of Arkansas for microscopic investigation of the involved damage mechanisms.
3. Identify/develop robust analytical models for simulating and predicting the creep, fatigue and C-F behavior using all the available data while carefully incorporating the damage mechanisms observed in the test material at the test temperature.
4. Evaluate the new C-F test standard ASTM E2714-09 with the RR test data and
   (i) report the inter- and intra-laboratory variability observed in the C-F data after following the guidelines prescribed in this standard.
   (ii) determine the presence of any inherent biases in C-F life test data that may be associated primarily with specimen sizes or geometries.
   (iii) define an appropriate terminology for characterizing C-F crack formation, and
   (iv) recommend a more definitive statement on precision and bias in the C-F data to be included in the E2714-09 standard.

1.3. Significance and benefits of the performed research

In-service grade P91 steel structural components are typically operated under complex loading conditions at elevated temperatures leading to complex time dependencies that vary considerably with temperature, stress and strain. Therefore, for sound design considerations under those conditions, a thorough understanding of the creep, fatigue and C-F deformation mechanisms is required. The acquired knowledge can greatly help in designing and fabricating better elevated temperature structural components that can provide improved thermal efficiency while significantly lowering hazardous CO_2 emissions. Knowledge of the mechanisms involved will also aid in the selection of appropriate inspection intervals and minimizing the risk of catastrophic structural failures and their subsequent economic consequences and danger to human safety. To quantitatively validate this claim, published literature has shown that 9-12% Cr steels have progressively helped USC power plants to reduce their specific CO_2 emissions by ~ 30% over the last few decades [**17**, **32**, **33**].

1.4. Overview of the dissertation structure

Chapter 2 will provide a generalized discussion on the fundamentals of the different elevated temperature deformation and damage mechanisms, namely creep, fatigue, C-F interactions and oxidation kinetics, for a given material under different loading conditions. This will be followed by a description of the test material, grade P91 steel, and various physical metallurgical concepts related to it such as chemical composition, microstructural features and typical heat treatment methodologies in Chapter 3. Chapter 4 outlines the existing published experimental and constitutive modeling results for the creep, fatigue, C-F (and oxidation) deformation response of grade P91 steel

under different testing conditions. Chapter 5 provides all the relevant details and methods for the experimental tests performed as part of the RR that are considered in this work. This chapter also very briefly discusses the statistical methodology employed for assessing the intra- and inter-laboratory variability in the test results and for formulating the precision and bias statements from the RR data. A thermodynamically consistent perspective of crystal plasticity is presented in detail in Chapter 6 along with the formulation of a novel constitutive model that is shown to accurately simulate/predict the fatigue and C-F behavior of grade P91 steel. A modified version of an existing model is also proposed in this chapter for simulating the test material's creep deformation and rupture behavior along with the approach followed for the constitutive modeling efforts in this work. All the experimental and constitutive modeling results will be presented in Chapter 7 along with a detailed discussion of these results and their significance. This will be followed by a condensed summary of the conclusions of this work and recommendations for future work in Chapter 8.

The original contributions from this dissertation work are discussed in Chapters 6 and 7 while Chapters 2 through 5 establish the scientific groundwork for understanding the concepts and results discussed in these two chapters.

Chapter 2: ELEVATED TEMPERATURE DEFORMATION MECHANISMS

2.1. The need to understand deformation and damage mechanisms

To propose sound solutions to address the objectives of this dissertation, it is important to thoroughly recognize and understand the microstructure-property relationships of typical elevated temperature components. As per this approach, a clear understanding of a material's microstructural response under a given loading condition will offer better insights about the relevant failure mechanism(s) and expected lifetimes. This knowledge is then useful in improving the relevant mechanical properties for a given application by engineering the required microstructural changes in that material. This knowledge can also be useful in developing novel materials with desired properties by incorporating the required microstructural aspects. It therefore necessitates a profound comprehension of the microstructural evolution for candidate structural materials – metals and metallic alloys – at elevated temperature and pressure (or equivalently, stress). This highlights the importance of understanding the fundamentals of the most common deformation and damage mechanisms – creep, fatigue, C-F interactions and oxidation – observed in such materials at elevated temperatures.

2.2. Fundamentals of creep

Metallic structural components operating continuously at elevated temperatures over extended periods of time slowly accumulate inelastic – that includes plastic and viscous components – strains, even when subjected to sustained mechanical stresses that are much lower than the material's yield strength. Such undesirable progressive time-dependent inelastic deformation of

materials at elevated temperatures is referred to as *creep* [**34**, **35**, **36**]. Creep is often the life limiting design consideration in engineering applications when the absolute operating temperature T approaches a material's homologous temperature – T/T_{m} – of 0.4 or greater, where T_{m} is its absolute melting temperature. Although creep damage *always* increases with increasing temperature and exposure time, the rate of deformation is particularly dependent on a material's microstructure and the applied load. Hence, structural materials are typically classified as creep-ductile or creep-brittle when the creep ductility – plastic strain at failure – is higher ($\geq$ 5%) or lower ($<$ 5%), respectively. In this juncture, it is imperative to clearly define what failure, as described in the earlier context, means in creep design considerations. The definition of "failure" is solely dependent on the class of a given application as explained below and as schematically illustrated in Figure 2.1 [**37**, **38**]:

a) Applications that need to maintain precise dimensional tolerances or clearances during operation, as in turbine blades and discs.
b) Situations that must account for creep-induced buckling – instability of slender columns – under compressive loading, as in pressurized pipelines.
c) Applications during which stress decreases with time – *relaxation* – at constant deformation, as in pretensioned cables or bolts.
d) Instances where dimensional tolerance is relatively immaterial, although fracture needs to be avoided, as in steam turbine quick stop valves.

2.2.1. Laboratory testing conditions

Due to its time-dependent nature, creep damage in in-service components typically accumulates over years before eventual failure or rupture. Due to constraints imposed by limited use of resources, most experiments conducted at research laboratories typically run for weeks or few

months at the maximum. It is therefore obvious that experiments conducted to understand the nature of creep deformation under laboratory conditions cannot be run at in-service timescales. Hence, laboratory tests to comprehend creep deformation are performed under accelerated loading – stress and/or temperature are considerably raised than in-service conditions – to expedite the dynamics of deformation. Laboratory tests at nominally constant elevated temperatures can be run either at constant sustained load or at constant material deformation. The former, referred to as creep test, measures increase in deformation with time and the latter, referred to as stress-relaxation test, measures decrease in load with time. Of particular interest to this work is the creep test and hence will be the only topic of further discussion.

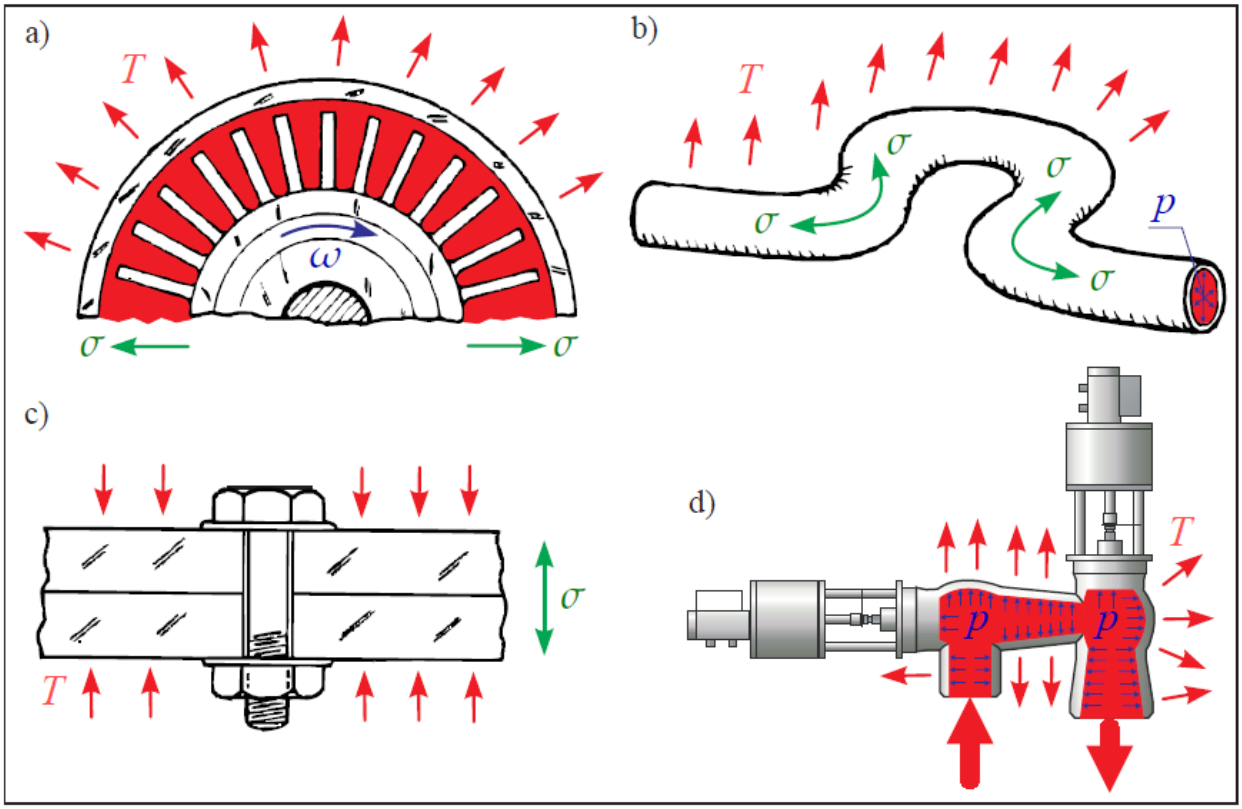

Figure 2.1. Importance of creep failure consideration as dictated by four classes of applications: a) displacement-limited, b) buckling-limited, c) relaxation-limited and d) rupture-limited, where T : exposure temperature, σ : external stress, ω : angular velocity and p : internal pressure [38].

2.2.2. Typical laboratory creep testing methodology

Creep tests of metallic materials are often conducted under constant tensile loads at a nominally constant temperature of relevance for the material under consideration. Cylindrical tension specimens are usually machined in accordance with guidelines established by the ASTM standard for creep testing, E139 [**39**]. A typical sequence of laboratory creep tests can be briefly outlined as follows:

(i) A standard cylindrical specimen of initial area A_0 is heated upto 0.4 T_m (where T_m is the absolute melting temperature) or higher and allowed to stabilize at the desired testing temperature (T) for few hours.

(ii) The external sustained mechanical load (F) for an experiment corresponds to an axial stress (σ_0) desired for evaluation and can be applied either in parts (pre-loading and/or interrupted loading at definite time intervals) or in full at the start of the experiment. It needs to be remembered that σ_0 is generally lower than the material's yield strength.

(iii) After thermal stabilization, the experiment begins wherein the deformation is measured by highly-sensitive and accurate transducers and continued till eventual failure or a predefined strain level.

As expected, the instantaneous material response (ε^{el}) is elastic (*i.e.,* no evident macroscopic permanent deformation occurs) [**40**]. With time, creep curves – specimen elongation (deformation or strain) graphically plotted against time – can be obtained, wherein the strain is measured over the specimen's reference or gage length [**41**]. If the creep tests are continued till eventual failure of the specimen, they are referred to as creep rupture tests. Hence, laboratory creep tests can be

interrupted at any point in time when the available data is deemed sufficient for the objective in hand.

2.2.3. Distinct regimes of creep deformation

Figure 2.2 shows a typical creep curve of metallic materials where the axial engineering strain ε is plotted against elapsed time t [**37**, **38**, **42**, **43**, **44**]. This curve shows the time-dependent strain increasing at varying rates of deformation over time. Accordingly, the creep curve can be identified with three distinct regimes of strain-rate as indicated by I, II and III in this figure [**41**, **42**, **45**].

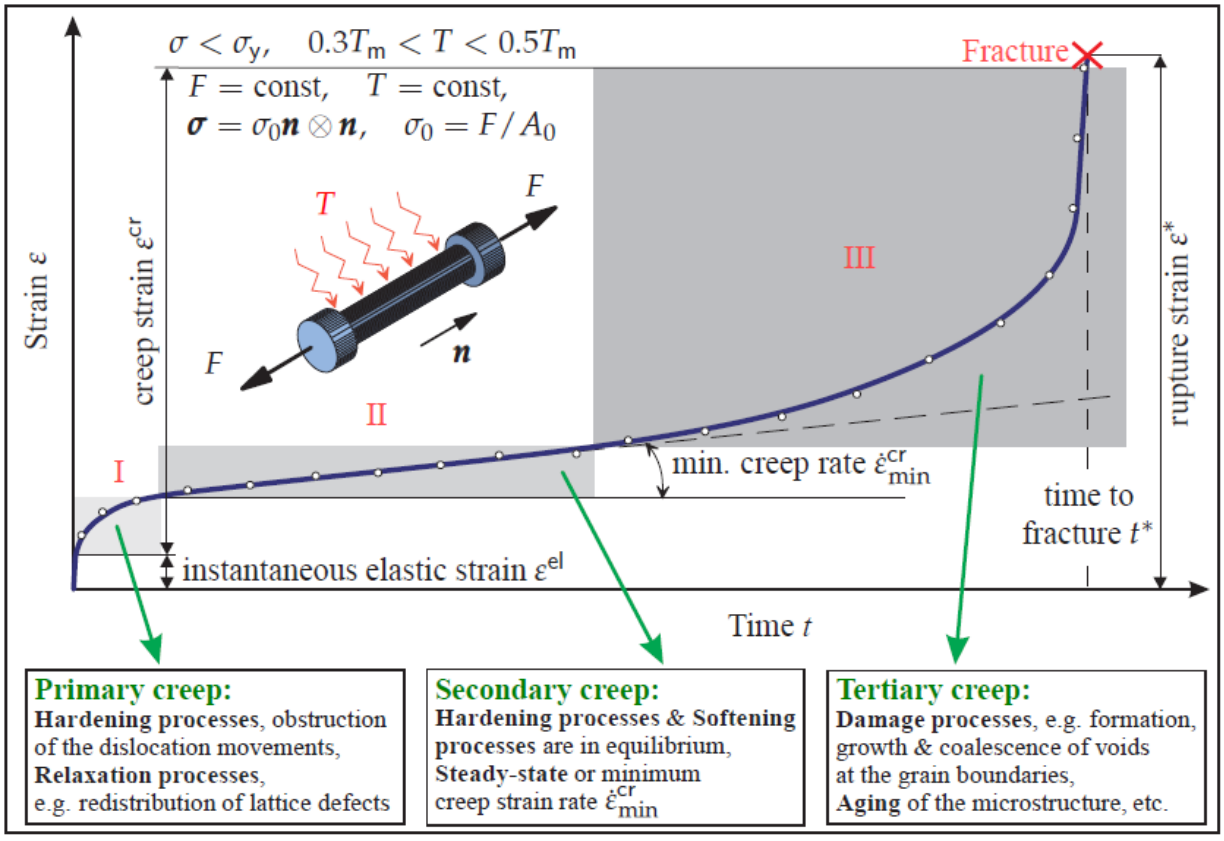

Figure 2.2. Schematic representation of a uniaxial creep curve of metallic materials where engineering strain is plotted against elapsed time under a constant tensile load *F* and temperature *T* (regimes: I – primary creep, II – secondary creep and III – tertiary creep), after [40, 43].

The first concave-shaped region of continuously decreasing creep strain-rate – regime I – is known as primary creep. During this transitory stage, the creep rate $\dot{\varepsilon}^{\mathrm{cr}}$ (see Equation (2.1)) decreases with time to that of a value in the subsequent stage (the minimum creep rate, $\dot{\varepsilon}^{\mathrm{cr}}_{\mathrm{min}}$). The decreasing creep rate is attributed to an increase in internal resistance to creep deformation by strain hardening – a phenomenon where dislocation density increases leading to increased stresses for deformation – or equivalently to a decrease in free or mobile dislocations [**40**].

$$\dot{\varepsilon}^{\mathrm{cr}} = \frac{d\varepsilon}{dt} \qquad \ldots\ldots\ldots \quad (2.1)$$

The second linear region of approximately constant creep strain-rate – regime II – is known as secondary or steady-state creep. During this stage, the creep rate remains nearly constant at $\dot{\varepsilon}^{\mathrm{cr}}_{\mathrm{min}}$ with time and is attributed to a state of equilibrium between the rate of generation of new dislocations that contribute to strain hardening and the rate of dynamic recovery (via diffusion mechanisms) of existing dislocations that contribute to softening [**40**]. As the dislocation density increases with strain hardening, the strain- (and internal-) energy of the material increases and provides the thermodynamic driving force for internal energy reduction via dynamic recovery at elevated temperatures. Hence, recovery happens by rearranging/annihilating existing dislocations into lower energy structures or sub-grain boundaries and leads to a consequent decrease in dislocation densities. It has been empirically observed that the minimum creep rate $\dot{\varepsilon}^{\mathrm{cr}}_{\mathrm{min}}$ and time to rupture t^* mostly follow an inverse relationship as per the Monkman-Grant Equation (2.2):

$$\dot{\boldsymbol{\varepsilon}}^{\mathbf{cr}}_{\mathbf{min}} = \frac{\boldsymbol{C}}{(\boldsymbol{t}^*)^{\boldsymbol{m}}} \qquad \ldots\ldots\ldots\ldots\ldots \quad (2.2)$$

where C is a constant that depends on the creep deformation strain (total elongation of the specimen) and m is a fitting constant often nearly equal to 1.

The third and final convex-shaped region of increasing creep strain-rate – regime III – is known as tertiary or accelerated creep. During this stage, the creep rate accelerates exponentially till eventual failure (rupture) at time t^*, due to softening induced by creep damage accumulation and localized deformation. Once necking – localized decrease in cross-sectional area along the specimen's gage length – begins as creep deformation proceeds, increase in local stress is considerably higher than the macroscopic or loading stress. Thus, necking expedites the specimen's rupture leading to rapidly increasing strain-rates at times closer to t^*. Increasing creep rates with time can also be attributed to microstructural evolution that usually consists of dynamic recovery and recrystallization, coarsening or over-ageing of secondary precipitates etc., that collectively decrease resistance to creep [**41**, **42**]. Physical damage to metallic specimens after creep rupture is found to have grain boundary separation and development of microstructural voids, and intergranular cavitation and cracking often along grain boundaries [**41**, **42**].

The uniaxial creep curve can be used to deduce a number of creep deformation properties of materials, with the most important of them being the value of the minimum or steady-state creep rate $\dot{\varepsilon}_{\mathbf{min}}^{\mathbf{cr}}$. A graphical plot of Equation (2.1) over time shows a "bath tub" shaped curve (see Figure 2.3), wherein the portion with the nominally constant minimum creep rate corresponds to the secondary creep stage (regime II) of the creep curve. This parameter is of utmost importance for design considerations as it provides some predictability of creep strain-rate with time under a given loading condition to avoid unexpected failures [**40**, **46**]. It is important to observe that primary creep is short-lived as compared to secondary creep regime. Moreover, in-service components also do not enter tertiary creep stage in practice and hence creep rates in this regime are not typically considered.

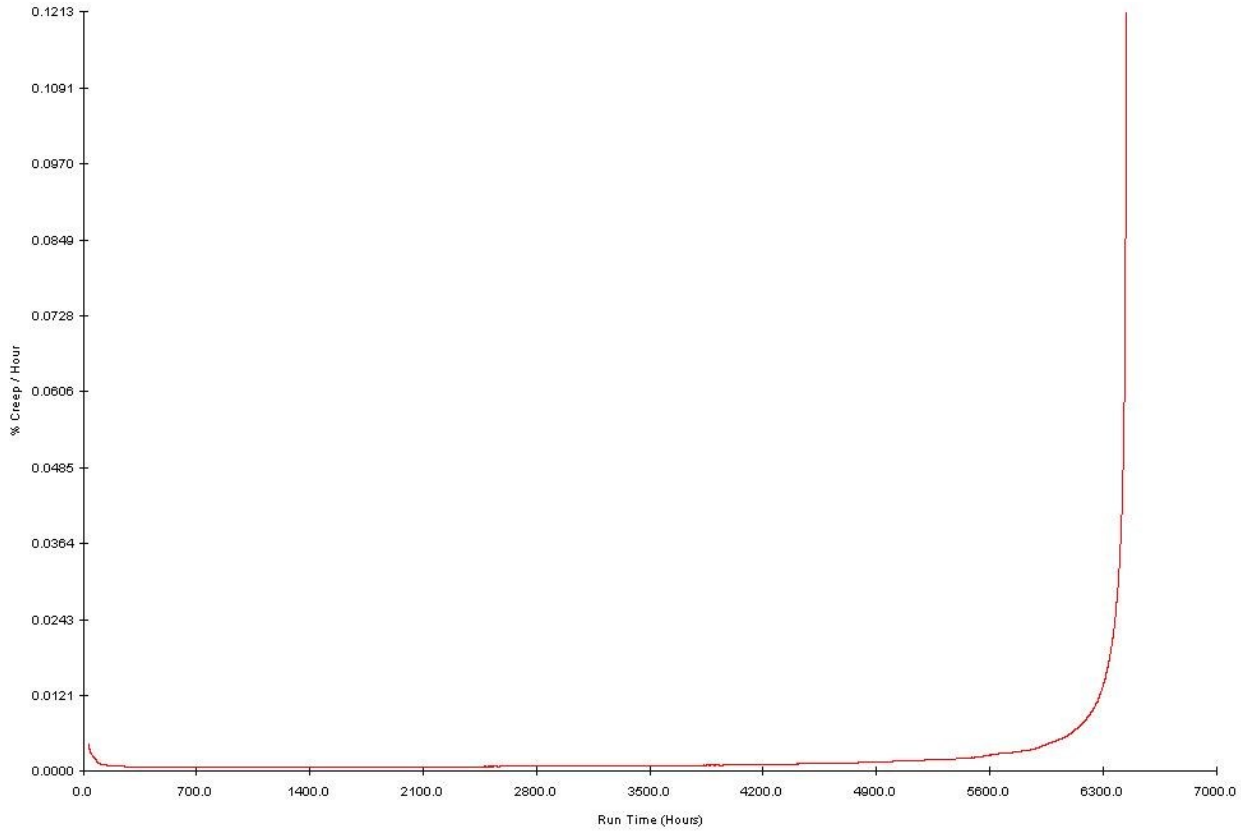

Figure 2.3. Variation of creep rate over time for a typical laboratory creep test.

As discussed earlier, the shape of the creep curve is determined by several competing reactions that include strain hardening, dynamic softening and damage evolution [**47**]. Of these microstructural responses, strain hardening tends to decrease the creep rate $\dot{\varepsilon}^{\mathrm{cr}}$, whereas the remaining two tend to increase the same. Balance among these responses under a given loading condition therefore effectively determines a creep curve's shape. As shown in Figure 2.4, both the test temperature and external stress level also influence the creep curve characteristics. Moreover, both these parameters naturally influence the duration and extent of strain accumulated during the three distinct regimes of creep deformation. At temperatures sufficiently below 0.4 T_{m} and after the instantaneous elastic response, accumulated creep strain is virtually independent of time. But as either temperature or stress increases, the following observations can be made [**40**]:

1) Increased instantaneous elastic strain at the instant of load application.

2) Considerable increase in the minimum creep rate, when regime II apparently exists.

3) Shorter rupture lifetime of the tested specimen.

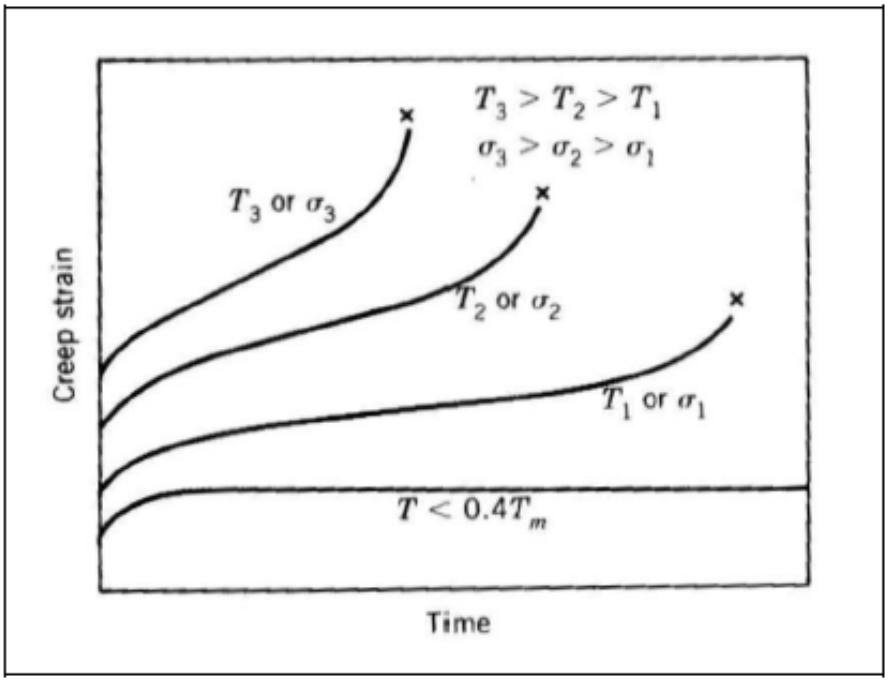

Figure 2.4. Schematic showing the influence of applied stress and test temperature on creep deformation characteristics [40].

It is important to remember that structural components employed in USC power plants are expected to operate at high pressure and temperature and/or aggressive environments for a service life of 30 years or more. Hence, materials that typically possess high creep resistance strengths are expected to be chosen for any given application. But because of prolonged exposure particularly to elevated temperature and stress, the material responds by continuous evolution of its microstructure mostly leading to gradual degradation of properties and eventual reduction in expected lifetime. The typical microstructural evolution during creep deformation of a metallic material is discussed next.

2.2.4. Microstructural damage evolution during creep deformation

After the instantaneous elastic response, creep damage begins to accumulate in the form of isolated internal cavities (voids) along grain boundaries in the secondary creep stage. At the end of this stage or beginning of tertiary creep stage, due to increasing deformation, the damage becomes orientated (under most conditions) and prominently visible under an optical microscope. These cavities tend to coalesce in the form of distinct microcracks most notably near or at the grain boundaries. Due to decreasing cross-sectional area to sustain the external loading F, localized stresses increase rather dramatically and lead to rapid localized deformation at multiple regions in the specimen. As the minimum creep rate is directly proportional to σ^{n} (where n is the Norton's power-law creep exponent), macroscopic creep rate increases faster than the external stress σ [**38**], although localized creep rates are much higher due to formation of macrocracks. Figure 2.5 shows a schematic of microstructural creep damage progression over time along with typical failure inspection intervals and probable measures after such checks.

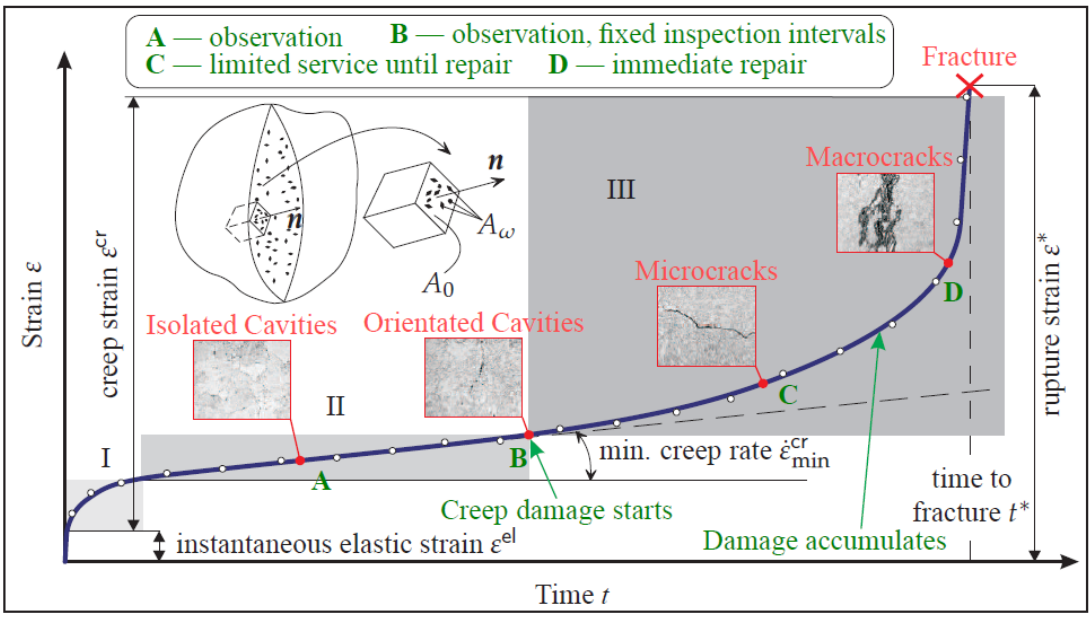

Figure 2.5. Schematic of creep damage evolution and common failure inspection operations in a high-temperature component, after [38, 48].

It has been proposed by Ashby [**49**] that six independent deformation mechanisms can occur during the creep damage of a material: defect-free flow, elastic deformation, dislocation glide, dislocation (or power-law) creep, volume diffusion flow and twinning. To graphically distinguish and compactly represent these different mechanisms, Frost and Ashby [**49**] developed the so-called "deformation-mechanism map" using an earlier methodology developed partly by Graham and Walles [**50**]. Figure 2.6 shows a schematic illustration of such a map at different creep strain-rates and it provides a snapshot of the mechanisms dominating creep damage at the different stress- and temperature-dependent regimes. Since twinning contributes limitedly to creep deformation, it is usually not represented in these maps. Contours of constant creep rates are presented in this map as functions of the normalized equivalent stress σ_{eq}/G and the homologous temperature T/T_{m}, where σ_{eq} is the equivalent stress that controls secondary creep and G is the shear modulus. This map also provides a good estimate of the expected creep rates ($\dot{\varepsilon}_i$, where i = 1, 2, 3 and 4 in Figure 2.6) at a given combination of temperature, T and uniaxial stress, σ. Furthermore, these different contours also indicate the range of σ and T in which one can expect to find each one of these different deformation mechanisms. Maps of this kind are available for many metallic and ceramic systems in the literature [**37**, **38**, **42**, **43**, **44**, **51**, **52**] and greatly help in the careful selection of a particular material for any elevated temperature application.

2.3. Fundamentals of fatigue

Rather than pure monotonic loads, engineering structural components are often subjected to cyclic loads that can fluctuate periodically or non-periodically over time. Under such loading conditions – scientifically termed as *fatigue* – cyclic stresses are induced in a material that can cause progressive structural damage and lead to eventual failure. Fatigue is defined by ASTM [**53**] as "*the process of progressive localized permanent structural changes occurring in a material subjected to conditions that produce*

fluctuating stresses and strains at some point or points and that may culminate in cracks or complete fracture after a sufficient number of fluctuations." Although fatigue failures are highly common in the aerospace industry, it is estimated that 85-90% of all structural failures occur under some degree of their influence [**54**].

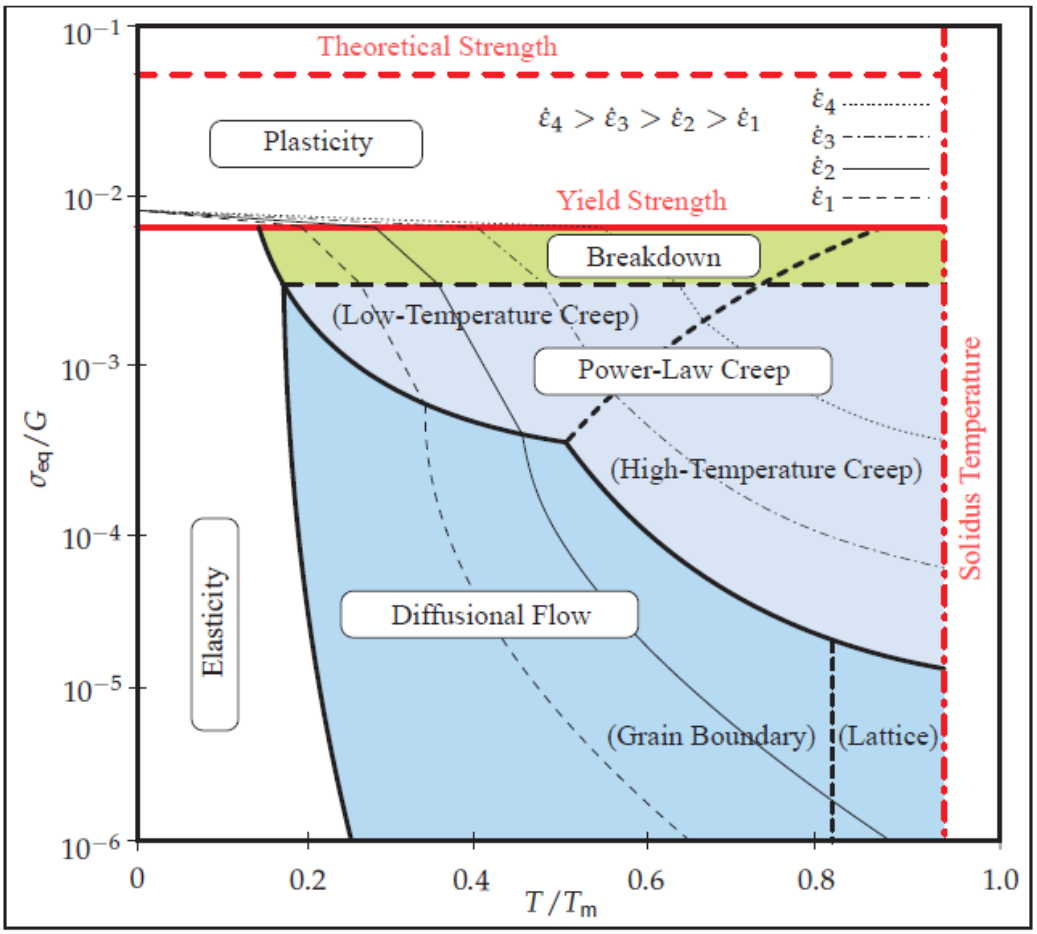

Figure 2.6. Schematic illustration of a typical creep deformation-mechanism map at different creep strain-rates, after [21, 49].

2.3.1. Two distinct domains of fatigue failure

The path to failure under cyclic loading conditions is broadly observed to exhibit two distinct domains depending on the amplitude of external strain applied *per cycle*. In the first domain – referred to as high cycle fatigue (HCF) – material response is predominantly elastic as the magnitude

of the maximum cyclic stress is considerably lower than its yield strength (point **B** in Figure 2.7). Consequently the material failure occurs after a large number of loading cycles (typically > 10^5) and in some cases, failure may not even occur. On the other hand, in the second domain – referred to as low cycle fatigue (LCF) – the material undergoes macroscopic plastic deformation as the magnitude of the maximum cyclic stress is always greater than its yield strength. Consequently the material failure occurs at much lower loading cycles (typically 10^3-10^4) depending on the applied strain amplitude per cycle and other test conditions. Of particular interest to this work is the LCF type of loading and hence will be the only topic of further discussion.

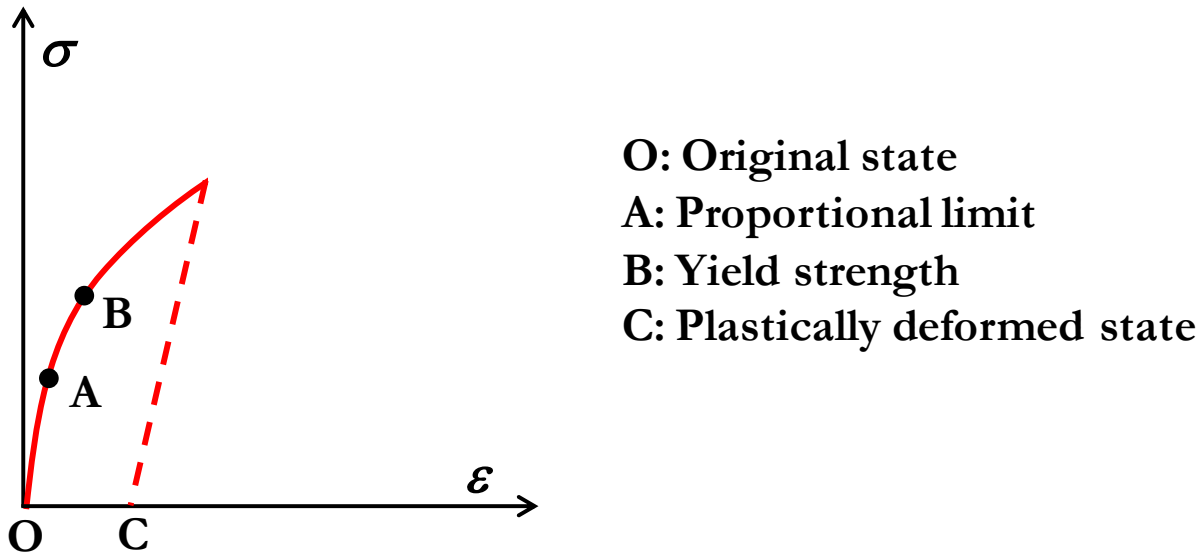

Figure 2.7. Typical stress-strain curve obtained for a uniaxial monotonic tensile test.

2.3.2. Discussion of fatigue related terminology

Figure 2.7 illustratively shows a typical stress (σ) – strain (ε) curve obtained for a uniaxial monotonic tensile test of a metallic specimen. If a material is strained from its original unstrained state (point **O**) till the proportional limit (point **A**), the strain response is predominantly elastic and no evident plastic deformation occurs. On the contrary, if the material is strained beyond its yield

strength (point **B**) macroscopic plastic deformation ensues until the external load is removed. When the material is completely unloaded at a point beyond **B,** the material reaches zero stress at some abscissa point **C** and the horizontal distance **OC** is numerically equal to the induced plastic strain. It is further noted herein that unloading is always elastic (*i.e.,* a linear plot) and hence the slope of this line is a better estimate of the elastic or Young's modulus.

The basic tenets discussed for uniaxial monotonic loading can be equally extended to uniaxial continuous LCF loading. Figure 2.8 illustratively shows a typical σ–ε loading history, also referred as a hysteresis loop, obtained for a uniaxial strain-controlled – between ε_T and ε_C – LCF test of a metallic specimen. The material is initially loaded from its original state (point **O**) till a desired tensile (assumed positive) strain amplitude, ε_T. During this loading, the stress within the material changes from zero to σ_{max}, respectively. The material is then unloaded completely till it reaches zero stress at point **C**. At the end of tensile unloading, the material is loaded compressively (assumed negative) till ε_C wherein the respective stress within the material is σ_{min}. If ε_T and ε_C are both equal in magnitude – or equivalently, zero mean strain – then it is termed as symmetrical loading and asymmetrical loading otherwise. The material then undergoes compressive unloading to reach zero stress at point **D**. Thus, four components – tensile and compressive loading and unloading – together constitute one continuous LCF hysteresis loop while the horizontal distance **CD** numerically corresponds to the inelastic strain generated at the end of the cycle. The above sequence of loading and unloading events will continue until the test is stopped or completed as per certain testing criteria. In this context, the following four definitions commonly used in cyclic testing can be defined in terms of stress, as shown from Equations (2.3) to (2.6). A similar set of definitions can also be obtained in terms of strain by replacing σ_{max} and σ_{min} with ε_T and ε_C, respectively.

$$\text{Mean stress, } \boldsymbol{\sigma_m} = (\boldsymbol{\sigma_{max}} + \boldsymbol{\sigma_{min}})/2 \quad \text{..... (2.3)}$$

$$\text{Stress range, } \boldsymbol{\Delta\sigma} = (\boldsymbol{\sigma_{max}} - \boldsymbol{\sigma_{min}}) \quad \text{..... (2.4)}$$

$$\text{Stress amplitude, } \boldsymbol{\sigma_a} = (\boldsymbol{\sigma_{max}} - \boldsymbol{\sigma_{min}})/2 \quad \text{..... (2.5)}$$

$$\text{Stress ratio, } \boldsymbol{R} = (\boldsymbol{\sigma_{min}}/\boldsymbol{\sigma_{max}}) \quad \text{..... (2.6)}$$

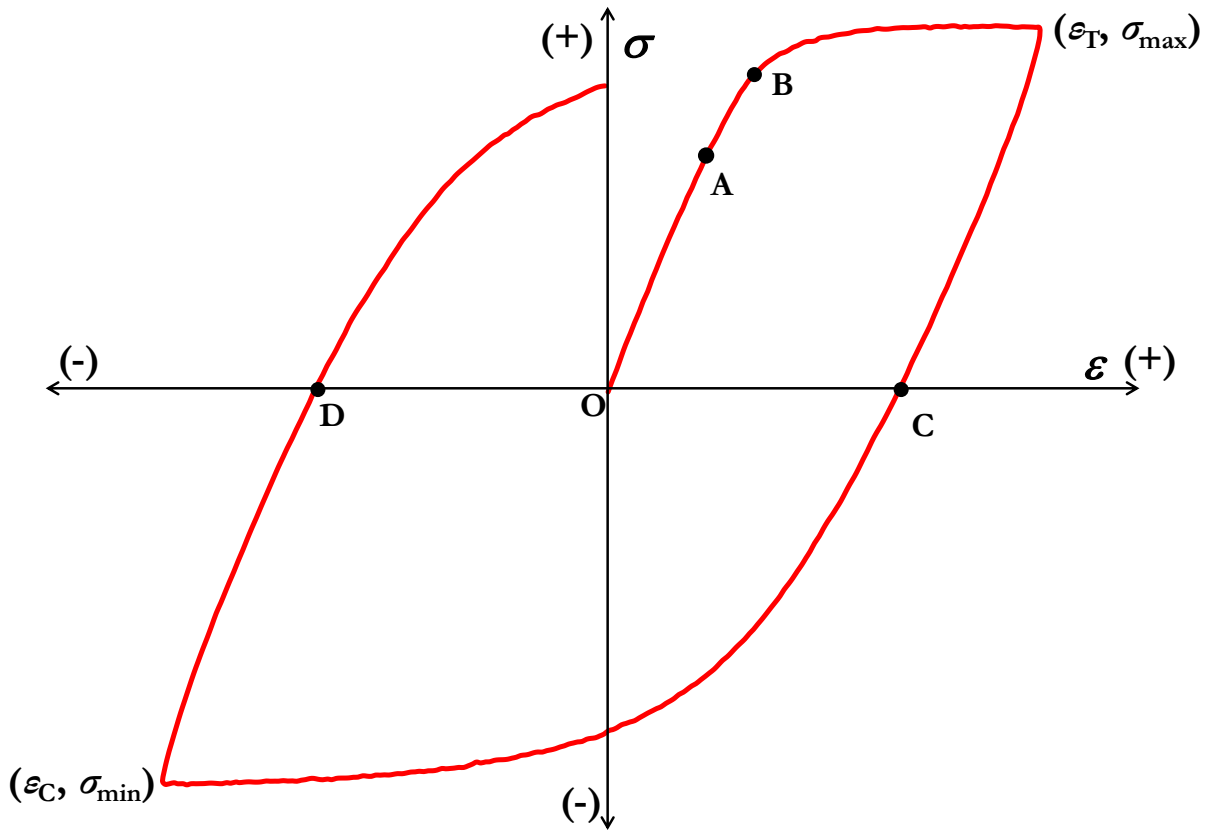

Figure 2.8. Typical hysteresis loop obtained for a uniaxial continuous LCF test.

It is important to understand that the cyclic hysteresis loops and their shape evolution with loading cycles N will vary depending on the material and accumulated inelastic strain. As dependent on the starting microstructure, strain amplitude and other test parameters, a metallic material may exhibit one of the following four characteristics under continuous LCF loading. For the sake of

analytical comparison, two loading cycles N_i and N_{i+1} are considered where i = 1, 2,… till end of testing.

- Cyclically harden: $|\boldsymbol{\sigma}_{\mathbf{max}}|_{N_i} < |\boldsymbol{\sigma}_{\mathbf{max}}|_{N_{i+1}}$ and $|\boldsymbol{\sigma}_{\mathbf{min}}|_{N_i} < |\boldsymbol{\sigma}_{\mathbf{min}}|_{N_{i+1}}$
- Cyclically soften: $|\boldsymbol{\sigma}_{\mathbf{max}}|_{N_i} > |\boldsymbol{\sigma}_{\mathbf{max}}|_{N_{i+1}}$ and $|\boldsymbol{\sigma}_{\mathbf{min}}|_{N_i} > |\boldsymbol{\sigma}_{\mathbf{min}}|_{N_{i+1}}$
- Remain stable: $|\boldsymbol{\sigma}_{\mathbf{max}}|_{N_i} \cong |\boldsymbol{\sigma}_{\mathbf{max}}|_{N_{i+1}}$ and $|\boldsymbol{\sigma}_{\mathbf{min}}|_{N_i} \cong |\boldsymbol{\sigma}_{\mathbf{min}}|_{N_{i+1}}$
- Mixed behavior: a combination of above behaviors depending on the test condition

Figure 2.9 schematically shows the first two aforementioned cyclic behaviors under strain-controlled LCF laboratory testing for a symmetrical triangular loading waveform. All of these characteristic material responses will be encountered until the formation or initiation of a macroscopic crack within a laboratory test specimen's gage length. Once a crack initiates, localized deformation and damage can proceed under lower stresses and gradually leads to a drop in the external load.

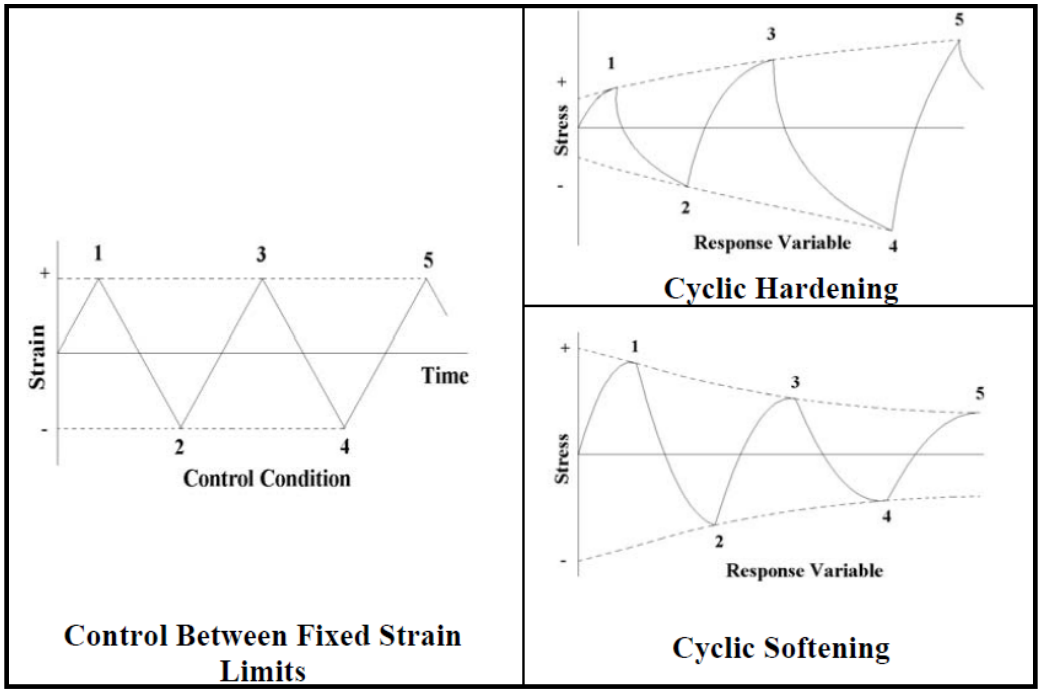

Figure 2.9. Cyclic hardening and softening behavior observed under strain-controlled LCF testing [54].

2.3.3. Typical laboratory LCF testing methodology

Strain-controlled LCF tests are typically conducted under cyclic loads at a nominally constant temperature and strain amplitudes of relevance for the material under consideration. Uniform-gage dogbone specimens are usually machined and surface-finished in accordance with guidelines established by the ASTM standard for strain-controlled fatigue testing, E606 [**55**]. A typical sequence of laboratory LCF tests can be briefly outlined as follows:

(i) A standard dogbone specimen of initial area A_0 is heated upto the desired testing temperature (T) and allowed to stabilize there for few hours.

(ii) An elevated temperature extensometer, usually a ceramic, is attached to the specimen gage length to measure its axial elongation/compression during testing. Since this transducer measures strain, it also monitors and controls the entire sequence of testing.

(iii) After adding the linear strain (due to thermal expansion) to the specimen's gage length, the desired strain amplitudes (ε_T and ε_C) are numerically estimated and set as the test control parameters. The external load (F), corresponding to an axial stress (σ), is applied using a moving ram and actuator setup that is commonly powered by a servo-hydraulic machine. Since it is a LCF test, it needs to be remembered that σ at the start of testing is considerably higher than the material's yield strength.

(iv) LCF loading cycles are continued till eventual fracture or a predefined termination condition, such as a drop in the external load. On further elapse of time, hysteresis loops – cyclic strain graphically plotted against cyclic stress – can be obtained for data analysis and interpretation.

2.3.4. Microstructural damage evolution during LCF deformation

As discussed earlier, LCF deformation induced damage and eventual failure proceeds progressively with every loading cycle (or equivalently, time) and can be broadly classified as a four-stage process as follows:

1) Cyclic hardening or softening
2) Crack nucleation and formation
3) Stage I and II crack growth or propagation
4) Final failure or fracture

This work deals exclusively only with the first two steps of LCF induced damage (that are discussed earlier) within the test material and hence the last two steps are not particularly considered for further discussion herein.

2.4. Fundamentals of creep-fatigue interactions

2.4.1. Degree of creep-fatigue interaction

Service lifetime of metallic structural components is expected to reduce considerably when they combiningly operate under cyclic loads at elevated temperatures. The degree of C-F interactions within a material will vary depending on the strain range, operating temperature, duration and type of hold time (the amount of time in a cycle where either the stress or strain is held constant during LCF loading), frequency of loading and ductility – plastic strain at failure – of the material. It is also possible to have predominantly creep or fatigue dominated deformation with very minimal contribution from C-F interactions. Figure 2.10 shows a schematic of the different types of C-F interaction based failure mechanisms possible in a polycrystalline metallic material at elevated temperatures and stress [**56**]. Furthermore, with prolonged elevated temperature exposure, oxidation

can significantly increase the physical damage along with these deformation mechanisms to reduce the life expectancy or endurance even further [**57**]. Hence, C-F interactions (along with oxidation kinetics discussed in section 2.5) in elevated temperature structural components need to be carefully considered as part of sound design practices.

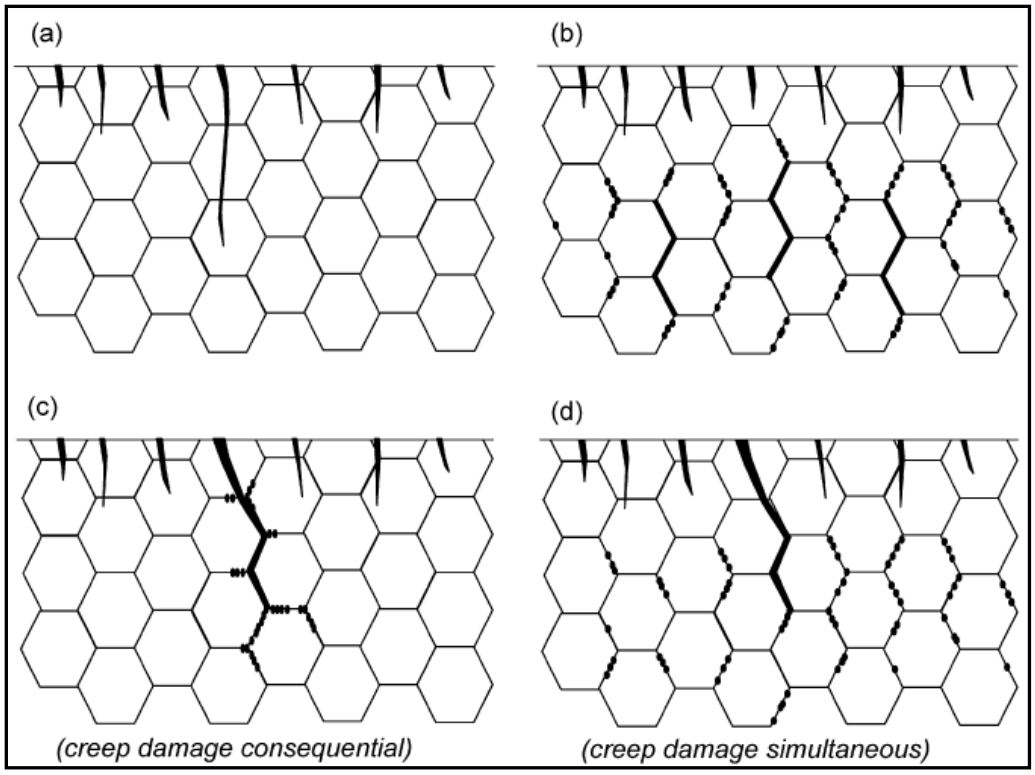

Figure 2.10. Schematic illustrations of the different failure mechanisms in polycrystalline metallic materials operating at elevated temperatures under C-F conditions, where damage can be dominated by (a) fatigue, (b) creep, and (c) and (d) by varying degrees of C-F interactions. In (c) the creep damage accumulates consequentially while in (d) it accumulates simultaneously [56].

2.4.2. Typical laboratory C-F testing methodology

Most of the characteristics explained earlier for LCF testing hold equally good for C-F testing. Rather than continuous LCF loading waveforms (shown in Figure 2.9), waveforms that contain a hold period at any desired value of tensile and/or compressive strain are typically

employed for strain-controlled C-F testing. The duration and type of hold depends on the material and actual service condition of the component under investigation and other scientific considerations. Figures 2.11(a) and (b) show the hysteresis loops obtained for strain- and stress-controlled C-F testing with a tensile hold at maximum strain and stress, respectively. The latter is not considered in this work and hence shown here only for illustrative comparison. Figure 2.11(a) also shows σ_{relax} that corresponds to the degree of stress relaxation observed during the tensile hold period. The degree of this stress relaxation can be better described by graphically plotting the stress variation during hold against the duration of hold time period, t_{h} (see Figure 2.12). This plot indicates that maximum stress (σ_{max}) is induced in the material at the start of hold and then the stress gradually relaxes with time during the hold period due to creep deformation.

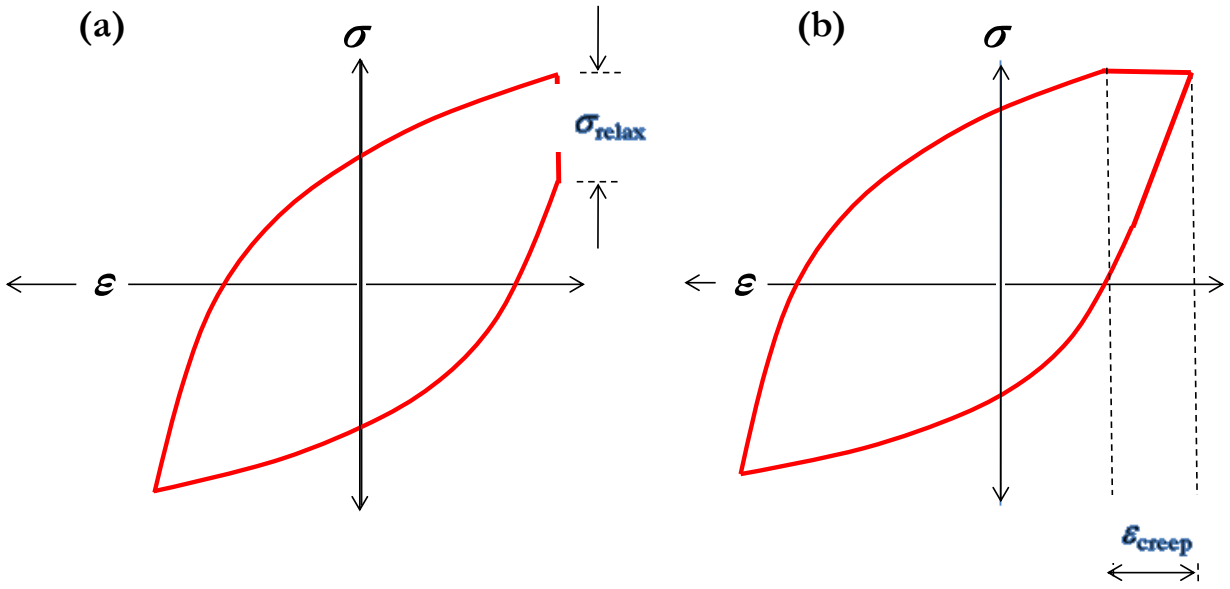

Figure 2.11. Schematic illustration of the cyclic stress-strain loading history of C-F tests with (a) a tensile hold at maximum strain in strain-control mode and (b) a tensile hold at maximum stress in stress-control mode, where σ_{relax} and $\varepsilon_{\text{creep}}$ denote stress relaxation and cyclic creep strain, respectively.

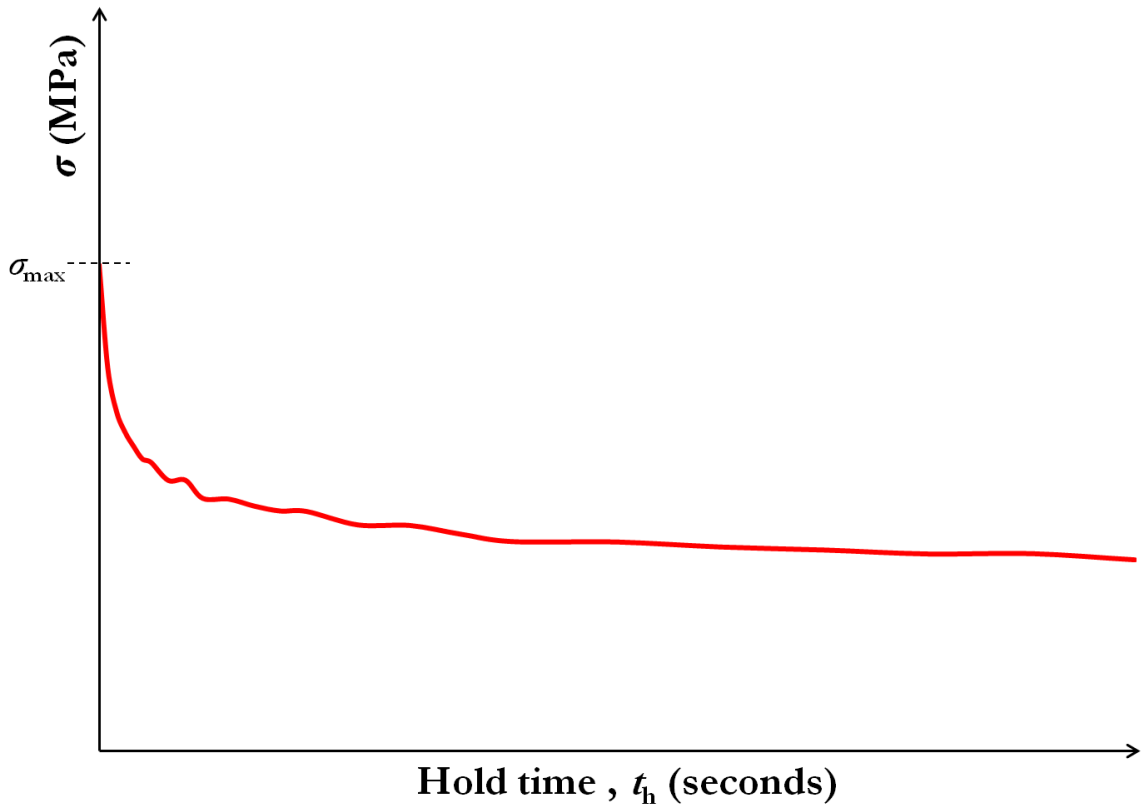

Figure 2.12. Graphical illustration of stress relaxation over time during the hold time period of a C-F test.

2.5. Fundamentals of oxidation kinetics

Along with other deformation mechanisms, environmental oxidation too plays a critical role in expediting the deformation rate of metallic materials at elevated temperatures. Oxidation is the progressive degradation of a metallic component (or substrate) due to its chemical interaction with the operating environment – specifically oxygen (O_2) – during in-service exposure. This effect is particularly pronounced at elevated temperatures due to thermodynamic instability of the substrate and enhanced vulnerability to chemical attack induced under such conditions. The rate of oxidation and oxide layer formation depends on several factors which can be broadly classified as follows:

- Chemical composition, heat treatment and surface finish of the substrate

- Gas composition and partial pressure of the operating environment
- Degree of strain enhancement
- Operating temperature
- Exposure time

Depending on the combination of these factors, oxidation kinetics can be very slow to the point that the substrate is virtually unattacked or comparatively very fast leading to enhanced localized damage that tends to generate stress concentrations. The last two abovementioned factors are particularly critical since oxidation kinetics *always* increase with temperature and time.

Figure 2.13 shows a schematic of the five stages typical of oxidation process during the elevated temperature operation of a metallic component. Stage 1 involves the heterogeneous nucleation and adsorption of dissociated oxygen ions (positively charged anions) on the metal substrate surface by inward atomic diffusion. This naturally leads to the formation and growth of surface oxide layers with varying thickness over time (Stage 2) under continuous elevated temperature exposure. Once an oxide film covers the substrate surface, oxidation continues via solid-state diffusion of the reacting species that increases the thickness of the existing surface layer. Internal oxidation can also occur below the substrate surface leading to the formation of random stress concentrations within the material (Stage 3). As dependent on other test parameters, development of microcracks, voids and cavities within the surface oxide layer(s) occurs that also serve as least resistance paths for accelerated diffusion in Stage 4. Finally, these microcracks can coalesce to form distinct macrocracks in Stage 5 that can chemically attack the underlying substrate surface and also assist other deformation mechanisms towards accelerated localized damage accumulation.

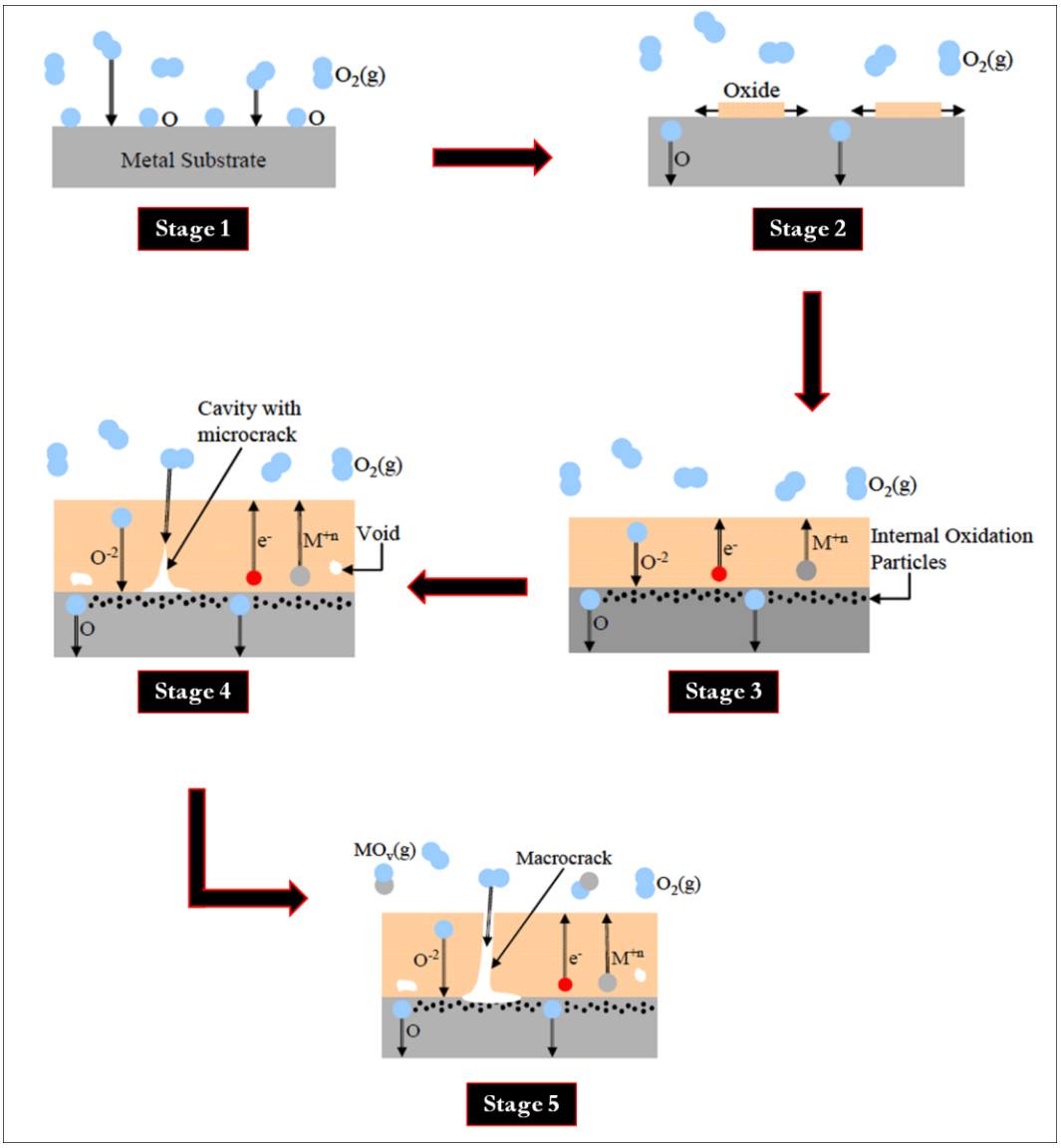

Figure 2.13. Schematic illustration of five stages of oxidation process between a metallic substrate and oxygen from the operating environment, based on [58].

Although a compact oxide film can be partly beneficial as a thermal insulation, development of multiple oxide layers – that are generally porous or brittle – eventually volatize and/or melt the underlying metallic substrate surface at elevated temperatures and can thus become detrimental.

Chapter 3: TEST MATERIAL

3.1. Background on 9-12% chromium martensitic/ferritic steels

It all began in 1912 when Krupp and Mannesmann [**59**, **60**] designed and produced the first member of this class of steels primarily for steam turbine blades: a 12% Cr steel alloyed with 2-5% Mo. In the 1920s, the Cr-Mo steels slowly began to find applications in conventional power generation plants. In the 1940s, the 2.25% Cr-1% Mo steel – designated by the ASTM as grade P22/T22 – was progressively developed and is still widely in use today. By adding 9% Cr for improved corrosion and oxidation resistance, grade P9 (9% Cr-1% Mo) came into existence and retrospectively both these steels constituted the zeroth generation of martensitic/ferritic steels. Further increments of Cr along with new alloying elements like V, niobium (Nb) and tungsten (W) for improved creep strengths constituted the first generation of these steels. Optimization of carbon (C), Nb and V with addition of nitrogen (N) in existing steels constituted the second generation that comprises grades like grade P91 (modified P9) [**61**]. Further optimization of alloying elements like Mo and addition of boron (B) and copper (Cu) constituted the third generation in the 1990s with much improved creep strengths and steam oxidation resistance [**62**, **63**, **64**, **65**]. The fourth generation represents all the development efforts beyond late 1990s till today [**66**, **67**, **68**, **69**, **70**, **71**, **72**]. A succinct summary of all the steel generations is presented in Table 3.1 [**73**].

The development of 9-12% Cr martensitic/ferritic steels has not only ensured better efficiency of fossil-fired steam power plants from an economic perspective, but also from environmental considerations [**5**, **7**, **20**, **74**, **75**, **76**, **77**, **78**]. To quantitatively illustrate the latter claim, ~ 30% reduction in specific CO_2 emissions has been reported over the last few decades, along with a doubling of creep strength [**17**]. Accordingly, it is obvious that this class of steels have increasingly

found many potential applications in thin- and thick-walled components of advanced steam power plants over the past five decades (see Figure 3.1) [**5**, **9**, **12**, **32**, **33**, **59**, **79**, **80**, **81**, **82**, **83**, **84**].

Table 3.1. Evolution of ferritic/martensitic steels for power-generation industry [73].

Generation Number	**Application Period**	**Steel Modification**	**10^5 h Rupture Strength,** 600 ºC (MPa)	**Steel Grades**	Max. Application Temperature (ºC)
0	1940-60		40	T22, T9	520-538
1	1960-70	Addition of Mo, Nb, V to the simple Cr-Mo steels	60	EM12, HCM9M, HT9, HT91	565
2	1970-85	Optimization of C,Nb,V, N	100	HCM12, T91, HCM2S	593
3	1985-95	Partial substitution of W for Mo & add. of Cu,N,B	140	NF616, E911, HCM12A	620
4	Future	Increase of W, Add. of Co	180	NF12, SAVE12	650

Of particular interest to this work is the grade P91 steel that belongs to the class of high-chrome martensitic/ferritic steels and will be elaborated next.

3.2. Background on grade P91 steel

Developed by metallurgically modifying ferritic steel grade P9, grade P91 steel was first studied under the Advanced Alloy Technology program at the Oak Ridge National Laboratory (ORNL) in the late 1970s [**19**, **85**, **86**, **87**]. The primary objective of developing this new alloy was to qualify it for use in structural components (pipes and vessels) of an liquid metal fast breeder reactor (LMFBR) [**2**, **13**]. It was designed to replace grade 304 austenitic stainless steels and grade P22 steels for some structural applications [**86**, **87**] requiring improved weldability and fracture toughness than

their existing 9-12% Cr counterparts [**87**]. Since 1980, grade P91 has found extensive use in conventional steam power plants [**85**, **88**] and was approved for construction under the rules of Section I and VIII of the American Society of Mechanical Engineers (ASME) Boiler and Pressure Vessel Code [**89**]. They are found to offer the best combination of superior creep strength, excellent steam oxidation and thermal fatigue resistance, improved anti-corrosion and environmental attack protection, high thermal conductivity and low thermal expansion, good weldability, minimal cost and good manufacturability [**23**, **82**, **90**]. Due to this reason, they are one of the preferred materials for USC power plant and petrochemical refinery components like steam generators, turbine blades and rotors, boilers, water-wall tubes, superheater and reheater tubes, main steam pipes, header pipes and bolting [**20**, **21**, **91**].

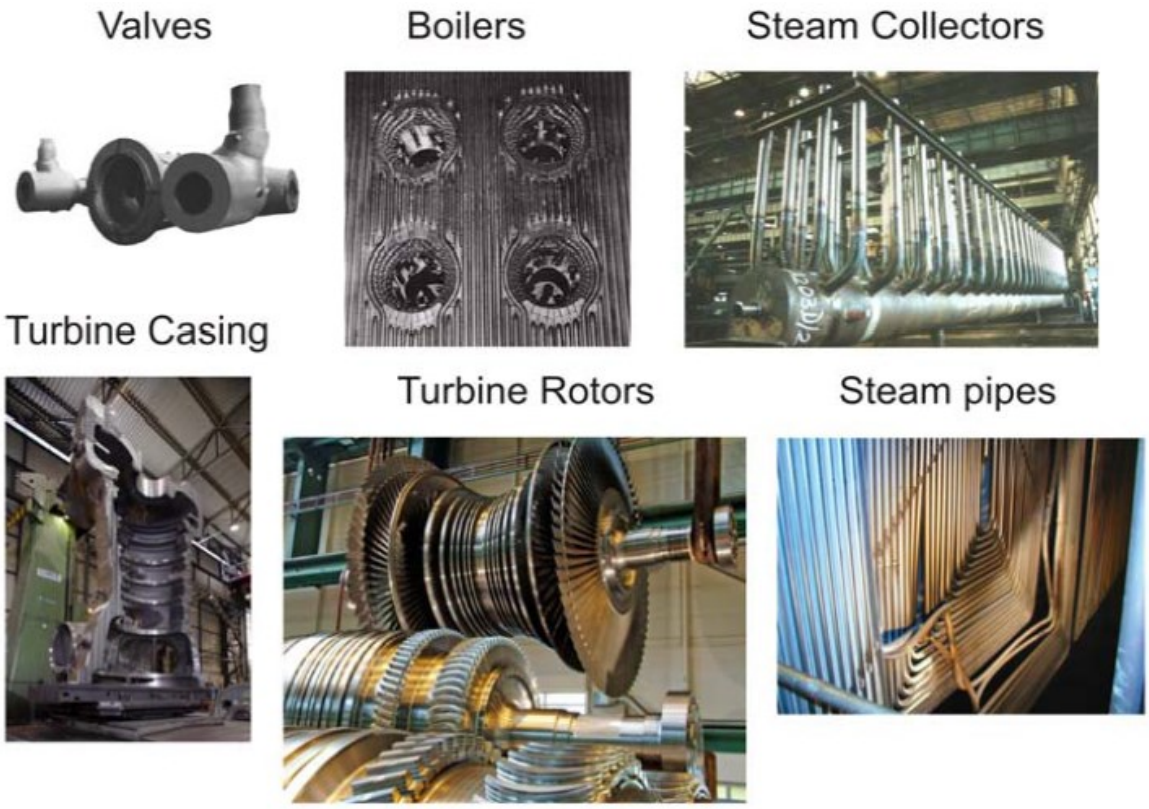

Figure 3.1. Various applications of the 9-12% chromium martensitic/ferritic steels in the fossil-fired steam power plant industry [92].

Grade P91 demonstrates excellent tensile and creep strengths and ductilities comparable or superior to other similar ferritics. Its yield strength, 415-547 MPa at room temperature and 275-325 MPa at 600°C, exceeds that of grade P9 and 304 stainless steel [**85**, **86**]. It's creep strength and toughness significantly exceed that of grade P9, and its strength is comparable to type 304 stainless steel up to 625°C [**86**, **88**]. To obtain grade P91 steel, the modification made to the grade P9 was the addition of 0.06-0.10% Nb and 0.18-0.25% V, which are strong carbide formers. Silicon content was also optimized. A brief description of the effect of each of the different alloying elements and the secondary phase precipitates on the elevated temperature properties of grade P91 steel is provided next.

3.3. Effect of alloying elements

The chemical composition of any alloy has a great bearing on the metallurgical phases formed and the sequence of secondary precipitates' formation. Similarly, for 9-12% Cr martensitic/ferritic steels, it is the metallurgical optimization and/or new additions that have resulted in better materials with improved properties over the years (see Table 3.2) [**21**, **73**]. The individual influence of a given element on an alloy's behavior is generally not determinable due to inter-element interaction that depends on its quantity and presence of other alloying elements and related kinetics [**14**, **21**, **27**, **93**]. Hence, alloying elements are typically grouped based on their contribution that is observed to be either beneficial or detrimental to existing properties. Most elements are added to stabilize certain phases or precipitates that are beneficial to long-term creep rupture strength while some are added to suppress phases that are detrimental. Few elements are added for solid solution strengthening or to improve the steam oxidation and corrosion resistance properties. The overall effect of main alloying elements on the elevated temperature properties of grade P91 steel is briefly described below:

Table 3.2. Overview of the historical development of basic and advanced 9-12% Cr martensitic/ferritic steels [21].

country		steel	Chemical composition (wt%)									Rupture strength at 600°C (MPa)	
			C	Cr	Mo	Ni	W	V	Nb	N	B	10^4h	10^5h
		Basic steels											
Germany	1	X22CrMoV12-1	0.22	12.0	1.0	0.50	-	0.30	-	-	-	103	59
UK	2	H 46	0.16	11.5	0.65	0.70	-	0.30	0.30	0.05	-	118	62
France	3	54T5	0.19	11.0	0.80	0.40	-	0.20	0.45	0.05	-	144	64
Japan	4	TAF	0.18	10.5	1.5	0.05	-	0.20	0.15	0.01	0.035	216	(150)
USA	5	11%CrMoVNbN	0.18	10.5	1.0	0.70	-	0.20	0.08	0.06	-	165	(85)
		Advanced steels											
USA	6	P91	0.1	9.0	1.0	<0.4	-	0.22	0.08	0.05	-	124	94
Japan	7	HCM 12	0.1	12.0	1.0	-	1.0	0.25	0.05	0.03	-	-	75
Japan		TMK 2	0.14	10.5	0.5	0.5	1.8	0.17	0.05	0.04	-	185	90
Europe	9	X18CrMoVNB 91	0.18	9.5	1.5	0.05	-	0.25	0.05	0.01	0.01	170	122
Europe	10	X12CrMoWVNbN	0.12	10.3	1.0	0.8	0.80	0.18	0.05	0.06	-	165	90
		E911	0.11	9.0	0.95	0.2	1.0	0.20	0.08	0.06	-	139	98
Japan	11	P92	0.07	9.0	0.50	0.06	1.8	0.20	0.05	0.06	0.003	153	113
Japan	12	P122	0.1	11.0	0.40 1.0Cu	<0.40	2.0	0.22	0.06	0.06	0.003	156	101
Japan	13	HCM 2S	0.06	2.25	0.20	0.2	-	0.25	0.05	0.02	0.003	-	80
Germany	14	7CrMoTiB	0.07	2.40	1.0	1.0	-	0.25	-	0.01	0.004 0.07Ti	-	60
Cost 522	15	FB2	0.13	9.0	1.5	0.15	-	0.20	0.05	0.02	0.0085	-	125
Cost 522	16	CB2	0.12	9.0	1.5	0.15	-	0.20	0.06	0.02	0.011	-	125

Carbon (C): Being the primary alloying element in steels, C has a major effect on steel properties. C tends to occupy the interstitial sites in both austenite and ferrite phases, although it stabilizes the former relatively better due to its greater solubility. Moreover, C causes the secondary hardening of grade P91 steel via the formation of carbides [**94**]. It has been observed that an increase in C content (up to ~ 0.8%) generally increases hardness and tensile strength while decreasing the ductility, impact energy and weldability of this material [**95**].

Chromium (Cr): Cr strongly promotes the formation of carbides (by chemical reaction with C) and is well-established as a ferrite stabilizing element in steels [**6**, **74**]. Carbides rich in Cr (for example, $M_{23}C_6$ and M_7C_3) typically form during tempering and improve the steel's hardenability, creep

strength and steam oxidation and corrosion resistance properties [**73**, **96**]. It also provides little solid-solution strengthening (with Fe) and considerable hardening (with Ni).

Tungsten (W): Due to its strong tendency to form carbides, W stabilizes ferrite by promoting the increased precipitation of Laves phase [**19**, **68**, **70**]. Furthermore, it increases the creep rupture strength of martensitic/ferritic steels via solid solution strengthening [**94**, **97**, **98**]. As reported by Abe *et al.* [**99**], the coarsening rate of $M_{23}C_6$ carbides is reduced with increased W concentrations in 9% Cr steels and consequently this delays the dynamic recovery of the lath martensitic microstructure [**100**]. But, its addition must also be limited to suppress the formation of δ-ferrite – a solid solution of Fe with maximum solubility of 0.09% C at 1495°C – that promotes the embrittlement of these steels.

Molybdenum (Mo): Apart from promoting carbide formation [**101**], addition of Mo stabilizes the ferritic phase, M_2X and $M_{23}C_6$ precipitates [**102**]. It raises the grain-coarsening temperature of austenite and enhances the corrosion resistance. Mo also counteracts steels' tendency towards temper brittleness [**73**] and improves their abrasion resistance.

Vanadium (V): V is principally added to steels to promote fine grain sizes, by raising the coarsening temperature of austenite. Moreover, it stabilizes the ferritic phase and improves the long-term creep rupture strength by significantly increasing the tendency towards formation of fine V-rich carbides, nitrides and carbonitrides (of the MX type) with C and N [**103**, **104**]. It is also known to resist tempering, increase hardenability (when dissolved) and to provide marked secondary hardening effect.

Nickel (Ni): Most commonly employed to prevent the formation of δ-ferrite, Ni also increases the toughness and strength of martensitic/ferritic steels [**73**]. It greatly assists (along with Cr) in improving the oxidation and corrosion resistance in these steels when added in large quantities. Its adverse effects include the accelerated coarsening of precipitates that lowers the steel's creep strength.

Silicon (Si): Primarily added to aid in the formation of protective silicon dioxide (SiO_2) surface layers [**105**, **106**] that provide superior corrosion resistance, Si stabilizes ferrite and also accelerates the precipitation and coarsening of Laves phase [**106**, **107**]. They also influence the kinetics of carbide precipitation [**108**]. But its addition promotes the formation of δ-ferrite and hence other austenite stabilizing elements are often added to counteract this adverse effect [**109**].

Manganese (Mn): Although they weakly stabilize the austenitic phase, increasing Mn contents tend to increase the growth rate of coarse M_6C precipitates that can remove W from the solid solution. It also undesirably causes dissolution of other important precipitates like $M_{23}C_6$ carbides and Laves phase [**110**]. They thus adversely affect the creep strength of grade P91 steels [**111**], but is usually added in small quantities to improve their hot working properties while slightly increasing strength, toughness and hardenability.

Niobium (Nb): Besides stabilizing ferrite akin to V, Nb also forms beneficial and stable carbide, nitride and carbonitride precipitates with C and N (of the MX type) [**112**] in 9-12% Cr steels. Small amounts of Nb addition to P91 steel increase its yield strength significantly and the tensile strength to a lesser extent. This improved strength and toughness is achieved by retarding the recrystallization of austenitic phase that results in a fine grain microstructure [**110**, **113**].

Copper (Cu): Cu is very effective in inhibiting the formation of detrimental δ-ferrite phase in this class of steels [**59**]. Due to its low solubility in ferritic phase, Cu-rich precipitates also provide nucleation sites for Laves phase formation [**114**].

Tantalum (Ta): Addition of Ta is analogous to that of Nb in that it stabilizes ferrite along with forming extremely stable Ta-rich MX precipitates with C and N [**19**, **73**, **95**] that are found to increase the long-term creep strength of P91 steels [**115**].

Nitrogen (N): N too occupies interstitial sites in the Fe lattice and is added to stabilize the austenitic phase. Increasing its concentration tends to stabilize the fine MX precipitates of 9-12% Cr steels and hence desired for improved creep strengths [**116**].

Cobalt (Co): Primarily employed to stabilize the austenitic phase [**19**], Co also enhances the toughness of martensitic/ferritic steels. By remaining in solid solution even at increased concentrations of up to 10 weight% [**117**], Co supposedly slows down diffusion processes and thereby reduces the tendency towards microstructural coarsening of the alloy precipitates [**118**].

Boron (B): Being a surface-active element, B exhibits low solubility in ferrite. Hence in many 9-12% Cr steels, only a small amount (~ 0.005-0.01%) is typically added [**119**]. Since B reduces the Ostwald ripening rate of thermally stable $M_{23}(C,B)_6$ fine precipitates via its enrichment near prior austenite grain boundaries [**72**, **120**], it stabilizes the lath martensitic microstructure and thereby increases the steel's hardenability and toughness.

3.4. Effect of common secondary phase precipitates

Of the precipitates that form in high-chrome steels, four are considered to play a significant role during their elevated temperature operation. Few of these precipitates are thermodynamically metastable and hence are not expected to remain stable with time. These metastable precipitates thus play a critical role in microstructural evolution during the elevated temperature service of these steels, during which they might be dissolved in favor of other stable precipitates. An example of a typical precipitation sequence (with varying evolution intervals) in these steels is given in Equation (3.1) [**27**].

$$M_3C \longrightarrow M_7C_3 + M_2X \longrightarrow M_{23}C_6 + MX \longrightarrow M_{23}C_6 + \text{Z-phase} \ldots\ldots\ldots\ldots (3.1)$$

A brief overview of the four common precipitates is provided below.

$M_{23}C_6$: Being the most common and important precipitate in most martensitic/ferritic steels, $M_{23}C_6$ is a generalized notation wherein M stands for any of Cr, Ni, Mo, W, V, Fe, Mn and B [**121**, **122**]. Among these elements, Cr-rich carbides ($Cr_{23}C_6$) are much more common and they impart improved creep rupture strength and excellent steam oxidation and corrosion resistance properties [**123**, **124**]. When the remaining elements partially substitute for Cr, precipitates such as $Fe_{21}Mo_2C_6$ (at high Mo contents) are common. Their strengthening effect depends strongly on the amount, size and dispersion distributions in the parent matrix. Known to nucleate heterogeneously at existing

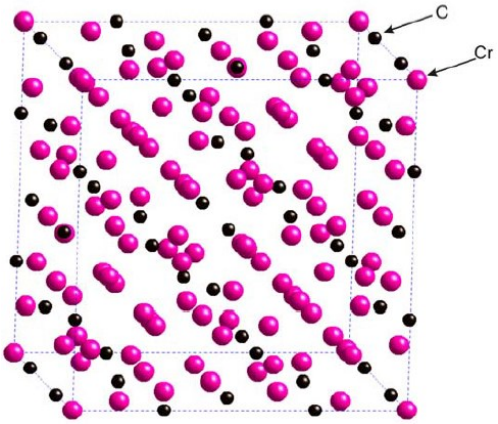

Figure 3.2. Schematic of FCC unit cell structure of $Cr_{23}C_6$ precipitates [125].

internal interfaces (*i.e.*, prior austenite grain boundaries and martensite laths or block boundaries), these carbides have a face centered cubic (FCC) crystal structure with lattice parameter (a) varying between 1.057 and 1.068 nm (see Figure 3.2) [**125**]. Although their average size after tempering is ~ 100 nm [**126**], their high coarsening rate at elevated temperatures leads to increasing sizes and decreasing strengthening effect with exposure time [**126**, **127**, **128**, **129**].

MX: When strong carbide and/or nitride forming alloying elements (like V, Nb, etc.) are added to high-chrome steels, it leads to the formation of fine MX carbonitrides [**18**, **65**, **75**, **104**]. These thermally stable precipitates are known to provide additional strengthening effect within the matrix and laths in these steels by pinning free dislocations and sub-grain boundaries [**118**, **130**, **131**, **132**, **133**, **134**]. They are also found to increase the dislocation density and retard their sustained motion too resulting in an increased strengthening effect [**73**, **135**]. Known for heterogeneous nucleation on existing dislocations within the matrix or stacking faults during tempering, these precipitates have a NaCl-like FCC crystal structure (see Figure 3.3) with lattice parameters (a) as shown in Table 3.3 [**125**]. But the measured a values often have intermediate values reflecting the existence of a solid solution among the various carbonitrides [**130**, **133**].

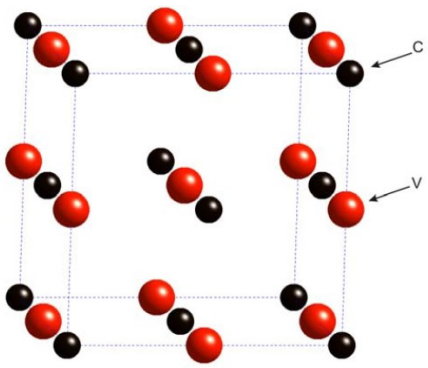

Figure 3.3. Schematic of FCC unit cell structure of VC precipitates [125].

Table 3.3. Unit cell parameter (a) of MX precipitates in 9-12% Cr steels [125].

Precipitate	NbN	NbC	TiN	TiC	VC	VN
a (nm)	0.439	0.447	0.424	0.433	0.417	0.413

Laves phase: By altering the Mo content and/or adding W to 9-12% Cr steels, an increase in the creep strength can be achieved [**136**, **137**]. These metallurgical changes typically lead to the precipitation of intermetallic Laves phase of the type $(Fe,Cr)_2(Mo,W)$ [**94**, **107**]. They have a hexagonal close packed (HCP) crystal structure with lattice parameters of a = 0.473 nm and c = 9.772 nm (see Figure 3.4) [**137**]. Often these equiaxed precipitates nucleate intergranularly during elevated temperature exposure [**100**, **138**], albeit at slower nucleation and growth rates [**136**, **139**] for Mo-based Laves phase than their W-based counterparts [**138**]. Moreover, their coarsening rate is also comparatively slow than $M_{23}C_6$ precipitates [**127**]. Presence of Si and Cu in the steel tends to accelerate the precipitation of these precipitates [**114**]. Although they are known to deplete W from steel during service, Laves phase provides additional precipitation strengthening within the matrix [**100**].

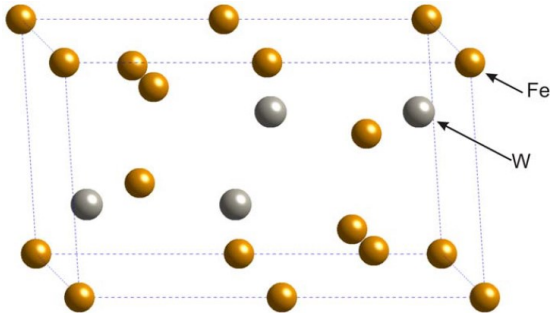

Figure 3.4. Schematic of HCP unit cell structure of Fe_2W precipitates [125].

Z-phase: Having a generalized notation of CrXN where X corresponds to Nb, V or Ta, coarse Z-phase precipitates are probably the most stable nitrides during long-term elevated temperature exposure of 9-12% Cr martensitic/ferritic steels [**140**]. Researchers had expressed diversified views on their crystal structures [**141**, **142**] earlier until Danielsen conclusively reported it to have a tetragonal structure [**143**, **144**, **145**]. As shown in Figure 3.5, precipitation of Z-phase causes the dissolution of MX precipitates that tends to increase the creep rupture strength of 9% Cr steels [**146**, **147**, **148**].

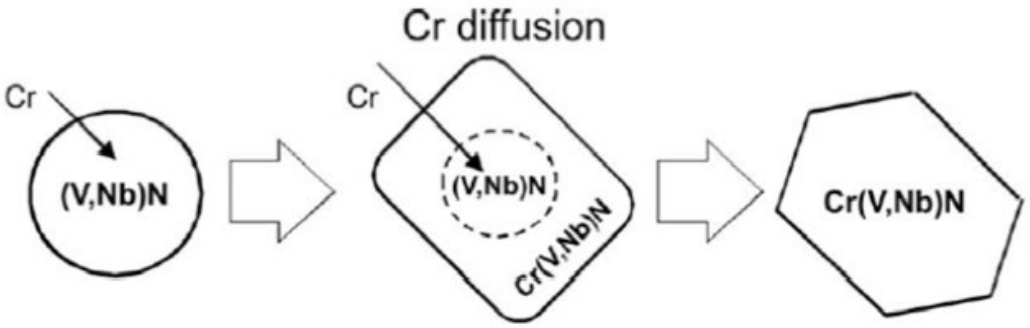

Figure 3.5. Precipitation of Z-phase by Cr diffusion from the martensitic/ferritic matrix of 9% Cr steels [146].

3.5. Physical metallurgy of grade P91 steel

The superior performance of 9-12% Cr martensitic/ferritic steels, as compared to that of their predecessors like austenitic grades, can be attributed to their well-engineered stable microstructures. In this section, the metallurgy – equilibrium phase diagram, heat treatment procedure and typical microstructure – of grade P91 steel is briefly discussed.

3.5.1. Equilibrium phase diagram

The equilibrium phase diagram of grade P91 steel is shown for illustration in Figure 3.6. As per this diagram, austenite (γ-iron phase with FCC structure) and ferrite (α-iron phase with body centered cubic (BCC) structure) are the two most important phases of scientific interest in this steel. Furthermore, both these phases do co-exist in a small window of temperature and chemical composition in this Iron-Carbide (Fe-C) phase diagram. When P91 steel is heated at temperatures above Ac_1 – the temperature above which austenite begins to form from ferrite – ferrite transforms to austenite by austenitization (also refer Figure 3.7 in the austenitic region from 820 to 1200°C at ~ 9% Cr content) [**149**, **150**]. The undesirable ferrite that remains after austenitization is usually designated as δ–ferrite and is detrimental to the steel's properties. Hence, optimized process control should be adopted to avoid or minimize the existence of this phase.

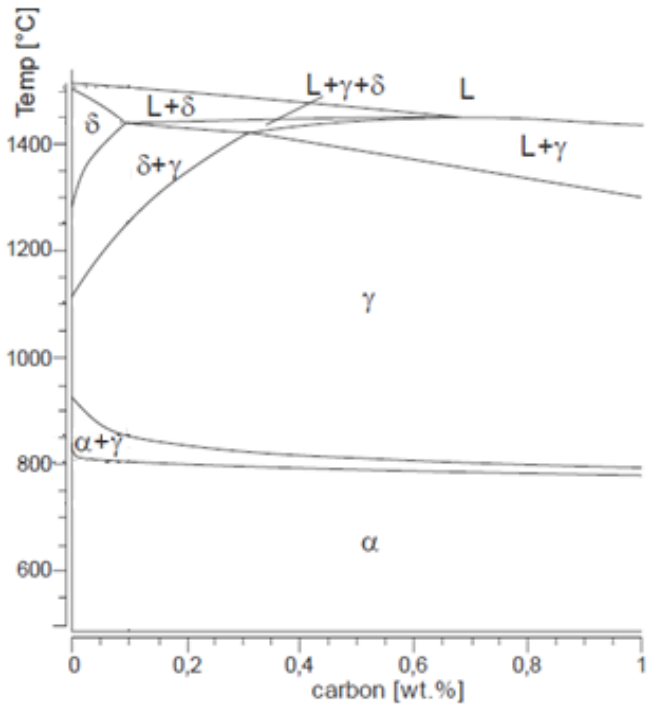

Figure 3.6. The equilibrium phase (Fe-C) diagram of grade P91 steel, where γ : austenite, α : ferrite and δ : ferritic phase different from the δ-ferrite considered in earlier discussion [135].

When austenite is very rapidly cooled or quenched, a displacive or diffusionless transformation into martensite takes place as low-solubility C atoms cannot diffuse at such rapid cooling rates. Moreover, the high amount of Cr retards C diffusion further and prevents the formation of α-ferrite [**151**]. Consequently, the ferrite nose in the CCT (continuous cooling transformation) diagram shifts to longer cooling times and this corresponds to a complete martensite transformation at rapid cooling rates [**150**, **152**, **153**]. The temperature at which austenite starts to transform and fully transforms to martensite is usually referred to as M_s and M_f, respectively. For 9-12% Cr steels, the M_s and M_f temperatures are typically in the range of 400°C and 100-150°C, respectively (see Figure 3.7) [**21**]. In this regard, the nominal chemical composition of a particular steel ultimately decides its M_s and M_f temperatures. For example, an empirical estimate of

the effect of various alloying elements (weight%) on the M_s temperature of 9-12% Cr steels is given in Equation (3.2) [**27**].

$$M_s = 550°C - 450C - 33Mn - 20Cr - 17Ni - 10W - 20V - 10Cu - 11Nb - 11Si + 15Co \ldots\ldots\ldots \quad (3.2)$$

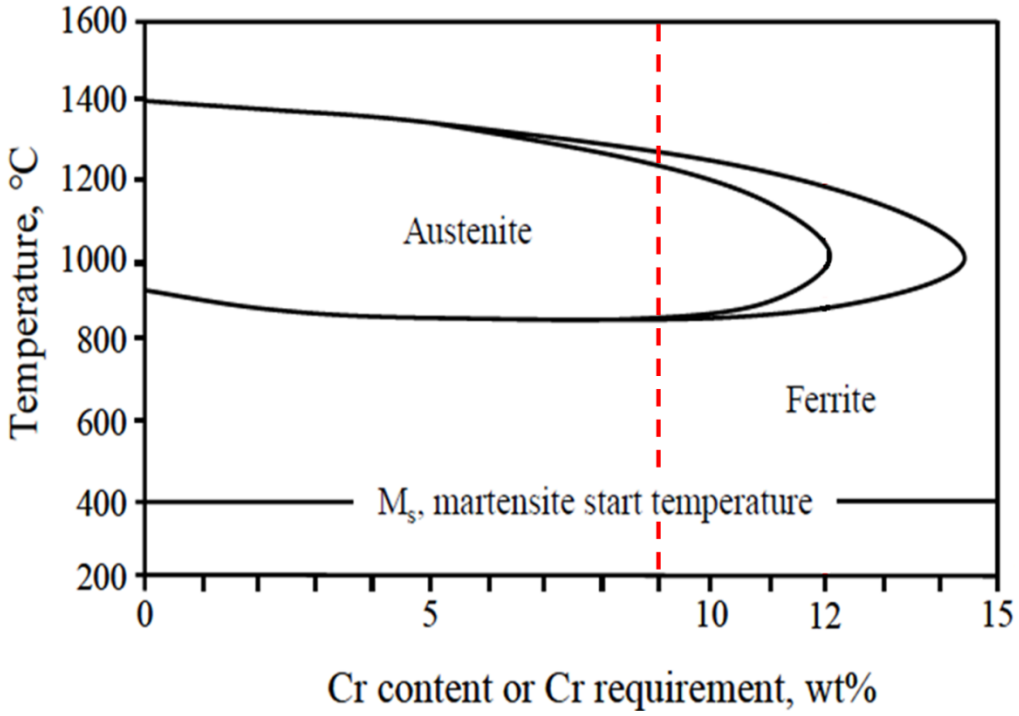

Figure 3.7. Constitutional diagram for Fe-Cr alloys, based on Ennis and Quaddakkers [154]. The broken line indicates the particular case of 9% Cr content for grade P91 steels.

As it can be seen, the only alloying element that raises the M_s temperature is Co and hence its addition is obviously considered critical in these steels. Grade P91 steel at this stage of processing is found to have a body centered tetragonal (BCT) crystal structure in a hardened state, representing that of martensite. It needs to be mentioned herein that martensite is a metastable state and hence not represented in this "equilibrium" phase diagram. During this stage, most of the martensitic transformation occurs preferentially at existing grain boundaries and hence it is customary to expect some quantity of retained austenite in this steel. It therefore requires M_f to be above room

temperature so that even retained austenite is completely transformed to martensite after quenching. Any such retained austenite in the microstructure will reduce the steel's strength.

3.5.2. Typical heat treatment procedure

The martensitic microstructure of grade P91 steel has a very high density of transformation dislocations in the order of 10^{14} m^{-2} [**155**, **156**]. Hence, this microstructural state is characterized by high mechanical strength, hardness and brittleness and the induced internal stresses ought to be relieved for achieving an optimal balance of strength and ductility [**157**]. Therefore, martensitic steels are tempered – a heat treatment methodology to trade strength for ductility – followed by air cooling to achieve desired levels of mechanical properties [**27**, **93**, **151**, **158**, **159**]. Tempering usually results in a martensitic/ferritic subgrain microstructure with precipitates forming at the distinct internal interfaces (see Figure 3.8). For grade P91 steel, austenitization (or normalization) and tempering are typically done at 1038-1100°C (for 1 hour) and 700-780°C (for 1-2 hours), respectively depending on the desired properties [**7**, **150**, **160**].

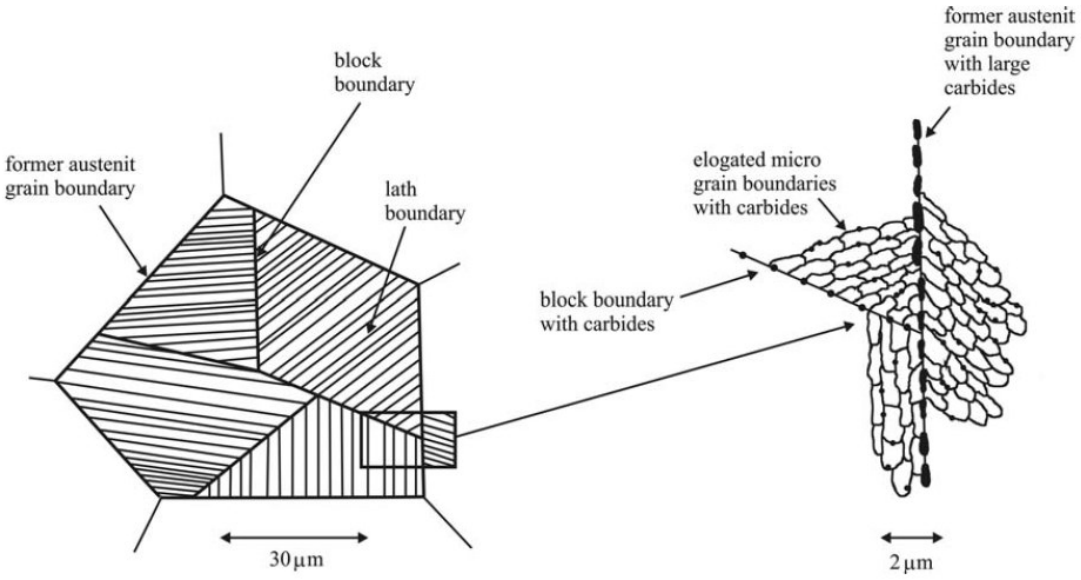

Figure 3.8. Schematic illustration of the typical microstructure of tempered martensitic grade P91 steels [125].

3.5.3. Typical microstructure

The resulting microstructure is fully tempered martensite, with strengthening observed at several distinct microstructural scales (see Figures 3.8 and 3.9). The mesoscopic scale consists of prior austenitic grains (PAGs, with mean diameter of 60-100 μm) that are each composed of original martensitic laths or packets having the same {111} habit plane fragmented by thick plate-like subgrains (as small as 350 nm) formed during tempering [**161**, **162**]. The PAG and subgrain boundaries are stabilized by extensive $M_{23}C_6$ and M_7C_3 secondary-phase carbides (average size of ~ 100 nm) where M represents Cr, Fe and Mo and C represents carbon [**121**, **163**, **164**]. Grade P91 steel also uses the homogeneous precipitation of finely dispersed Nb/V carbonitrides of the type MX (average size of ~ 50 nm) in ferrite as additional strengthening agents inside the matrix [**165**, **166**]. These precipitates can have a spherical Nb(C,N) center with plate-like ellipsoidal V-rich wings emanating from the sides (see Table 3.4) [**167**, **168**]. All these precipitates are relatively stable and effective obstacles against dislocation motion, resulting in an increase in the elevated temperature strength of this steel.

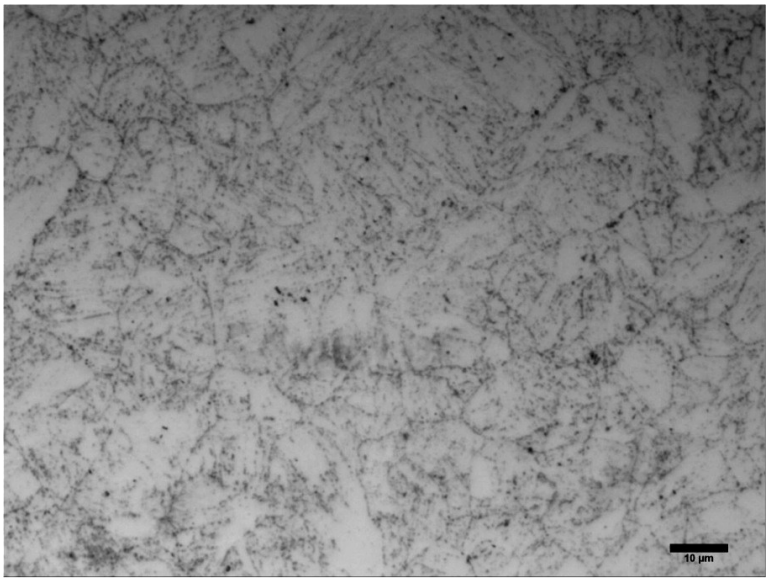

Figure 3.9. Optical micrograph of the tempered microstructure of grade P91 steel (scale shown is 10 μm). The optical micrograph is obtained by chemically etching the heat treated metallographic specimen with Nital (3% nitric acid in methanol) solution.

Table 3.4. Precipitates in grade P91 steel [167, 168], wherein the underlined term in each precipitate's formula represents the primary strengthening element.

Precipitate	Formula	Morphology	Remark
$M_{23}C_6$	$(\underline{Cr}, Fe, Mo)_{23}C_6$	Coarse	Precipitate during tempering
MX	(<u>Nb</u>, V) (N,C)	Fine & spheroidal	Undissolved during austenitization
MX	(<u>V</u>, Nb) (N,C)	Fine & ellipsoidal	Precipitate during tempering

Chapter 4: LITERATURE REVIEW

In this chapter, published literature that talks about the various aspects of creep, fatigue, C-F and oxidation deformation response of grade P91 steel under different loading conditions is discussed in detail. The discussed literature includes both experimental and constitutive modeling efforts and also indicates the need for investigating few of the major research objectives proposed as part of this work.

4.1. Creep deformation response of grade P91 steel

Before discussing the existing literature on the creep deformation response of grade P91 steel, a brief summary of the strengthening mechanisms that improve its creep properties is outlined next. It is imperative that this topic is discussed first for a better comprehension of the existing literature and reported results.

4.1.1. Creep strengthening mechanisms

A material's creep rupture strength – a measure of the stress at which it ruptures (fails) in a given period at a given temperature – is typically a combination of various strengthening mechanisms operating at the distinct microstructural scales. For grade P91 steel, these include solid solution hardening, precipitation or dispersion hardening, dislocation hardening and boundary/sub-boundary hardening [**120**, **169**]. A brief overview of these different mechanisms is presented next.

4.1.1.1. Solid solution hardening

By introducing substitutional or interstitial point defects in the microstructural matrix (solvent), localized crystallographic aberrations are induced by the addition of an alloying element

(solute) in a material. These tensile/compressive lattice distortions offer an additional strengthening effect – known as solid solution hardening – by hindering the motion/propagation of dislocations that interact with the solute's stress fields [**170**]. In grade P91 steel, substitutional solute atoms such as Mo have much larger atomic radii than Fe and hence are effective solid solution strengthening elements.

4.1.1.2. Precipitation or dispersion hardening

Rather than isolated point defects, clusters of such aberrations – termed as precipitates – can constitute regions of a different phase to provide additional creep rupture strengthening. Precipitates such as $M_{23}C_6$, M_7C_3, MX etc., and intermetallic compounds like Laves phase offer considerable precipitation hardening in these steels by preferential nucleation especially at the vicinity of grain boundaries [**171**]. The threshold stress that corresponds to the stress required for a dislocation to penetrate through these precipitates is described by several mechanisms such as the Orowan mechanism [**21**]. It has also been reported that the strengthening effect of solid solution and dispersion hardening mechanism is practically so inter-dependent that an additive rule does not generally hold good [**99**, **169**, **172**].

4.1.1.3. Dislocation hardening

Due to high density of dislocations (~ 1-10 * 10^{14} m^{-2}) in grade P91 steels even after tempering [**173**], effective strengthening is achieved by these linear defects due to their reduced mean free paths – the distance traveled by a free dislocation before it collides another one in its motion – at ambient temperatures only. Their contribution to long-term strengthening at elevated temperatures is rather subdued due to the reduced activation energies for dislocation motion under such conditions.

4.1.1.4. Boundary/sub-boundary hardening

The laths and blocks that commonly exist in the martensitic/ferritic microstructure of grade P91 are often considered as elongated sub-grains and due to their presence, dislocation motion is often impeded along their boundaries. Thus, an additional strengthening effect of this kind is common in these steels [**169**]. Further enhanced dislocation and sub-boundary hardening is achieved when the fine carbonitride precipitates can stabilize the free dislocations in the matrix and the sub-grain structure, respectively against recovery [**104**, **174**].

When grade P91 steels are exposed to elevated temperatures and stress, the precipitation and dislocation strengthening effects drop markedly over long durations. These phenomena, in turn, accelerate microstructure evolution that results in a loss of sub-boundary hardening [**175**]. Hence, all of these individual strengthening mechanisms are highly linked as regards their effective contribution to the material's creep rupture strength.

4.1.2. Microstructural degradation

It can be expected that a material in-service at elevated temperatures will continuously and gradually respond to the imposed loading by internal microstructural changes. More often than not, this microstructural evolution degrades the material's properties with time and hence this needs to be considered for sound design practices [**18**, **176**]. If accumulated damage reach or exceed critical levels, catastrophic failure ensues that may lead to human and/or economic loss. Moreover, long-term in-service behavior prediction is usually made from *extrapolation* of creep rupture strengths from short-term laboratory experiments. Hence fatal overestimation of the residual lifetime of components is possible without this consideration [**35**, **177**, **178**, **179**, **180**, **181**, **182**, **183**, **184**, **185**, **186**].

As discussed earlier, the martensitic/ferritic matrix of grade P91 steels contains numerous internal interfaces including PAG boundaries, lath boundaries, sub-grain and block boundaries, and a very high dislocation density before tempering. Moreover, different kinds of precipitates like $M_{23}C_6$ carbides and MX carbonitrides co-exist in the microstructure [**187**, **188**]. After tempering, the dislocation density decreases and these internal interfaces exist at thermodynamic equilibrium (see Figure 4.1(a)). But, once a component made of this material is exposed to elevated temperature (up to 650°C) and stress during service, the material gradually responds by microstructural evolution as shown in Figure 4.1(b). Because of coarsening of precipitates and intermetallic compounds ($M_{23}C_6$, Laves phase), coarsening of sub-grains [**127**, **189**, **190**] and precipitation of undesirable phases (Z-phase, δ-ferrite), the creep rupture strength reduces considerably under these conditions [**16**, **191**]. A brief overview of these aspects of microstructural evolution will follow next.

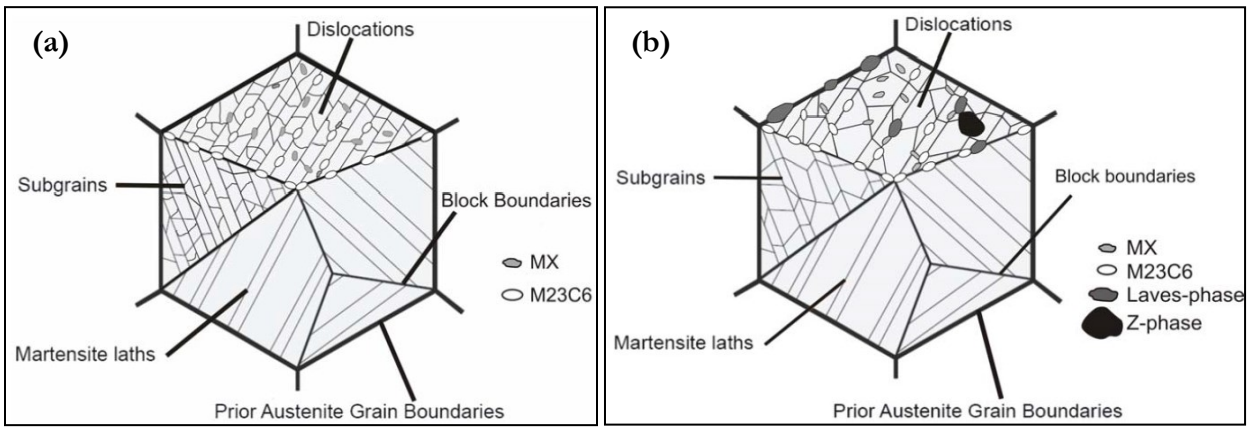

Figure 4.1. Schematic illustration of pristine microstructure of grade P91 steel (a) after tempering (internal interfaces and precipitates) and (b) evolution with exposure to elevated temperatures and external stress (adapted from [192]).

4.1.2.1. Precipitate coarsening (Ostwald ripening)

The coarsening of precipitates, particularly carbides, during the elevated temperature service of grade P91 steels profoundly degrades their creep rupture strength. This topic is briefly discussed

herein. By controlling the average size of precipiates in solid solution [**193**], precipitate coarsening effectively dictates the strength rendered by precipitation hardening [**98**, **186**]. Coarsening in a solid solution typically occurs in three successive stages – nucleation and/or growth of the more stable phase in the metastable solid solution followed by coarsening or ripening of this phase. As proposed by Ostwald where large particles grow at the expense of less-stable smaller ones to reduce the material's interfacial energy [**7, 194**], coarsening typically occurs under situations where the volume fractions of the phases are nearly at their equilibrium values (see Figure 4.2). An increase in the average size of large particles will thus reduce the total system's thermodynamic free energy. Lifshitz, Slyozov and Wagner (LSW) [**195**] show that this increase occurs with time as $t^{1/3}$ and the average number of particles per unit volume decreases as t^{-1} with the volume fraction remaining constant (see Equations (4.1) and (4.2)). Similar Ostwald ripening rules for M_aC_b carbides in Fe-based alloys is discussed elsewhere [**67**, **196**].

$$\boldsymbol{d^3 - d_0^3 = kt} \qquad \text{..... (4.1)}$$

$$\boldsymbol{\rho_n = \frac{k'}{t}} \qquad \text{..... (4.2)}$$

where d and d_0 are average particle sizes at times t and $t = 0$, respectively, k is particle growth rate, k' is a material constant and ρ_n is the average number of particles per unit volume [**166**].

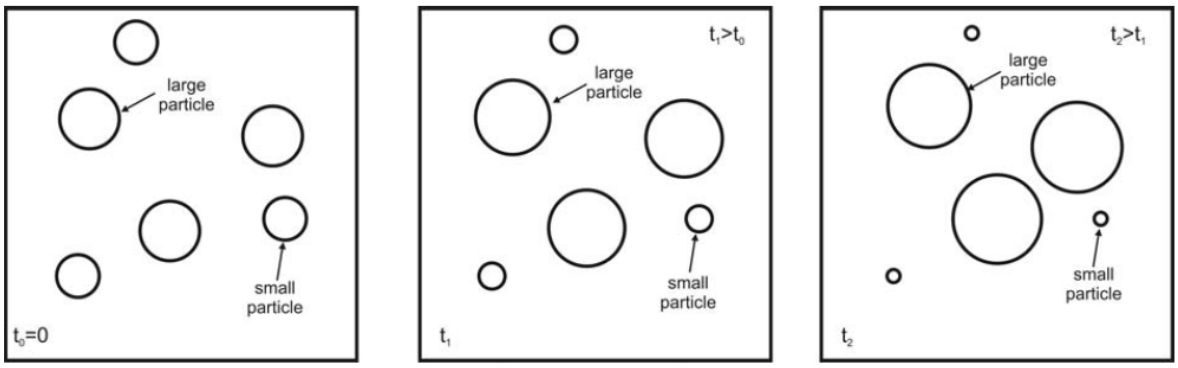

Figure 4.2. Schematic of Ostwald ripening mechanism in which large particles grow at the expense of smaller ones that eventually dissolve into the matrix [125].

4.1.2.2. Sub-grain coarsening

A sub-grain structure, that is characterized by frequency distributions of boundary misorientations and spacing, results in grade P91 steels after tempering due to the precipitation of solute atoms and recovery of dislocation cell structure [**10**, **197**]. It has been reported [**198**] that these sub-grains share their boundaries with PAGs, martensite lath blocks of similar orientation and martensite laths and other sub-grains within the laths. Although the PAG and block boundaries are of the high-angle type with misorientations generally above 10-15°, the martensite laths and sub-grains within the laths have comparatively low-angle boundaries characterized by lower misorientations [**199**]. Consequently, low-angle boundaries constitute planar dislocation networks whereas high-angle boundaries tend to interrupt the lattice coherency of adjoining crystals. Although these high-angle boundaries offer considerable resistance to sustained dislocation motion, they however allow grains sharing a common interface to relatively slide and thereby provide an effective path of least resistance for atomic diffusion.

The initial sub-grain size that also corresponds to the width of martensitic laths and blocks in tempered martensite is typically 0.3-0.7 μm and most commonly 0.4 μm [**10**, **191**]. As is the case in most structural applications of these steels, sub-grain coarsening occurs during creep deformation when the initial sub-grain size is smaller than that of steady-state sub-grains. In laboratory experiments where sub-grains were forced to coarsen within relatively short periods with negligible changes in the precipitate structure, reduction in creep rupture strengths due to sub-grain coarsening has been reported [**16**]. It was further found that when the maximum stress in such tests is sufficiently low, the size of sub-grains grows fast towards that of instantaneous stress-dependent steady-state sub-grains, with accumulating inelastic strain. Such sub-grain coarsening phenomenon is also shown to even increase the minimum creep rate by an order of magnitude [**16**]. Rather

interestingly, Blum *et al.* [**200**] have argued that it is possible for the migration of sub-grain boundaries to accommodate dynamic dislocation recovery during creep deformation.

4.1.3. Experimental test results

The minimum or steady-state creep rate and creep rupture strength/ductility are the most preferred creep values of merit for design considerations and creep rupture tests are typically performed at a variety of stress and temperatures to determine them. It is also vital to obtain the values of these parameters at the design temperatures and stresses reliably either using extrapolation of short-term test data or through long-term test data itself (both performed in a laboratory). ORNL did the first creep rupture assessment for grade P91 steel in 1983 using data of about 30 heats with the longest test duration being 30,000 hours. The 10^5 hours creep rupture strength was then determined to be 98 MPa at 600°C [**201**]. Similar assessments performed in 1990 yielded a value of 93 MPa [**202**] and 94 MPa in 1995 [**203**]. Figure 4.3 shows the 10^5 hours creep rupture strength of high-chrome ferritic steels at their typical operating temperature as assessed in 2001. In 2005, Bendick *et al.* [**204**] performed a comprehensive work on reassessing the creep rupture strength with cumulative test data duration of $1.8 * 10^7$ hours. Table 4.1 shows a list of grade P91's creep rupture strength at different temperature levels and expected lives obtained after this reassessment. This work also highlighted that these values are independent of the product forms (tubes, pipes, plates, bars, forgings) from which the data heats are obtained. This observation also implicitly implies the consistency of microstructure between these various product forms. Laboratory experiments to understand creep deformation and rupture characteristics of grade P91 steel from various product forms like pipes and tubes have been conducted at various elevated temperatures and published elsewhere [**166**, **205**, **206**, **207**, **208**, **209**, **210**, **211**, **212**, **213**, **214**, **215**].

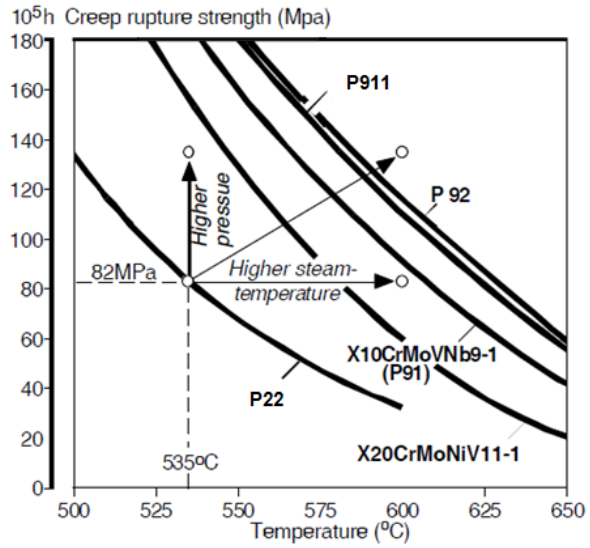

Figure 4.3. Creep rupture strength of high-chrome ferritic steels [216].

Temperature °C	Values of new assessment (MPa)		
	10^4 h	10^5 h	2×10^5 h
500	289	255	245[a]
510	270	236	225[a]
520	251	217	206[a]
530	233	199	188
540	216	182	170
550	200	164	153
560	183	148	136
570	167	132	121
580	152	117	106
590	137	103	93
600	122	90	81
610	109	79	71
620	97	70	63
630	86	62	56[a]
640	76	55	49[a]
650	68	48	43[a]
660	61	42	36[a]
670	54	36	

[a] Extended time extrapolation.

Table 4.1. Recently assessed creep rupture strength values of grade P91 steel [203].

Since this work will involve the creep rupture testing of grade P91 steel specifically at 625°C, published literature near this temperature range will be focused on next. Figure 4.4 shows three different creep deformation curves for grade P91 steel obtained at 600°C under different stress conditions [**166**]. As it can be seen from these characteristic curves, the duration and amount of strain accumulated during the three distinct regimes vary considerably depending on the external stress. In grade P91 steel, the microstructural evolution that contributes to an increase in creep rate at 600°C can be characterized by the following sequence of events: (i) dislocation density decreases as there is rearrangement and annihilation of excess transformation dislocations; (ii) finer equiaxed subgrains develop from the former tempered martensitic microstructure; (iii) dissolution of the finely dispersed carbonitride precipitates (NbC, VC); (iv) redistribution of $M_{23}C_6$ carbides from stringers to a homogeneous distribution in ferrite and (v) coarsening of the $M_{23}C_6$ carbides and Nb and V carbonitrides and their interparticle spacing increases as well [**217**].

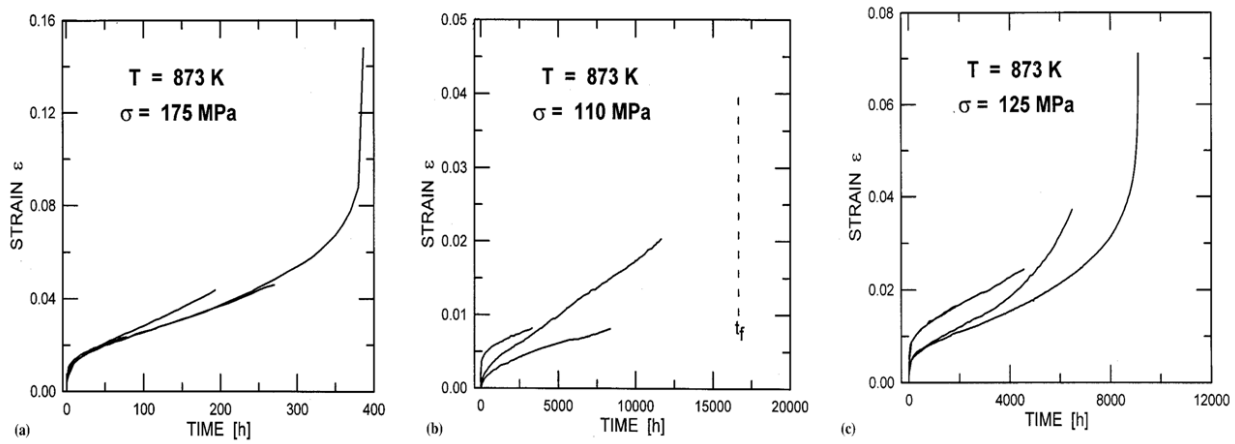

Figure 4.4. Characteristic creep deformation curves for grade P91 steel [166].

Other than creep rupture time, the typical numerical quantities that are reported for creep rupture tests can be analytically expressed and presented next. The instantaneous elastic strain ($\boldsymbol{\varepsilon^{el}}$) before regime I can be estimated as shown in Equation (4.3):

$$\boldsymbol{\varepsilon^{el} = \sigma/E} \qquad \text{……..….. (4.3)}$$

where $\boldsymbol{\sigma}$ is the external stress and $\boldsymbol{E}$ is the material's elastic modulus at the test temperature. The stress dependence of the steady-state creep rate ($\boldsymbol{\dot{\varepsilon}^{cr}_{min}}$) in regime II can be described by a well known equation of the form (see Equation (4.4)):

$$\boldsymbol{\dot{\varepsilon}^{cr}_{min} = A_n \cdot \sigma^n \exp\left(-\frac{Q}{k_B T}\right)} \qquad \text{……..….. (4.4)}$$

where A_n and n are constants at a given absolute temperature T, Q represents the activation energy and k_B is the Boltzmann's constant. The stress exponent n decreases with increasing temperature and the observed values range between 15 at 575°C, 12 at 600°C and 5 at 650°C [**218**]. Table 4.2 summarizes the reported values of steady-state creep parameters for tests conducted on P91 steel

only between 600 and 650°C. It has been proposed that in high stress conditions the dislocations can overcome particles of secondary phases by the Orowan mechanism, while at low stress conditions a dislocation climb mechanism is predominant [**217**]. Also, it was reported that irrespective of the creep loading history, the failure mode is *always* ductile transgranular in P91 steel [**77**].

Table 4.2. Reported experimental steady-state creep parameters for grade P91 steel.

Temperature (°C)	Low stress region	High stress region	Reference
	Slope, n_1	Slope, n_2	
600 - 650	1	12	[**208**, **211**, **215**]

The previously discussed concept of creep deformation-mechanism map is shown in Figure 4.5 for this material, wherein it shows the importance of dislocation (or power-law) creep and viscous (or linear) creep mechanisms. Although dislocation creep generally includes high stress ranges and viscous creep that of moderate and low stress ranges in this map, both need to be considered for overall creep deformation predictions and constitutive modeling efforts [**209**, **211**]. Figure 4.6 shows the minimum creep rate plotted against applied stress with the available data from creep tests at three different temperatures for P91 steel with their application ranges. Moreover, this figure also shows the transition between the two creep mechanisms of importance for this material.

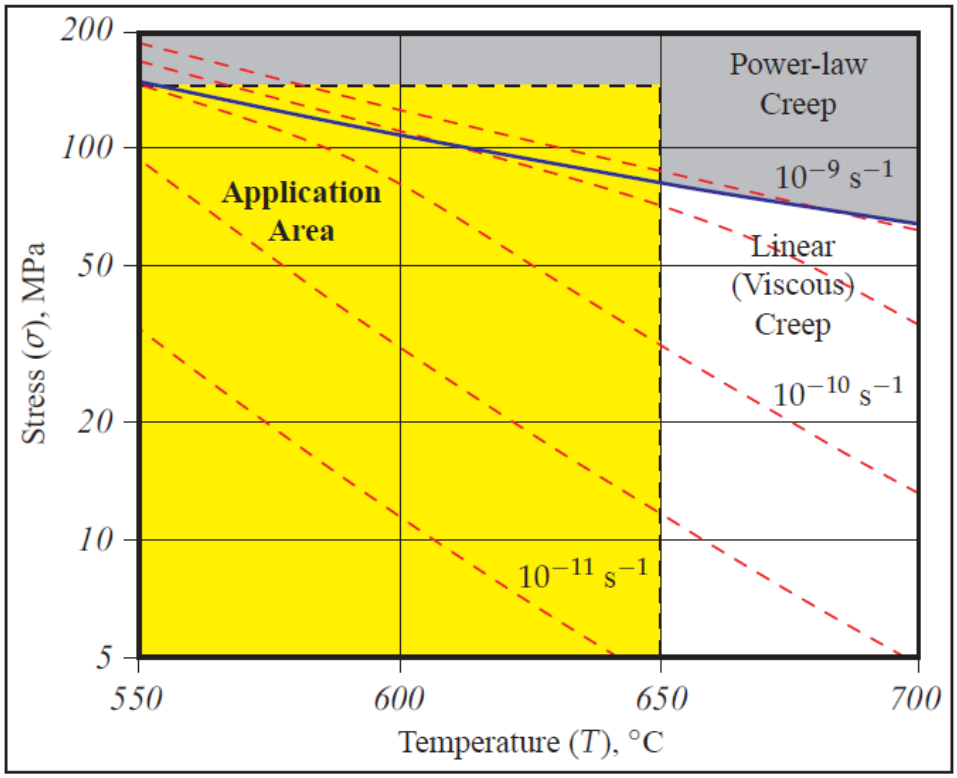

Figure 4.5. Creep deformation-mechanism map of grade P91 steel, after [209, 211].

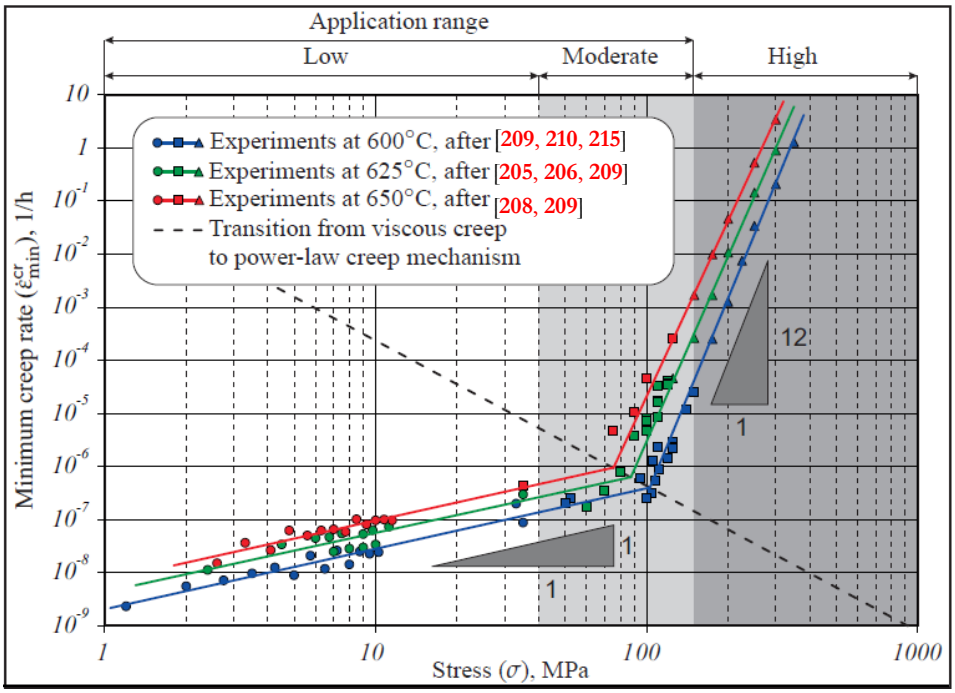

Figure 4.6. Minimum creep rate plotted against stress for grade P91 steel with experimental data from tests after [205, 206, 208, 209, 210, 215].

4.1.4. Reliable long-term creep predictions

As time-scales associated with creep deformation usually is in terms of years, performing tests in a laboratory to closely mimic in-service conditions is not practically feasible. Hence, tests are often performed under accelerated loading conditions wherein either stress and/or temperature are increased considerably to induce failure in shorter periods. Such tests can be performed uninterrupted (*i.e.,* continuously measured) as the creep strain is monitored by an extensometer attached within the test specimen's gage length or interrupted at planned time intervals. The creep data thus obtained can then be extrapolated: (i) to longer times; (ii) to conditions of variable stress and temperature; (iii) to multi-axial states of stress and (iv) to conditions of external environments not readily achievable in the laboratory.

Different methods have been developed to predict long-term creep behavior of materials from short-term experimental observations or from using analytical approaches. A detailed summary of the analytical models currently in use for predicting creep strain at any time t is provided in Table 4.3 [**21**]. Generally, for better accuracy, it is a common practice to use a combination of these models to predict creep rupture behavior at any time t in a given material, as there is a lack of models that can closely predict the whole creep curve *all* by itself. A list of analytical models currently used for predicting the creep rupture behavior of grade P91 steel is provided in [**219**, **220**]. A single expression model generally provides more robustness (via less number of fitting constants) in mathematical modeling, as compared to a combination of them. Hence, this work will present such a single expression constitutive relation that is a modified version of an existing model and the relevant details and results will be discussed later in Chapters 6 and 7, respectively.

Table 4.3. List of analytical constitutive models generally used for creep modeling [21].

Model reference	Creep equation
Norton, (Norton, 1929)	$\dot{\varepsilon}_{t,min} = d_1 \exp(-Q/RT)\sigma^n$
Modified Norton	$\dot{\varepsilon}_{t,min} = b_1 \exp(-Q_b/RT)\sigma^n + c_1 \exp(Q_c/RT)\sigma^n$
Norton–Bailey	$\varepsilon_f = d_1\sigma^n t^p$
Bartsch	$\varepsilon_f = e_1 \exp(-Q_b/RT)\sigma \exp(-b_1\sigma)t^p$
(Bartsch, 1995)	$+ e_2 \exp(-Q_b/RT)\sigma \exp(b_2\sigma)t$
Garofalo, (Garofalo, 1965)	$\varepsilon_f = \varepsilon_0[1 - \exp(-b_1 t)] + \dot{\varepsilon}_{t,min} t$
Modified Garofalo	$\varepsilon_f = \varepsilon_{01}[1 - \exp(-g_1(t/t_{12})^{g_2})$
(Granacher, *et al.*, 2001)	$+ \dot{\varepsilon}_{t,min} t + c_{23}[t/t_{23})^{f}]$
BJF	$\varepsilon_f = n_1[1 - \exp(-t)]^{\beta} + n_2 t$
(Jones and Bagley, 1996)	where $t = (\sigma/A_1)^n \exp(-Q/RT)$
Li–Akulov model	$\varepsilon_f = \frac{\dot{\varepsilon}_{t,min}}{k} \ln\left(1 + \frac{\dot{\varepsilon}_i - \dot{\varepsilon}_{t,min}}{\dot{\varepsilon}_{t,min}}(1 - \exp(-kt))\right) + \dot{\varepsilon}_s t$
(Li, 1963; Akulov, 1964)	$+ \varepsilon_T(\exp(t/t_t) - 1)$
Theta	$\varepsilon_f = \theta_1[1 - \exp(-\theta_2 t)] + \theta_3[\exp(\theta_4 t) - 1]$
(Evans and Wilshire, 1985)	where $\log(\theta_i) = a_i + b_i T + c_i\sigma + d_i\sigma T$
Modified Theta	$\varepsilon_f = \theta_1[1 - \exp(-\theta_2 t)] + \theta_m t + \theta_3[\exp(\theta_4 t) - 1]$
	where $\theta_m = A\sigma^n \exp(-Q/RT)$
Graham–Walles	$\varepsilon_f = at^{1/2} + dt + ft^3$
(Graham and Walles 1955)	
Modified Graham–Walles	$\dot{\varepsilon}_f = e^{(Q_1/T)} 10^{A_1} \left(\frac{\sigma(1+\varepsilon)}{1+\omega}\right)^{n_1} \varepsilon^{m_1}$
	$+ e^{(Q_2/T)} 10^{A_2} \left(\frac{\sigma(1+\varepsilon)}{1+\omega}\right)^{n_2}$
	where $\dot{\omega} = e^{(-Q/T)} 10^{AD} (\sigma(1+\varepsilon))^{nD} \varepsilon^{mD}$
Rabotnov–Kachanov	$\dot{\varepsilon} = \frac{b_1\sigma^n}{(1-\omega)} \quad \dot{\omega} = \frac{k_1\sigma^v}{(1-\omega)^{\zeta}}$
(Kachanov, 1986)	
Dyson and McClean,	$\dot{\varepsilon}_f = \varepsilon\dot{\varepsilon}_0(1 + D_d)\exp(-Q/RT)\sinh\left(\frac{\sigma(1-H)}{\sigma_0(1-D_p)(1-\omega)}\right)$
(Dyson and McClean, 1998)	
Baker–Cane model	$\varepsilon_f = At^n + \varepsilon_p + \phi\varepsilon_x + \varepsilon_s(\lambda - \phi)\left[1 - \frac{t/t_s - \phi}{1-\phi}\right]^{\frac{1-\phi}{1-\alpha}}$
(Baker and O'Donnell, 2003)	where $\lambda = \varepsilon_x/\varepsilon_p$, $\varepsilon_s = \dot{\varepsilon}_m t_s$ and $\phi = t_p/t_s$
Mech. E (CSWP, 1983)	$R_{\sigma/T} = (a_1 + b_1/\varepsilon - c_1\varepsilon^2)R_{\sigma/T} + d_1 + e_1/\varepsilon + f_1/\varepsilon^2 - g_1\varepsilon^2$
Characteristic strain	$\varepsilon_f(\sigma) = \varepsilon(R_{\sigma/T}/R_{\sigma/T} - 1)/(R_{\sigma/T}/\sigma - 1)$
model (Bolton, 2005a)	
MHG model, (Grounes, 1969)	$t_c = \exp(T F(\varepsilon, \sigma) + C)$ where the $F(\varepsilon,\sigma)$ function is
(Holmström and	freely selected from multilinear combinations of σ
Auerkari, 2004)	and ε with an optimised value of C
Omega, (Prager, 1995)	$\dot{\varepsilon}_f = \dot{\varepsilon}_{t,min}/(1 - \dot{\varepsilon}_{t,min}\Omega t)$
Modified Omega	$\varepsilon_f = \left(\frac{1}{\Omega} - \frac{1}{2C_{11}}\right)(-\ln(t_s - t) + \ln(t_s))$
(Merckling, 2002)	$+ C_{12}(1 - \exp(m_1 t))$

4.2. Fatigue and C-F deformation response of grade P91 steel

In-service P91 steel components are typically operated under repeated cyclic loading (startup and shutdown) conditions at elevated temperatures with hold times as long as a month, leading to complex time-dependencies that vary with temperature, stress and strain. Therefore, for sound design considerations under those conditions, reliable fatigue and C-F data are required along with creep rupture behavior.

4.2.1. Different types of micromechanisms

The formation (or initiation) of macroscopic cracks at elevated temperatures in most metallic materials occurs by a combination of micromechanisms operating at several microstructural length scales. As discussed earlier, creep and/or fatigue can interact to varying degrees with environmental oxidation at elevated temperatures and stress to cause a reduction in service lifetime compared to either creep or fatigue by itself. Since fatigue is a phenomenon that is dependent of surface characteristics, fatigue induced crack initiation is quite commonly observed in laboratory tests where either the deformation rate (or equivalently, microstructural evolution) is accelerated by creep or the inherently-brittle surface oxide layers that spall on cyclic loading [**221**]. Suresh [**222**] has described the five different micromechanisms responsible for elevated temperature crack initiation and propagation namely, cyclic slip leading to persistent slip bands, grain boundary cavitation, grain boundary sliding, void nucleation at inclusions or precipitates, and oxidation or corrosion.

4.2.2. Experimental test results

When cyclic loading is applied at elevated temperatures, the microstructural evolution kinetics as described earlier for pure creep is accelerated. Under LCF loading at temperatures between 450°C and 600°C, grade P91 steel is shown to exhibit significant gradual cyclic softening over a wide range of fatigue lives [**223**, **224**, **225**, **226**, **227**], following initial hardening or softening [**226**] depending on the strain range applied. Fournier *et al.* [**161**, **224**, **225**] have attributed the coarsening of the subgrains in the martensitic/ferritic microstructure as the primary driver behind the observed softening effect in these steels and contend that this effect depends strongly on the applied plastic strain per cycle [**161**], with higher plastic strains causing more pronounced microstructural coarsening. Other observations suggest that this coarsening might also be due to other phenomena such as the annihilation of dislocations, coarsening of precipitates and increases in

effective applied stress due to surface oxidation [**156**, **228**, **229**]. In addition to the evolution of the precipitation state and a decrease in dislocation density, rate of coarsening of laths and subgrains is also faster. But, a clear description of these various microstructural changes is still under investigation and not yet quantified clearly [**161**]. Microstructural coarsening that occurs under cyclic loading is also shown to severely degrade the creep resistance properties of grade P91 steel [**161**, **230**]. These results show that average creep deformation rate is significantly higher during hold times under cyclic loading than seen in pure creep tests at the same stress levels and it rises significantly starting from the very first cycle.

Although Wood *et al.* [**231**] observed no obvious effect of increasing hold times on the C-F endurance of grade P91 steels at 525°C, a large number of other researchers have observed reduced C-F endurances with increasing hold times while conducting tests at 525-600°C [**232**, **233**, **234**, **235**]. Notably, Fournier *et al.* [**161**, **224**, **225**, **230**, **236**, **237**, **238**] have extensively researched the influence of hold times at either of the maximum tensile or compressive stress or strain under C-F loading conditions. Figure 2.11 shows the loading cycles used in those studies. It was shown from their research that the fatigue life and micromechanisms responsible for C-F crack formation and growth endurances are significantly influenced by introducing hold times, with compressive holds tending to be much more deleterious than tensile holds. It was also noted that fatigue lives were comparatively shorter with hold times than that observed for pure LCF tests with no hold time. The presence of hold times during C-F loading is shown to significantly accelerate the microstructural coarsening (and cyclic softening) with more equiaxed cells tending to evolve at low dislocation densities [**16**].

Fournier *et al.* [**237**] attributed the mean stress effects – where mean stresses of opposite sense are developed during cyclic deformation with the introduction of a given type of hold – as the

primary reason behind the deleterious nature of compressive holds. Since compressive holds give rise to tensile mean stresses within the surface oxide layer, the tendency towards forming/growing a crack is much higher than it would be for tensile holds. Irrespective of the type of hold, creep dominant damage accumulation in the form of grain boundary cavitation was not evident and hence C-F crack formation and growth occur primarily via a transgranular mode of failure [**226**, **227**, **236**].

C-F tests conducted at 550°C showed significant variation of the bulk Young's modulus during cycling indicating the possibility of specific environmental interactions [**225**]. The significant role of oxidation in the C-F deformation behavior of grade P91 steel is further highlighted in numerous research works [**236**, **237**, **238**, **239**, **240**]. Kannan *et al.* [**241**] conducted C-F tests at 550°C and 600°C under ambient and controlled environments with similar test parameters and found that cycles to C-F crack formation and overall endurances to increase under the latter condition. Fournier *et al.* [**236**] found that two distinctly different domains of crack formation exist in an oxidizing environment at 550°C that depend on the kind of loading and the applied cyclic strain range. Figure 4.7 graphically depicts both these distinct domains as observed at 550°C under C-F loading of grade P91 steel. As it can be seen from this figure, the critical strain range partitioning the two domains decreases as the hold time increases.

Domain 1 is typically characterized by thin surface oxide layers (2-3 μm) and no environmentally assisted crack nucleation was observed as confirmed by the intact oxide layers. Hence, C-F cracks formed due to the well-known fatigue dominated micromechanisms and propagated transgranularly with branching (see Figure 4.8(a)). This domain was noted to be characteristic of pure fatigue tests and C-F tests with a relatively low strain range [**236**]. In contrast, domain 2 is characterized by very thick (~ 20 μm) and multilayered oxide layers around cracks. This

indicates the possibility of oxidation influencing C-F crack formation via an environmental attack through the brittle oxide layers that tend to become progressively porous under cyclic loading and consequently develop stress concentrations in the material in regions of thick oxides [**238**]. Figure 4.8(b) shows the contrastingly different optical micrograph characteristic of this domain with widely opened cracks filled with oxides propagating predominantly along a straight path. This domain was noted to be characteristic of C-F tests especially with a high strain range.

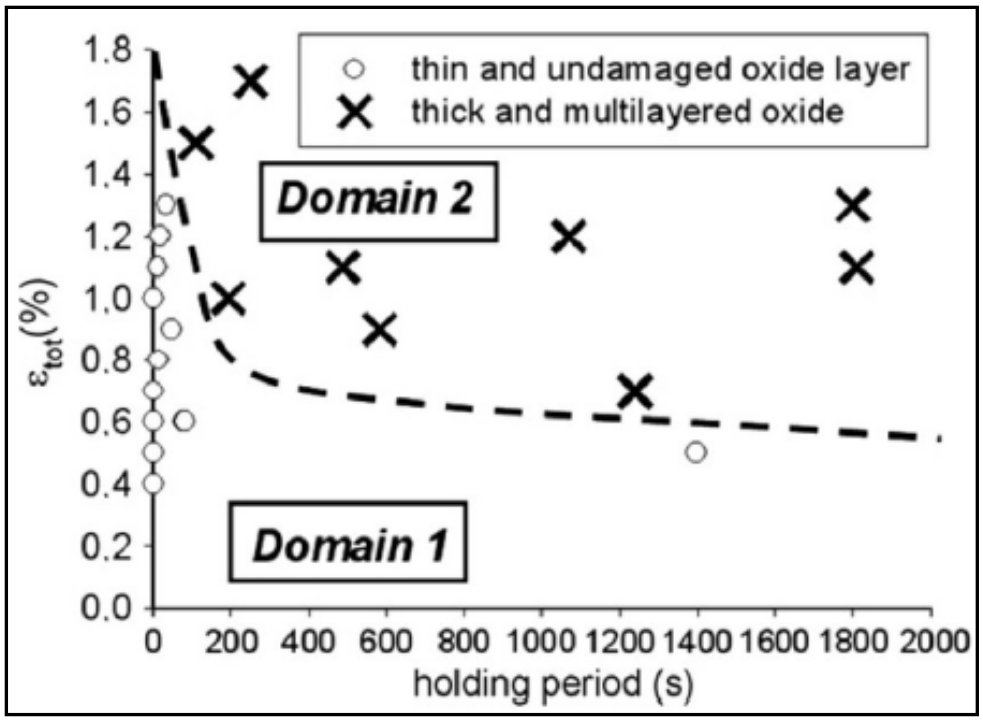

Figure 4.7. Existence of two distinct domains of oxidation damage mechanisms during C-F crack formation in grade P91 steel at 550°C [236], where total strain, ε_{tot} = fatigue strain range + ε_{creep}.

An earlier C-F based RR conducted in Japan on grade P91 steel at 550°C found conclusions that fall in line with these reported observations, both for LCF and hold time tests [**242**]. Figures 4.9(a) and (b) show the effect of tensile and compressive hold times, and testing environment, respectively as reported from this RR.

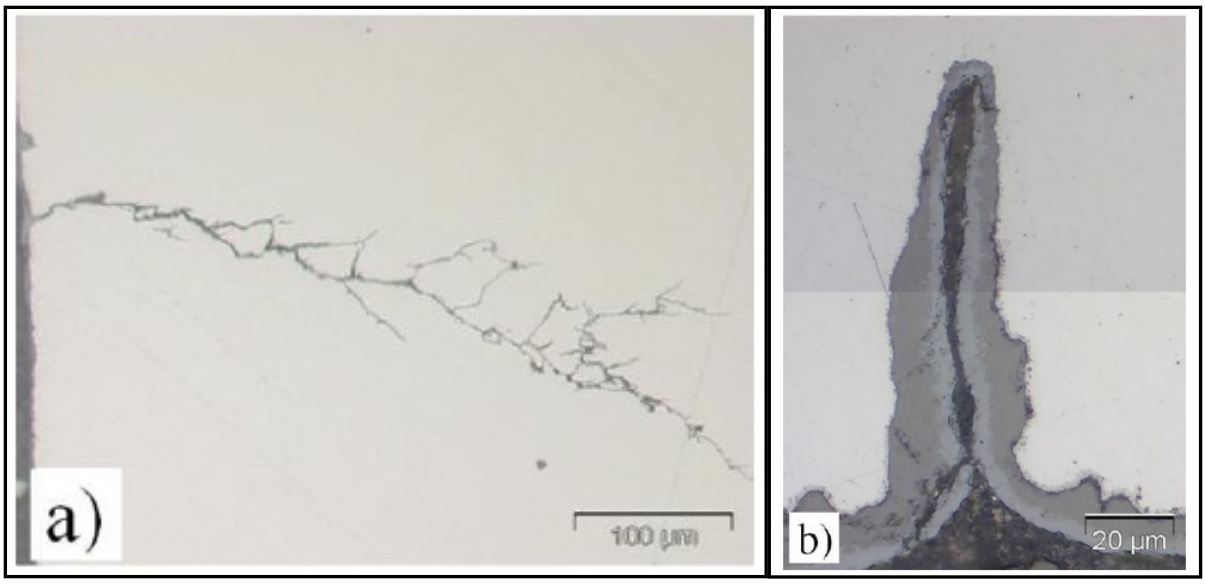

Figure 4.8. Optical micrographs showing the existence of two distinct domains of environment induced oxidation damage during C-F deformation of P91 steel [236], with (a) domain 1 damage and (b) domain 2 damage.

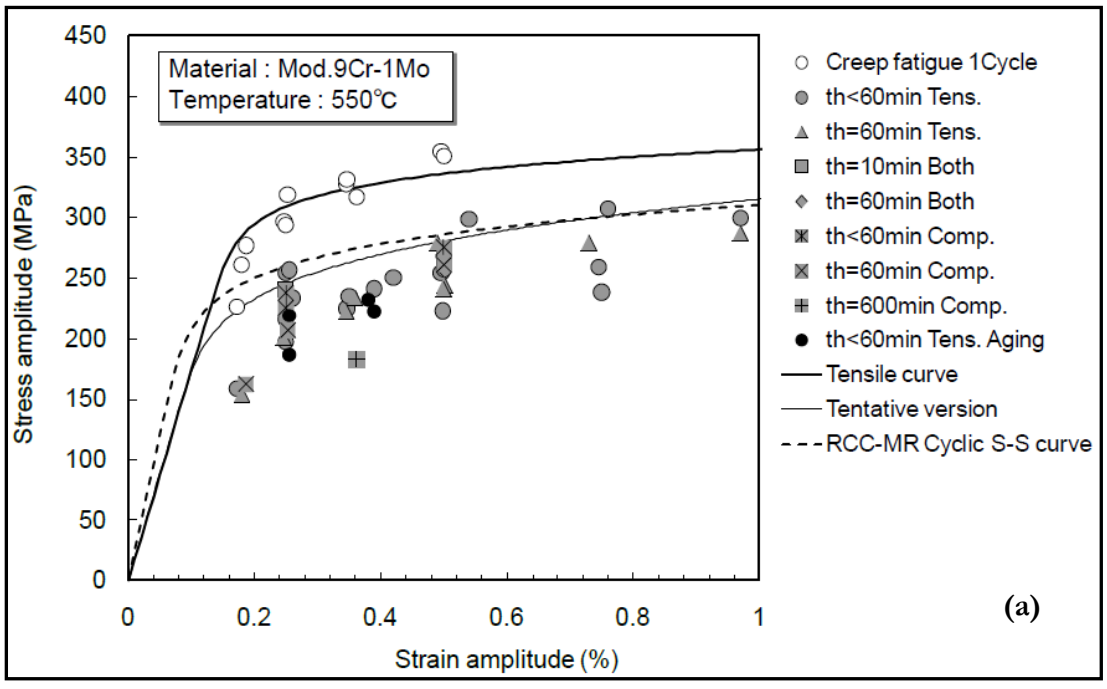

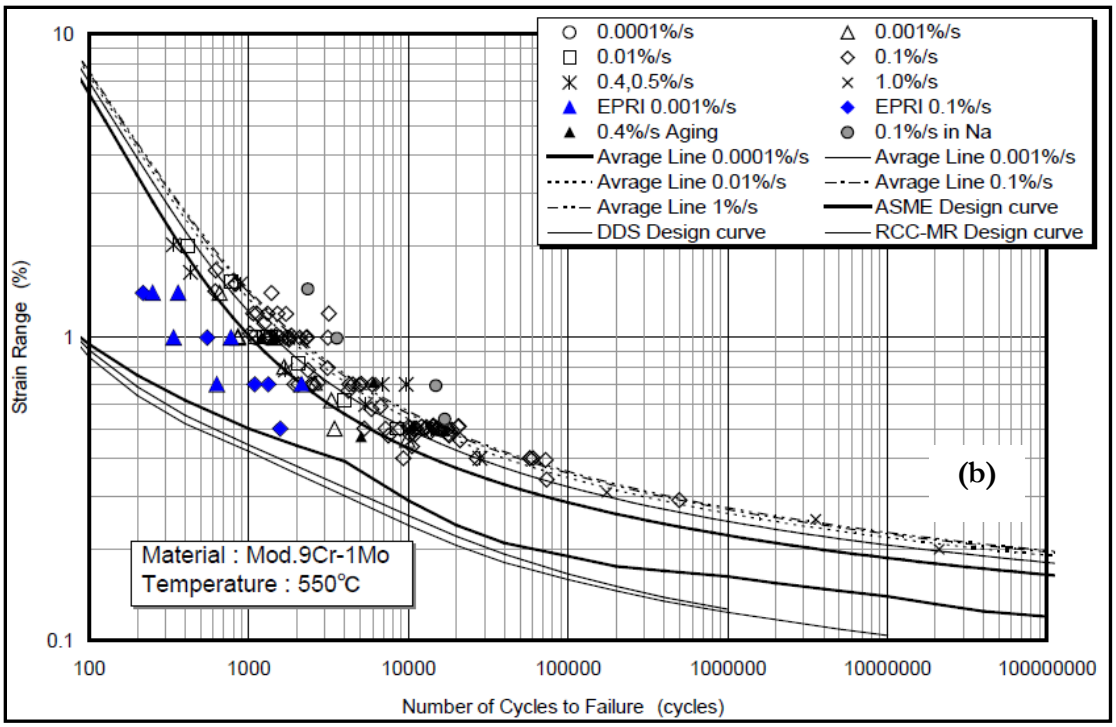

Figure 4.9. (a) Monotonic and cyclic stress-strain curves and (b) C-F test curves at 550°C from a Japanese round-robin study of grade P91 steel [242].

4.2.3. Constitutive modeling efforts

4.2.3.1. Need for developing a novel constitutive relation

Predicting the lifetimes of elevated temperature materials under LCF and C-F loading is very important for structural applications and remains an area yet to be understood clearly. Fournier *et al.* [**238**] predicted the C-F lifetimes in P91 steels as two distinct types of competing interactions between creep, fatigue and oxidation. They predicted number of cycles for C-F crack initiation using Tanaka and Mura's model [**243**] and for crack propagation using the Tomkins model. Although these models compared well with experimental data under the tested conditions, there were considerable limitations. Other common C-F lifetime prediction models for grade P91 steels include time fraction rule [**244**], modified ductility exhaustion method by Takahashi [**245**], strain range

separation method by Hoffelner [**246**], approach for pressure vessel applications by Prager [**247**], hybrid method of time fraction and ductility exhaustion [**248**] and simplified model approach by Jetter [**249**]. All of these models have applicability limitations and suffer from certain drawbacks as outlined in [**242**].

4.2.3.2. Background for model's formulation

Laboratory specimens, contrary to components in-service, are mostly tested under accelerated loading conditions to expedite the rate of deformation and specimen failure within realistic cost- and time-bounds. Predictive constitutive modeling thus plays a pivotal role in characterizing a material's response under a certain loading condition, with required input(s) from laboratory test data. The goodness of the prediction, however, depends on the basis and robustness of a particular constitutive model and the scope of its applicability. Since dislocations directly correspond to the degree of plasticity, constitutive models based on their density evolution and interaction characteristics should be able to predict a material's microstructural evolution under *any* loading condition. Moreover, dislocations are responsible for the various physical mechanisms observed during deformation; hence dislocation-based models are comparatively more robust for predicting long-term deformation during service from short-term laboratory test data.

Constitutive fatigue and C-F modeling of various elevated temperature materials have not only indicated the importance of the as-received microstructure and starting dislocation densities, but also both their evolution kinetics upon cyclic deformation [**250**, **251**, **252**, **253**, **254**, **255**, **256**, **257**, **258**, **259**, **260**, **261**]. All these studies also indicate the complex nature of varying dislocation interactions at the distinct microstructural scales that renders constitutive modeling as rather cumbersome. This has manifested in the form of multiple parametric definitions for the different

types of interactions with each requiring non-unique set(s) of fitting parameters that vary, at least, with temperature [**262**]. Thus, in effect, multiple parameters need to be identified for different loading conditions that render the models less robust and their extrapolation capabilities rather limited. Similarly, numerous constitutive models that can explicitly account for temperature and strain-rate – or equivalently, plastic shear rate – effects exist [**263**, **264**, **265**, **266**, **267**, **268**, **269**] but they are generally restricted by their scope of applicability and capability to be extended to other materials. Although preliminary efforts have shown promise [**270**], further progress in the development of constitutive models that can account for thermo-mechanical loads also still faces challenges [**271**]. Therefore, there is an ever-increasing need for generalized analytical frameworks based on sound underlying mechanics that can link all the relevant parameters of importance with minimal fitting parameters.

Although quite a few constitutive fatigue and C-F models exist for martensitic/ferritic steels in general [**272**, **273**] and grade P91 steels in particular [**274**, **275**, **276**, **277**, **278**], only a small number of them have both the evolution of dislocation densities and their interactions as the fundamental basis of their formulation [**279**, **280**, **281**, **282**]. The last set of modeling efforts are based on relatively strong assumptions and their robustness mostly depends on the careful selection of model parameters that are accordingly modified depending on the nature of loading. Moreover, these efforts require the use of considerable computational resources for identifying the tensor-based model parameters that are usually greater than 10 in number. From a mechanistic perspective, these constitutive models also do not account for strain-rate effects that are shown to have considerable influence on the cyclic behavior (especially with hold time) of martensitic/ferritic steels [**283**]. In an endeavor to address these issues, one of the major objectives of this work lies in the constitutive modeling of grade P91 steels under fatigue and C-F loading, with inputs from laboratory test data at

625°C, using a minimal approach based on dislocation densities' evolution and their interactions. The formulated constitutive model requires very minimal computational resources with the need to fit very minimal model indices that are mostly kept constant for a given material (refer Chapter 6 for detailed description). In this regard, the starting values of the model indices – obtained from the first loading cycle – serve to inherently characterize the initial microstructural variability among nominally homogeneous test specimens. This model will also represent the *first* effort in explicitly linking all the loading parameters (including temperature and strain-rate) considered important for characterizing the fatigue and C-F behavior of grade P91 steels. Demonstration of the model's robust simulation and predictive capabilities for characterizing this material's uniaxial monotonic and cyclic behavior (with and without hold time) is provided in Chapter 7 of this work.

Chapter 5: EXPERIMENTAL METHODS AND DETAILS

As mentioned in Chapter 1, the experimental data used in this work is obtained from a RR conducted for supporting the recently developed ASTM standard for C-F testing, E2714-09 [**31**]. The background and basic nuggets of this RR along with other experimental details will be descriptively outlined in this chapter.

5.1. Round-robin testing

5.1.1. Background and need

Because of the large number of experimental variables involved during laboratory C-F testing that can introduce variability in the data, it is beneficial to code the best practices in a standard test method. To respond to this need, the ASTM Task Group on C-F Crack Formation (E08.05.08), with concerted global support enabled by EPRI (Electric Power Research Institute), developed a new standard E2714 in 2009 [**31**]. Specifically, this standard deals with and is limited to the formation of a macroscopic crack in a specimen that was initially un-cracked, to a size detectable by a technique stated in the standard.

To support and achieve completeness of this new standard, it is necessary to develop the precision and bias statements that describe the intra-/inter-laboratory variations expected within/among the different laboratories worldwide, while following the specified testing procedure on a nominally identical material. A definitive statement on precision* and bias* is also necessary for a provisional standard to become a permanent one as per ASTM rules (**refer end of the paragraph for definitions*). To this end, a voluntary RR program began in 2009 with the primary objective of

conducting C-F tests (at 625°C) on grade P91 steel to characterize the number of cycles required for crack formation. This RR also included monotonic, continuous LCF and creep rupture tests that were conducted as per existing ASTM standards E8 [**284**], E606 [**55**] and E139 [**39**], respectively for completeness with regard to characterizing the test material.

* **Precision**: the closeness of agreements between independent test results obtained under stipulated conditions
* **Bias**: the difference between expectation of the test results and an accepted reference value

5.1.2. Testing conditions

Since the highest in-service temperature of grade P91 steel in current applications is in the range of 580-600°C, it was proposed to conduct all the RR experiments at 625°C to accelerate the microstructural evolution/damage kinetics for reasons described earlier. To finalize the other important testing parameters like strain ranges, type and duration of hold times, loading and unloading waveforms and strain rates, 2 of the RR participants volunteered to conduct the so-called pilot tests – a trial run of tests under different loading conditions to finalize the testing protocols – on grade P91 steel at their respective laboratories. Dr. Stuart Holdsworth (EMPA, Switzerland) and Dr. Yukio Takahashi (CRIEPI, Japan) conducted these strain-controlled tests at strain ranges, $\Delta\varepsilon$ = 1% and 1.5% with hold times (t_h) varying from 0 to 3600 seconds using triangular loading and unloading waveforms at a strain-rate of 0.025% per second. The pilot test study results obtained from these tests are shown in Figure 5.1 and after a careful examination of the test results, the RR test parameter matrix was finalized as described next.

The isothermal, strain-controlled C-F tests would be conducted at strain ranges of 0.5%, 1% and 1.5 % – or equivalently, strain amplitudes of ± 0.25%, ± 0.5% and ± 0.75%, respectively – all at

625°C with hold times of either 0, 600 or 1800 seconds at the maximum (peak) tensile strain (see Figure 5.2). The strain-rate was chosen to be 0.025% per second, uniformly ramped under triangular loading/unloading waveforms. Thus the cycle times for the three strain ranges without hold times will be 40, 80 and 120 seconds, respectively. As stated in the standard, a 2% load drop – or equivalently, reduction in maximum force – was stipulated as the end-of-life criterion for these tests. With knowledge from the pilot tests, it was expected that the test temperature, strain ranges and hold times chosen were sufficiently high for C-F interactions to be a factor during the tests.

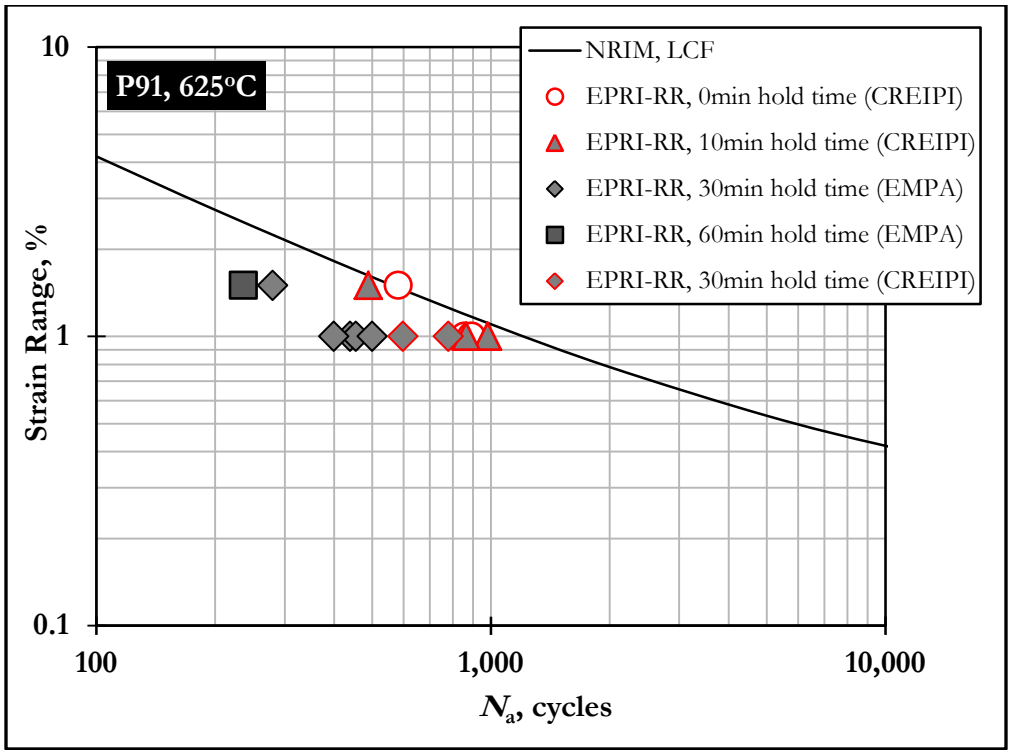

Figure 5.1. Pilot test results from C-F testing of grade P91, where N_a corresponds to the number of cycles required to form a C-F crack as per 2% load drop criterion. Data courtesy of Dr. Stuart Holdsworth (EMPA, Switzerland) and Dr. Yukio Takahashi (CRIEPI, Japan).

Table 5.1 shows the list of different testing conditions as assigned to the participating laboratories in the RR and each test was conducted in duplicate in an effort to estimate the intra-laboratory variability or repeatability. On average, each participant was thus committed to

conducting 6 to 8 tests under 3 or 4 different testing conditions. From existing literature on LCF induced deformation [**285**], a continuous cyclic softening behavior was expected in grade P91 steel at elevated temperatures. Hence, the RR participants were requested to follow the corresponding end-of-test criterion from the C-F test standard [**31**], as shown in Figure 5.3. In this approach, the maximum tensile stress (σ_{max}) is plotted as a function of the number of loading cycles. The figure also shows the suggested methodology for determining the C-F life of a test specimen; the C-F life corresponds to a X% drop in maximum stress (or equivalently, load).

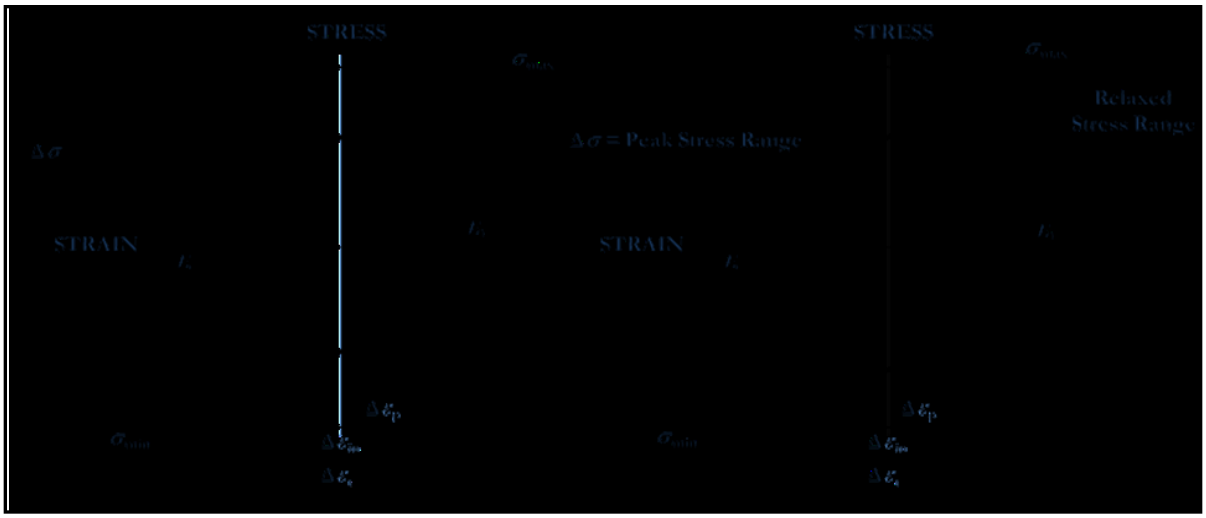

Figure 5.2. Hysteresis loops for the RR tests (a) without hold time and (b) with hold time (under strain control) [31].

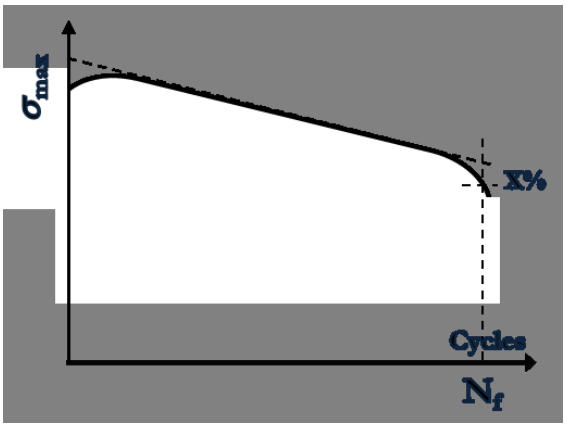

Figure 5.3. Crack formation and end-of-test criterion based on reduction of peak stress for continuously softening materials [31].

Table 5.1. Test parameter matrix of the E2714-09 round-robin, where number entries indicate the total number of tests planned under those conditions [286].

Participants ↓	P91 Crack Formation					
Strain Amplitude %→	±0.25 %	±0.5 %	±0.75 %	±0.5 %/10 min Hold	±0.75 %/10 min Hold	±0.5 %/30 min Hold
Idaho National Laboratory: Laura Carroll	2	2		2		
EMPA Switzerland: Stuart Holdsworth				4		4
Tech U. Darmstadt: Alfred Scholz	2	2	2			
CRIEPI, Japan: Y. Takahashi		2	2	2	2	2
GE, Schenectady: David Knorr		2	2		2	
BAM, Berlin: Hellmuth Klingelhoeffer	2		2	2		
NASA, Glenn: Brad Lerch			2	2	2	
ANSTO Australia: Warwick Payton	2			2	2	
Georgia Tech: Rick Neu	2	2		2	2	
Tohoku Univ.: A. T. Yokobori	2	2		2	2	
NRC, Canada: Jonathan Tsang			2		2	2
Univ. of Arkansas: Ashok Saxena	Conduct creep deformation and rupture testing and metallography and TEM of the test material					
MPA Stuttgart: Andreas Klenk/Karl Meile						6
British Energy: Mike Spindler	2	2	2	2		
Politecnico di Milano: S. Beretta					2	2
BiSS, India: R. Sunder		2		2		4

5.1.3. Test specimen geometries and machining plan

All of the P91 specimens used for this RR were obtained from a retired ex-service pipe donated by EPRI, Charlotte, USA (see Figure 5.4 inset). The pipe material was re-normalized to ensure consistency with the original tempered martensitic/ferritic microstructure of these steels. The physical dimensions of this pipe are as follows: outer diameter: 482 mm, wall thickness: 47.5 mm and a length of approximately 1 m. A graphical illustration of this pipe that also shows the 2 cuts along its length to obtain 3 sections is presented in Figure 5.4. The chemical composition of the test material employed in this work (in weight%) is given in Table 5.2 [**287**].

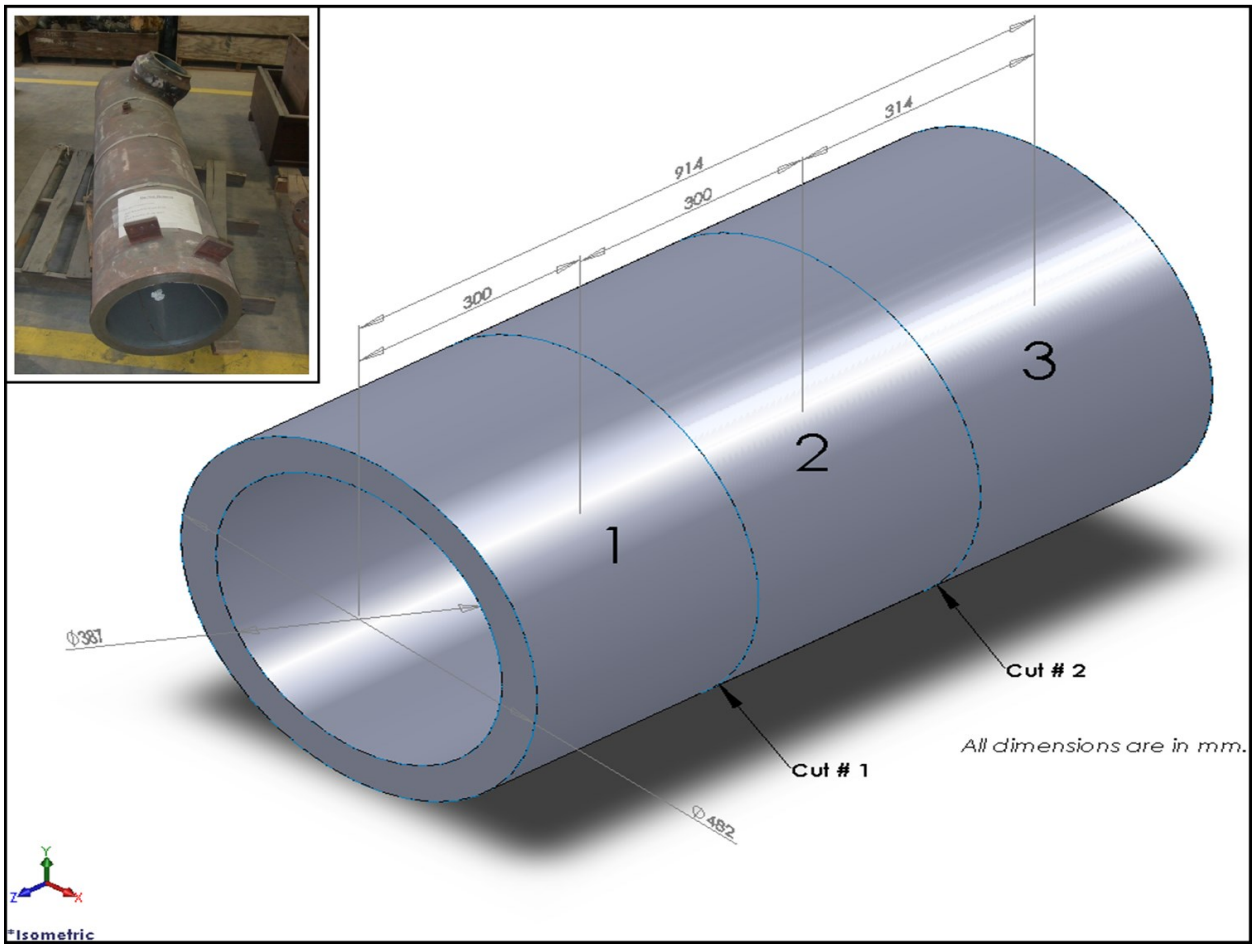

Figure 5.4. A graphical illustration of the retired P91 pipe used for the ASTM RR with the inset showing the actual pipe donated by EPRI, Charlotte, USA.

Table 5.2. Actual chemical composition of the test material (in weight%) [287].

C	Si	Mn	P	S	Ni	Cr	Mo	As	V	Nb	Cu	N	Sb, Sn	Fe
0.11	0.31	0.45	0.011	0.009	0.19	8.22	0.94	0.005	0.21	0.07	0.16	0.039	0.001	Bal.

The 3 cut segments were respectively labeled as sections 1, 2 and 3 and only the cut section 2 was used for this RR. The cut section 2 was further cut into 6 equal subsections along the pipe's

cross-section and labeled as shown in Figure 5.5. All the RR participants were given their choice of either receiving machined specimens or specimen blanks that they would use for machining specimens. A comprehensive collection of all the specimen drawings used in this RR is provided in [**288**]. It was stipulated that all of the test specimen geometries must comply with the guidelines recommended by the test standard E2714-09 (see Figure 5.6). All the test specimens were machined in the axial orientation around the pipe's circumference. The machining layouts of the various subsections (2-1 to 2-4) used for machining the specimen blanks and the machining plan employed for extracting blanks/specimens is comprehensively described in [**288**].

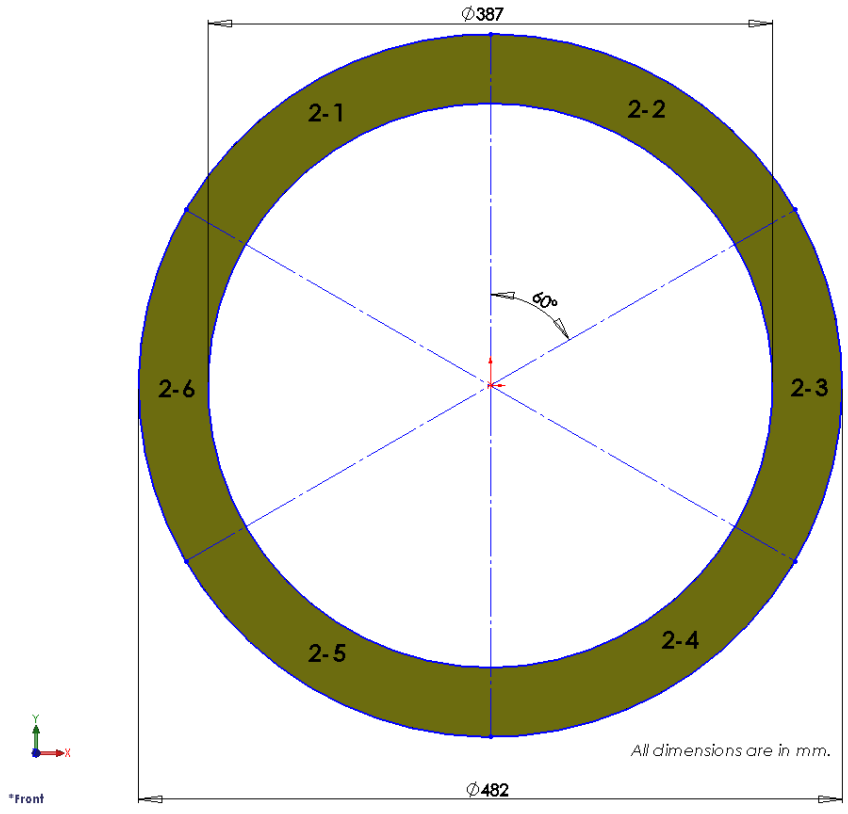

Figure 5.5. Cross-sectional view of the pipe section 2 as used for the RR.

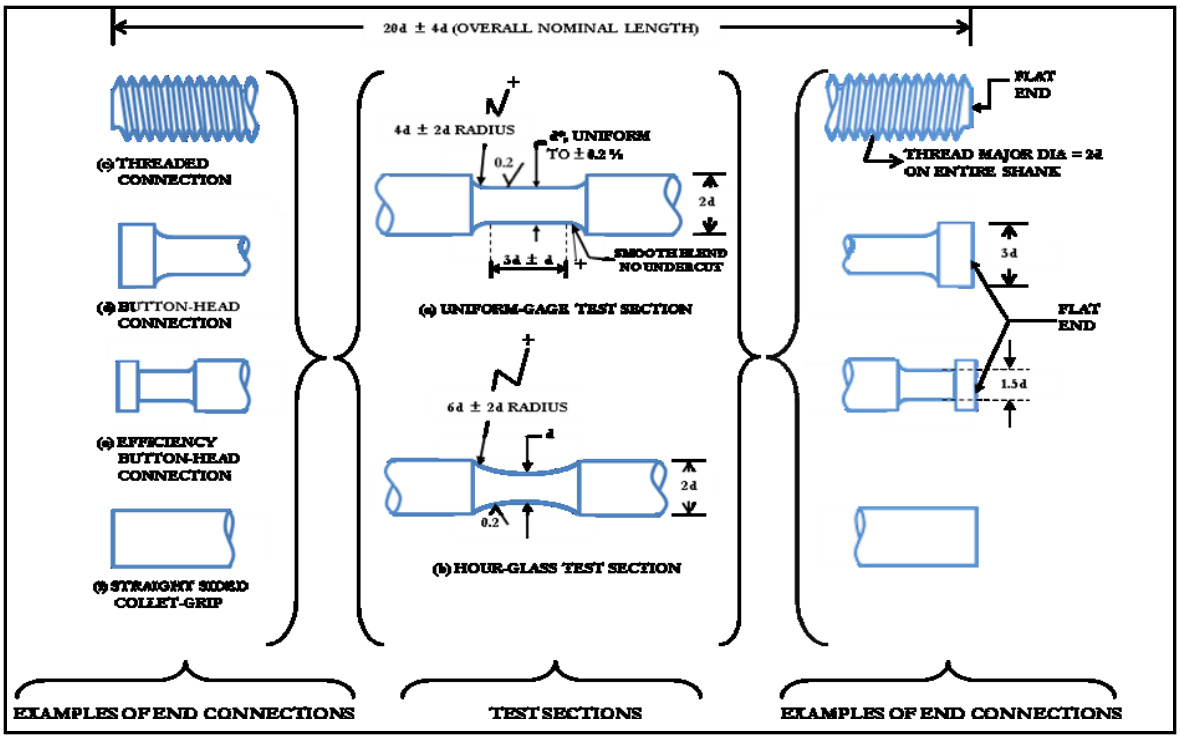

Figure 5.6. Test specimen configurations for C-F testing as recommended by the ASTM C-F test standard, E2714-09 [31].

5.1.4. Statistical analyses of reported test data

To formulate the precision and bias statements needed for supporting the C-F test standard, statistical analyses of the reported RR data were also performed. These analyses provide a measure of the inter- and intra-laboratory variability also termed as reproducibility and repeatability, respectively. Statistical analyses are performed as per the guidelines prescribed in the ASTM standard E691-09 [**289**].

5.2. Round-robin contribution

As part of characterizing the RR test material, University of Arkansas (UA) volunteered to conduct creep deformation and rupture tests, and monotonic tensile tests on grade P91 steel. They also performed the metallographic evaluation of the failed test coupons from these tests and of test

specimens forwarded by other RR participants. Transmission electron microscopy (TEM) analysis of grade P91 steel material behavior under different loading conditions is already well documented (referenced in Chapter 4) and hence is not deemed necessary in this work.

5.2.1. Creep deformation and rupture testing

Creep tests were conducted on smooth round specimens with a gage length and diameter of 25.4 mm and 5.08 mm, respectively that were designed as per ASTM E139 standard (see Figure 5.7). Tests were carried out at 625°C (898 K) under uniaxial static (constant load and temperature) loading conditions in a lab-controlled atmosphere (20 ± 2°C and 50% relative humidity) using dead weights. A calibrated LVDT (linear variable differential transformer) transducer with a repeatability of 0.1 μm was employed to measure specimen elongation during the tests. The test temperature was monitored continuously to be within ± 2°C of the test temperature during the tests using two K-type thermocouples wound mechanically at the top and bottom ends of the specimen gage length.

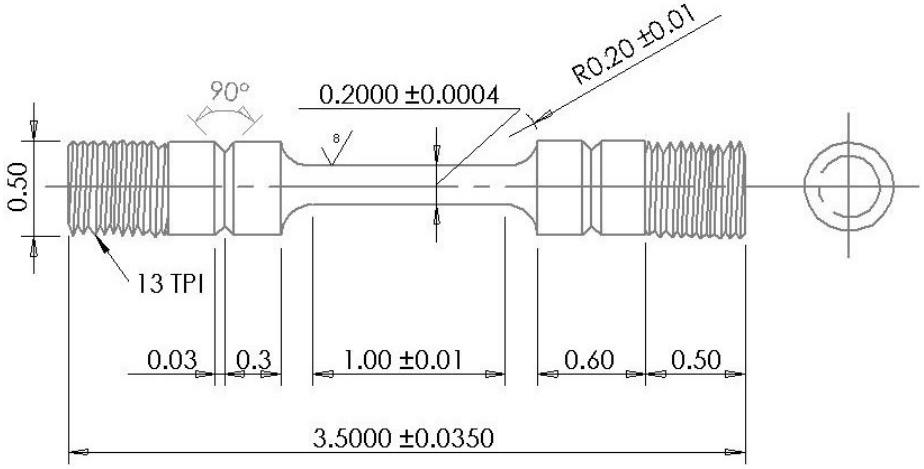

Figure 5.7. Drawing of specimen used for the creep deformation and rupture testing of grade P91 steel (all dimensions in inches).

The test durations varied from as low as few days to as high as few months (see Table 5.3). The test parameters were finalized using a model based on the Larson Miller parameter (LMP), one

of the well-established time-temperature parameters (TTP). This parameter provides an analytical relation between the absolute temperature (T) and expected rupture time (t_r) in hours. Figure 5.8 shows such a plot for grade P91 steel wherein stress is plotted against the LMP, with the constant **C** being equal to 30 [**290**]. All tests were continued until final rupture except the one at 117.5 MPa stress condition that was deliberately stopped at expected mid-life to understand the microstructural evolution under creep loading conditions.

Table 5.3. Test parameter matrix for the creep deformation and rupture testing conducted by University of Arkansas on grade P91 steel.

Type of Testing	Test Temperature, °C	Expected Life, hours	Stress Required, MPa
Creep deformation and rupture	625	5000	101.5
		2000	117.5
		1000	130.0
		750	136.8
		500	138.3
		300	142.7
		150	151.5

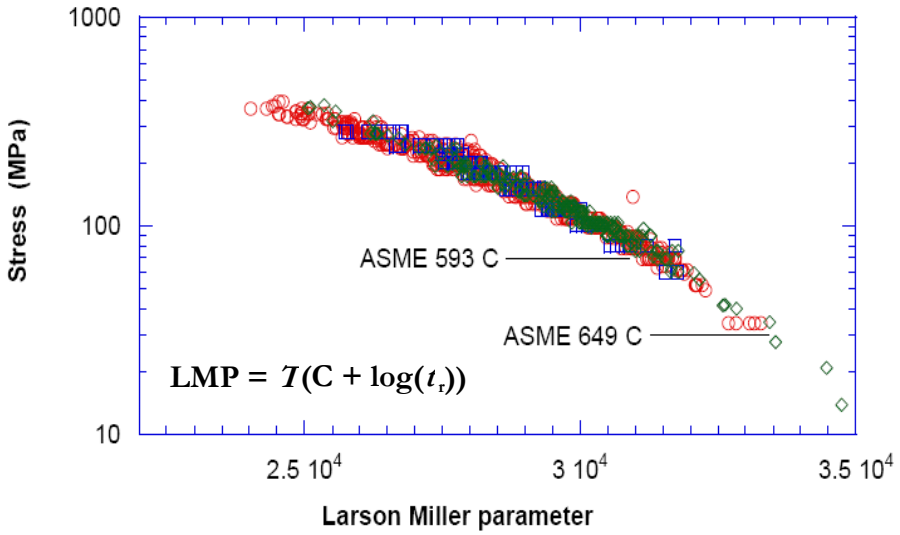

Figure 5.8. A plot of stress versus Larson Miller Parameter (LMP), that is commonly used for estimating the creep rupture test parameters, for grade P91 steel [290].

5.2.2. Monotonic tensile testing

Uniaxial monotonic tensile tests were conducted (on-site at BiSS, India) on cylindrically threaded dogbone specimens with a gage length and diameter of 12.7 mm and 5.08 mm, respectively as per ASTM E8 standard [**284**]. These tests were performed both at room temperature (24°C) and at 625°C at a quasi-static strain-rate of 0.00192 s^{-1} in a lab controlled atmosphere (20 ± 2°C and 50% relative humidity). A high temperature ceramic extensometer was used to measure the specimen elongation during testing.

5.2.3. Post-test inspection

Before the tested specimens were mechanically sectioned for metallography and further optical microscopic examination, high resolution digital photographs of the as-tested specimens were obtained for the records. All these photographic images were obtained from a Nikon digital single-lens reflex (DSLR) camera. Visual inspection of these specimens was carried out and prominent characteristics of the specimen morphology and the presence of any geometric instability (or bulging) were carefully noted. Metallographic specimens from the failed test coupons were then prepared by standard practices to facilitate in further microstructural investigation. After mounting in transparent holders, the established routine of 2 steps of grinding and polishing – coarse and fine – each using SiC (silicon carbide) papers of different grit sizes and abrasives is followed in this regard. In order to reveal the fine microstructural features like grain and lath boundaries, the specimens were chemically etched using either Vilella's reagent (1 gram picric acid, 5 ml hydrochloric acid and 100 ml ethanol) or Nital (3% nitric acid and 97% methanol). In this context, few RR participants did complete some aspects of post-test inspection studies at their respective facilities and the results from such work will be referenced accordingly in Chapter 7. These results are also intermingled with UA's metallographic studies.

Chapter 6: CONSTITUTIVE MODELING METHODS AND DETAILS

6.1. Introduction

Constitutive modeling plays a vital role in characterizing a material's response under long-term in-service conditions with required input from short-term laboratory test data. Sound analytical models can thus greatly assist in minimizing the extensive resources required for conventional laboratory testing. Factors such as the amount of available and required computational resources, number of fitting constants or indices etc., effectively dictate the applicability and degree of robustness of such models for a given objective. Besides interpolative simulations, demonstration of extrapolative predictive capabilities of such constitutive models is also considered important. With all these considerations in mind, the physical basis and formulation of constitutive models employed in this work for simulating and predicting the creep, fatigue and C-F behavior of grade P91 steels will be descriptively outlined in this chapter.

6.2. Modeling creep deformation and rupture behavior

The effectiveness of a creep model to represent a material's characteristic curve shape can depend on the relative proportions of the three creep regimes as fractions of strain and time at rupture, and the way in which they vary over (σ, T) of interest. Such analytical models are essential and play an integral role for subsequent data- and structural- analysis. Since the existing literature on P91 steel indicates the relative importance of all three distinct creep regimes, the focus of this exercise was on choosing a single expression model that is capable of representing these regimes *all* by itself. Furthermore, this model should also analytically account for changes in deformation kinetics as a function of stress and temperature. A comprehensive compilation of existing

constitutive models as applicable to any elevated temperature candidate material and specifically grade P91 is already provided in Table 4.3 and [**219**, **220**], respectively. After carefully evaluating all of these models, the logarithmic creep strain prediction (LCSP) model was found to be most suitable for the available creep data [**220**]. This model has the least number of fitting constants and its mathematical form has the natural shape of a creep curve at nominally constant stress and temperature. However it was found that in its current form, this model suffers from two obvious shortcomings:

1) The model does not reduce to the correct form (or provide expected value) when the boundary conditions at the start and end of a typical creep rupture test (*i.e.,* as one asymptotically approaches time $t = 0$ and $t = t^*$) are applied.
2) The model does not take full advantage of parameters that can be obtained from actual experiments to reduce the number of fitting constants for further robustness.

Hence, a modified LCSP model is proposed here by addressing the above shortcomings of the original model (see Equation (6.1)). As per the modified model, at any time t in a creep rupture test beyond 1 hour, engineering creep strain ε_t is given as

$$\log(\varepsilon_t) = \left[f_s\left(\frac{\log(t^*)+\beta}{\log(t_\varepsilon)+\beta} - 1\right) + f_j\right]^{1/p} - C \qquad \text{(6.1)}$$

where,

$$f_s = \frac{\beta}{\log(t^*)}[(\log(\varepsilon_1) + C)^p - (\log(\varepsilon_{ru}) + C)^p]; \quad f_j = (\log(\varepsilon_{ru}) + C)^p$$

$p(\sigma, T_c) = p_0 + p_1 \log(\sigma) + [p_2/(T_c + 273)]$ and β, p, C are fitting parameters

T_c = test temperature (°C); σ = applied external stress (MPa)

ε_t = engineering creep strain at time t

t^* = time to failure by creep rupture (hours)

t_ε = time to given engineering creep strain (hours)

ε_1, ε_{ru} = ε_t at time t = 1 hour and uniform strain at rupture, respectively

As discussed earlier, typically from 95% of t^* and beyond, macro-cracking starts to appear because of localized necking and results in an unstable specimen response thereafter. We also know that the reduction in area varies significantly based on the necking characteristics. Hence, the engineering creep strain at rupture (ε_t at time $t = t^*$) is taken to be the measured uniform strain at rupture, ε_{ru} (*i.e.,* strain generated in the specimen's gage length before the onset of necking in a localized region). This strain can be empirically obtained by evaluating the reduction in area (A_{red}) in the specimen gage length at regions away from that of necking. Rather than using the conventional ductility equation for A_{red}, an analytical form as shown in Equation (6.2) is employed in this work. As shown in Figure 6.1, the cross-sectional diameter of the specimen at locations 1, 2 and 3 is measured and averaged to obtain d_{unif} and this value is used to compute A_{unif}.

$$A_{red} = \frac{A_{orig} - A_{unif}}{A_{orig}} \quad \text{..... (6.2)}$$

where A_{orig} = Original cross-sectional area in the specimen gage length

A_{unif} = Uniform cross-sectional area obtained by using d_{unif} (the average of diameters at regions away from the necked region)

Minimizing human measurement errors and the effect of complex strain profiles across the specimen gage length were the primary reasons to compute d_{unif} rather than using a single diameter value in the unnecked region. The choice of position of locations to compute d_{unif} does not seem

to play a significant role, as long as they are chosen to be approximately equidistant (to capture the diameter variation across the specimen gage length of the creep ruptured specimen) away from the necked region to the edge of the gage length markers. Also, it was observed in this work that a choice of 3 such locations is optimal and more number of locations do not make a considerable difference to the averaged d_{unif} value.

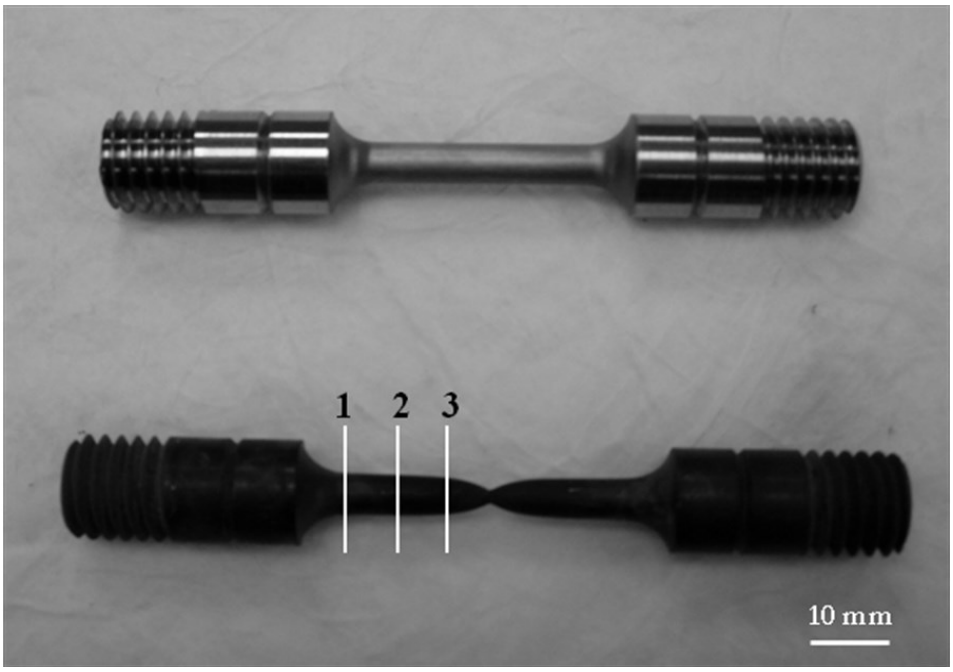

Figure 6.1. Pictorial representation for the empirical measurement of uniform strain at rupture, $\varepsilon_{\mathrm{ru}}$. Vertical lines numbered 1, 2 and 3 indicate locations where diameter is measured to compute d_{unif} . Untested specimen in the top is kept as a reference for the creep ruptured specimen below.

6.3. Modeling fatigue and creep-fatigue behavior

A novel constitutive model for simulating and predicting the fatigue and C-F behavior of grade P91 steel is proposed in this work for reasons discussed earlier in section 4.2.3**.** The physical basis of this equation-of-state relation is based on a thermodynamically consistent perspective of crystal plasticity and will be discussed first for uniaxial monotonic behavior. Based on the proposed

mechanism, a constitutive relation based on dislocation densities and their interaction is formulated. The underlying mechanism will then be extended for cyclic behavior followed by the formulation of the cyclic version of the constitutive model.

6.3.1. Need for an advanced plasticity framework

Plasticity is the ability of a material to deform irreversibly in response to an external load and is a critical consideration to minimize the unexpected catastrophic failures of in-service structural components. Plasticity in crystalline solids is classically interpreted as an incompressible and dissipative mechanism of shearing interatomic bonds sequentially through the component crystal lattices. In polycrystalline materials, plasticity is mediated either through slip of dislocations – ubiquitous atomistic scale linear defects – that continuously nucleate from Frank-Read sources and partial dislocations (*i.e.,* stacking faults) or perfect dislocations that emit from stress concentrations. The plastic shear rate or strain-rate – as expressed quantitatively by Orowan – is directly proportional to the Burgers vector $|\vec{b}|$ of a mobile dislocation and averaged quantities of their densities and velocities along active slip systems [**291**]. The Orowan relation thereby implicitly projects crystal plasticity to be macroscopically smooth and steady and suitable for a mean-field analysis.

Recent technological advancements have enabled researchers to report experimental observations that increasingly challenge these conventional descriptions of crystal plasticity. Rather interestingly, crystal plasticity is shown to be temporospatially heterogeneous [**292**, **293**] originating either from dislocations that cannot be currently observed [**294**] or even remarkably in the absence of sustained dislocation motion [**295**]. So, fundamental questions still remain unresolved about the existence, origin and nature of dislocations. These results also inarguably suggest a pressing need for

the development of advanced frameworks to characterize crystal plasticity [**296**, **297**, **298**], particularly its onset in the atomistic scale [**292**, **295**, **299**, **300**, **301**, **302**]. Since plasticity corresponds to a very complex material response and dislocations individually symbolize it, thermodynamics is ideally suited for addressing this issue [**303**]. But difficulties in employing thermodynamics to study dislocation behavior are epitomized by Cottrell, who cites work-hardening as "*the most difficult remaining problem in classical physics*," and that a material's failure is thermodynamically irreversible and governed by its weakest links [**304**].

Most of the published literature referenced in the upcoming discussion consists of experimental observations reported by researchers on the different aspects of material response during crystal plasticity. However, a mechanistic framework that can convincingly describe and possibly link all these seemingly unrelated experimental results is still lacking. The crystal plasticity mechanism proposed next is presented from a thermodynamically consistent perspective and in the process it seamlessly connects all these distinct observations.

6.3.2. Proposed crystal plasticity mechanism

Crystallographic defects, including dislocations, represent imperfections in a crystal lattice and collectively personify its weakness. Such imperfections increase the entropy – a measure of disorder or randomness – within a material and their existence is necessary for its thermodynamic stability as per Gibbsian mechanics. Generally crystalline solids contain random pockets of such aberrations that are naturally formed or intentionally engineered during material processing to modify certain structural property. The entire group of atom(s) that constitute these imperfections is termed a crystallographically imperfect zone (CIZ) among an otherwise-perfect continuum of crystallographically perfect zones (CPZs). CIZs include point defects that involve just one

constituent atom whereas other CIZs like grain boundaries, voids and secondary-phase precipitate interfaces can involve multiple constituent atoms. Figures 6.2(a) and (b) show schematics of the various CIZs typically observed in microstructured polycrystalline materials. A room temperature quasi-static uniaxial tensile test record for a face centered cubic polycrystalline material is considered herein for further discussion [**305**], where ε_{PL}: proportional limit strain and ε_{UTS}: strain at ultimate tensile strength.

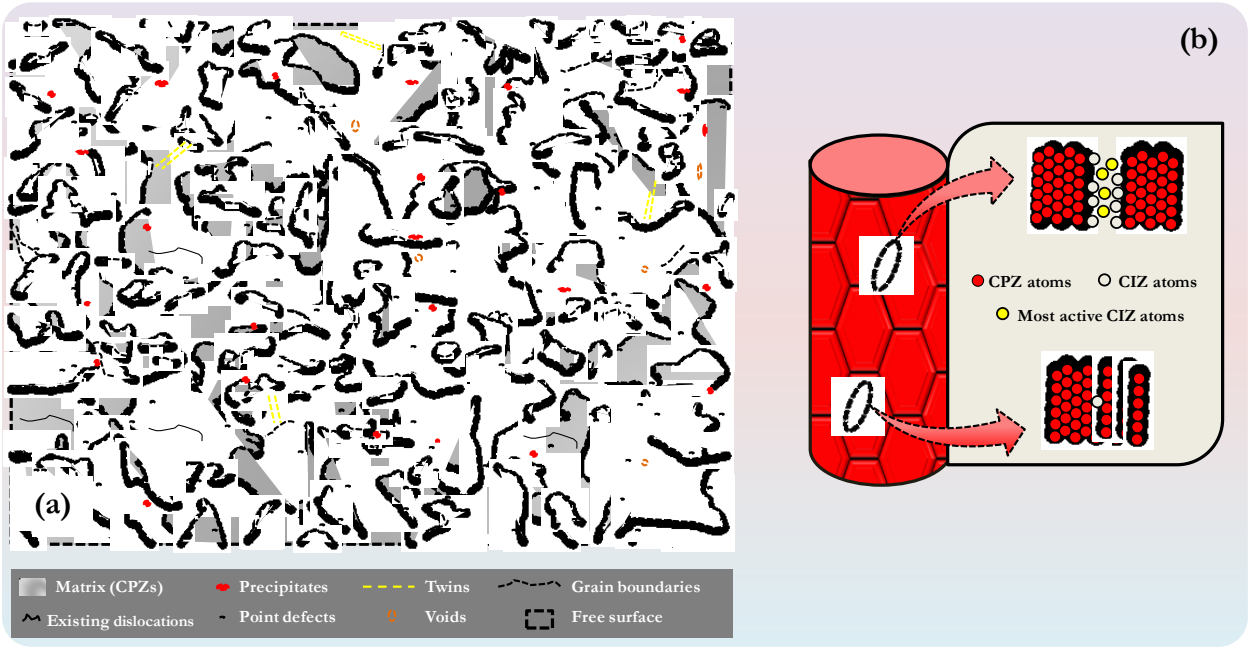

Figure 6.2. (a) Various types of crystallographically imperfect zones (CIZs) typically present among crystallographically perfect zones (CPZs) in polycrystalline materials and (b) Schematic illustrating the zone of influence for two different sized CIZs – one, a high angle grain boundary and another, a point defect (vacancy).

A crystalline metallic material's internal degrees of freedom can be approximately split into relatively-slow configurational (or structural) and fast vibrational (or thermal) components. In this context, it is noted that other components of free energy or their entropies – like magnetic, electronic – are usually neglected in metallic crystalline solids. In the absence of external driving forces, CIZs with a single constituent atom tend to locally distort the lattice structure of adjacent

CPZ atoms. They can have increased structural or vibrational entropies depending on the type of CIZ. Alternatively, atoms within multiple constituent CIZs tend to be highly mobile and also possess weaker restraining and unbalanced interatomic forces than their CPZ counterparts. Such CIZs not only exhibit increased structural entropy due to their limited range atomic ordering, but also exhibit comparatively higher vibrational entropy (mobility) due to their reduced coordination number induced surface tension. As this naturally corresponds to a non-equilibrium thermodynamic state, CIZ atoms with unsatisfied bonds tend to drive themselves closer to adjoining CPZ interfaces to minimize their high interfacial free energies [**303**, **306**]. Accordingly, *all* CIZs within a material are expected to be energetically more stable than CPZs in the absence of external driving forces.

The behavior of CIZs in the presence of external driving forces like thermo-mechanical strains however will vary significantly. The localized distortion behavior of CIZs with a single constituent atom only gets enhanced and hence does not significantly influence macroscopic behavior for any magnitude of external strain. In contrast, the magnitude of the external strain has a significant influence on those CIZs with multiple constituent atoms. For external strains $\varepsilon < \varepsilon_{\mathrm{PL}}$ (***regime I***), the initiated Brownian motion within such CIZs – particularly those characterized by pockets of excess free volume like high angle grain boundaries – becomes dynamically heterogeneous (see Figure 6.3). Such dynamic heterogeneity in a disordered phase is strongly linked to transitory structural ordering irrespective of the nature of involved interatomic forces [**307**]. Although a solid's total entropy is cumulatively approximated by its structural and vibrational entropy components, vibrational entropies do not *always* equally compensate such a transitory loss in structural entropies [**308**, **309**]. Under such a condition, thermodynamically unstable localized transient entropy losses result within a crystal. In this context, it is important to emphasize that entropy losses are energetically unfavored, but *probable* if it is transitory and involves just a limited

number of atoms [**309**, **310**]. Moreover, as per the second law of thermodynamics (SLT), a decrease in entropy is permissible *only* when some work is done on the system. As dependent on these local entropy differences, local configurational symmetries (due to reduced structural entropy induced kinetic slowdown), varying interatomic separations and much weaker interatomic bonding characterize such transiently ordered CIZ atoms [**308**, **311**].

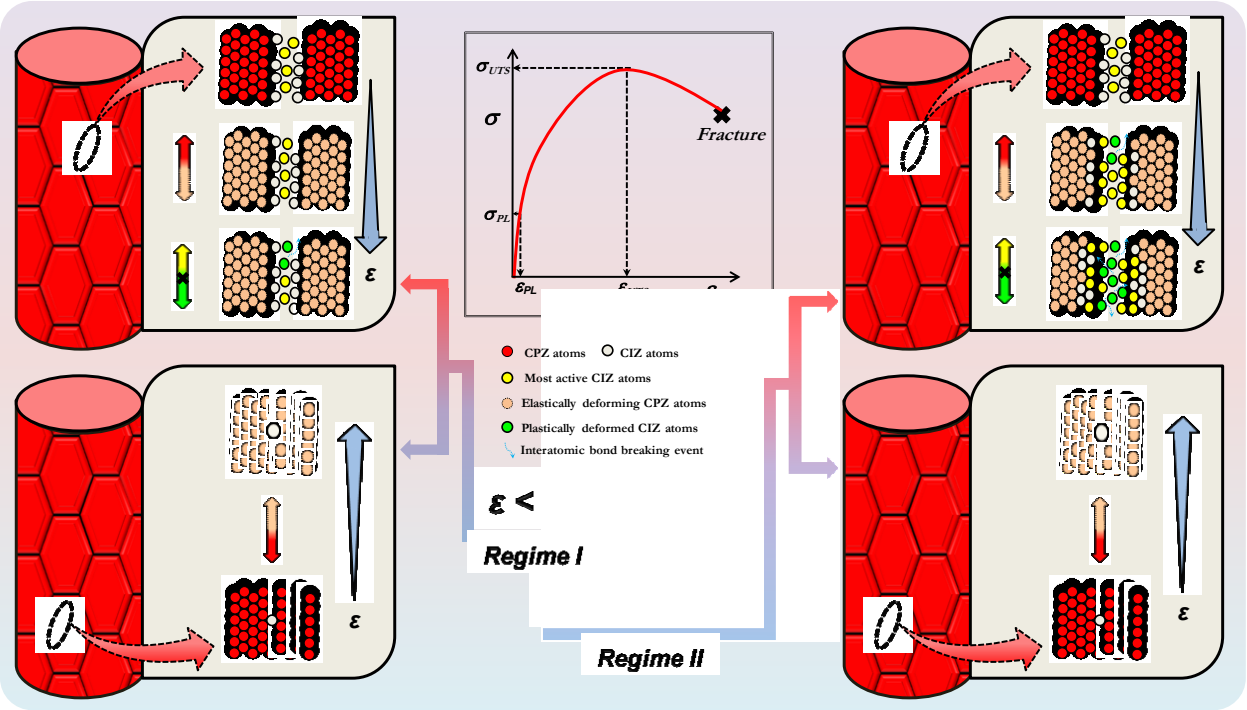

Figure 6.3. Illustrative schematic of the proposed dislocation mechanics during the two distinct regimes (*I* and *II*) of loading. Arrows in the figure indicate if the induced deformation is reversible or not, with the "x" marker indicating irreversibility.

After every such transitory structural ordering event, few interatomic bonds are broken to perpetuate this dynamics as high mobility atoms unite and disintegrate non-sequentially in "relatively close-packed" localized clusters – named *short-range dislocations* – of dynamic equilibrium [**312**, **313**, **314**]. Development of localized stress inhomogeneities due to local density or free volume fluctuations thus drives the flow of dislocations (carriers of plasticity) just as electric potential

differences drive the flow of electrons (carriers of charge). Therefore, localized yielding (plasticity) initiates instantaneously within multiple constituent CIZs at the onset of loading with varying lengths of short-range dislocations even in macroscopically dislocation-free volumes [**295**, **302**, **312**, **315**, **316**]. As this heterogeneous dynamic motion simultaneously involves restricted non-diffusional material transport, plasticity remains local within CIZs while core CPZ atoms maintain their equilibrium positions. As dependent on the nature and spatial/geometrical orientation of a CIZ, CPZ-CIZ interfaces accommodate nearby disorder state by elastic deformation [**297**, **312**]. As short-range dislocations leave CPZ lattices undistorted and unrotated, no long-range internal stresses are developed and hence can be considered as statistically immobile. Due to inherently low energies, their mobility upstream is also very limited due to increased activation energies and lack of higher driving forces. Moreover, these dislocations possess localized strain fields, exhibit no characteristic slip system and predominantly move in a direction orthogonal to the plane of the adjoining interface due to transverse nature of response [**314**]. Short-range dislocations are assumed to increase at a rate proportional to their size at any instant during loading and can therefore be mathematically represented by an exponential growth function. Thus, short-range dislocation densities evolve *exponentially* with increasing strain at very low hardening rates.

As external strain increases ($\varepsilon_{PL} < \varepsilon < \varepsilon_{UTS}$, ***regime II***), the accelerating dynamic heterogeneity within CIZs causes the maximum rheological interaction (*i.e.,* dynamic roughening) along adjoining elastic CPZ-CIZ interfaces [**317**]. Consequently, strain energy density localization and anisotropic gradients in elastic free energy are expected to develop across adjacent CPZ interfaces. This phenomenon leads to stress concentrations (or lattice curvatures) that are susceptible to interfacial yielding and also induces a thermodynamic driving force for heterogeneous CIZ migration [**311**, **318**, **319**, **320**, **321**]. The interatomic bonding at these interfaces is energetically

unfavorable and hence weaker than that of pristine CPZ atoms. Thus short-range dislocations quantitatively increase with increasing strain after multiple such transitory structural ordering and subsequent localized plasticity routines. Localized plasticity starts to rise in the ever-increasing CIZ, with highest localized strains obtained in locations where CIZs are densest in the crystal structure. As CIZs begin their *permanent* zone expansion via gradual transverse encroachment (see Figure 6.3), the material's global entropy also gradually rises. Such global entropy gains occur at the expense of transitory local entropy losses and tend to evolve a system towards more complicated and advanced states [**316**]. This is also consistent with the SLT requisite that global entropy production – or equivalently, energy dissipation – rate be non-negative (*i.e.,* Clausius-Duhem inequality). As externally applied strain-rate must comply with the loading direction, it is important to realize that short-range dislocation displacements and velocities tend to be anti-symmetric. The rate of heterogeneous interatomic shearing is accordingly greater along orientations – minimal resistance paths offering maximal driving force – with the largest local resolved shear stress in a CPZ. This marks the onset of macroscopic plasticity along crystallographically active slip systems in the form of bursts via highly mobile *long-range dislocations* [**311**]. During such dynamic bursts, it is reported that the instantaneous rate of deformation may exceed the external strain-rate by several orders of magnitude [**322**].

Since macroscopic plasticity can evolve heterogeneously within a material's CPZ at stresses considerably less than its Peierls-Nabarro strength, homogeneous dislocation nucleation/depinning within CPZs is *not* typically favored. Due to restricted dynamic heterogeneity, glide motion is rather subdued on non-active slip systems and therefore internal stresses are rapidly enhanced in such CPZs especially the dimensionally smaller ones because of finite size effects [**323**]. Internal stresses are further built-up by the mutual trapping of short-range dislocation clusters, long-range dislocation

pile-ups [**324**, **325**, **326**] and intermittent avalanches of long-range dislocation dynamic bursts in proximity. Mesoscale unequilibrated moments induced by these internal stress fluctuations need to be balanced by further asymmetric stress division – one dynamic and the other, elastic – that perpetuates macroscopic plasticity [**327**]. Moreover, the enhanced local stress-state begins to depin other *pinned* CIZs that require activation (like existing dislocations and point defects) to accelerate and sustain the plasticity dynamics [**302**]. As per this mechanism, it is imperative to comprehend that macroscopic yielding is not an event but rather a critical transition process that is marked by long-range dislocations' nucleation/depinning. Depending on their character, polarity and orientation, to maintain line continuity, long-range dislocations respond to internal mean shear via gradual rotation and alignment, propagation and coalescence/annihilation. Thus, long-range dislocations are characterized by increasing internal degrees of freedom, high hardening rates [**291**] and also act as triggering agents for nucleating/depinning numerous other long-range dislocations.

Owing to long-range internal stresses or backstresses, long-range dislocations elastically interact and propagate during their drive to minimize the crystal's internal energy. Macroscopic work or strain hardening – resistance to glide – occurs predominantly due to the hindrance rendered by evolving CIZ yield fronts to the mobility of long-range dislocations. Moreover, long-range dislocation mobility against short-range dislocation clusters further enhances this resistance. This typically leads to strong kinematic hardening and overstresses within CPZs. In addition to self-interactions that tend to straighten them, long-range dislocations' elastic interactions with other entanglements also effect localized pinning [**328**]. Hence, increasing stress is required to mitigate these combined obstacles for plastic strain increments. In essence, macroscopic plasticity evolves gradually as the frequency and size of discrete, short-lived and intermittent avalanches increase with external strain due to multiple pinning/depinning excursions [**293**, **304**]. Analogous to other physical

phenomena [**329**], these temporospatial avalanches thus force the material into a self-organized criticality. Thus, macroscopic plasticity exhibits a *power-law* dependence – a relationship that is characterized by time and scale invariance – on the applied strain [**296**, **326**, **330**, **331**]. Although macroscopically homogeneous plasticity is mediated by discrete long-range dislocation avalanches, localized heterogeneous plasticity is accommodated by continuous short-range dislocation encroachments at comparatively negligible strain-rates. This behavior thus closely characterizes plastic response as a point process – comprising discrete and localized events. As plastic deformation gradually progresses, multiple slip systems are activated and imply high hardening rates as the crystalline CPZs align themselves with the imposed loading via rotation. As described earlier, backstresses influence the elasto-plastic transition and also increase work-hardening with increasing strain. Depending on the direction of loading and plastic deformation gradients involved, migration and accumulation of vacancies (*i.e.,* voids) and loss of density occurs within multiple constituent CIZs.

At sufficiently large strains (ε *approaching* ε_{UTS}), localized coalescence of long-range dislocations – necking as characterized by a drop in hardening rate – becomes pronounced leading to the formation of shear bands. Necking can thus be also interpreted as a global instability phenomenon resulting due to bifurcation from macroscopically homogeneous plastic deformation. Aligning themselves orthogonal to external loading, these shear bands glide relatively resulting in a characteristic "cup-and-cone" ductile shear fracture. Random perturbations (like second-phase precipitates/inclusions) can impede the overall dynamics, imposing higher activation energies and stresses for dislocation mobility. Interestingly, the stochastic spatial/geometrical distributions of CIZs accordingly render variability in the mechanical behavior of "nominally" homogeneous materials [**292**, **298**].

6.3.2.1. Influence of temperature and strain-rate on crystal plasticity

Relative contributions of vibrational and structural entropies to total entropy also influence a material's behavior at increasing temperatures and strain-rates, respectively and deserve a discussion herein. It has become quite customary to consider only the structural fluctuations (like mean-squared displacement) of a crystal with an increase in temperature. But, the amplitude of atomic vibrations – which exist even at absolute zero as per quantum mechanics – increases with increasing temperature as CPZ atoms transiently oscillate from their crystalline periodicity. Consequently, interatomic bonding forces become weaker and activation energies for atomic motion are relatively less for both CPZ and CIZ atoms as compared with that at room temperature. Short-range dislocations particularly exhibit significant mobility – particularly in multiple constituent CIZs characterized by free volume like grain boundaries (GBs) – at increasing temperatures as their thermal activation is further pronounced. Due to increased thermal excitation, the length of short-range dislocations also prominently decreases. Therefore with increasing temperature, the plastic deformation mechanism discussed earlier at room temperature is dynamically accelerated. Hence even at considerably lower flow stresses, macroscopic plasticity initiates (*i.e.,* thermal softening) as short-range dislocations (and CIZs) begin their transverse encroachment towards adjoining CPZ interfaces. As considerable energy is utilized towards increasing the global entropy, work done (and recoverable energy stored through dislocations) on a material by external stress quantitatively decreases. This consideration thus accounts for the reduced work-hardening and increased ductility with increasing temperatures. To minimize the internal energy, grain growth – dynamic recovery and recrystallization through accelerated atomic motion – and coalescence also become thermodynamically favored at high temperatures.

At higher strain-rates, higher structural entropy contributions accelerate dynamic heterogeneity and subsequent macroscopic crystal plasticity. Therefore as strain-rate increases, long-range dislocation rate-hardening effect becomes considerably weaker and slower although their densities become larger.

6.3.3. Development of a novel constitutive model

6.3.3.1. Need for a constitutive relation

It is rather difficult with conventional scientific approaches – either experimental or analytical – to validate the nucleation and cumulative behavior of two types of dislocation densities that operate concurrently at two different length scales. Although long-range/short-range dislocations can be readily observed and characterized with advanced TEM tools, such investigations can only approximate the dislocation densities using mean-field approaches like the line intersection method. Such an *average* approximation of a quantity suffers from several critical drawbacks. Besides tedious sample preparation procedures, such an approximation inherently assumes the dislocation density distribution to be homogeneous. It is also impractical to clearly segregate the total dislocation density in terms of active and statistically stored dislocation components. Most importantly, existing approaches typically estimate dislocation densities from post-test specimens and by doing so, dislocation density evolution during actual loading and stress relaxation effects are qualitatively ignored [**294**, **299**].

Analytical computational methodologies like molecular dynamics (MD) or dislocation dynamics (DD) simulate atomic motion by numerically solving the classical Newtonian equation of motion over finite time intervals [**300**, **328**, **332**, **333**]. Although classical mechanics can effectively describe the long-range dislocation dynamics after activation and/or depinning, it is not expected to

satisfactorily capture the Brownian dynamics of short-range dislocations or analytically solve their stress fields. The probabilistic nature of interatomic shearing in multiple constituent CIZs also cannot be qualitatively explained by such deterministic techniques. Finally, linking the dynamics of two different types of dislocation densities that simultaneously nucleate, move and operate at two distinct length- and time- scales necessitates the need for extensive computational resources. Statistical thermodynamic calculations of entropies, specifically the vibrational entropy, of short-range dislocations during early stage plasticity can be an immensely complex task just by itself [**308**, **334**]. All these considerations render both the experimental and analytical approaches rather limited to corroborate the proposed mechanism.

For this objective, a constitutive modeling approach to relate both the dislocation densities and their cumulative interaction to the stress induced in the material under external loading offers the most viable solution currently. A physical based model is not considered in this regard due to uncertainties in the measurement of several quantities – like dislocation density – that ought to be primarily input for model calibration. A phenomenological model is therefore formulated in this work with the proposed mechanism as its underlying framework. Specifically a minimal parameter relation is desired as it concurrently minimizes both the model's degrees of freedom (*i.e.,* fitting parameters) and input from experimental results. Such a minimal approach should be feasible since dislocation interactions temporospatially determine a deforming crystal's local yielding and its subsequent microstructural evolution until failure. This consideration also ensures that specific mechanism(s) deemed important for a material at a given loading condition – like dislocation climb, cross-slip – need not be explicitly expressed. As consistent with the microstructural response during crystal plasticity [**292**, **332**, **335**, **336**, **337**], this constitutive relation should relate the various

independent testing variables – total strain, strain-rate and temperature – to the evolving stress and also be devoid of any mathematical singularity.

6.3.3.2. Analytical formulation

Since long-range and short-range dislocation densities operate in conjunction to induce stresses macroscopically and locally, respectively, a power-law distribution with an exponential cutoff is considered mathematically optimal. Since uniaxial monotonic tensile tests are commonly performed to characterize a material behavior, it is chosen first for model description. The proposed constitutive relation for simulating uniaxial monotonic behavior is expressed analytically in Equation (6.3).

$$\boldsymbol{\sigma = A.\ \sigma_{0.1\%\varepsilon}\ .\ \underbrace{\left(\frac{\sigma_{UTS}}{\sigma_{0.1\%\varepsilon}}\ .\ \frac{\varepsilon}{T}\right)^{\frac{a}{\dot{\varepsilon}^{b}}}}_{\text{Macroscopic plasticity}}\ .\ \underbrace{\exp\left[-\left(\frac{c}{\varepsilon}+fT\right)\right]}_{\text{Localized plasticity}}} \qquad \text{…….. (6.3)}$$

where,

σ : flow stress developed within a material upon loading (in MPa)

A : dimensionless proportionality index; does not vary with the type of loading for a material

$\sigma_{0.1\%\varepsilon}$: stress at 0.1% total strain (assumed to be the strain value at the proportional limit of a material) under any loading condition (in MPa)

σ_{UTS} : ultimate tensile strength (in MPa)

ε : total strain at any instant of loading

T : temperature ratio, with the numerator being the test temperature in K and the denominator being 1 K

a : macroscopic plasticity index (in $(1/s)^{b}$)

$\dot{\varepsilon}$: nominal applied strain-rate (in $1/s$)

b : dimensionless strain-rate sensitivity index; does not vary with the type of loading for a material

c : dimensionless index to quantify for short-range dislocation behavior (structural component)

f : dimensionless index to quantify for localized thermal effects (vibrational component)

Equation (6.3) is formulated to work only up to the UTS, beyond which triaxiality effects should be considered for strain localization. It can also be observed that σ_{UTS} and $\sigma_{0.1\%\varepsilon}$ are the only two direct inputs from experimental test data.

As it can be seen from Equation (6.3), the evolving stress in a material is directly proportional to the product of both the dimensionless terms corresponding to macroscopic and localized plasticity. The term $\sigma_{0.1\%\varepsilon}$ is incorporated in the right hand side of the equation for dimensional equality and is assumed as the proportional limit stress for a crystalline material under any type of loading. The power-law exponent, $a/\dot{\varepsilon}^{b}$, in the macroscopic plasticity term quantifies the effect of long-range dislocations at a given total strain ε and temperature T. The stress ratio, $\sigma_{\mathrm{UTS}}/\sigma_{0.1\%\varepsilon}$, in the base of the power-law term gives a measure of the degree of strengthening induced by macroscopic work-hardening in the material. The ratio, ε/T, explicitly implies the direct and inverse relationship between total strain and temperature with stress, respectively during macroscopic plasticity. Since the nominal strain-rate is expected to have an inverse relationship with macroscopic work-hardening, it is expressed in the denominator of the power-law exponent. At a given T, localized plasticity is expected to increase linearly with increasing ε until the critical transition cutoff strain beyond which negligible short-range dislocation interactions occur (see Figure 6.4(a)). At a given ε, localized plasticity is expected to decrease gradually with increasing T due to the increased dynamic heterogeneity of short-range dislocations and the eventual early initiation of macroscopic plasticity (see Figure 6.4(b)). As per this description, the corresponding

exponential term for localized plasticity is found to have a direct and inverse relationship between temperature and total strain with stress, respectively. Although homogeneous macroscopic plasticity occurs as per the applied strain-rate, heterogeneous localized plasticity takes place at comparatively negligible strain-rates as dictated by the local stress fields. Consequently, only the total strain and temperature were considered important in the exponential term for localized plasticity. Thus, the proposed analytical form is carefully chosen in accordance with the expected inter-dependence among independent variables during testing.

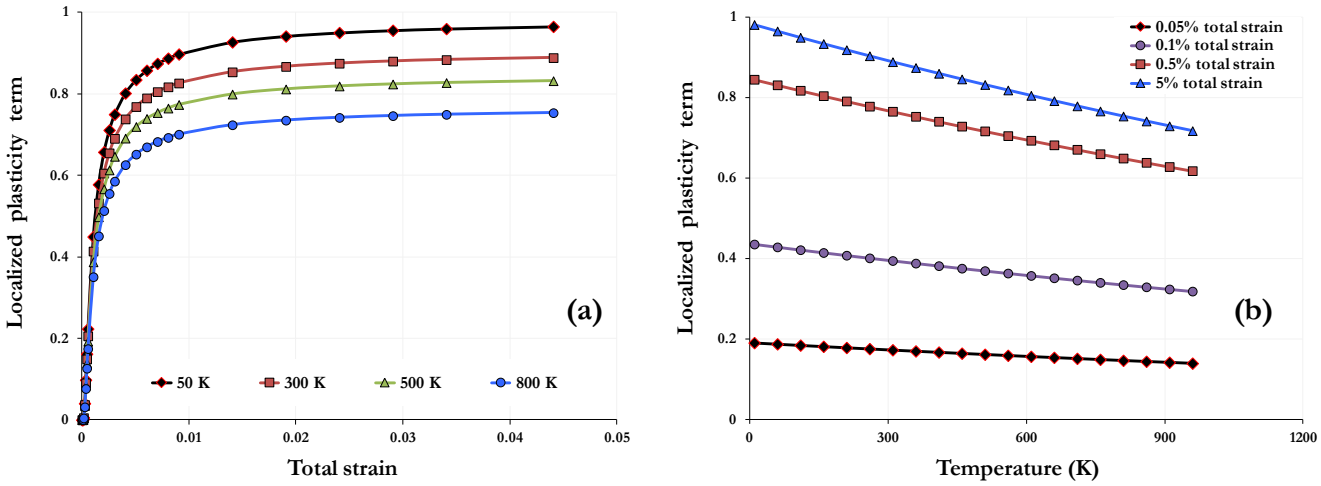

Figure 6.4. Expected influence of localized plasticity (a) at a given temperature and increasing total strain and (b) at a given total strain and increasing temperature. Only the exponential localized plasticity term in Equation (6.3) is considered for illustration.

The importance of the model's five indices also deserves a brief discussion. The dimensionless index A is introduced for proportionality and does not vary with the type of loading for a given material. Assuming a hypothetical scenario wherein plasticity is non-existent – or equivalently, other four indices set to zero – upon loading at any temperature T, the evolving stress in a material is equal to the product of A and $\sigma_{0.1\%\varepsilon}$ as per Equation (6.3). This product, as expected, corresponds to the ideal strength of the material at that particular temperature. Thus the index A is

an invariable and it characterizes a material's behavior regardless of the influence of other indices that depend on the test conditions. Work-hardening index, a, accounts for macroscopic work- or strain-hardening during monotonic loading and tends to be an evolutionary parameter for characterizing cyclic behavior. The strain-rate sensitivity index, b, for a material does not vary with the type of loading and quantifies a material's microstructural response to strain-rate fluctuations. Indices c and f correspond to the *instantaneous* mechanical (structural) and thermal (vibrational) response of a material, respectively and collectively quantify localized plasticity. Index c is also an evolutionary parameter that quantifies localized plasticity effects during cyclic loading and unloading.

Although numerous phenomenological or micromechanical constitutive relations currently exist, they are largely limited in terms of a mechanistic foundation and general applicability to different materials [**338** and relevant references therein, **339**]. Hence, it is vital for the proposed constitutive relation to not only closely model experimental data, but also to reproduce other empirical observations of scientific importance. Such a capability makes the constitutive relation and its underlying physics more valuable and robust. In conventional approaches, the transition from the elastic to the plastic deformation regime in a uniaxial tensile test record is referred to as the yield point. The slope of the stress-strain data within the elastic regime also offers an analytical estimate of the elastic (Young's) modulus. As discussed earlier, the proposed mechanism assumes (localized) plasticity to develop instantaneously on loading. Consequently the total strain is not decomposed as the sum of elastic and inelastic – that includes plastic and viscous – components. Rather, as per this mechanism, the yield point is interpreted as the critical transition cutoff beyond which macroscopic plasticity takes over from localized plasticity under increasing stress. Moreover, the second partial derivative of Equation (6.3) with respect to total strain (treating temperature and strain-rate as constants) yields a second-order quadratic equation. Mathematically, this quadratic equation provides

the rate of change of slope of stress with respect to strain and can be plotted as a function of strain (see Figure 6.5). The broken line in Figure 6.5 corresponds to the strain where the second partial derivative equals zero and indicates the deviation in stress behavior from linearity to non-linearity.

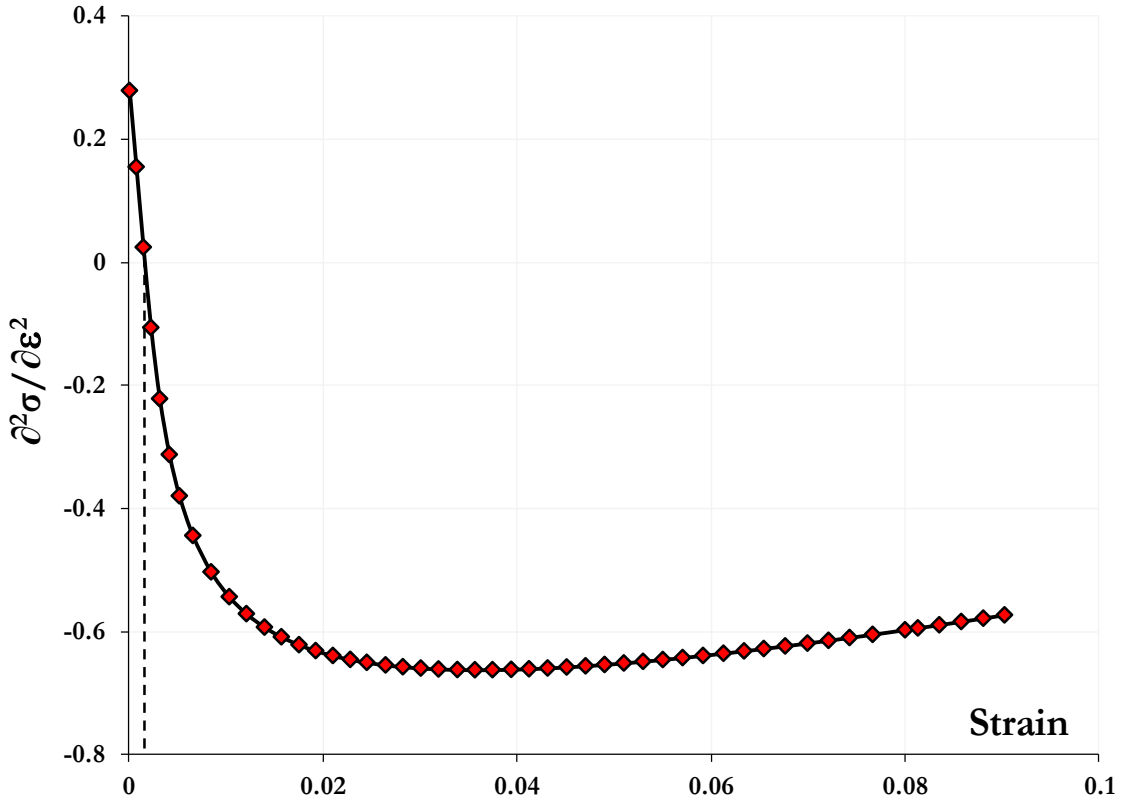

Figure 6.5. Schematic illustrative of the rate of change of slope of stress as a function of strain (at constant temperature and strain-rate) for a material under uniaxial loading. The broken line indicates the strain where the ordinate axis changes sign from positive to negative.

From an analytical viewpoint, out of the 2 possible roots (R_1 and R_2; see Equation (6.4)) for this quadratic equation, only one of them will be valid (R_2) and that valid root denotes the strain at the proportional limit (ε_{PL}). By substituting this value of strain in Equation (6.3) while retaining other model indices, the corresponding stress can be evaluated and the respective stress to strain

ratio provides an accurate estimate of the conventional Young's modulus. The judgmental errors involved in identifying a material's stiffness can thus be greatly minimized.

$$\boldsymbol{R_1} = \frac{\left[c-\left(\frac{2ac}{\dot{\varepsilon}b}\right)\right]+\left[c\sqrt{\left(1-\frac{4a}{\dot{\varepsilon}b}\right)}\right]}{\left[\frac{2a^2}{\dot{\varepsilon}2b}\right]}; \quad \boldsymbol{R_2} = \frac{\left[c-\left(\frac{2ac}{\dot{\varepsilon}b}\right)\right]-\left[c\sqrt{\left(1-\frac{4a}{\dot{\varepsilon}b}\right)}\right]}{\left[\frac{2a^2}{\dot{\varepsilon}2b}\right]} \qquad \text{…….. (6.4)}$$

6.3.4. Mechanism extension for cyclic plasticity

For tension-compression cyclic loading, the mechanism proposed earlier for monotonic tensile loading is expected to hold good equally. At the end of any tensile loading, core CPZ atoms are *still* deforming elastically even as CIZ atoms gradually expand their domain of influence via dynamic heterogeneity. After tensile elastic unloading, core CPZ atoms experience elastic strains and are characterized by varying backstresses (of compressive nature) as a consequence of heterogeneous inelastic CIZ expansion. Upon subsequent compressive loading, atoms within CIZs can flow at much lower absolute stresses in the "opposite" direction to induce early reverse plasticity. After compressive elastic unloading, core CPZ atoms experience elastic strains and also heterogeneously varying backstresses of tensile nature. A similar experimental observation has been reported by Levine *et al.* using X-ray microbeam measurements [**340**]. The experimentally observed Bauschinger effect, an important feature of anisotropic cyclic deformation, can thus be conveniently rationalized by the proposed mechanism along the lines of the hard-soft composite model by Mughrabi [**341**]. It needs to be noted that each and every CIZ expansion along the crystallographically active slip systems within adjacent CPZs in the form of long-range dislocation avalanches corresponds to a slip event. Hence after each cycle of tensile-compressive loading, multiple slip events can occur in both the directions normal to the applied uniaxial load as dependent on the crystal structure considered.

6.3.5. Formulation of constitutive model's cyclic version

The constitutive model as expressed in Equation (6.3) for monotonic loading can be modified to obtain its cyclic version as shown in Equations (6.5) and (6.6), where σ_T and σ_C corresponds to stress under tensile and compressive loading, respectively.

$$\boldsymbol{\sigma_T = A.(\sigma_{0.1\%\varepsilon})_{cycle\,1}.\left(\left[\frac{\sigma_{max}}{\sigma_{0.1\%\varepsilon}}\right]_{cycle\,1}.\frac{\varepsilon}{T}\right)^{\frac{a}{\dot{\varepsilon}b}}.\exp\left[-\left(\frac{c}{\varepsilon}+fT\right)\right]} \quad \text{..... (6.5)}$$

$$\boldsymbol{\sigma_C = A.(\sigma_{0.1\%\varepsilon})_{cycle\,1}.\left(\left[\frac{\sigma_{min}}{\sigma_{0.1\%\varepsilon}}\right]_{cycle\,1}.\frac{\varepsilon}{T}\right)^{\frac{a}{\dot{\varepsilon}b}}.\exp\left[-\left(\frac{c}{\varepsilon}+fT\right)\right]} \quad \text{..... (6.6)}$$

The cyclic version of the model differs only slightly from its monotonic counterpart, with both the maximum stress σ_{max} or σ_{min} – instead of σ_{UTS} – and $\sigma_{0.1\%\varepsilon}$ values chosen from the first loading cycle. It is expected that the stress ratio will vary with loading cycles as dependent on the cyclic behavior of a material at a particular loading condition. However, it can be kept constant to facilitate capturing the *entire* macroscopic microstructural evolution with the evolutionary index in the macroscopic plasticity term, a. Work-hardening index, a, is an evolutionary parameter that accounts for macroscopic work- or strain-hardening and its variation with loading cycles corresponds to changes in long-range dislocation behavior accordingly. Increasing values of a correspond to an increased frequency of long-range dislocation avalanches and the converse also holds true. The localized deformation can be similarly quantified by the evolutionary index in the localized plasticity term, c. Decreasing values of the evolutionary parameter c with loading cycles indicate increasing dynamic heterogeneity and a comparatively heterogeneous localized deformation. Hence, a and c are the only evolutionary indices to characterize plastic deformation under both

tensile and compressive loading. Furthermore, indices c and f in the localized plasticity term are expected to accommodate all the microstructural response upon unloading. Therefore, of the five indices considered in monotonic loading, *only* 2 will be evolutionary each for cyclic loading (a and c) and unloading (c and f) while A and b will remain the same for a typical tensile-compressive loading cycle.

The constitutive model can also offer further insights into the nature of material deformation under cyclic loading using the two evolutionary indices a and c. If the rate of change of index c is faster than that of a, it implies that the deformation is comparatively more localized with loading cycles. Localized deformation phenomena such as grain boundary cavitation and formation of intergranular microcracks are expected to be pronounced under this case scenario. Conversely, if the rate of change of a is faster than that of c, macroscopic plasticity is expected to dominate via mechanisms like free-surface cracking and formation of transgranular cracks. Such observations can also be reiterated by carefully analyzing the relative contribution of both the plasticity terms in Equations (6.5) and (6.6), with loading cycles. Thus, the relative significance of different deformation mechanisms at the two different microstructural scales at any loading condition can be qualitatively explained.

6.3.5.1. Model implementation protocol

Few preliminary preparation steps need to be completed with the as-received laboratory test data before implementing the analytical model represented by Equations (6.5) and (6.6). Figures 6.6 and 6.7 show cyclic hysteresis loops of a symmetrically loaded LCF and a C-F test with hold time at the peak tensile strain, respectively for illustration. For each cycle of laboratory test data, the following mathematical procedure is executed with the involved steps followed in order:

(1) From the (x, y) data corresponding to strain (*x-axis*) and stress (*y-axis*), pick the two successive data points (x_1, y_1) and (x_2, y_2) where the ordinate changes sign from negative to positive, *i.e.*, stress changes from being compressive to tensile, as indicated by '1' in Figures 6.6 and 6.7.

(2) Similarly, pick the two successive data points (x_3, y_3) and (x_4, y_4) where the ordinate changes sign from positive to negative, *i.e.*, stress changes from being tensile to compressive, as indicated by '2' in Figures 6.6 and 6.7.

(3) Linearly interpolate the *x-axis* co-ordinates x_1 and x_2 to obtain the strain at zero stress, x_5.

(4) Linearly interpolate the *x-axis* co-ordinates x_3 and x_4 to obtain the strain at zero stress, x_6.

(5) Starting from (x_2, y_2), add the absolute magnitude of x_5, $|x_5|$, to each subsequent *x-axis* co-ordinate until the data point until (x_3, y_3).

(6) Starting from (x_4, y_4), subtract each subsequent *x-axis* co-ordinate from the absolute magnitude of x_6, $|x_6|$ until (x_1, y_1).

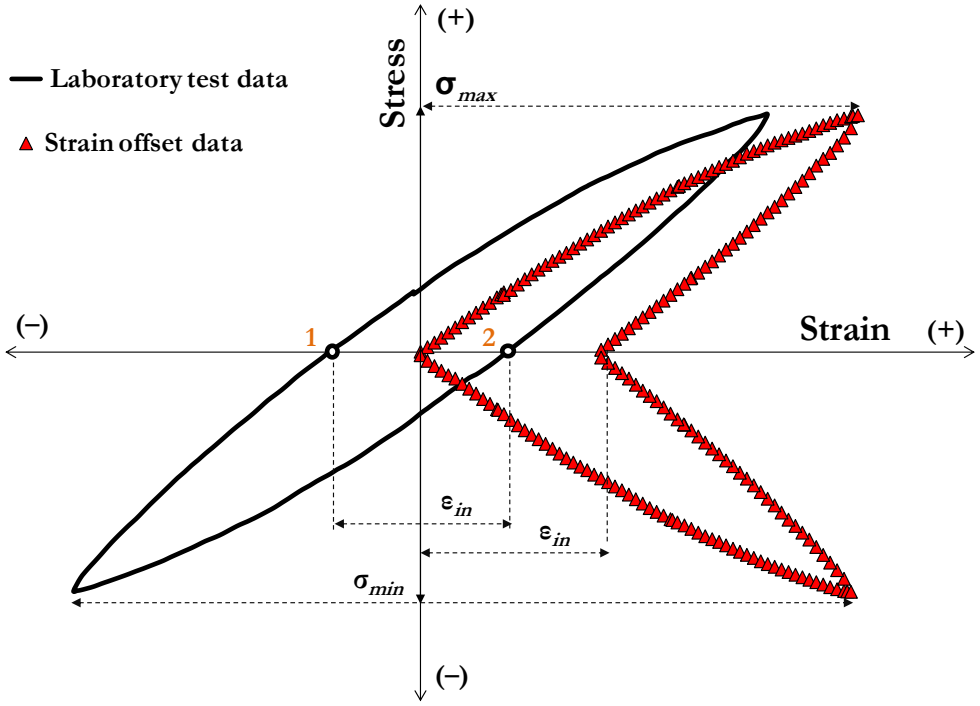

Figure 6.6. Illustrative cyclic stress-strain loading history of a symmetrically loaded LCF test. Here, σ_{max} and σ_{min} correspond to the maximum tensile and compressive stresses, respectively and ε_{in}, the total inelastic strain accumulated till the end of the loading cycle under consideration.

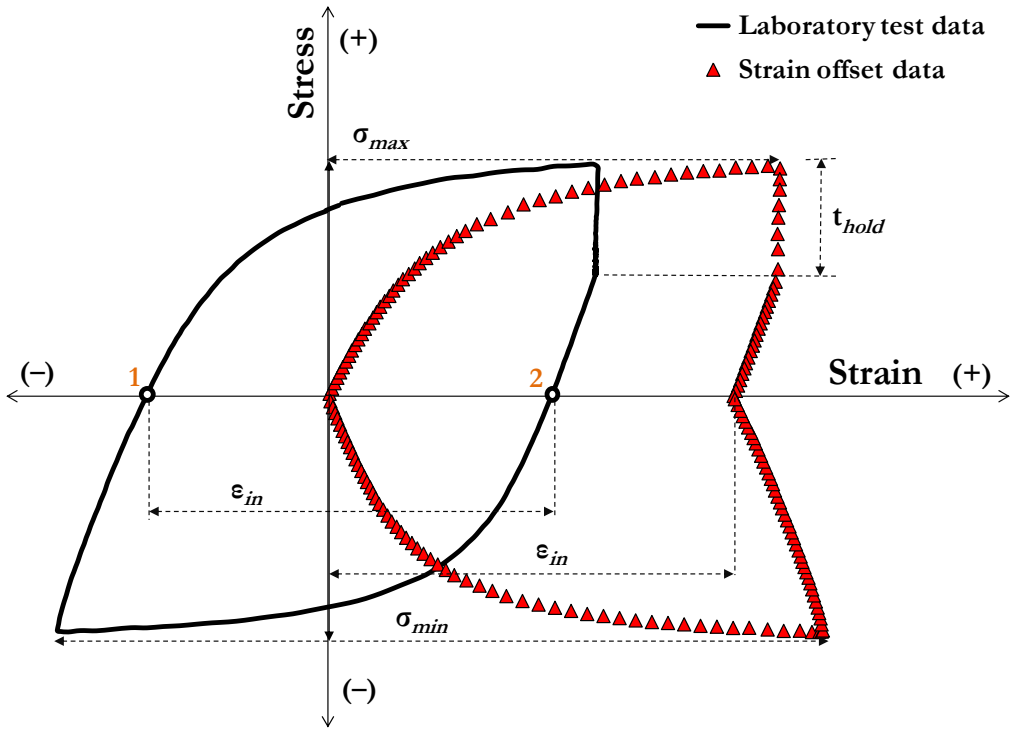

Figure 6.7. Illustrative cyclic stress-strain loading history of a C-F test with hold time at the peak tensile strain. Here, σ_{max} and σ_{min} correspond to the maximum tensile and compressive stresses, respectively, t_h, the hold time and ε_{in}, the total inelastic strain accumulated till the end of the loading cycle under consideration.

It is important to realize that the above procedure *just* offsets the cyclic strain data without affecting the corresponding stress values. Figures 6.6 and 6.7 also show the stress-strain loading histories obtained by following the above procedure – for offsetting the strain – with data from a conventional LCF and C-F hysteresis loop, respectively. The stress evolution from zero to σ_{max} denotes the tensile loading and that from σ_{max} to zero denotes the tensile unloading; similarly, compressive loading varies from zero to σ_{min} and unloading from σ_{min} to zero. The sum of the absolute magnitudes $|x_5|$ and $|x_6|$ is the total inelastic strain, ε_{in}, accumulated from the beginning of loading until the cycle under consideration. After offsetting the cyclic stress-strain data, each stress-strain loading history can be visualized as a combination of the following distinct components:

tensile loading and unloading, compressive loading and unloading and hold time (for C-F tests only). Equations (6.5) and (6.6) can then be used to simulate all these cyclic components with different values of model indices for each component.

6.4. Round-robin tests considered for model validation

From the 78 isothermal LCF and C-F tests completed in the ASTM RR at strain amplitudes of ± 0.25%, ± 0.5% and ± 0.75% with hold times of 0, 600 and 1800 seconds, 12 tests are arbitrarily chosen for model validation herein. Two tests are randomly chosen at each loading condition (see Table 5.1) with the tests performed at different laboratories as per guidelines prescribed in the ASTM standard, E2714-09. Tables 6.1 and 6.2 show a summary of the details and results from the 6 LCF and C-F tests, respectively considered for discussion [**288**]. It was decided that fitting parameters identified from the lower strain amplitude LCF tests (± 0.25% and ± 0.5%) will be used at the higher strain amplitude (± 0.75%) for evaluating the predictive capabilities of the model. In a similar approach for the C-F tests, fitting parameters identified from the lower hold time C-F tests (600 seconds) will be used at the higher hold time (1800 seconds).

Table 6.1. A brief summary of the 6 LCF test conditions under consideration [288].

Uniaxial testing specifications	Strain amplitude	Test number	Specimen diameter (mm)	Reported LCF life (cycles)
Test control: axial strain Test temperature: 625°C (898 K) Duration of hold: 0 seconds (LCF) Strain-rate: 0.025% per second Load/unload waveform: triangular Type of ramping: uniform End-of-life criterion: 2% load drop	± 0.25%	1	7.5	5511
		2	6	3438
	± 0.50%	3	8	858
		4	6.4	1091
	± 0.75%	5	6.4	450
		6	8	583

Table 6.2. A brief summary of the 6 C-F test conditions under consideration [288].

Uniaxial testing specifications	Strain amplitude	Duration of hold (s)	Test number	Specimen diameter (mm)	Reported C-F life (cycles)
Test control: axial strain Test temperature: 625°C (898 K) Hold location: peak tensile strain Strain-rate: 0.025% per second Load/unload waveform: triangular Type of ramping: uniform End-of-life criterion: 2% load drop	± 0.50%	600	7	8	867
			8	6.4	932
	± 0.75%	600	9	8	489
			10	6.4	450
	± 0.50%	1800	11	8	599
			12	8	780

6.4.1. Parameter identification procedure

Tables 6.1 and 6.2 highlight the well-known observation that even specimens tested under nominally identical loading conditions tend to offer a wide range of lifetimes. This could be due to variability in test conditions and/or variability in the starting microstructure or equivalently, initial density and spatial distribution of crystallographic imperfections. Accordingly, the inelastic strain evolution, macroscopic and localized plasticity responses are expected to vary quantitatively during the various cyclic stages, while exhibiting similar qualitative trends. Thus, the evolutionary model indices that characterize cyclic plasticity are also expected to exhibit identical qualitative trends, but different quantitative values. The model indices' values from the monotonic tensile modeling effort of grade P91 steel provided the expected bounds for the five indices. The proportionality index A and strain-rate sensitivity index b are shape parameters and are held constant for all the components of the hysteresis loops. The value of index f is numerically assumed the same for both the cyclic loading components. The evolutionary indices a and c are adjusted each cycle for the various cyclic stress-strain *loading* data obtained after executing the strain offset procedure.

Unloading can be explained as the state of a material upon removal of external stress. Under such a condition, plastic deformation is not possible in accordance with the Kuhn-Tucker conditions of plasticity [**342**]. In the proposed mechanism, long-range dislocations need increasing stress – both external and internal – for their activation or nucleation, and for initiation and sustenance of macroscopic plastic deformation. Since macroscopic plasticity is thermodynamically irreversible during unloading, it implies that the microstructural response is predominantly localized. Localized internal stresses are thus generated and built-up after each cycle of loading even as stress nominally drops to zero in laboratory experiments. In light of this, only the localized plasticity should be influential during tensile and compressive cyclic unloading. Consequently, by maintaining the respective index a_i for any cycle i, evolutionary indices c and f are adjusted for both the tensile and compressive *unloading* components. Figures 6.8 and 6.9 outline the description of the five model indices for the cyclic components of a typical LCF and C-F hysteresis loop, respectively.

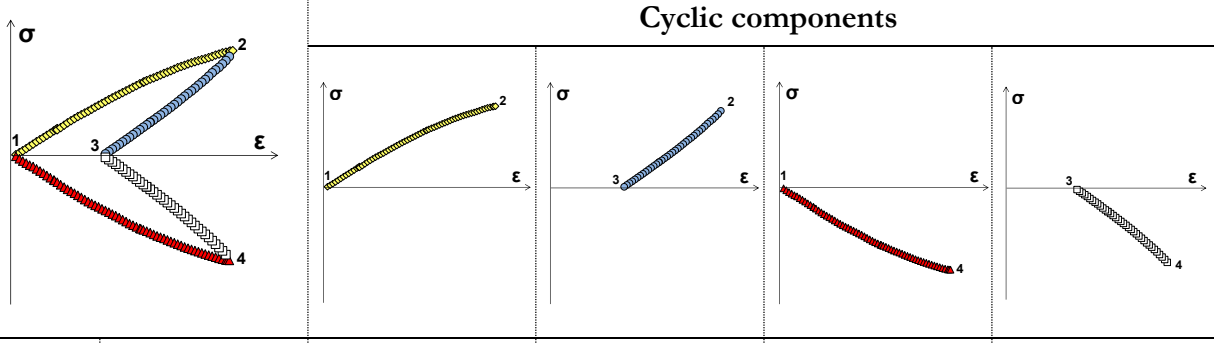

Model Indices	Monotonic tensile loading	Tensile loading (TL)	Tensile unloading (TUL)	Compressive loading (CL)	Compressive unloading (CUL)
A	7.95	7.95	7.95	7.95	7.95
a	0.034	$a_{i,TL}$ for cycle i	$a_{i,TL}$ for cycle i	$a_{i,CL}$ for cycle i	$a_{i,CL}$ for cycle i
b	0.111	0.111	0.111	0.111	0.111
c	0.00083	$c_{i,TL}$ for cycle i	$c_{i,TUL}$ for cycle i	$c_{i,CL}$ for cycle i	$c_{i,CUL}$ for cycle i
f	0.00033	0.00033	$f_{i,TUL}$ for cycle i	0.00033	$f_{i,CUL}$ for cycle i

Figure 6.8. Description of the five model indices for the four components of a typical LCF loading history obtained after following the strain offset procedure.

	Cyclic components				
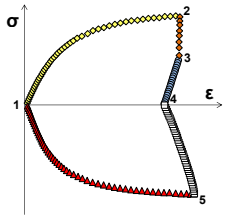	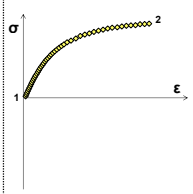	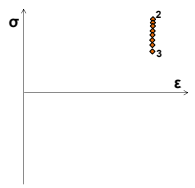	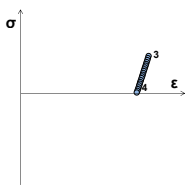	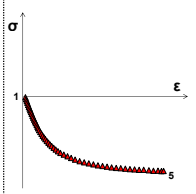	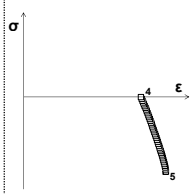
Model Indices and strain-rate	**Tensile loading (TL)**	**Tensile hold (TH)**	**Tensile unloading (TUL)**	**Compressive loading (CL)**	**Compressive unloading (CUL)**
$\boldsymbol{A}$	7.95	7.95	7.95	7.95	7.95
$\boldsymbol{a}$	$a_{i,TL}$ for cycle i	$a_{i,TL}$ for cycle i	$a_{i,TL}$ for cycle i	$a_{i,CL}$ for cyc. i	$a_{i,CL}$ for cycle i
$\boldsymbol{b}$	0.111	0.111	0.111	0.111	0.111
$\boldsymbol{c}$	$c_{i,TL}$ for cycle i	$c_{i,TL}$ for cycle i	$c_{i,TUL}$ for cyc. i	$c_{i,CL}$ for cyc. i	$c_{i,CUL}$ for cyc. i
$\boldsymbol{f}$	0.00033	0.00033	$f_{i,TUL}$ for cyc. i	0.00033	$f_{i,CUL}$ for cyc. i
$\dot{\boldsymbol{\varepsilon}}$	Applied value	Gradually varying	Applied value	Applied value	Applied value

Figure 6.9. Description of the five model indices and applied strain-rate for the five components of a typical C-F loading history obtained after following the strain offset procedure.

6.5. Optimization of model indices

Along with the formulation of the constitutive relation with minimal fitting parameters, it is also important to minimize the computational resources required for the simultaneous optimization of those parameters. To optimize the various model indices simultaneously, either local or global optimization algorithms can be employed. Local algorithms are very sensitive to the initial starting values of indices and also do not always lead to a globally optimal solution. On the contrary, global algorithms do not suffer from these drawbacks, but they instead demand much more computational power. In this work, to achieve the most optimal fit between experimental and predicted data with least computational resources, the SOLVER routine available within Microsoft Excel® is employed. Since this multi-parameter optimization routine is reportedly based on a local algorithm, starting values for the indices are obtained from a physically reasonable range before optimization. It

however needs to be mentioned herein that accuracy of the obtained fits can be improved with global algorithms at the expense of additional computational resources, if desired. The modeling accuracy of the current model is quantified by the root mean square (RMS) error calculated between the experimental ($\sigma_{\mathbf{exp}}$) and corresponding predicted ($\sigma_{\mathbf{pred}}$) stress values (see Equation (6.7)), where $n_{\mathbf{d}}$ is the number of data points considered.

$$\mathbf{RMS} = \left\{ \frac{\sum[\mathbf{log}(|\sigma_{\mathbf{exp}}|) - \mathbf{log}(|\sigma_{\mathbf{pred}}|)]^2}{n_{\mathbf{d}}} \right\}^{\mathbf{0.5}} \quad \text{..... (6.7)}$$

The error thus quantified is subsequently minimized using the scatter factor (Z) formulation, defined as shown below (see Equation (6.8)) [**343**]:

$$Z = \mathbf{10}^{(\mathbf{2.5} * \mathbf{RMS})} \quad \text{..... (6.8)}$$

After minimization, smaller Z values are preferred as a value of one implies a perfect fit. But, Z values *slightly* above unity are desirable to account for data measurement errors and/or other testing uncertainties especially at elevated temperatures. From empirical observation, lower Z values are expected for tests conducted in a single laboratory; but for data from multiple laboratories in a RR, Z can even reach values greater than 5.

6.5.1. Range of optimization

For creep deformation and rupture modeling effort, Z is minimized for all strain values beyond the first hour of loading till specimen rupture. For monotonic, LCF and C-F modeling efforts, Z is minimized only for strains $\varepsilon > \varepsilon_{\mathrm{PL}}$ (assuming $\varepsilon_{\mathrm{PL}}$ as 0.001) during loading to closely capture the work-hardening behavior at increasing strains and simultaneously disregard the

experimental scatter at very low strains. For $\varepsilon \leq \varepsilon_{PL}$ during loading, predicted stress is therefore obtained by multiplying strain values with the elastic modulus estimated by the model (described earlier in section *6.3.3.2*.) for the loading component under consideration. Similarly, Z is minimized only for strains $(\varepsilon - \varepsilon_{in}) > 0.05\%$ during unloading to disregard the influence of localized residual stresses, where ε_{in} is the inelastic strain accumulated at the end of unloading. For strains $(\varepsilon - \varepsilon_{in}) \leq 0.05\%$ during unloading, predicted stress is obtained by multiplying $(\varepsilon - \varepsilon_{in})$ with the average elastic modulus of the unloading component under consideration and its subsequent loading component of the hysteresis loop.

Chapter 7: RESULTS AND DISCUSSION

The main results – both experimental and constitutive modeling – of this dissertation work will be elaborately discussed in this chapter. In this context, it is imperative to recollect the major objectives of this work once again which are summarized as follows:

1. Characterize the creep, fatigue and C-F interactions in grade P91 steel at 625°C.
2. Understand the deformation and damage accumulation mechanisms under sustained and cyclic loading conditions.
3. Identify/develop robust constitutive models for simulating and predicting the creep, fatigue and C-F behavior of grade P91 steel at 625°C.
4. Evaluate the new C-F test standard ASTM E2714-09 with the RR test data and
   (i) report the inter- and intra-laboratory variability observed in the C-F data.
   (ii) determine the presence of any inherent biases in C-F life test data.
   (iii) define an appropriate terminology for characterizing C-F crack formation, and
   (iv) recommend a more definitive statement on precision and bias.

All the experimental results from the ASTM E2714-09 RR (incorporating test data from all the RR participants) will be discussed first followed by the constitutive modeling (performed solely at UA) results obtained with the RR experimental data as input. Pertaining to aforementioned objective 4, only a brief discussion will be provided herein for brevity and keeping in mind the other major objectives of this dissertation work; the reader is encouraged to refer [**288**] for a much more detailed description in this regard. Since all the experimental results are intermingled, individual contributions from a particular RR participant will also be accordingly acknowledged in the discussion as required.

7.1. Experimental results

7.1.1. Monotonic tensile behavior

The uniaxial monotonic tensile response of grade P91 steel both at room (24°C) and elevated temperature (625°C) is summarized in Table 7.1. These results agree quite well within the reasonable range reported in the literature for this grade of steels.

Table 7.1. Uniaxial monotonic tensile test results of grade P91 steel.

Test temperature (°C)	0.2% Yield strength (MPa)	Ultimate tensile strength (MPa)	Elongation (%)
24	532.6	708.4	26
625	325.1	343.7	33

7.1.2. Creep deformation and rupture behavior

As mentioned earlier, UA conducted the creep deformation and rupture tests on grade P91 steel under different stress conditions at 625°C as part of the ASTM RR. All the creep curves obtained from these tests are shown in Figure 7.1, which agree well with published literature under comparable loading conditions for this material [**166**, **205**, **206**, **208**, **209**, **210**, **212**, **215**]. Figure 7.2 shows the LMP plot for grade P91 steel from [**290**], with overlaid markers indicating the results from the RR tests. This plot also clearly shows that the creep characteristics of grade P91 compare favorably with data from the literature.

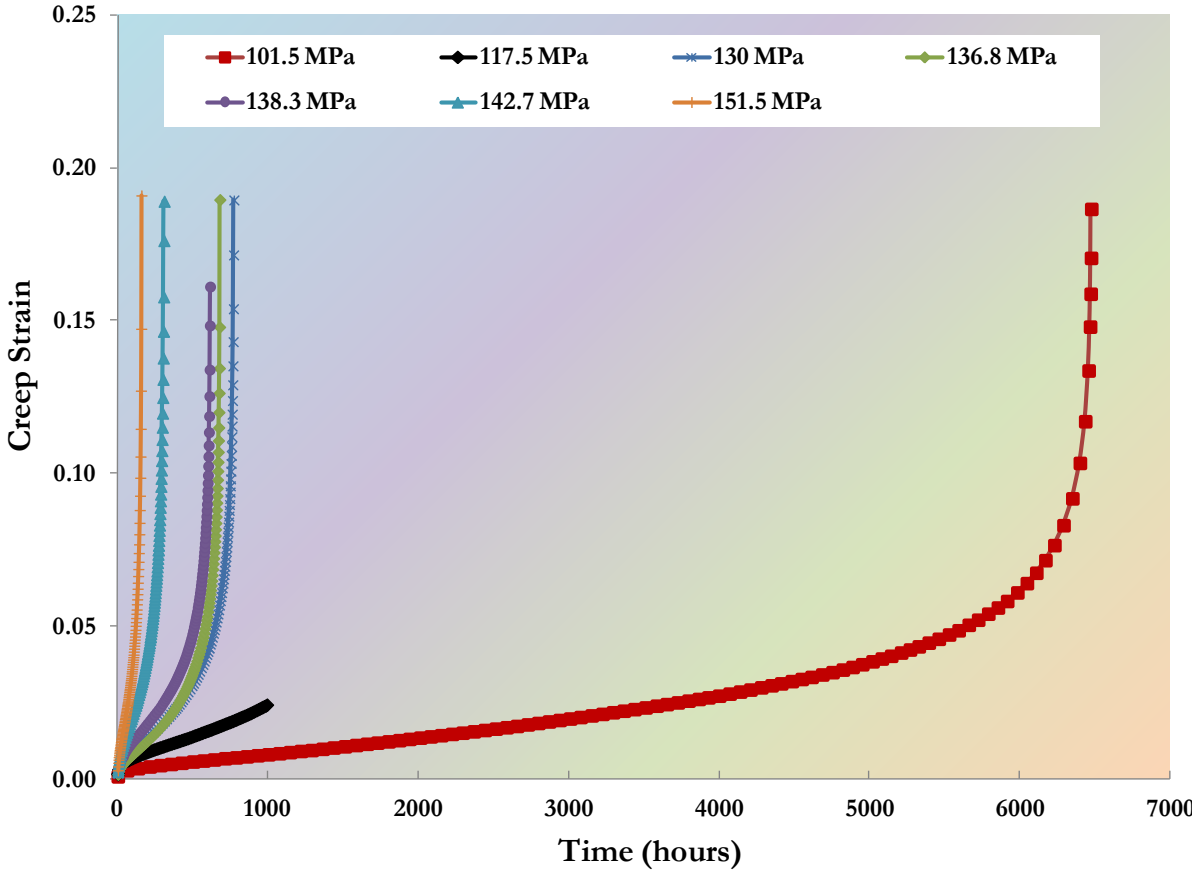

Figure 7.1. Creep deformation and rupture results at different stress levels for grade P91 steel at 625°C.

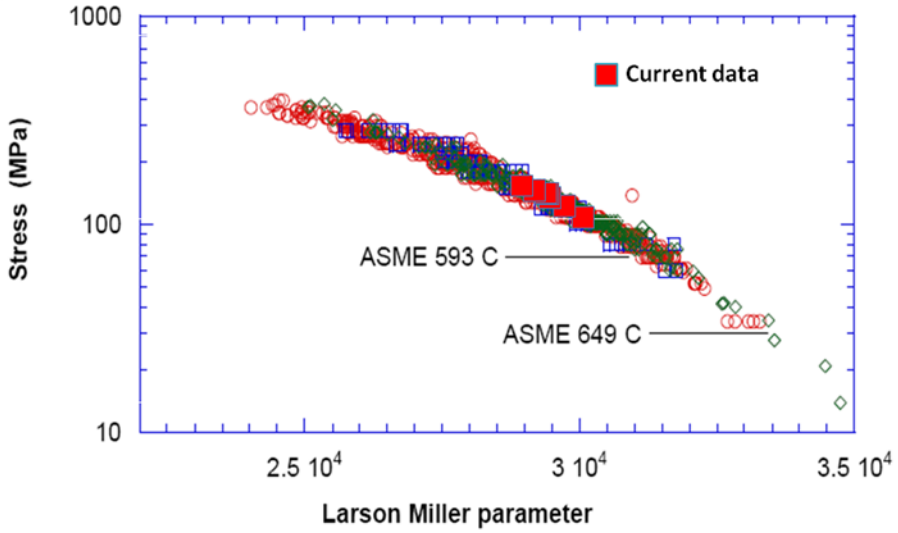

Figure 7.2. Larson Miller Parameter plot from [290], overlaid with data from the round-robin tests.

In a typical creep test for P91 steel, the deformation mechanism can be dominated, as a function of stress and temperature, by cross-slip or dislocation climb (> 70 MPa) and grain boundary diffusion (< 70 MPa) [**205**]. It has been found by others that for martensitic steels, the metallurgical changes are of vital importance as they strongly affect creep resistance properties leading to loss in creep rupture strength [**188**]. From a microstructural perspective for grade P91, it has been observed that the $M_{23}C_6$ precipitates link up by rapid directional coarsening during the primary creep regime. The resistance to creep plastic deformation by hindering dislocation motion is increased by the evolution of this grain structure during the final stages of primary creep and the entire secondary creep regimes. This behavior can also be observed from the creep curves wherein the secondary creep rate remains constant until the start of tertiary creep [**344**].

As dependent on the external stress, creep strain versus time curves typically exhibit very short primary (~ 10% of t^*), relatively substantial secondary or steady-state and tertiary creep regimes (see Figure 7.1). Because of dynamic creep recovery due to sub-grain growth and dislocation migration/annihilation in grain sub-boundaries, the primary creep rate starts to decrease until it reaches a plateau at the onset of secondary or steady-state creep. Secondary creep regime represents a dynamic equilibrium between work hardening and creep recovery processes, wherein a balance between generation of new dislocations and annihilation of existing dislocations is achieved [**345**]. The minimum creep rate ($\dot{\varepsilon}^{\mathrm{cr}}_{\mathrm{min}}$) observed in the secondary creep regime can be linearly fit using Norton's power-law – as defined earlier in Equation (4.4) where $A_{\mathrm{t}} = A_{\mathrm{n}} * \exp\left(-\frac{Q}{k_{\mathrm{B}}T}\right)$ – and the power-law exponent (n) and coefficient (A_{t}) values are found to be ~ 8 and 9.5 * 10^{-21}, respectively (see Table 7.2).

Table 7.2. Steady-state creep rate as a function of stress for P91 steel at 625°C.

Applied stress (MPa)	Steady-state creep rate (% h^{-1})	Norton's power-law constants
101.5	0.00035	$A_t = 9.53 * 10^{-21}$ $n = 8.24$
130.0	0.00166	
136.8	0.00381	
138.3	0.00523	
142.7	0.00779	
151.5	0.00748	

The creep rupture ductility for P91 steel is high with the final longitudinal elongation varying from 16-19%. It can also be observed from Figure 7.1 that creep strain generated in the primary and secondary creep regimes is cumulatively less as compared to that in the tertiary creep regime. As a result of localized necking at ~ 95% of the creep rupture time (t^*) for any given test, macro-cracking appears to have triggered superplastic behavior, postponing the rupture event and contributing further to rupture elongation. The superplastic behavior has been observed in similar works earlier for this class of steel at elevated temperatures [**161**, **188**, **205**]. From metallographic analysis of ruptured specimens, it is found that the failure mode during creep rupture is predominantly transgranular ductile fracture as array of microvoids nucleate along certain crystallographic orientations towards the final rupture location (see Figure 7.3(a)). It is also interesting to observe that these arrays are mostly found near the material inclusions (precipitates and/or secondary phases etc., see Figure 7.3(b)). This aspect of preferential material deformation needs to be focusedly investigated further with specimens tested under several other stress and temperature loading conditions and will be part of future work recommendations.

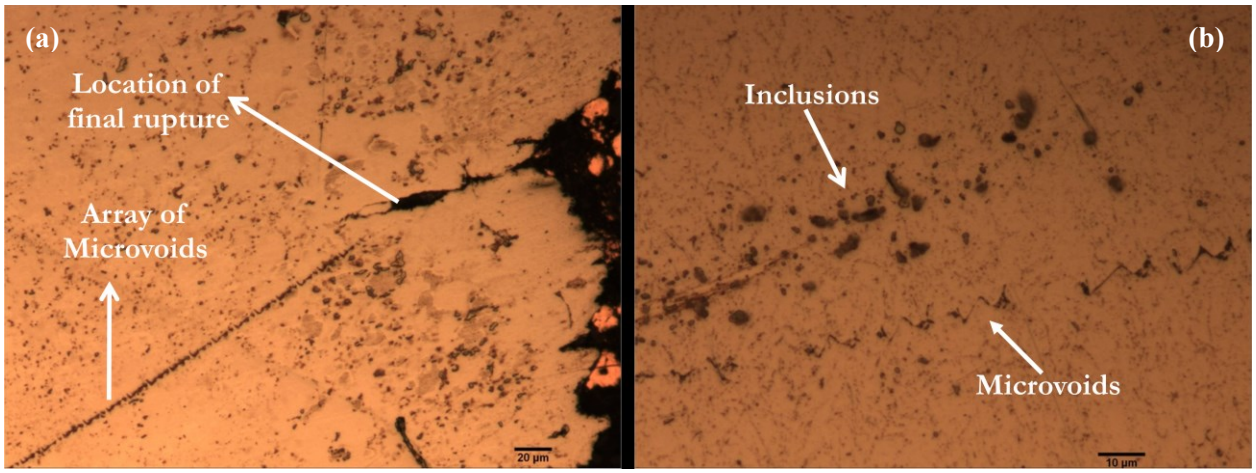

Figure 7.3. Transgranular ductile fracture as observed in creep ruptured P91 steel specimen (a) before and (b) after etching with Nital solution (test condition: 151.5 MPa, 625°C).

7.1.3. Low cycle fatigue behavior

This section will focus only on the results obtained from cyclic tests conducted with no hold time. Under such loading conditions, the LCF endurance is expected to be dominated by fatigue based micromechanisms (and oxidation) with little or no creep deformation. A total of 32 tests were completed by 10 RR participants under three strain ranges of 0.5%, 1% and 1.5% at 625°C while following the test procedure prescribed in ASTM E2714-09. Figure 7.4 shows a typical plot – maximum and minimum stress (σ_{max} and σ_{min}, respectively) vs. cycles to failure, N_f – obtained under cyclic testing without hold time. It is observed that grade P91 steel undergoes rapid cyclic softening. The magnitude of peak stresses decreases as loading cycles increase during the initial cycles followed by a linear softening stage for considerably longer duration before softening accelerates again marking the onset of crack formation [**31**]. The endurance results presented for discussion in this section are based on 2% percent deviation in the maximum stress from the extended linear softening phase.

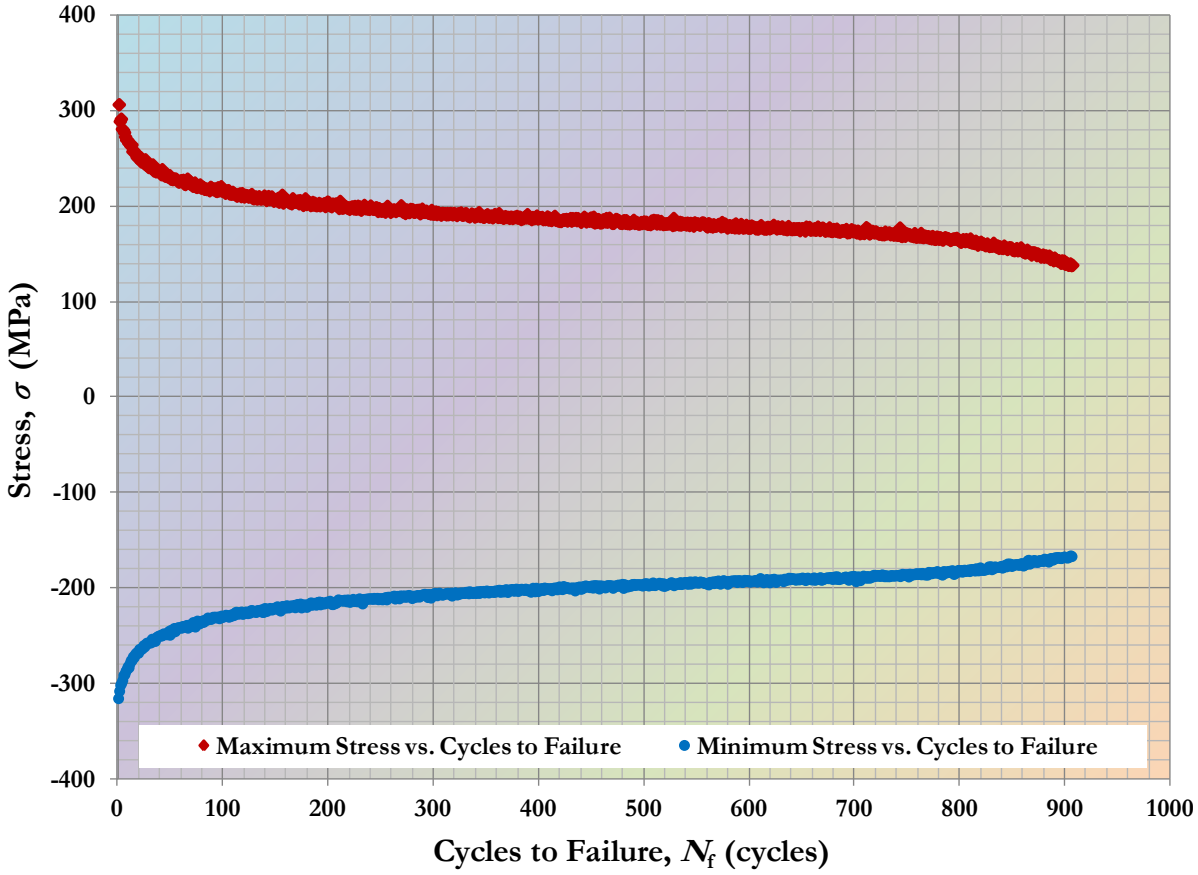

Figure 7.4. Typical variations in maximum and minimum stress with loading cycles as observed in cyclic deformation response of grade P91 steel without hold time (Data courtesy of one of the RR participants).

Since the RR participants employed different specimen heating methods, the results are grouped by the heating method employed. The specific influence of specimen location within the pipe section for any bias in the endurance results is also investigated. All the test results for macroscopic crack formation under LCF loading conditions are summarized in Table 7.3. The standard deviations in the mean values are also presented if there had been more than one test conducted at any given strain amplitude by any of the RR participants. On careful observation, it can be noted that the number of cycles for macroscopic crack formation decrease with increasing strain amplitudes regardless of the specimen location within the pipe and the type of specimen heating

employed. In addition to this obvious result, several other significant observations can be made on further analysis. At the lowest strain range, the resistance heating method seems to result in lower LCF lives as compared to radiation heating but significantly higher compared to the one test performed with induction heating. Since only one test result was reported at this strain range with induction heating, it is not possible to definitively conclude that heating method was responsible for differences in C-F lives. At the other strain ranges, no biases in lives were detected that could be linked to the heating methods. Specimen location 2-4 also appears to yield the highest lives at all the 3 strain ranges.

Table 7.3. Mean number of cycles, along with standard deviation, to form a macroscopic crack based on the 2% load drop end-of-life criterion for the RR LCF tests.

Specimen location	Type of heating method	Number of tests (strain range)			Strain amplitude during creep-fatigue testing (with no hold time)		
		0.5%	1%	1.5%	± 0.25%	± 0.5%	± 0.75%
2-1	Resistance	1	6	3	3438	832 ± 208	478 ± 29
	Induction						
	Radiation						
2-2	Resistance		2	2		877 ± 26	443 ± 198
	Induction						
	Radiation	2	2	2	5585 ± 294	857 ± 33	482 ± 4
2-3	Resistance						
	Induction	1	2	2	2202	783 ± 264	448 ± 3
	Radiation						
2-4	Resistance	3	2	2	4939 ± 2398	1181 ± 56	610 ± 5
	Induction						
	Radiation						
Number of completed tests		**7**	**14**	**11**	Total number of completed tests: **32**		

Figure 7.5 shows the typical evolution of cyclic hysteresis loops with time during the cyclic deformation of grade P91 steel at 1% strain range with no hold time. The magnitude of peak stresses decreases with increase in number of loading cycles showing the cyclic softening behavior of grade P91 steels along with the observation that hysteresis loops get wider with time because of increases

in the accumulated inelastic strain ε_{in}, with increasing number of cycles. The LCF tests are typically continued until an obvious cusp appears in the hysteresis loops prior to fracture, rather than the 2% load drop point that is used later to establish the lifetime analytically.

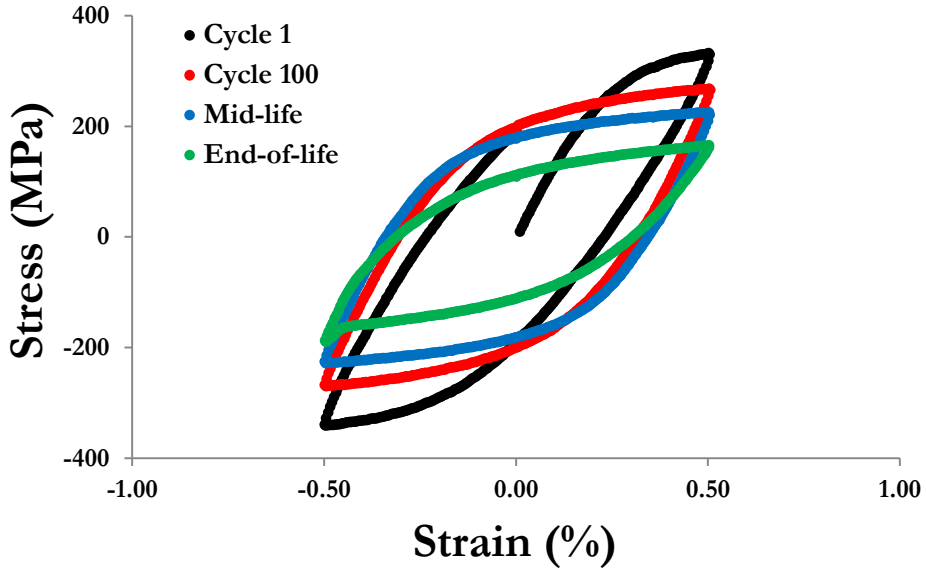

Figure 7.5. Evolution of cyclic hysteresis loops at different stages of the life cycles. The curves are plotted from data obtained at 1% strain range with no hold time, as reported by one of the RR participants.

7.1.4. Creep-fatigue behavior

This section will focus on the results obtained from cyclic tests conducted with hold time – 600 and 1800 seconds – at the maximum (peak) tensile strain during loading with 2% load drop as the C-F crack formation and end-of-life criterion. It is expected that under such loading conditions, the C-F endurance is still dominated by fatigue based micromechanisms (and oxidation) with creep deformation contributing somewhat marginally to the accumulated damage. A total of 46 such tests were completed by 11 RR participants under two different strain ranges (1% and 1.5%) at 625°C while following the test procedure prescribed in ASTM E2714-09.

Figure 7.6 shows a typical plot – maximum and minimum stress (σ_{max} and σ_{min}, respectively) vs. cycles to failure, N_f – obtained under cyclic testing with/without hold time for P91 steel at 1% strain range, as reported by one of the RR participants. It can be easily observed that P91 steel qualitatively shows similar cyclic softening behavior with hold time as in tests without hold time, except that the C-F lives were on the average shorter under the hold time condition. Increasing the hold time for the same strain range was found to further decrease the C-F life. Although both these observations were not noted in all of the RR tests, the majority of the test results followed this trend.

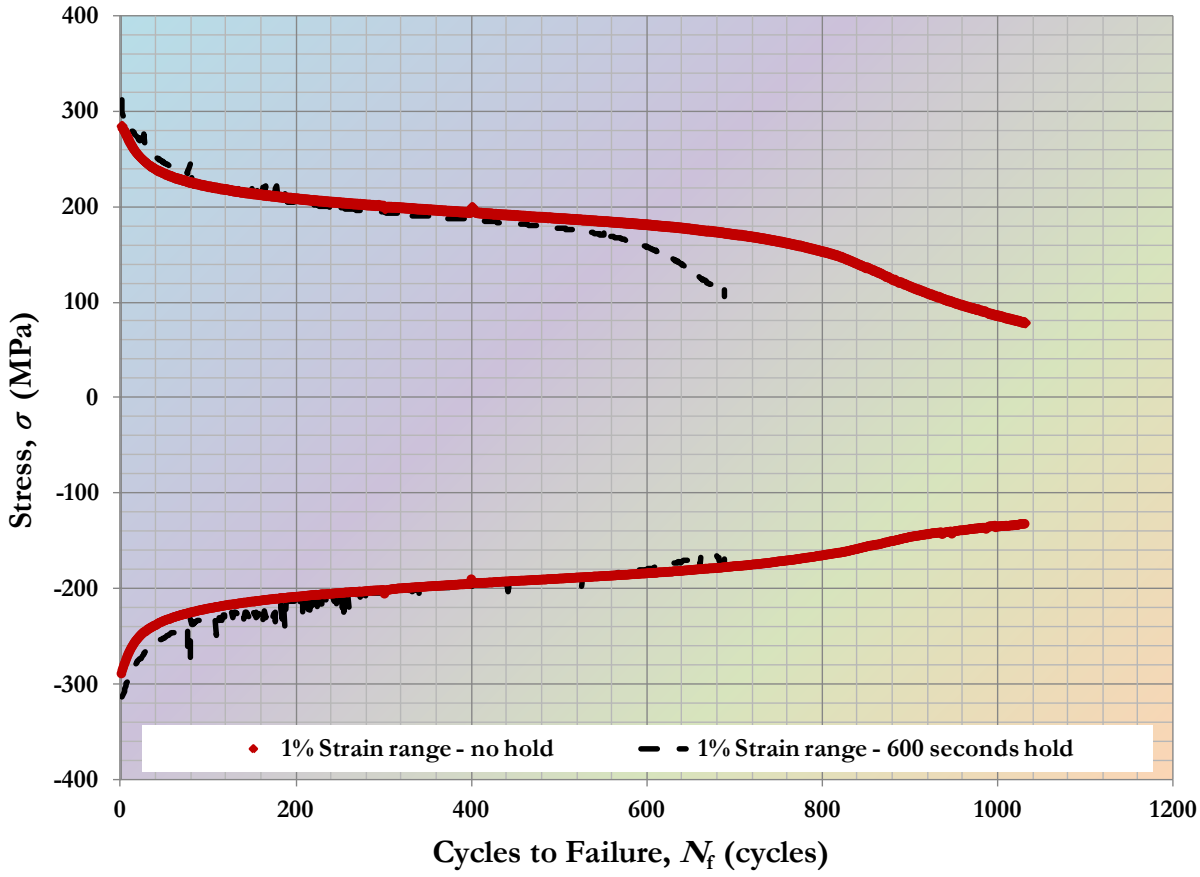

Figure 7.6. Typical plots of peak stress as a function of cycles for tests conducted with no hold time (red solid line) with those conducted with a 600 seconds hold (black dash line).

Similar to the methodology followed for LCF tests, the results for C-F tests will be grouped according to the heating method and specimen location within the pipe. The average of all the results obtained by considering a 2% load drop as the end-of-life criterion for C-F crack formation is summarized in Table 7.4. The standard deviations along with the mean values are presented if there had been more than one test conducted at any given strain amplitude by any of the RR participants.

Table 7.4. Mean number of cycles (± standard deviation) to form a macroscopic crack using 2% load drop as the end-of-life criterion for C-F tests under different strain amplitudes, as reported by the RR participants.

Specimen location	Type of heating method	Number of tests			Strain amplitude (with 600 and 1800 seconds hold at peak tensile strain)		
		1% (600 sec.)	1.5% (600 sec.)	1% (1800 sec.)	± 0.5% (600 sec.)	± 0.75% (600 sec.)	± 0.5% (1800 sec.)
2-1	Resistance	4	2	3	412 ± 98	409 ± 52	703 ± 287
	Induction						
	Radiation						
2-2	Resistance	7	2	6	735 ± 149	448 ± 59	529 ± 141
	Induction						
	Radiation						
2-3	Resistance		1			429	
	Induction	4	6	1	990 ± 42	485 ± 50	> 1039
	Radiation						
2-4	Resistance	4	4	2	816 ± 213	483 ± 182	945 ± 82
	Induction						
	Radiation						
Number of completed tests		**19**	**15**	**12**	Total number of completed tests: **46**		

The existing literature on the C-F interaction of P91 steel (refer section 4.2) has shown that the introduction of hold time decreases the material's C-F endurance as compared with LCF tests. Although most of the current RR results concur with these observations, it is not observed with all of the reported test results. As noted earlier for LCF tests and based on limited data, the resistance

furnace based heating systems typically lead to lower specimen lives as compared to when induction heating systems are used. This trend is clearly in contrast with that observed for LCF tests. The specimen location also seems to affect C-F endurance for hold time tests, with pipe subsection 2-4 having the highest C-F endurance under the different strain ranges. This trend is consistent with that observed for LCF tests. Figure 7.7 shows the evolution of stress-strain hysteresis loops with time during the cyclic deformation of grade P91 steel at 1% strain range with no hold and 600 seconds hold at peak tensile strain, as reported by one of the RR participants. As observed earlier for LCF tests, the magnitude of peak stresses decrease with increase in number of loading cycles showing the cyclic softening behavior of P91 steel along with the observation that hysteresis loops get wider with time.

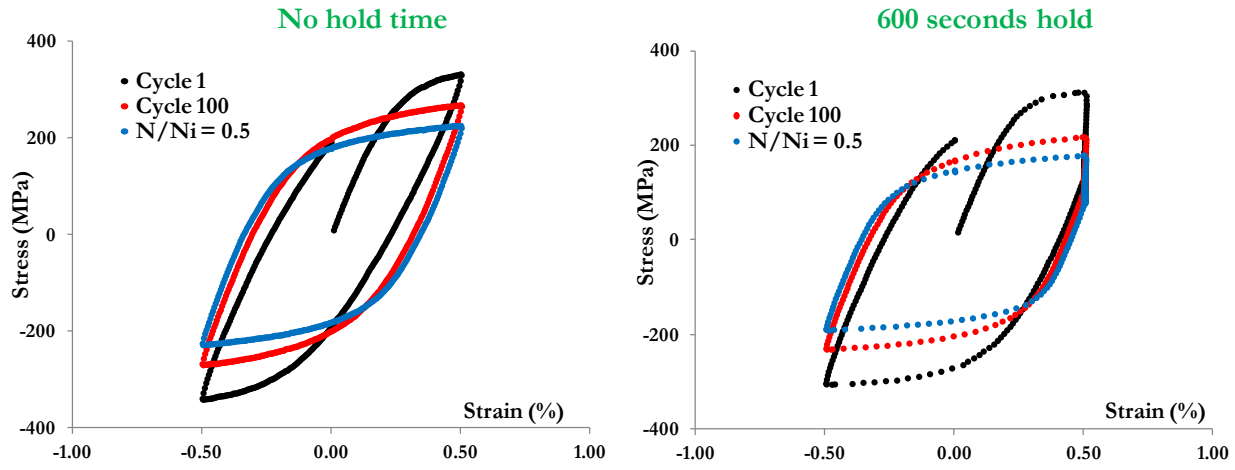

Figure 7.7. Evolution of stress-strain hysteresis loops at different stages of life starting from cycle 1 till mid-life. The curves are plotted from data obtained at 1% strain range with no hold time and 600 seconds hold, as reported by one of the RR participants.

Figure 7.8 shows the cyclic stress relaxation behavior obtained by plotting stress vs. time during hold time per cycle at 1% strain range and 600 seconds hold at peak tensile strain as reported by three different RR participants. The exponential decrease in stress over time is in agreement with

observed and expected stress relaxation behavior for this class of steels. These plots indicate that maximum stress is induced in the material at the start of tensile hold and then the stress gradually relaxes with time during the hold period due to creep deformation. As the peak stress decreases due to cyclic softening, the stress relaxation curves shift downwards over time as observed in Figure 7.8.

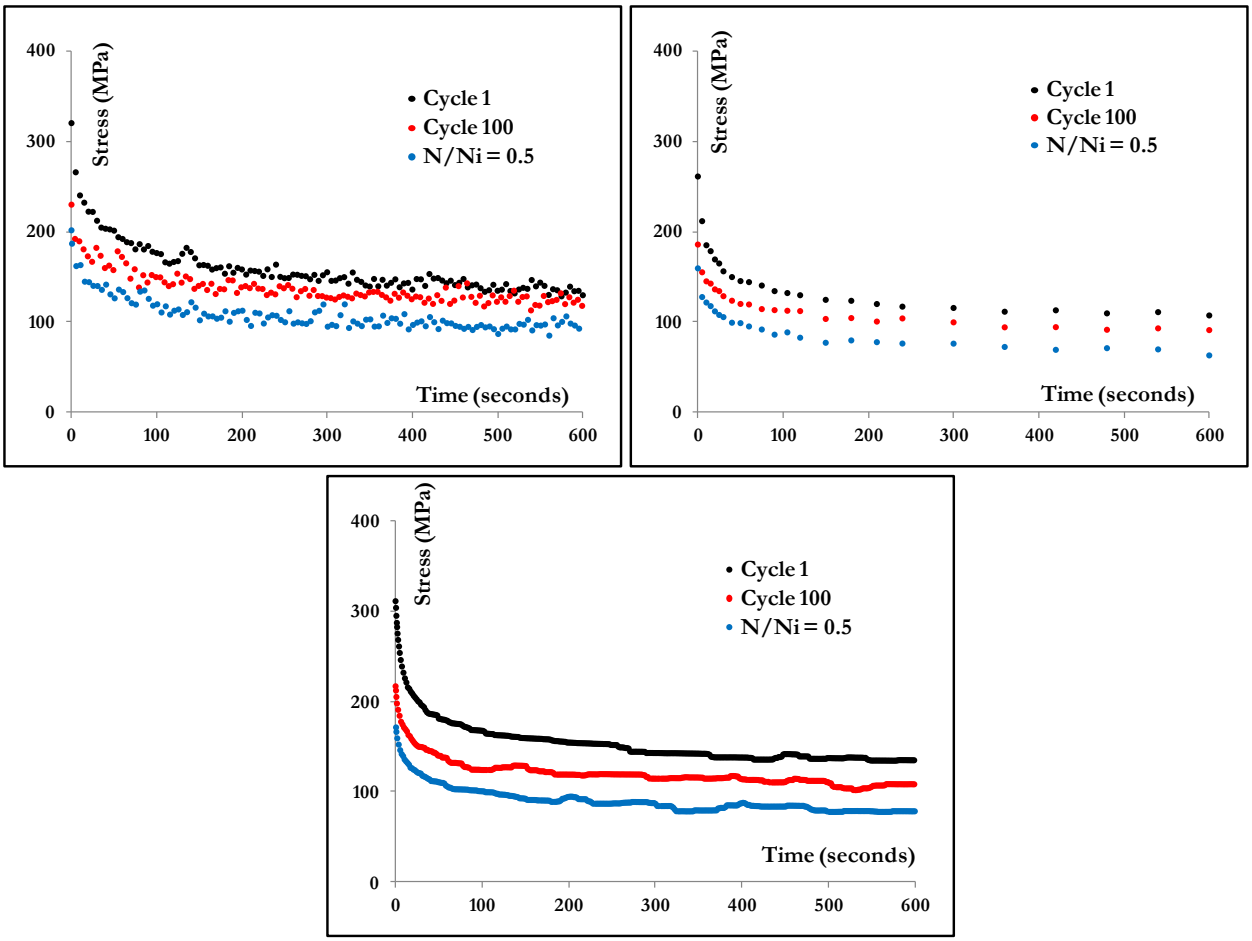

Figure 7.8. Evolution of cyclic stress relaxation characteristics at different stages of the C-F life starting from cycle 1 till mid-life. The curves are plotted from data obtained at 1% strain range with 600 seconds hold time, as reported by three different RR participants.

Cyclic stress-strain hysteresis loops are plotted in Figure 7.9, as reported by one of the RR participants who tested specimens at 0, 600 and 1800 seconds hold time. Widening of the hysteresis

loops with increasing hold time are indicative of higher accumulated inelastic strain ε_{in}, and consequently reduced C-F endurances with increasing hold times.

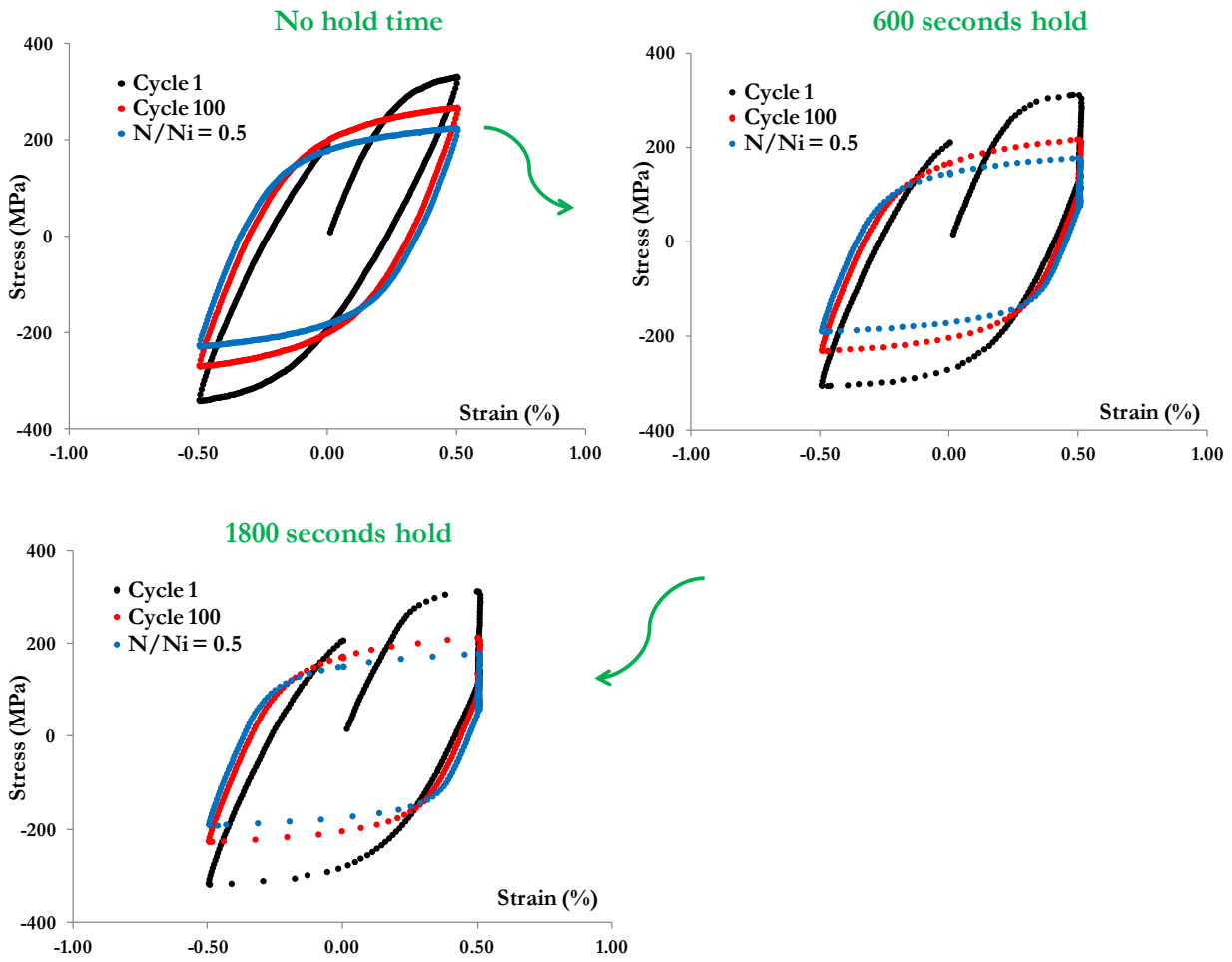

Figure 7.9. Evolution of cyclic hysteresis loops at different stages of C-F life starting from cycle 1 to mid-life. The curves are plotted from data obtained at 1% strain range with 0, 600 and 1800 seconds of hold time, as reported by one of the RR participants.

7.1.5. Post-test inspection

7.1.5.1. Visual inspection

Before the tested specimens were mechanically sectioned for metallography and further optical microscopic examination, high resolution digital photographs of the as-tested specimens

were obtained. Visual inspection of these specimens was carried out and prominent characteristics of the specimen morphology and the presence of any geometric instability (or bulging) were carefully noted. The main features from these visual and digital observations are summarized as follows:

1) Pure LCF (no hold time) test specimens show extensive crack branching, but no significant bulging.
2) All C-F (hold time) test specimens show no significant crack branching, but bulging becomes more pronounced with increasing hold times.
3) Bulging is much more noticeable for tests conducted with induction heating as compared to tests conducted using resistance furnaces under the same test condition. This is indicative of localized hot spots and perhaps non-uniform temperatures in the specimen during induction heating.
4) Oxidation and specimen dimensions may also play a vital role in the formation of bulges; specimens tested by one RR participant (that have comparatively smaller diameters) do not show any indication of bulging even for 1800 seconds hold time tests.
5) Specimen location does not seem to play any noticeable role on the type and morphology of C-F crack(s) for any of the tests.
6) In several tests conducted by a particular RR participant, the fatal cracks originate at the ceramic bead applied in the gage length to avoid extensometer slippage (Figures 7.10 and 7.11). The thermal expansion mismatch between the metal and the ceramic may have influenced the lifetimes in these tests.
7) One of the RR participants used both induction and resistance heating systems and reported variations in cycles to macroscopic crack formation; however, no visible difference exists in the external appearance of the tested specimens.

Figures 7.10 and 7.11 present examples of tested specimens that illustrate the above observations. The specimen lengths noted in these figures are from a digital Vernier caliper and are considered only to be approximate.

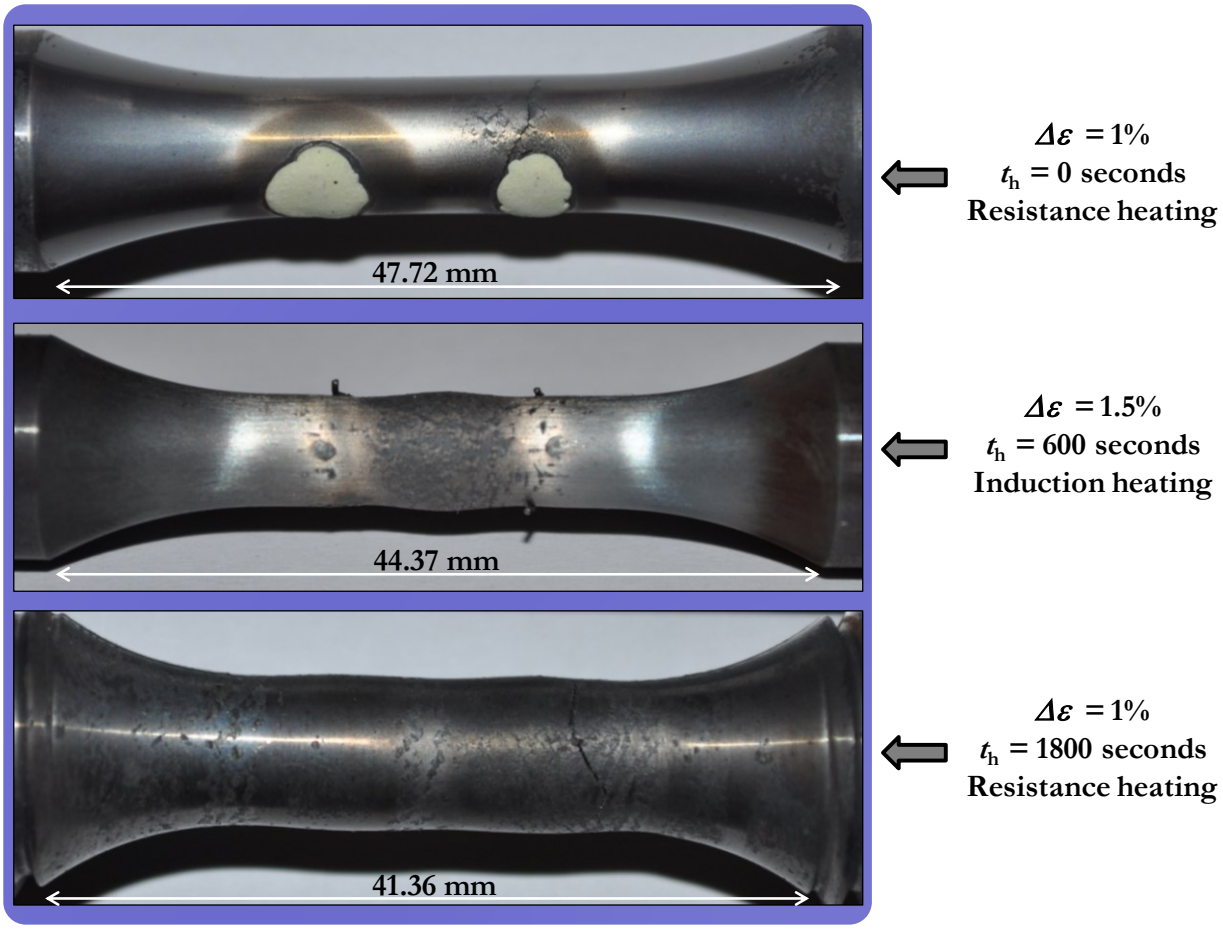

Figure 7.10. High resolution digital photographs of different test specimens as received from the RR participants.

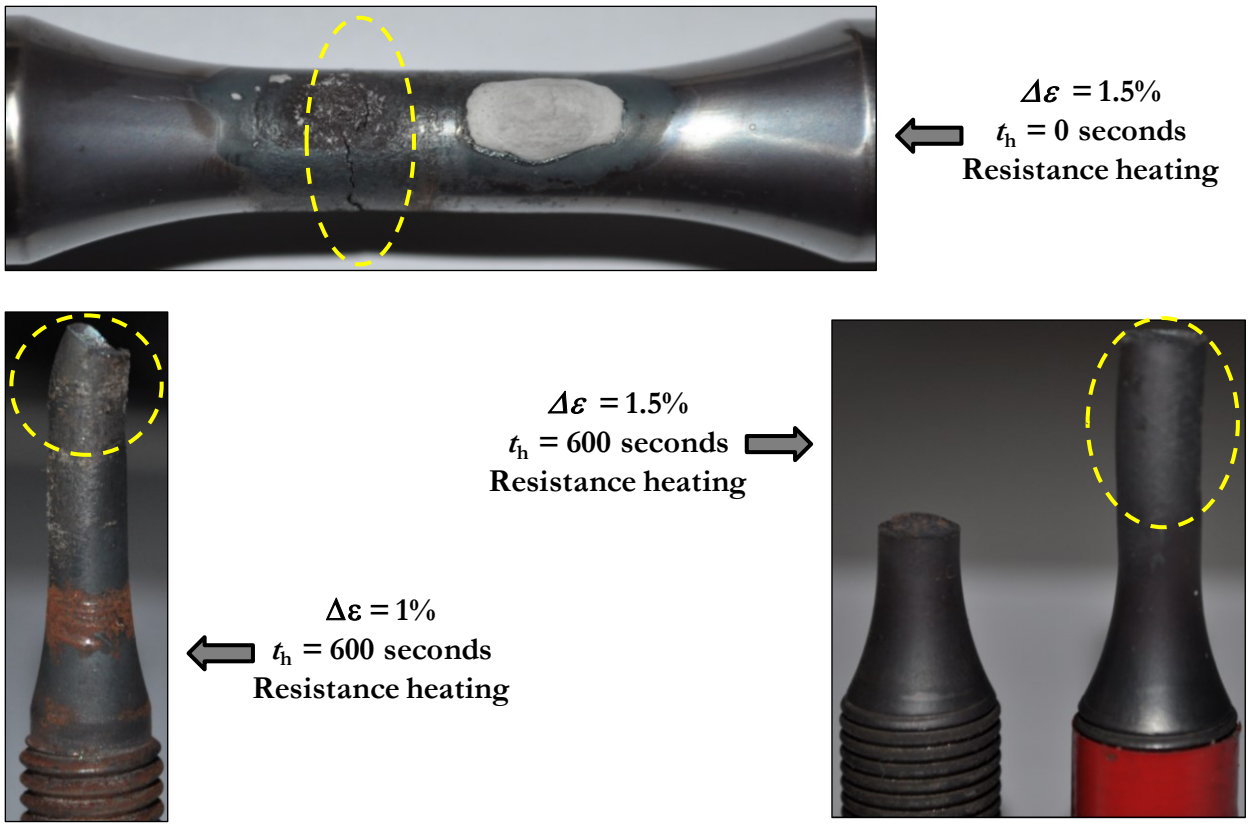

Figure 7.11. High resolution digital photographs of different test specimens as received from the RR participants. These specimens specifically showed reduced C-F lifetime as compared with other test results. The encircled regions show features that may provide explanations for the low lifetime.

7.1.5.2. Metallographic analysis

The metallographic specimens were examined primarily using an optical microscope and scanning electron microscopic analyses followed, if warranted. One of the RR participants indicate the presence of both equiaxed and elongated inclusions, possibly manganese sulfide commonly found in martensitic/ferritic steels that typically form during processing. The presence of these inclusions in the test material is an exception rather than typical. Figures 7.12(a) and (b) show such inclusions, respectively with the latter usually observed parallel to the loading direction. Highly localized oxide accumulation can also be seen at the specimen cross-section where the C-F induced

cracks are observed for hold time tests, with greater accumulations found at cracks that are considerably longer and deeper (see Figure 7.12(c)).

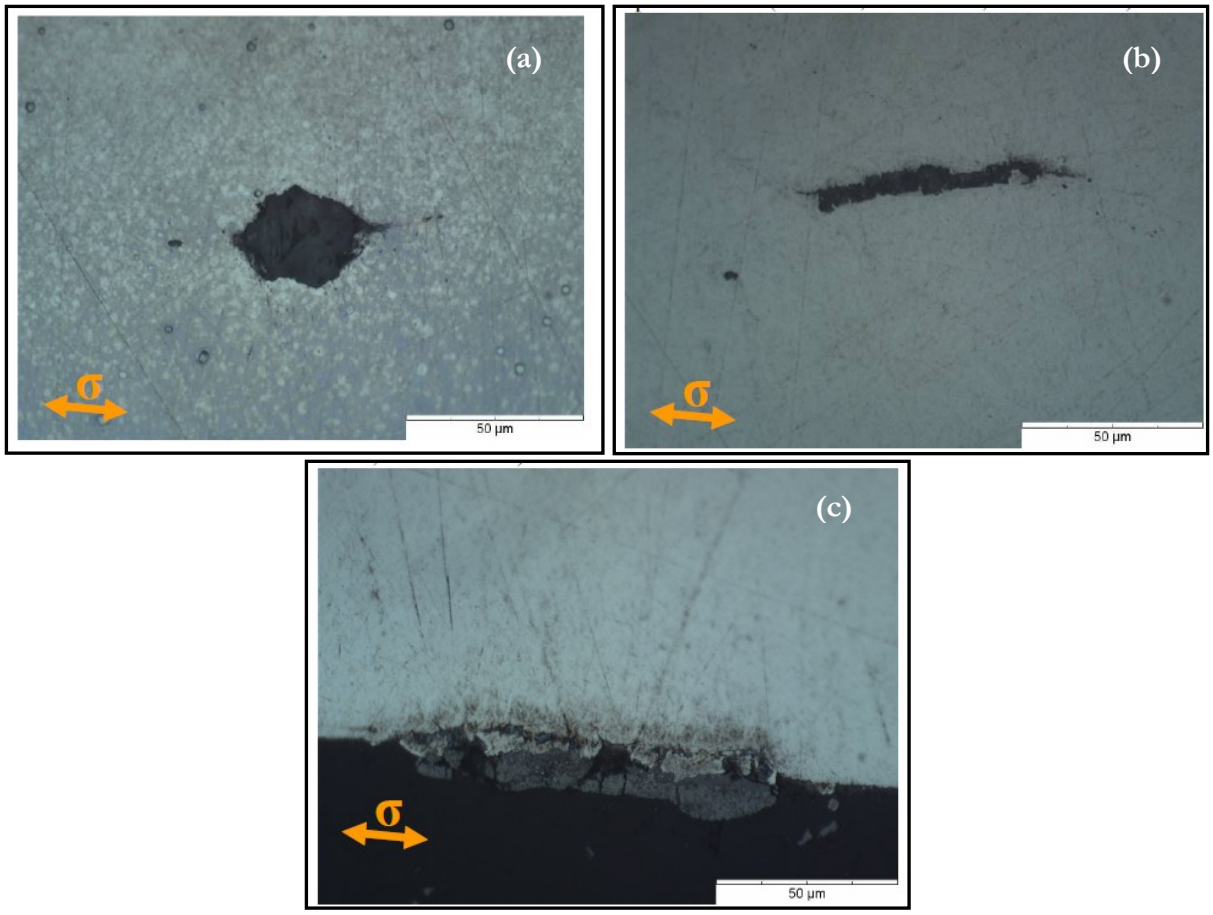

Figure 7.12. Optical microscopic images of (a) equiaxed and (b) elongated inclusions in grade P91 test specimens, as obtained from one of the RR participants, where σ refers to the fact that stress was applied along the loading direction as indicated by the double-headed arrow. (c) Localized accumulation of surface oxide layers is also observed for hold time test specimens.

Rather than crack formation at inclusions and/or other internal microstructural features, cracks predominantly form on specimen surfaces and propagate normal to the loading direction with secondary branching of cracks in specimens tested under C-F loading with a hold time (see Figures 7.13(a) and (b)). The surfaces of almost all the primary cracks that propagated and opened due to

plastic/creep deformation are covered with thick oxide layers (see Figure 7.13(c)), although the thickness of these layers seems to vary significantly for specimens tested under similar conditions but by different participants. Figure 7.13(c) also shows two comparatively smaller cracks just initiated in the oxide layer. All the above observations are predominantly characteristic of domain 2 type of C-F cracking, although the highly branched cracking under LCF tests resembles that of domain 1 as described similarly by Fournier *et al.* [**236**] and as discussed earlier in section 4.2.

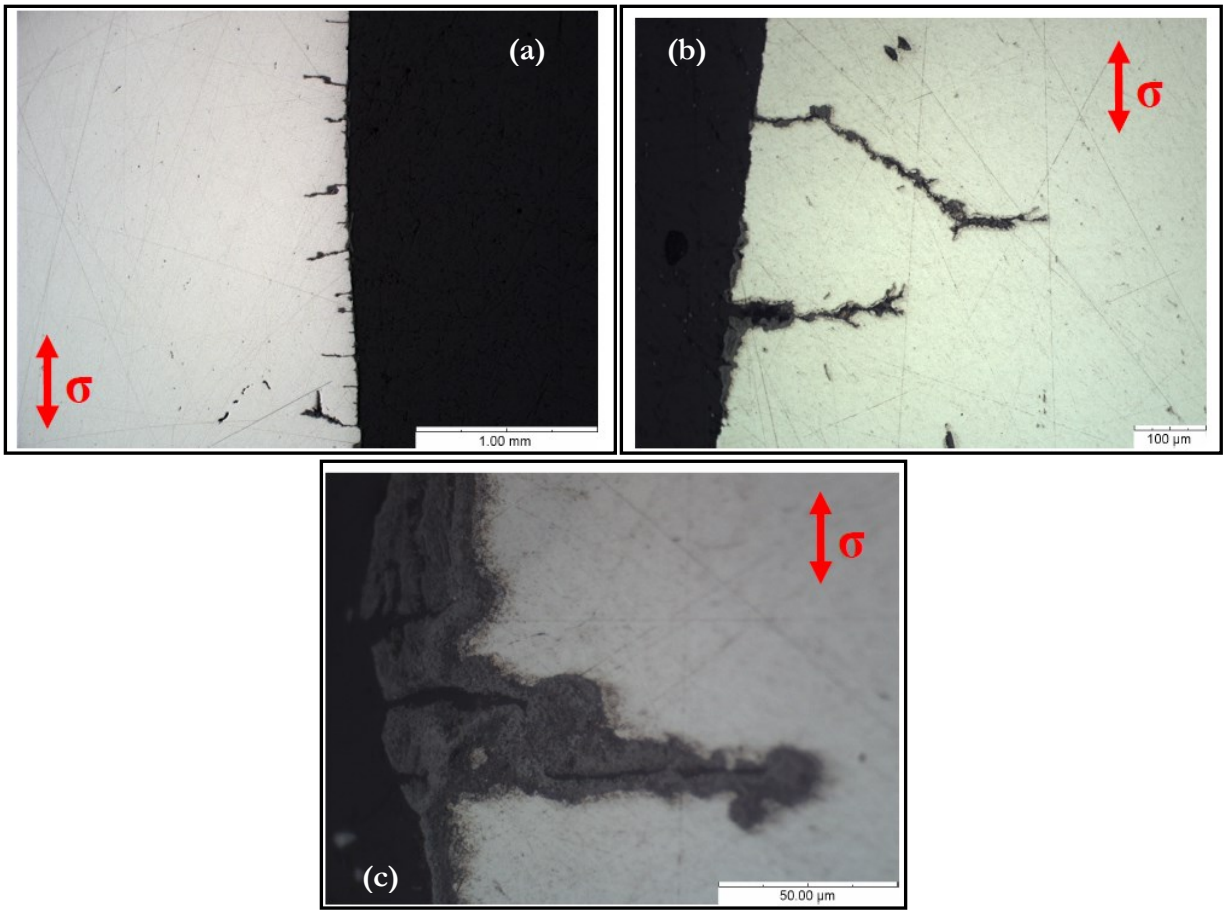

Figure 7.13. Optical microscopic images showing (a) mostly perpendicular propagation of surface cracks to the loading direction with (b) limited secondary branching in specimens tested with a hold time, as obtained from one of the RR participants. Figure (c) shows the development of thick oxide layers that grow along the primary crack propagation path.

Creep damage, normally associated with grain and lath boundary cavitation is not visible in any of the "chemically unetched" metallographic specimens. Therefore, these specimens were etched using chemical etchants that are known to preferentially etch these boundaries. Since 1% strain range is the only test condition under which three different hold times (0, 600 and 1800 seconds) were employed, the results from only this test condition are presented in Figure 7.14. The specimens are taken from three different RR participants all using resistance heating method system. It is clearly seen that creep damage is present in the specimen tested less than 1800 seconds hold time but not in specimens tested under 0 seconds hold time. There is also evidence of some cavitation damage in the 600 seconds hold time tests. These images indicate that creep might be actively involved in enhancing deformation micromechanisms with increasing hold times, but does not seem to contribute significantly to damage for hold times less than 1800 seconds.

Figure 7.15 shows the micrographs of two specimens tested at 1% strain range and 1800 seconds hold at peak tensile strain; one tested using resistance heating method with a reported life of 400 cycles and the other tested using induction heating method with a reported life greater than 1039 cycles. The damage characteristics between the two specimens are quite different in that the specimen with the lower life (resistance furnace heated) shows lot more creep and oxidation damage than the one with longer life (induction furnace heated). The significant difference in C-F endurance between the two specimens and the accompanying damage states indicate that differences in heating method can contribute to systematic biases in the C-F life, with resistance heating associated with comparatively lower C-F lifetimes. It is highly probable that tests involving induction heating for ferritic metals offer high endurances as compared with that of resistance based heating due to differences in the way temperature control is managed in these methods. Moreover, the location of thermocouple beads in the specimen – either within the gage length or at the radius of curvature of

specimen's shoulder – can also be an important consideration to account for this observation. This aspect of elevated temperature testing needs further detailed investigation and can be one of the paths along the future research direction.

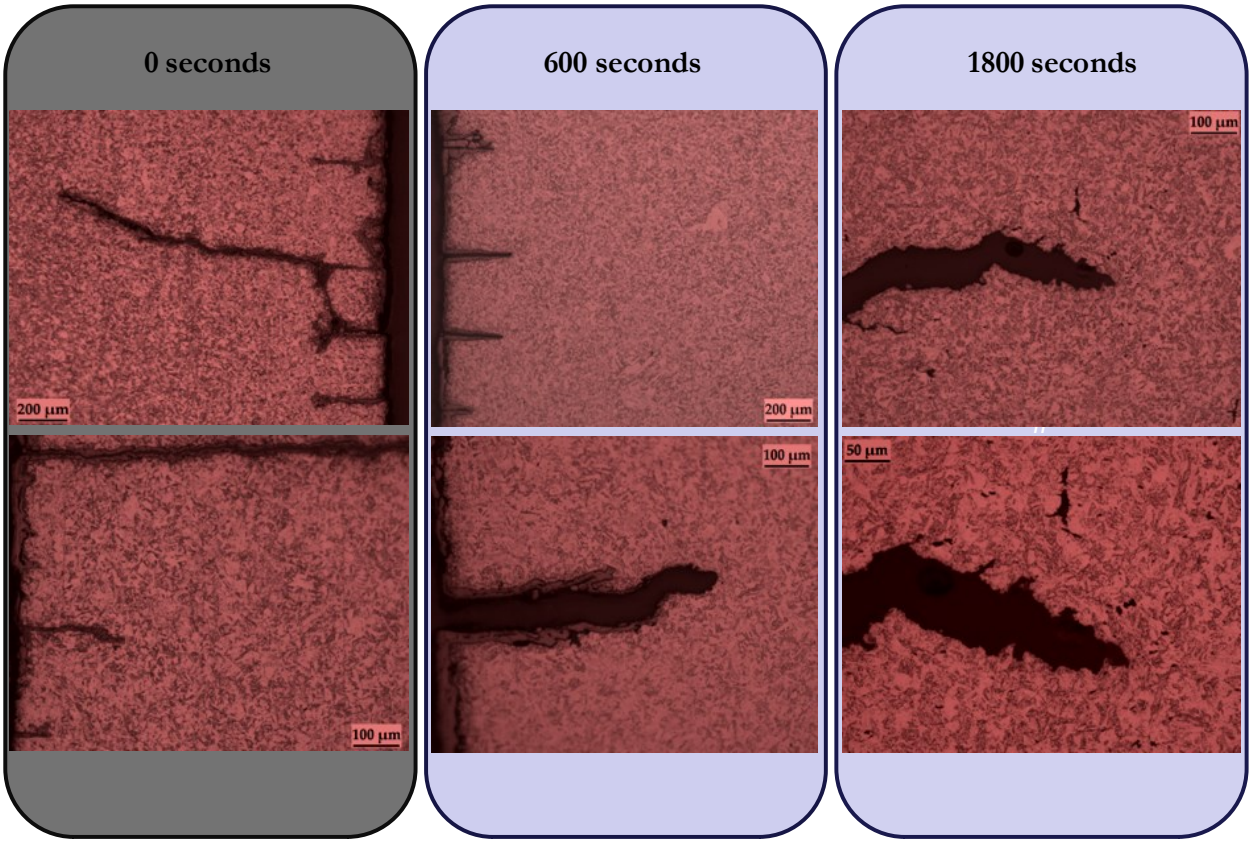

Figure 7.14. Optical microscopic images showing the effect of hold time (at peak tensile strain) during C-F tests at 1% strain range using a resistance type furnace heating. The images are optically enhanced to clearly highlight the presence of small creep cavities, if any.

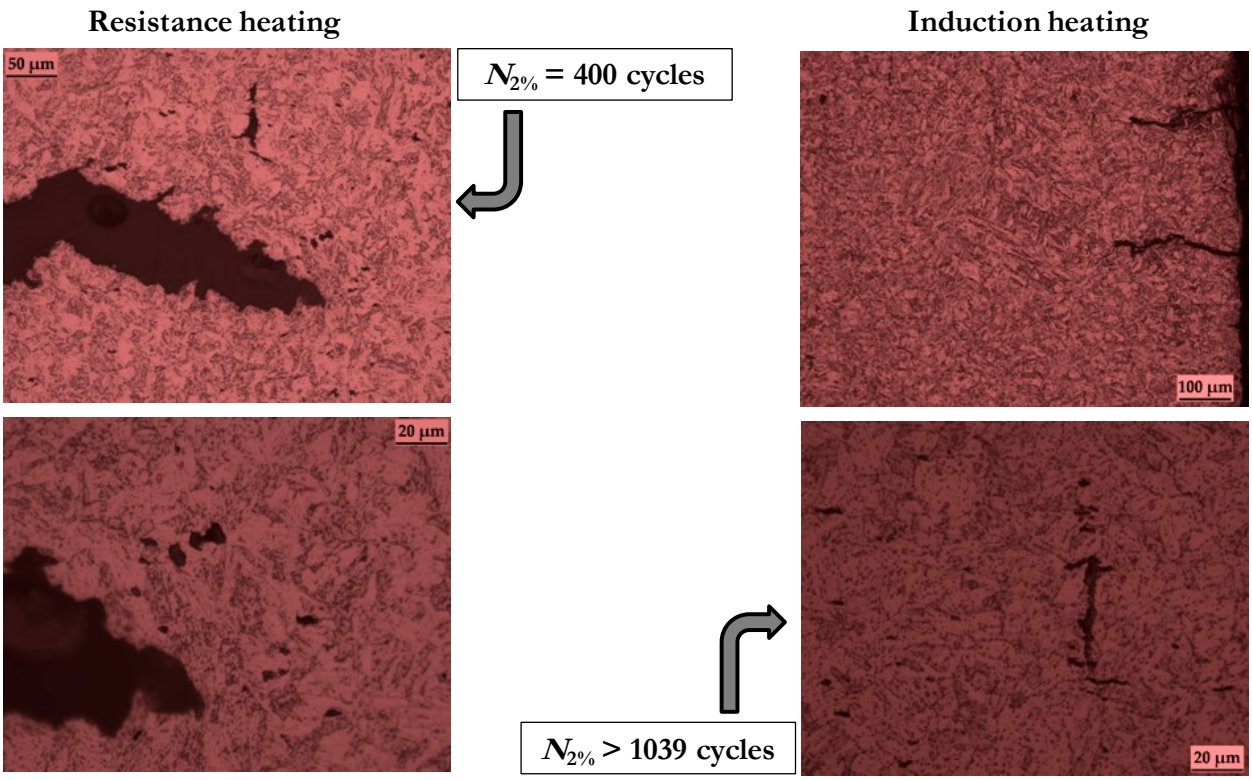

Figure 7.15. Optical microscopic images showing the effect of type of furnace heating during the C-F deformation of grade P91 steel at 1% strain range and 1800 seconds hold at peak tensile strain. The arrows indicate the reported C-F life. The images are optically enhanced to clearly highlight the presence of small creep cavities, if any.

7.1.6. Statistical analysis of RR data

One of the major objectives of this dissertation work is the statistical analysis of the RR test data and subsequent formulation of the precision and bias statements intended for supporting the C-F test standard ASTM E2714-09. This section therefore just explores the statistical variability in the test results rather than scientific aspects of material behavior. The test standard in its current version does not precisely specify a detailed procedure for determining the number of cycles corresponding to the end-of-life at the 2% load drop. An analytical procedure is developed to precisely choose the cycles corresponding to a 2% load drop as demonstrated in Figure 7.16. The procedure, as described

in Figure 7.16, consists of five steps and minimizes the participant-to-participant variability in choosing the cycles at end-of-life.

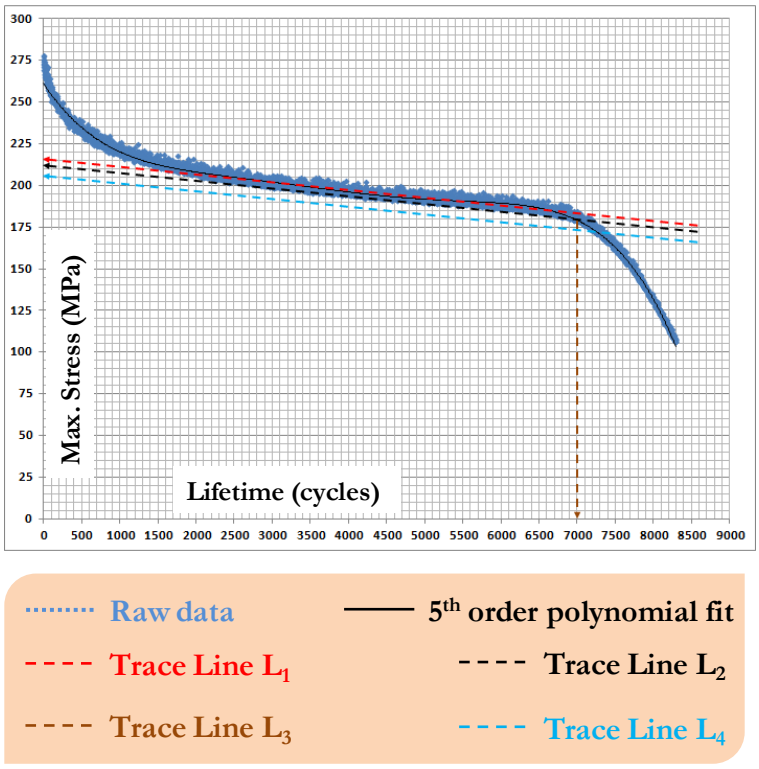

❶ Fit a 5th order polynomial to obtain a trendline from the digital data

❷ Draw a line (L_1) that matches the linear portion of this curve, and trace it to the ordinate axis to obtain the intercept (y_1)

❸ Draw a line (L_2) parallel to L_1 from an ordinate value equal to 0.98 *y_1 (2% load drop stress)

❹ Trace the point of intersection of line L_2 and the polynomial fit to the abscissa and obtain required lifetime (x_1) by drawing a line (L_3)

❺ Draw a line (L_4) parallel to L_1 from an ordinate value equal to 0.95 *y_1 (5% load drop stress) ……

Figure 7.16. The analytical procedure proposed in this work to determine the end-of-life based on x% load drop.

Table 7.5 shows the intra- and inter-laboratory variability (or equivalently, repeatability and reproducibility, respectively) estimated using statistical calculations with the C-F endurance data. The end-of-life as reported by the RR participants following the current guidelines in E2714-09 is tabulated under *Participants' Assessment* and the end-of-life based on the five step procedure described in Figure 7.16 is tabulated separately and labeled as the *Analytical Method*. Although the mean C-F endurance and its standard deviation do not significantly vary between the two assessment methods, the repeatability in tests involving higher hold times is better when the analytical procedure is

utilized. The reproducibility, on the other hand, appears to be substantially unchanged. This indicates that utilizing the analytical procedure described herein for determining the 2% load drop life in C-F testing is beneficial, but the benefits are marginal. After careful consideration with reported results, it is also determined that a 2% load drop criterion will suffice as a satisfactory criteria for determining the end-of-life in laboratory C-F testing.

Table 7.5. A measure of mean C-F endurance, defined by 2% load drop, and the standard deviation in the RR data. The intra- and inter-laboratory variability is also computed and presented as per both assessment procedures.

Test Condition Strain Amp. (hold time)	Participants' Assessment		Analytical Method	
	Mean $N_{2\%}$ ± Std. Dev. (cycles)	Repeatability/ *Reproducibility* Std. Dev. (cycles)	Mean $N_{2\%}$ ± Std. Dev. (cycles)	Repeatability/ *Reproducibility* Std. Dev. (cycles)
± 0.25%	5920 ± 474	547 / *612*	5938 ± 499	523 / *621*
± 0.5%	911 ± 174	47 / *177*	880 ± 180	47 / *183*
± 0.75%	491 ± 68	40 / *74*	489 ± 71	37 / *75*
± 0.5% (10 min. hold)	741 ± 235	51 / *238*	753 ± 244	51 / *246*
± 0.75% (10 min. hold)	457 ± 97	18 / *98*	479 ± 102	27 / *103*
± 0.5% (30 min. hold)	697 ± 203	82 / *211*	672 ± 207	44 / *210*

Figure 7.17 shows the C-F endurance plot for the different test conditions in the current RR as reported by the RR participants. This figure clearly indicates that C-F endurances decrease with increasing strain ranges and increasing hold times (as discussed earlier). In this context, the precision and bias statements, as formulated by ASTM, are systematically formulated and discussed elaborately in [**288**].

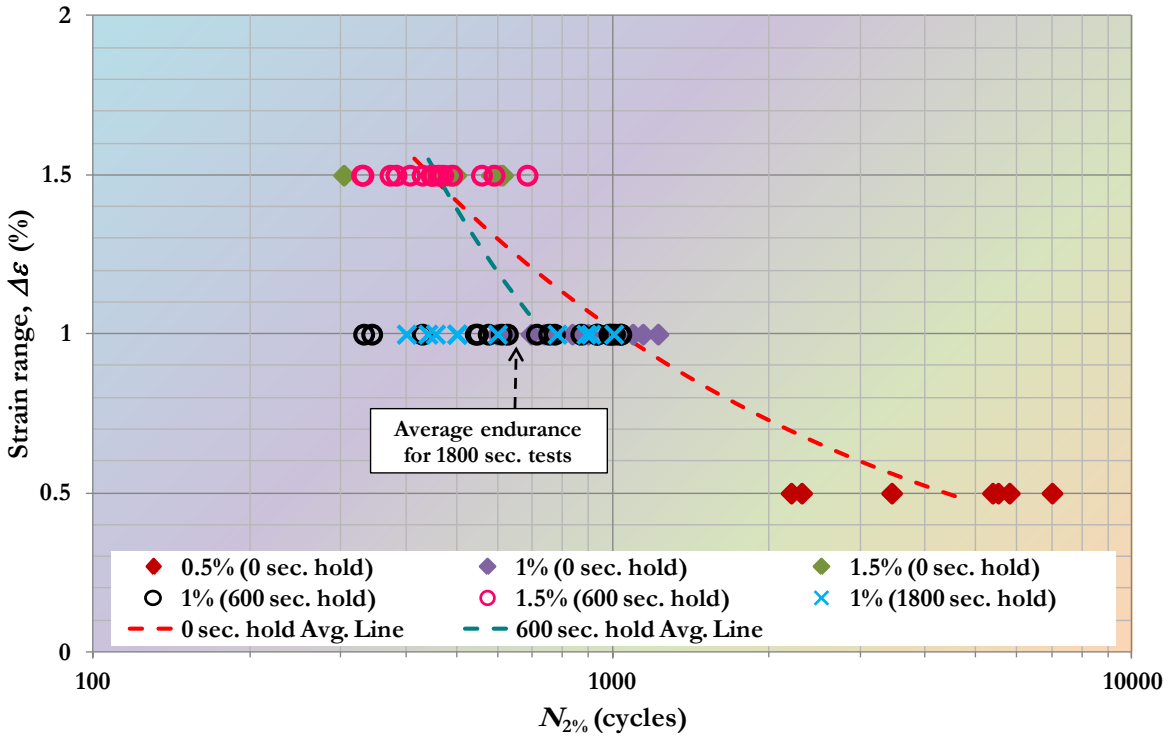

Figure 7.17. Creep-fatigue endurance plot containing all the RR test data.

The data obtained from few test specimens such as those specifically illustrated in Figure 7.11 might have resulted in unusually reduced C-F lives and thus significantly increase the scatter among the results. These specimens show that in one case, the crack emanates from the region where the extensometer was attached and in the other two cases, there is clear evidence of bending in the specimen. These and other test specimens that contributed to increased scatter were analyzed thoroughly via visual examination and optical metallography. After due diligence, some of these test results were deemed to not qualify as valid data to meet the current test standard. To quantify the reduction in scatter before and after excluding few such invalid test results, the variability factor – ratio of maximum to minimum C-F life obtained from the 95% confidence interval bands – is calculated for the different test conditions. For LCF tests, the variability factor reduces from 10, 3 and 2 to 3, 3 and 2 for the strain ranges of 0.5%, 1% and 1.5%, respectively. For 600 seconds hold

time tests, the variability factor reduces from 4 and 3 to 3 and 3 for the strain ranges of 1% and 1.5%, respectively. The variability factor remains at 5 for the 1800 seconds hold time tests at 1% strain range, as none of the test results from this condition was excluded as invalid.

7.1.7. Recommendations for improving the current C-F standard

The current C-F test standard does not explicitly provide any guidelines for qualifying test data using the stress-strain (or other relevant) plots recorded during the tests. Figures 7.18, 7.19 and 7.20 show few such cases where issues related to machine control may have influenced the test results. Specifically, Figure 7.18 shows two instances from the reported RR results where a spike seems to occur during the linear softening stage of grade P91 steel's C-F deformation. Although these cases may be rare, such occurrences do happen during laboratory testing and hence the test standard could provide clear guidelines/notes for analyzing such test results. Figures 7.19 and 7.20 show instances where good machine control was lacking. In all these instances, the tests are considered as valid C-F tests as per the current test standard but clearly there were experimental issues which would not be evident if the stress-strain histories were not considered in any way during data analysis.

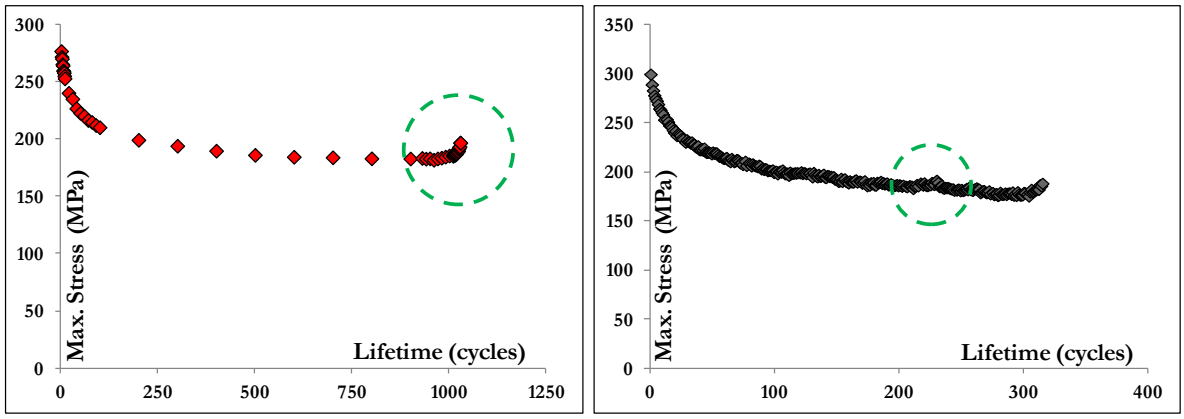

Figure 7.18. Unexpected spike(s) during C-F testing can occur for reasons varying from crack formation at regions outside gage length to imperfect machine control.

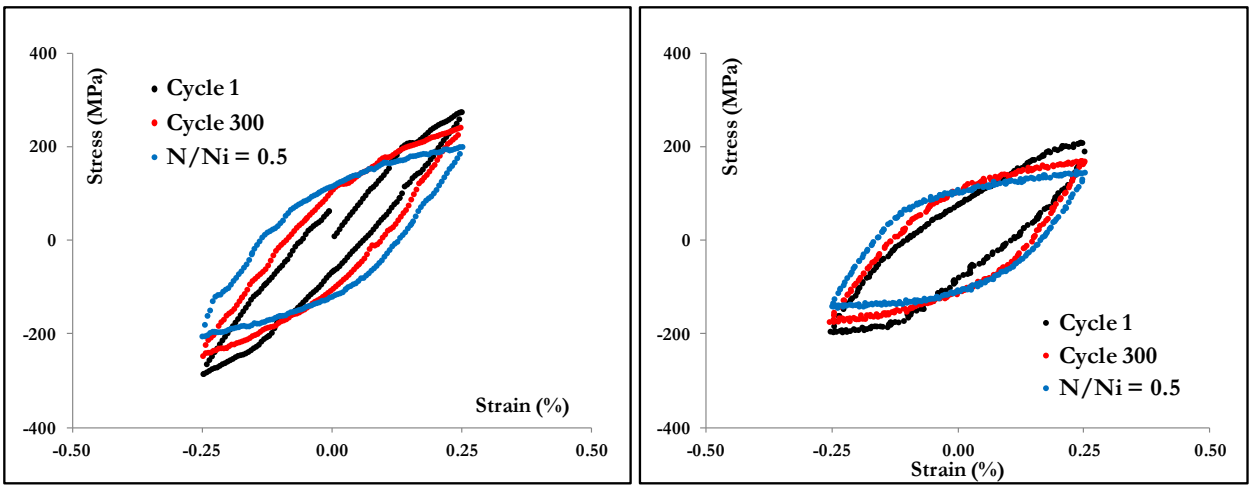

Figure 7.19. Although both these creep-fatigue tests are considered valid, one of the RR participants had imperfect control of strain during testing, whereas another participant had started the strain-controlled test at non-zero strain.

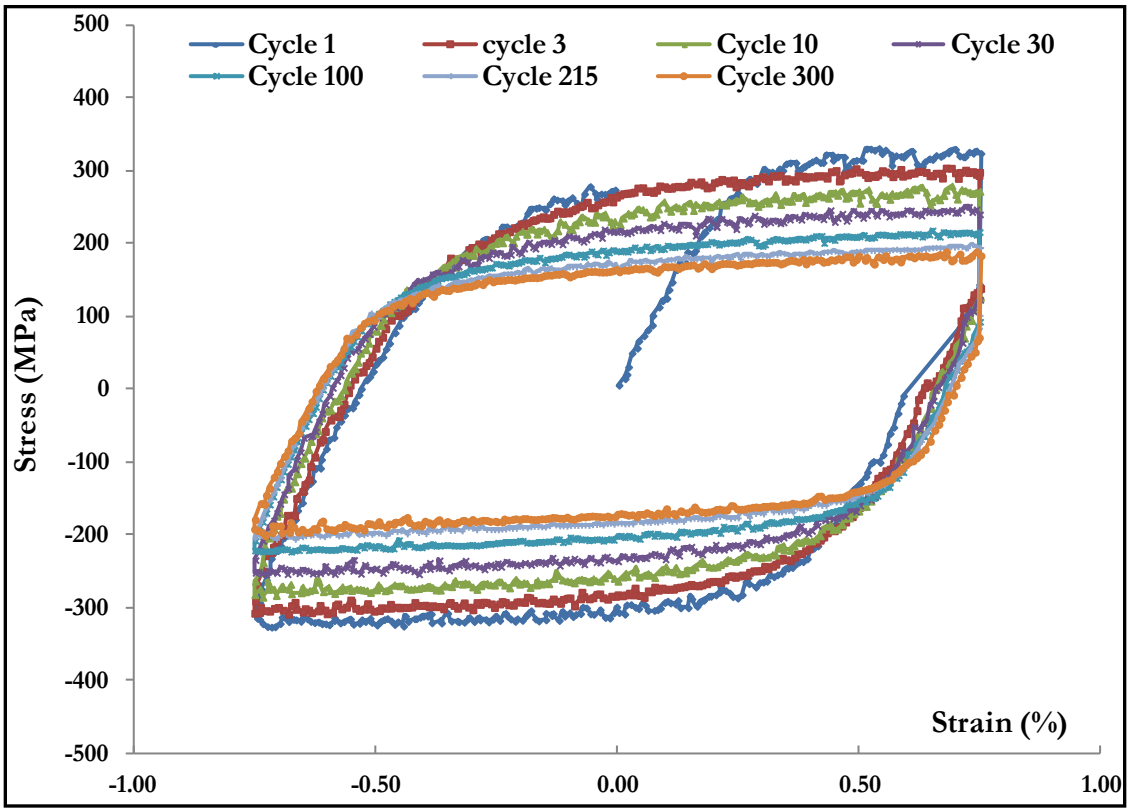

Figure 7.20. Evolution of stress-strain hysteresis loops shows the control of strain response during cyclic loading portion of the creep-fatigue test, with data as reported by one of the RR participants.

7.2. Constitutive modeling results

7.2.1. Creep deformation and rupture behavior

From the available creep deformation and rupture data for grade P91 steel, the modified LCSP model fitting constants obtained after Z optimization are provided in Table 7.6. The modified LCSP model, as expressed earlier in Equation (6.1), describes the whole creep curve *all* by itself, has only three fitting constants and therefore inherently has more robustness [**220**]. The strain versus time histories as predicted by this model are compared to experimental data in Figure 7.21 where it can be seen that the model successfully simulates the data at various stress levels. The creep curves corresponding to 101.5 MPa and 117.5 MPa stress levels are not compared in this figure to clearly show the model simulations under high stress levels. Since Z values are optimized till t^*, the transition from secondary creep regime II to tertiary creep regime III is not simulated well, especially when stress levels decrease. If this aspect of model simulation is deemed necessary, much more accurate simulations can be obtained by optimizing Z for times little less than t^* (say 90% of t^*). The scatter factor Z also provides a useful indication of a model's effectiveness [**346**] in this regard and for well-distributed, single-cast creep curve datasets, Z values of < 2 are desirable. With the modified LCSP model, maximum Z value of ~ 1.35 is achieved for all the simulations, indicating further the model's robustness. Figures 7.22(a) and (b) also demonstrate the fitting efficiency of this model when the degree of correlation is compared between predicted and measured creep rates. Since all the creep tests are performed at one temperature (*i.e.,*

Parameter	Value
$\boldsymbol{\beta}$	0.27
$\boldsymbol{p_0}$	-1.65
$\boldsymbol{p_1}$	-9.15
$\boldsymbol{p_2}$	2553.74
$\boldsymbol{C}$	6.8

Table 7.6. Modified LCSP model parameter values for grade P91 steel.

isothermal), the temperature capability of the chosen model however cannot be verified from the current data set.

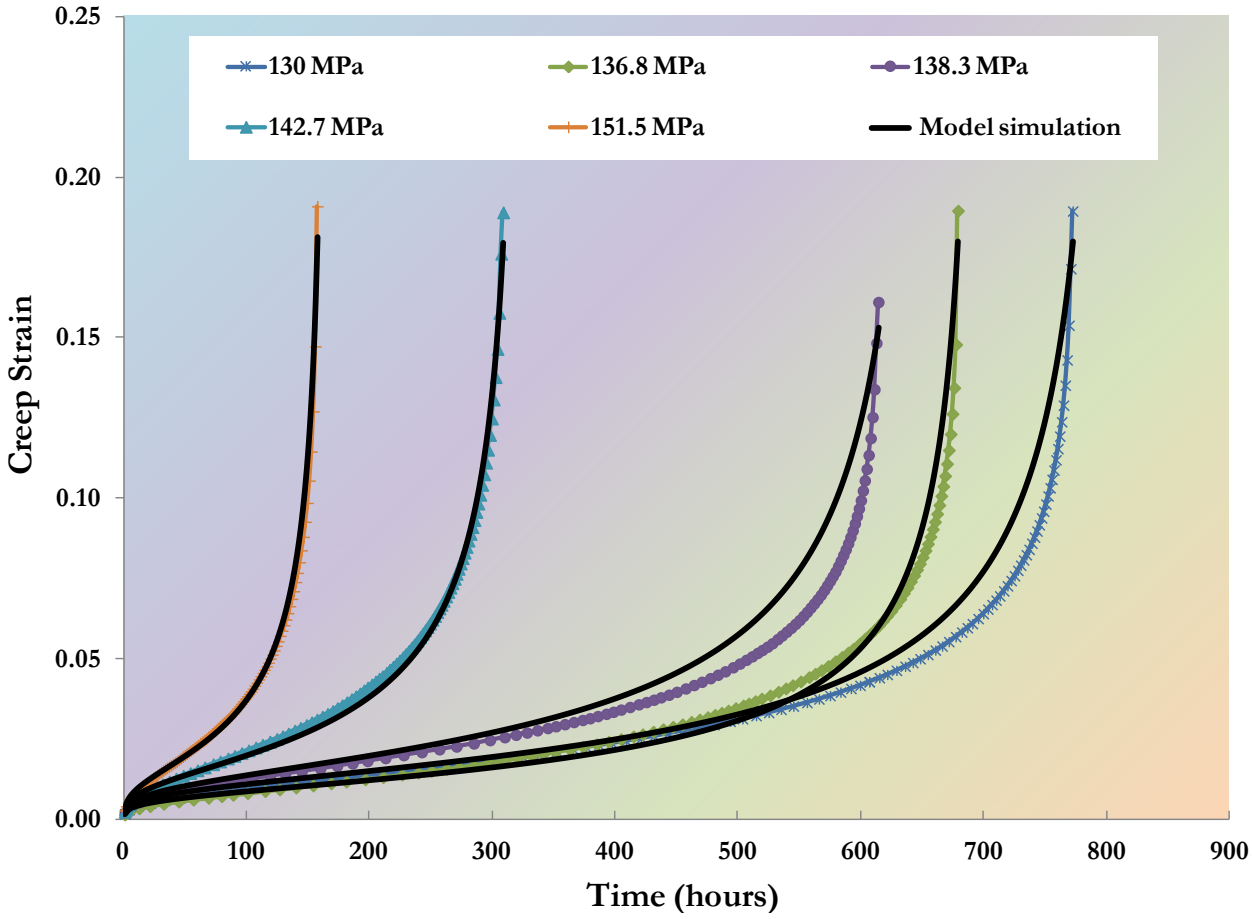

Figure 7.21. Isothermal creep deformation and rupture curves under high stress levels for grade P91 steel, with marker lines representing experimental data and continuous lines representing model simulations.

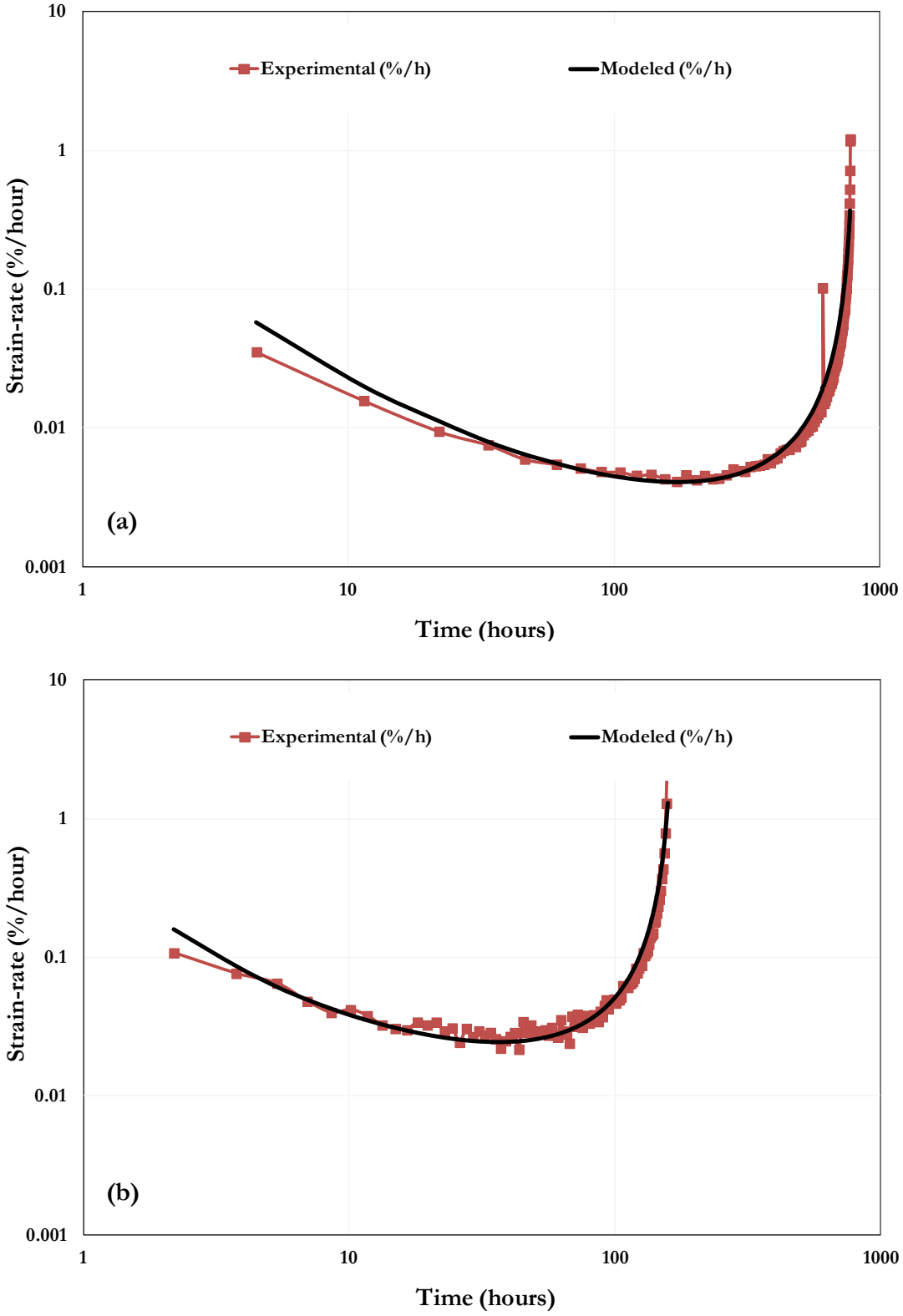

Figure 7.22. Predicted creep strain-rate by modified LCSP model for grade P91 steel as compared with that of experimental values for two different isothermal stress levels: (a) 130 MPa and (b) 151.5 MPa.

7.2.2. Monotonic tensile behavior

Experimental monotonic stress-strain data is best-fit with Equation (6.3) to obtain the optimized model indices by Z minimization. Table 7.7 provides the value of the five different model indices for the two different tests along with the scatter factor values for each test. As discussed earlier, indices A and b do not vary with the nature of loading or the microstructural variability of nominally homogeneous test specimens. Since index f quantifies the localized thermal response during loading/unloading, it is not expected to vary for tests that involve just monotonic loading. Hence these three indices are maintained the same for both the test simulations (see Table 7.7). But, indices a and c inherently characterize the plasticity response at the macroscopic and localized level, respectively and hence are expected to vary for every test specimen. The scatter factors indicate very minimal scatter for the simulation results as compared with their experimental counterparts and also allude to the robustness of the formulated constitutive relation. Figure 7.23 shows the goodness of fit between the experimental and simulated stress-strain curves for the tensile test at 24°C using the model indices listed in Table 7.7. It is noted that these curves are plotted only until σ_{UTS}, the proposed model's maximum point of applicability in a test record.

Table 7.7. Model indices and scatter factors obtained after Z minimization for the two uniaxial tensile tests conducted at a nominal strain-rate of 0.00192/s.

Test temperature (°C)	A	a ((1/s)^b)	b	c	f	Scatter factor, Z
24	7.95	0.033	0.111	0.00137	0.00033	1.067
625		0.037		0.00078		1.131

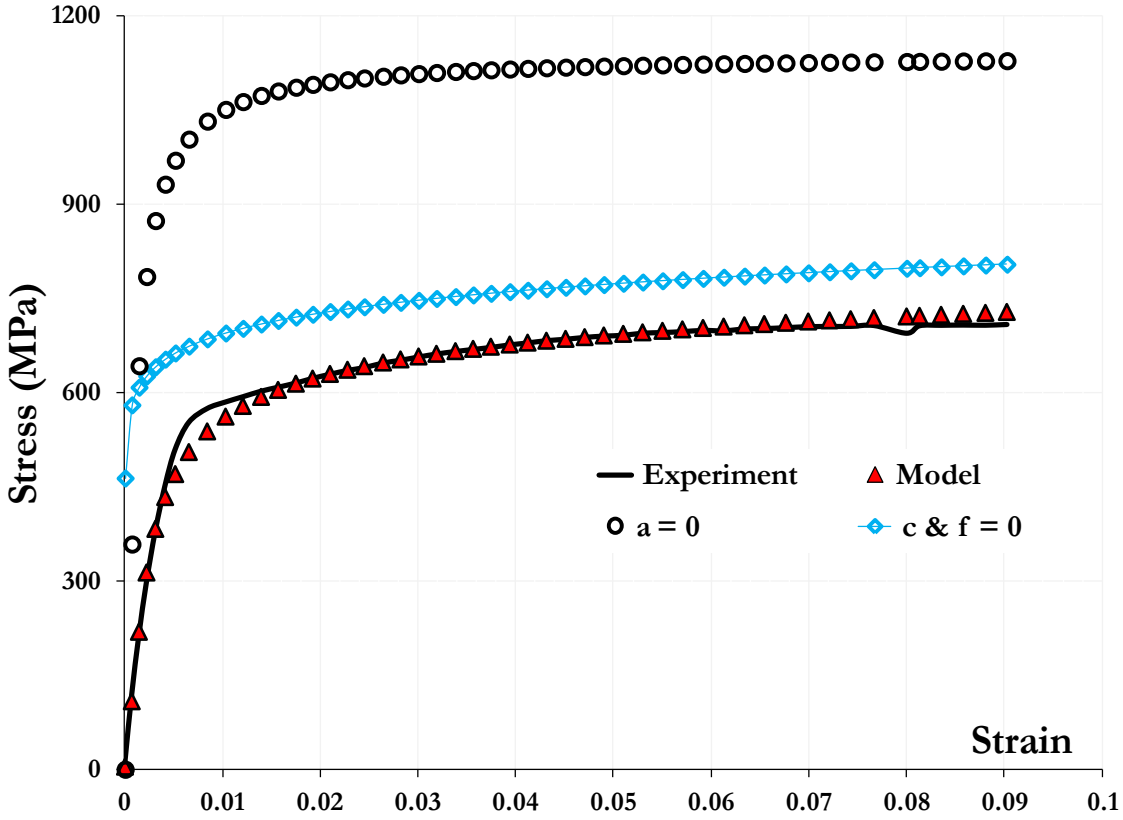

Figure 7.23. Experimental stress-strain curve of grade P91 steel obtained from a monotonic tensile test (24°C, nominal strain-rate of 0.00192/s) compared with model simulations using indices listed in Table 7.7. Two different curves ($a = 0$, and c and $f = 0$) have also been plotted to show the effect of not including macroscopic and localized plasticity effects, respectively.

Figure 7.23 also shows stress-strain curves generated if the localized plasticity effect is neglected by assuming (c and $f = 0$) or if the macroscopic plasticity effect is neglected ($a = 0$) while retaining the other model indices for 24°C. In the former case, assuming *complete* absence of short-range dislocation effects, higher stresses are required to nucleate/depin long-range dislocations but once they are active, macroscopic work-hardening becomes significant even at relatively low stresses. In the second case, assuming *complete* absence of long-range dislocation effects, localized plasticity initiates instantaneously but global plasticity and work-hardening occur at comparatively higher

stresses and negligible strain-rates, respectively. These hypothetical figures also clearly show that only the cumulative interaction between these two dislocation densities tend to lower stresses within a material via plasticity.

7.2.2.1. Predictive capabilities

As per the proposed mechanism, crystal plasticity under any loading condition can be effectively described by considering the two dislocation densities and their cumulative interactions. In this regard, the predictive capabilities of the proposed model are checked under different "virtual monotonic tensile testing" conditions (see Figures 7.24(a)-(c)). These illustrative plots are obtained by employing the stress values – $\sigma_{0.1\%\varepsilon}$and σ_{UTS}– and model indices from the tensile tests conducted at 24°C and 625°C only and the other test parameters are varied accordingly for each of these virtual tests. Since grade P91 steel is primarily intended for elevated temperature applications, most of the published literature deals exclusively with their deformation response under creep and/or fatigue loading conditions. Due to this reason, it is not possible to quantitatively compare all of the plots with existing literature and hence the exercise is meant only to qualitatively demonstrate the model's predictive capability.

Figure 7.24(a) shows the predicted variation of stress to 0.2% and 1% strain, and to UTS at temperatures varying from 273 to 900 K at a nominal strain-rate of 0.00192/s. The plotted curves are compared with experimental data obtained from the metallic material database Kinzoku, a section of Japanese National Institute for Materials Science (NIMS) database. The predicted and experimental UTS curves compare well with each other except at intermediate temperatures where modified P91 steel is shown to exhibit significant softening due to dynamic strain ageing effects [**347**, **348**]. A good correlation trend can also be observed between experimental offset yield strength

(YS) and modeled (to 1% strain) curves in this figure. It is assumed that 1% strain mostly matches with the strain at macroscopic yielding for modified P91 steel except at temperatures above 800 K. Predictions made to 0.2% strain is not compared due to lack of experimental data for this particular condition, although the trend observed is in qualitative agreement with empirical observations.

Strain-rate sensitivity plots are often used to validate the robustness of a constitutive relation's – particularly a single-expression's – robustness [**338**]. Therefore, Figure 7.24(b) shows the variation of UTS as a function of nominal strain-rates (of 8 decades) predicted at the two test temperatures. Experimental data from published literature at 585 K is also presented in this figure to qualitatively compare similar trends for modified P91 steel [**349**]. To the author's knowledge, this is the *first* time that a single-expression constitutive relation has shown such wide-range predictive capabilities in simulating a complex trend (smooth, gradual progression from negative to positive strain-rate sensitivity) for any material. It can also be observed that the curves are not extended for very high strain-rates due to lack of experimental data to corroborate the predictions.

Figure 7.24(c) shows engineering stress-strain curves predicted for four temperatures at a nominal strain-rate of 0.00192/s up until UTS values. The inset shows a magnified trend of the stress-strain behavior at very low strains. Experimental stress-strain curves do exist for modified P91 steel [**348**, **349**] but with different chemical compositions and hence not compared in this figure. All of these predictions fall in the range of expected behavior once again demonstrating the potential capabilities of the model.

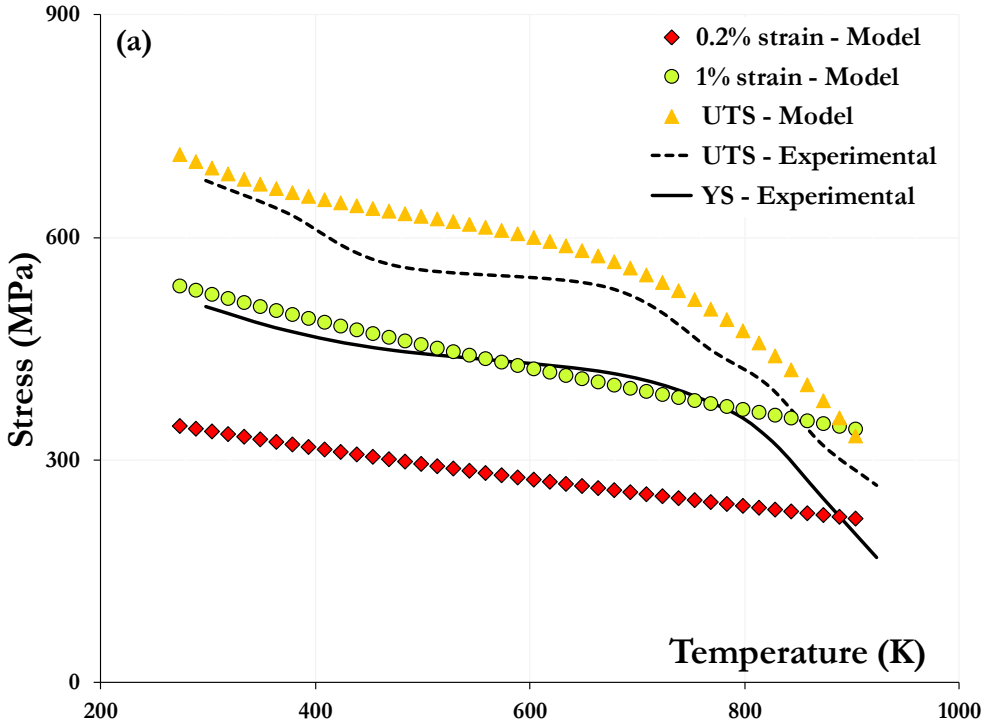
(a)
0.2% strain - Model
1% strain - Model
UTS - Model
UTS - Experimental
YS - Experimental
Stress (MPa)
Temperature (K)
900
600
300
0
200
400
600
800
1000

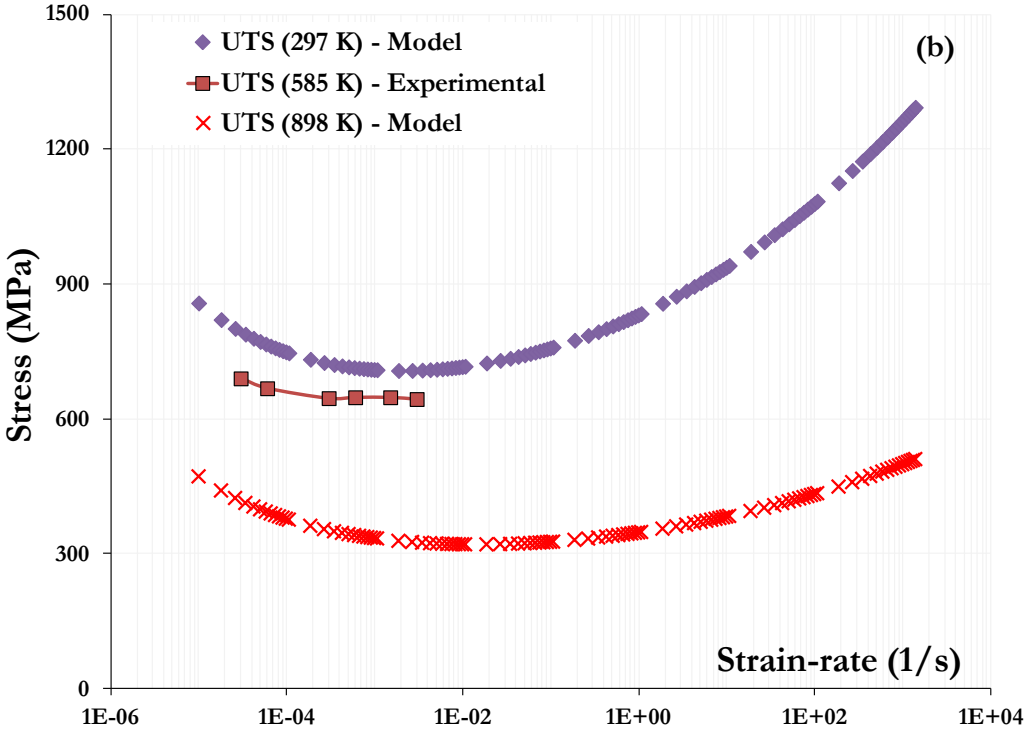
(b)
UTS (297 K) - Model
UTS (585 K) - Experimental
UTS (898 K) - Model
Stress (MPa)
Strain-rate (1/s)
1500
1200
900
600
300
0
1E-06
1E-04
1E-02
1E+00
1E+02
1E+04

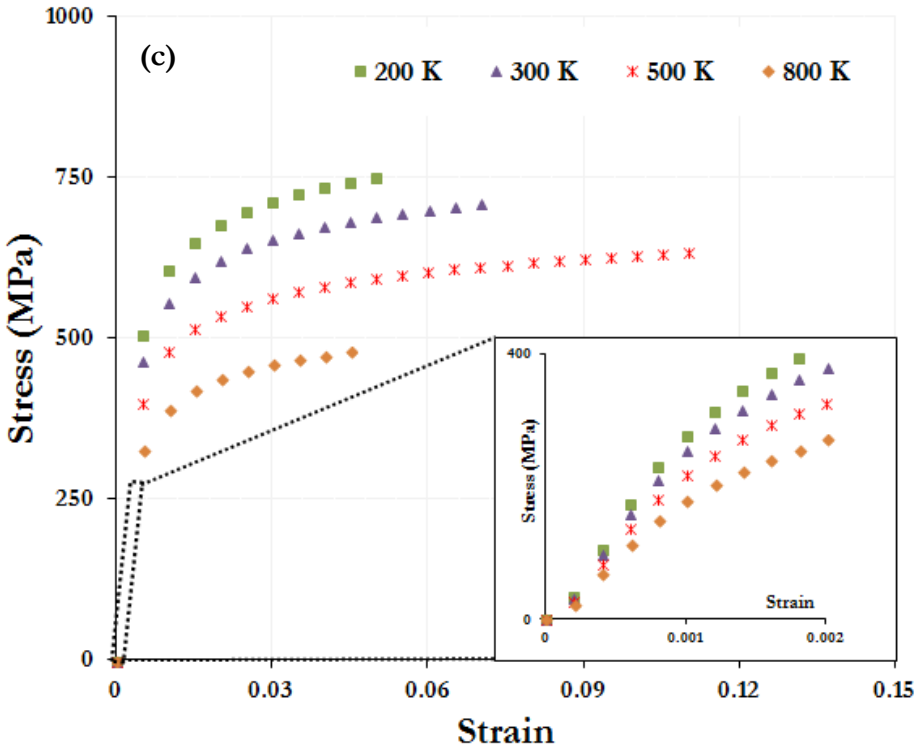

Figure 7.24. Qualitative demonstration of predictive capabilities of the formulated constitutive relation for grade P91 steel: (a) stress vs. temperature (b) stress vs. nominal strain-rate at two different temperatures and (c) stress vs. strain at different temperatures with the inset showing a more detailed variation until 0.2% total strain.

7.2.3. Low cycle fatigue behavior

7.2.3.1. Parameter identification for cyclic loading components

The cyclic stress-strain loading data, obtained after executing the protocol for strain offset, is best-fit with Equations (6.5) and (6.6) for each cycle to adjust the values of the evolutionary indices a and c by Z minimization. If the first loading cycle starts at zero strain and continues under tension, the cyclic stress-strain data after strain offset will consist of an additional tensile loading component that can also be fit using Equation (6.5). This routine is initially performed only for the lower strain amplitude data ($\pm$ 0.25% and $\pm$ 0.5%) to identify the evolution trends for indices a and

c. On careful analysis of the experimental data, it is observed that inelastic strain accumulated at both these strain amplitudes exhibits a power-law relationship with loading cycles (see Figure 7.25(a)). The coefficient of regression (R^2) of such a fit for each of these 4 tests varies between 0.9699 and 0.9962. The power-law coefficient $(\varepsilon_{\text{in}})_0$ and exponent m quantify the inelastic strain accumulated after the first loading cycle ($N = 1$) and its increment per additional cycle, respectively. Although exponent m is ideally expected to be equal for a given strain amplitude, slight variations are obtained in practice due to inherent differences in specimen microstructure and possible variations in the test conditions (refer Table 7.8). As expected, the macroscopic plasticity index a also demonstrates a power-law relationship with loading cycles similar to that of macroscopic plasticity (see Figures 7.25(b) and (c)). The power-law coefficient a_0 is indicative of macroscopic plasticity induced in the material after the first cycle ($N = 1$) and exponent n quantifies the incremental evolutionary characteristics during each loading cycle. Table 7.8 provides the numerical quantities for both these parameters for tests numbered 1 to 4. It is clearly seen that macroscopic plasticity characteristics also vary quantitatively even for experiments conducted under identical testing conditions, although the behavioral trends are in perfect qualitative accord. It is further noticed that the localized plasticity index c exhibits a logarithmic dependence on loading cycles (see Figures 7.25(b) and (c)). The constant c_0 and logarithmic coefficient p correspond to the interaction between short-range dislocations at the start of loading ($N = 1$) and increments per loading cycle, respectively. Table 7.8 also provides the numerical values of the index c for tests numbered 1 to 4, along with the maximum Z value obtained after minimization for *any* loading cycle of a given test. The robustness of the constitutive relation in predicting cyclic loading data is hereby clearly illustrated with minimal scatter indicated by these maximum Z values.

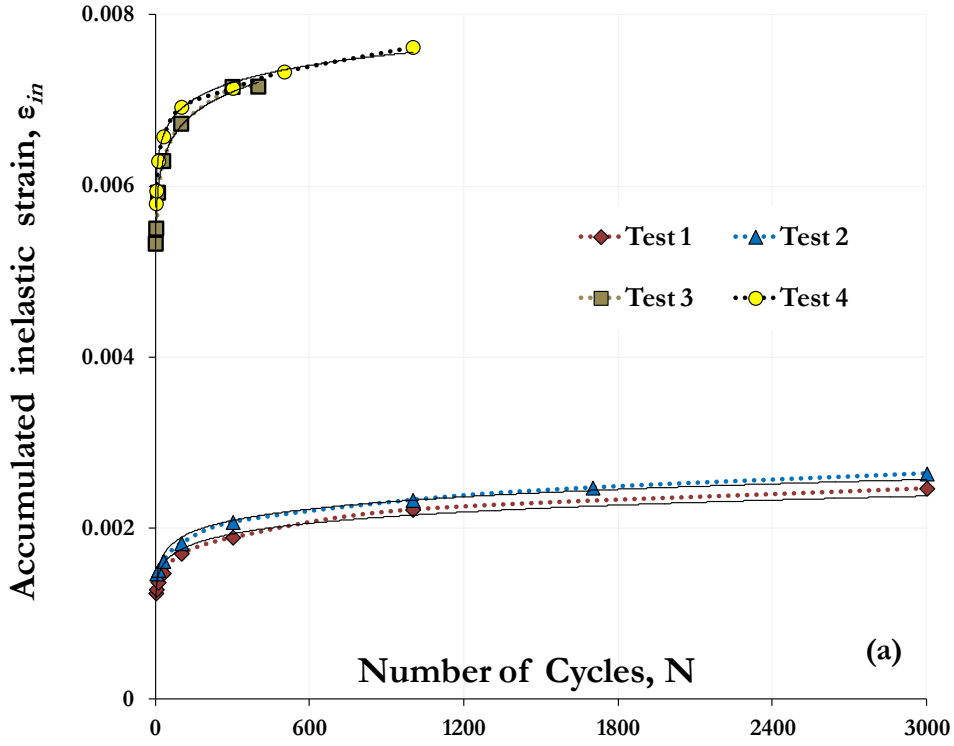
Accumulated inelastic strain, ε_{in}
0.008
0.006
0.004
0.002
0
Test 1
Test 2
Test 3
Test 4
Number of Cycles, N
(a)
0
600
1200
1800
2400
3000

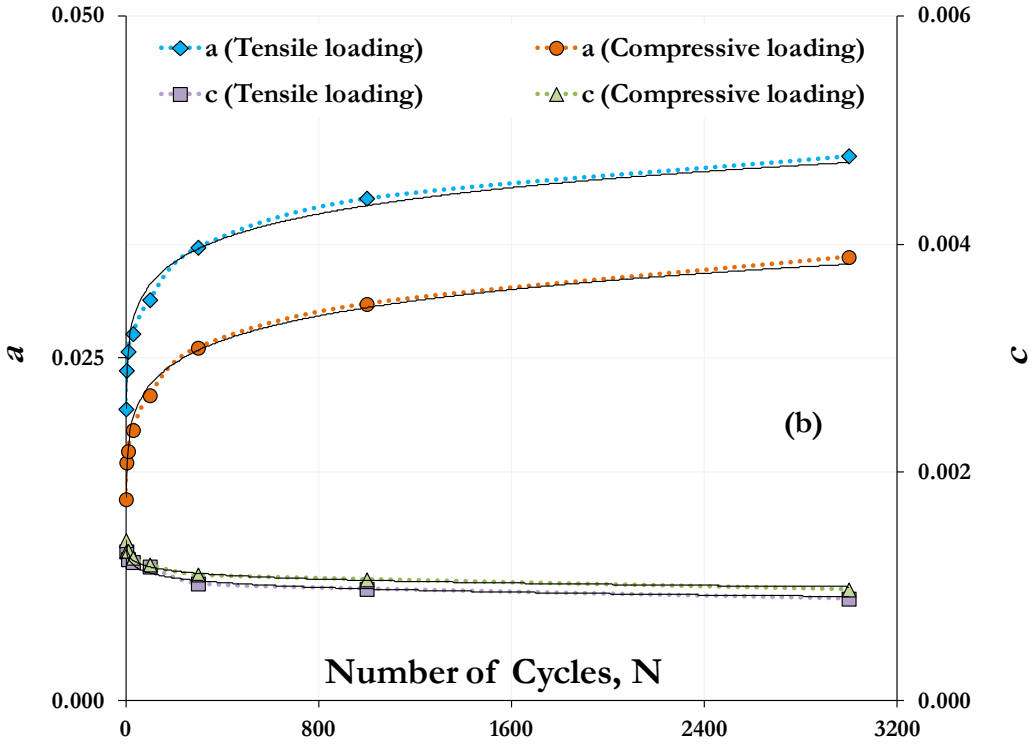
a
c
0.050
0.025
0.000
0.006
0.004
0.002
0.000
a (Tensile loading)
a (Compressive loading)
c (Tensile loading)
c (Compressive loading)
(b)
Number of Cycles, N
0
800
1600
2400
3200

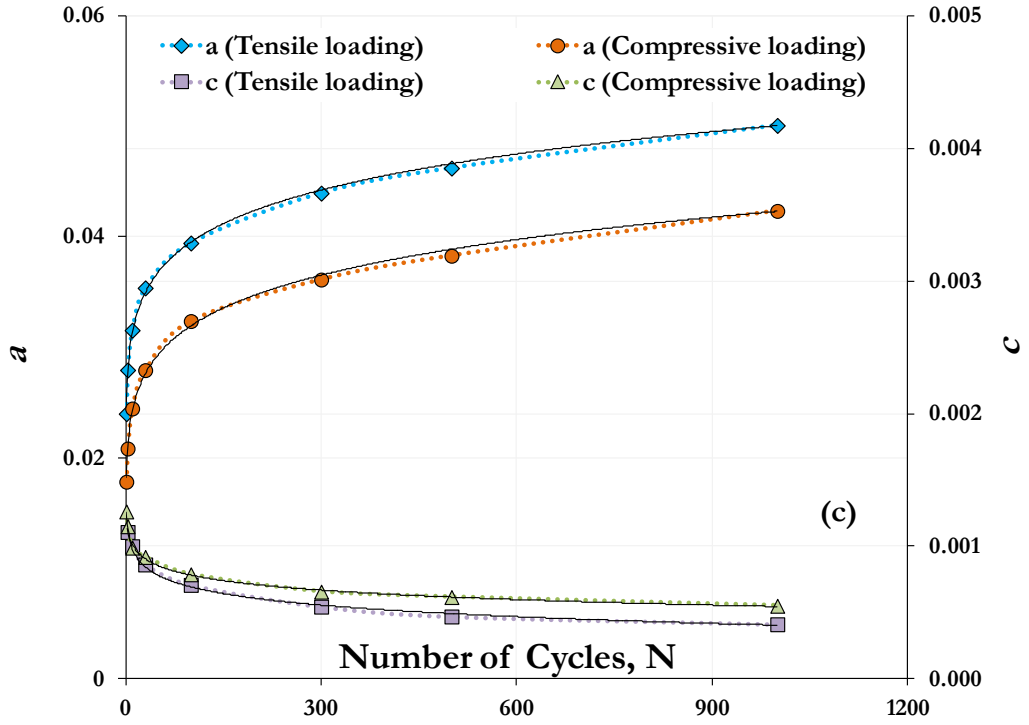

Figure 7.25. Relationship between accumulated inelastic strain, evolutionary indices a and c, and the number of loading cycles N is presented for the 4 LCF tests under consideration (a) and for Test 1 (b) and Test 4 (c). The continuous black line in all the plots refers to the trendline for the involved relationship.

Table 7.8. Accumulated inelastic strain and evolutionary indices identified for tensile and compressive loading components for any LCF cycle N where N = 1, 2,…..till failure. The maximum scatter factor obtained after minimization for a given test is also provided.

Test number	Accumulated inelastic strain, ε_{in} $(\varepsilon_{in})_N = (\varepsilon_{in})_0 . N^m$	Tensile loading		Compressive loading		Max. Z
		a $a_N = a_0 . N^n$	c $c_N = c_0 + p . ln(N)$	a $a_N = a_0 . N^n$	c $c_N = c_0 + p . ln(N)$	
1	$(\varepsilon_{in})_0$: 0.001158 m : 0.089730	a_0: 0.0214 n : 0.0761	c_0: 0.001395 p : -0.000060	a_0: 0.0148 n : 0.0958	c_0: 0.001407 p : -0.000051	1.090
2	$(\varepsilon_{in})_0$: 0.001249 m : 0.090054	a_0: 0.0143 n : 0.1142	c_0: 0.001450 p : -0.000082	a_0: 0.0155 n : 0.1071	c_0: 0.001401 p : -0.000072	1.067
3	$(\varepsilon_{in})_0$: 0.005264 m : 0.052517	a_0: 0.0271 n : 0.0953	c_0: 0.001407 p : -0.000135	a_0: 0.0138 n : 0.1517	c_0: 0.001485 p : -0.000124	1.085
4	$(\varepsilon_{in})_0$: 0.005748 m : 0.039719	a_0: 0.0246 n : 0.1029	c_0: 0.001271 p : -0.000126	a_0: 0.0182 n : 0.1222	c_0: 0.001256 p : -0.000103	1.100

Increasing values of macroscopic plasticity index a with LCF cycles indicate that the frequency of long-range dislocation avalanches increases with loading cycles. It also corresponds to the fact that long-range dislocation densities tend to gradually decrease from their initial values and consequently, the material is cyclically losing its strength. Decreasing values of localized plasticity index c with LCF cycles indicate that the expansion of CIZs into adjacent or nearby CPZs is gradually increasing and correlates to decreasing backstresses within CPZ interiors. It also corresponds to the fact that CIZs – like lath/subgrain boundaries, precipitate-matrix interfaces – gradually coarsen with LCF loading.

7.2.3.2. Parameter identification for cyclic unloading components

Since localized material response is always structural (or mechanical) and vibrational (or thermal), both the indices c and f are gradually adjusted for both the unloading components. Both the indices exhibit a logarithmic relationship with loading cycles N and their evolution is almost identical for both tensile and compressive unloading at a given strain amplitude (see Figures 7.26(a) and (b)). The index f noticeably changes its sign from positive during loading to negative during unloading. This alludes to the observation that heat is locally absorbed during unloading in clear contrast to localized heat generation via plasticity during loading. Moreover, the constants and logarithmic coefficients herein carry a description similar to their loading counterparts. Table 7.9 provides the numerical quantities of both these indices for tests numbered 1 to 4, along with the maximum Z values obtained after minimization. Although the maximum Z values for unloading data are still quite low, they are comparatively higher than cyclic loading component predictions.

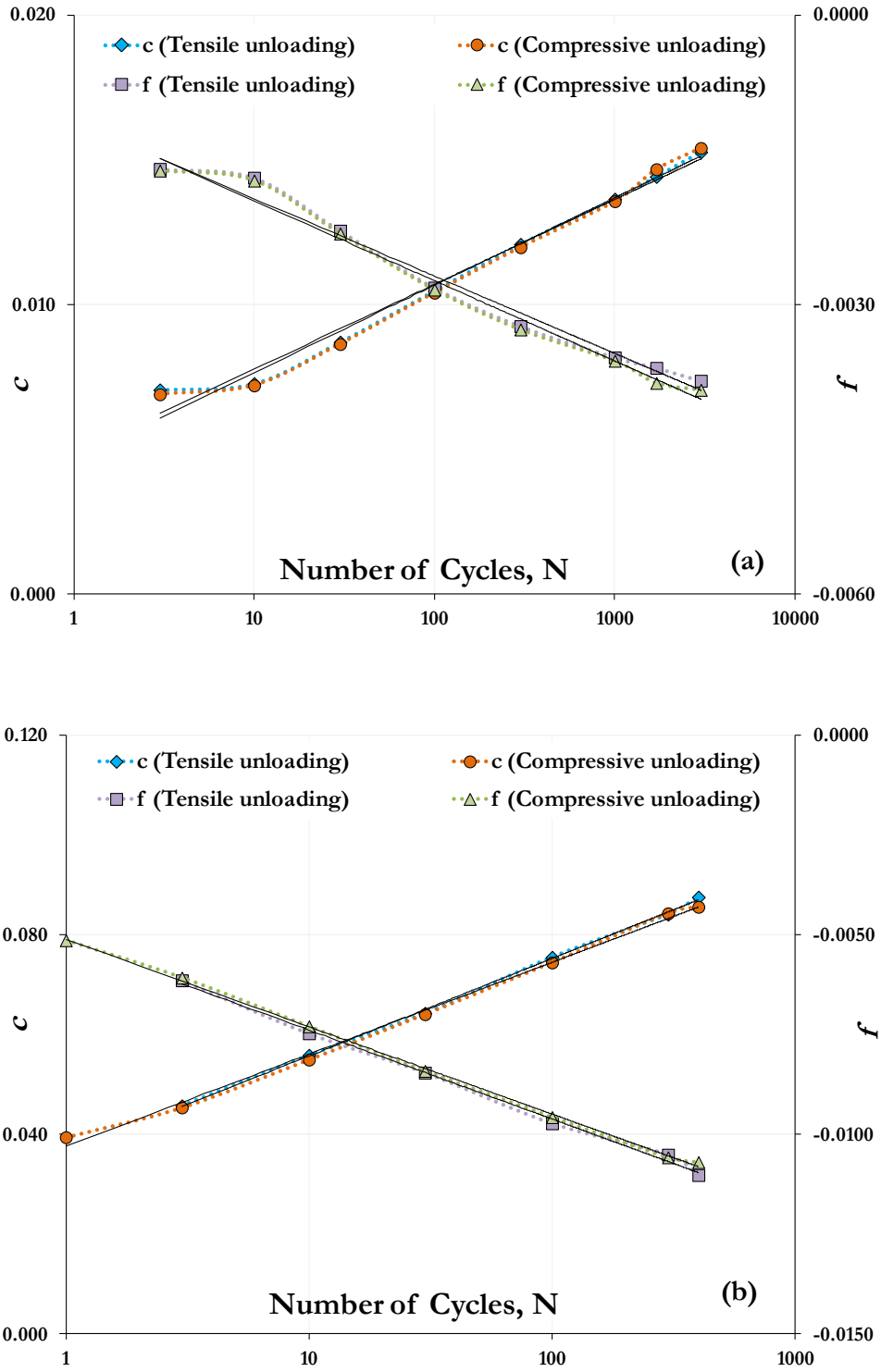

Figure 7.26. Relationship between the unloading evolutionary indices c and f, and the number of loading cycles N is presented for Test 2 (a) and Test 3 (b). The continuous black line in the plots refers to the trendline for the involved relationship.

Table 7.9. Evolutionary indices for the tensile and compressive unloading components for any LCF cycle N where N = 1, 2,…...till failure along with the maximum scatter factor obtained after minimization for a given test.

Test number	Tensile unloading		Compressive unloading		Max. Z
	c $c_N = c_0 + q.ln(N)$	f $f_N = f_0 + r.ln(N)$	c $c_N = c_0 + q.ln(N)$	f $f_N = f_0 + r.ln(N)$	
1	c_0: 0.0039 q : 0.0013	f_0: -0.00085 r : -0.00035	c_0: 0.0047 q : 0.0011	f_0: -0.00095 r : -0.00031	1.204
2	c_0: 0.0048 q : 0.0013	f_0: -0.00110 r : -0.00035	c_0: 0.0046 q : 0.0013	f_0: -0.00109 r : -0.00036	1.172
3	c_0: 0.0362 q : 0.0085	f_0: -0.00516 r : -0.00097	c_0: 0.0377 q : 0.0080	f_0: -0.00511 r : -0.00095	1.268
4	c_0: 0.0417 q : 0.0091	f_0: -0.00573 r : -0.00107	c_0: 0.0457 q : 0.0076	f_0: -0.00618 r : -0.00088	1.194

7.2.3.3. Simulation of hysteresis loops

The cyclic stress-strain data obtained after Z minimization, in the form of conventional hysteresis loops, for tests numbered 1 to 4 are compared and presented in Figures 7.27(a)-(d). Although perfectly symmetrical hysteresis loops are expected for LCF tests under zero mean strain, the evolutionary tendencies of inelastic strain along with indices a and c during loading and indices c and f during unloading indicate that slight deviations from this ideal behavior are expected (refer Tables 7.8 and 7.9). It is clearly observed that the general profile of the loops is accurately reproduced at different stages of LCF lives for all the lower strain amplitude tests. Most importantly, the loading components that involve work-hardening behavior are better replicated in comparison to unloading components for these different tests. Such robust predictions also lend more credence to the analytical formulation of the proposed constitutive model and the presumed underlying dislocation mechanics.

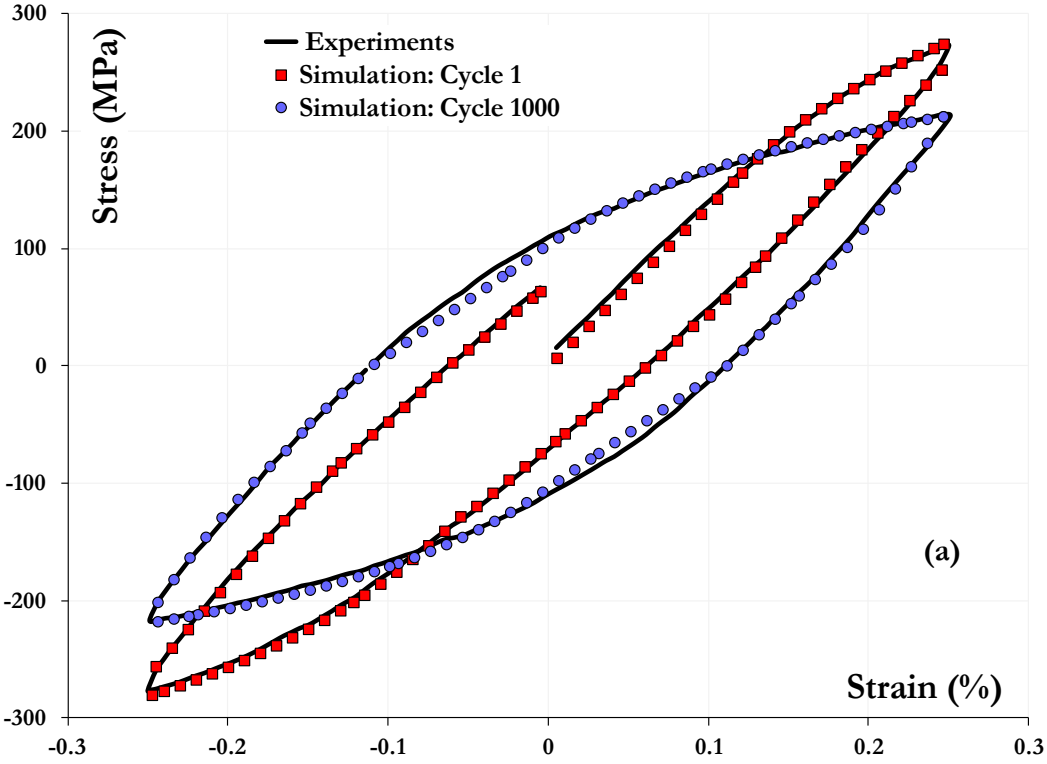
Experiments
Simulation: Cycle 1
Simulation: Cycle 1000
Stress (MPa)
Strain (%)
(a)
300
200
100
0
-100
-200
-300
-0.3
-0.2
-0.1
0
0.1
0.2
0.3

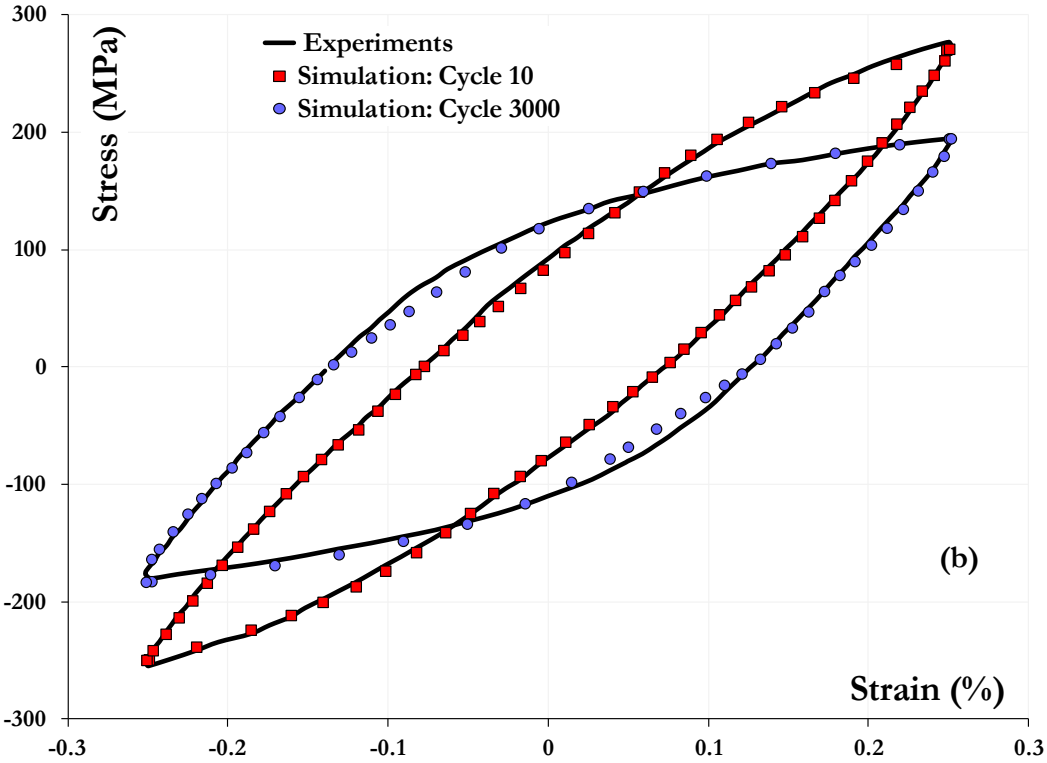
Experiments
Simulation: Cycle 10
Simulation: Cycle 3000
Stress (MPa)
Strain (%)
(b)
300
200
100
0
-100
-200
-300
-0.3
-0.2
-0.1
0
0.1
0.2
0.3

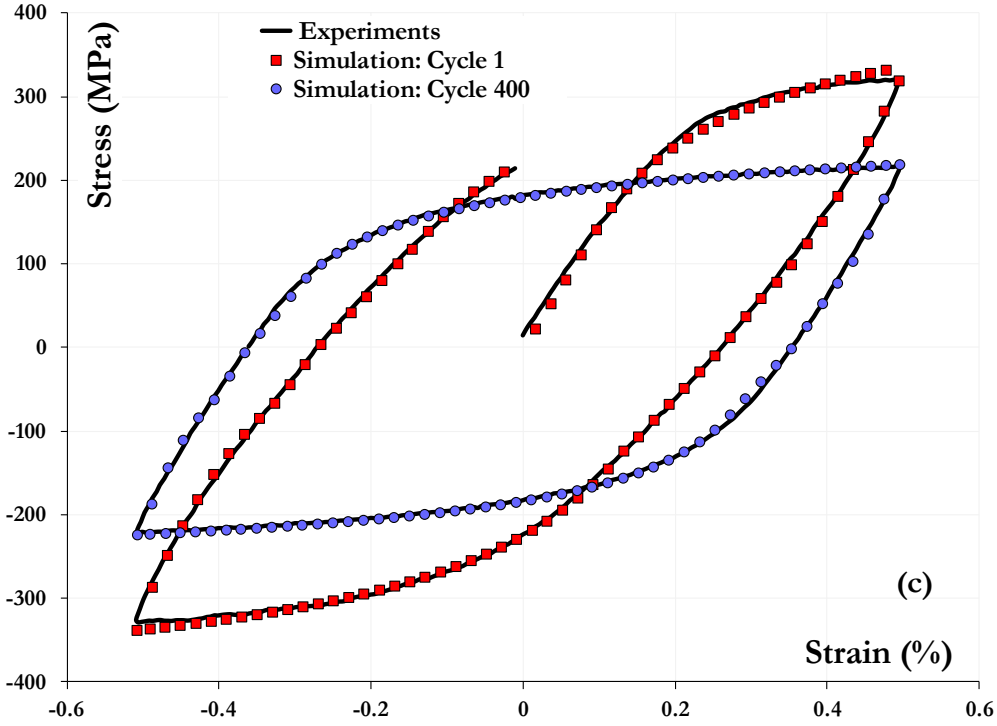

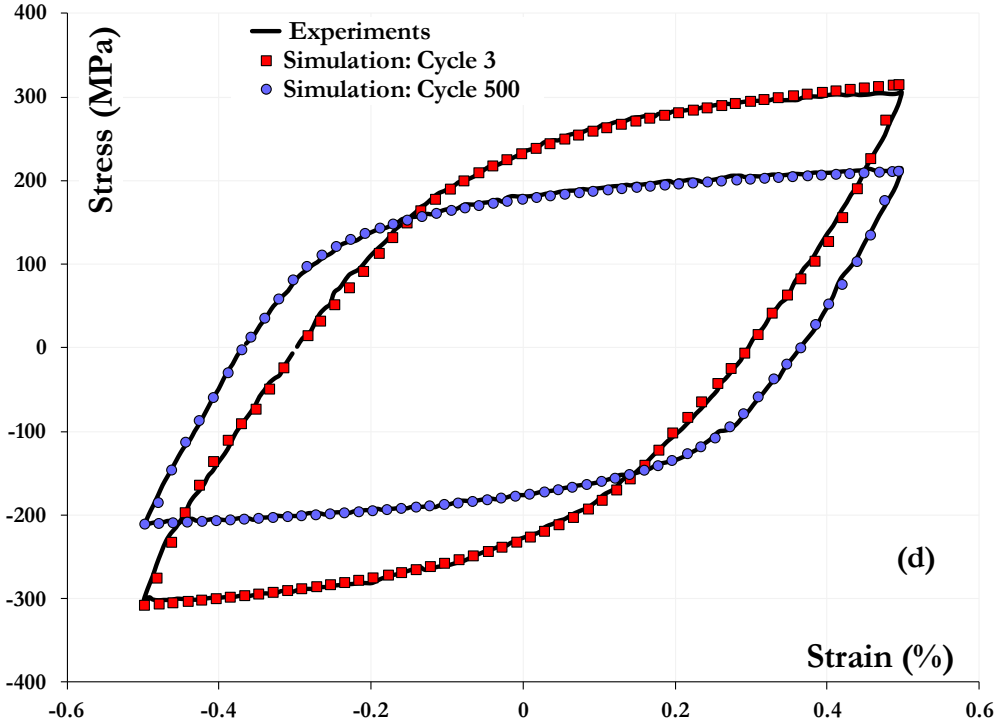

Figure 7.27. Comparison between the simulated (markers) and experimental (continuous) conventional hysteresis loops at different stages of the LCF life for (a) Test 1 ($\Delta\varepsilon = 0.5\%$), (b) Test 2 ($\Delta\varepsilon = 0.5\%$), (c) Test 3 ($\Delta\varepsilon = 1\%$) and (d) Test 4 ($\Delta\varepsilon = 1\%$).

7.2.3.4. Simulation of cyclic softening

The most prominent feature of grade P91 steels under LCF loading at elevated temperatures is its cyclic softening behavior. For this material, the absolute tensile (and compressive) peak stresses typically vary with loading cycles N in three different stages: a rapid rate of softening for the initial few cycles followed by gradual linear softening for a significant part of the LCF endurance after which the softening rate accelerates again as a consequence of macroscopic crack(s) formation. Figures 7.28(a) and (b) present both the experimental and simulated peak stress curves for two different lower strain amplitude tests. The model predictions closely represent the first two stages (till end-of-life) of the actual cyclic softening of grade P91 steels at 625°C. It can also be clearly seen that this effect does not depend on the applied strain amplitude, with higher strain amplitudes corresponding to a stronger degree of softening.

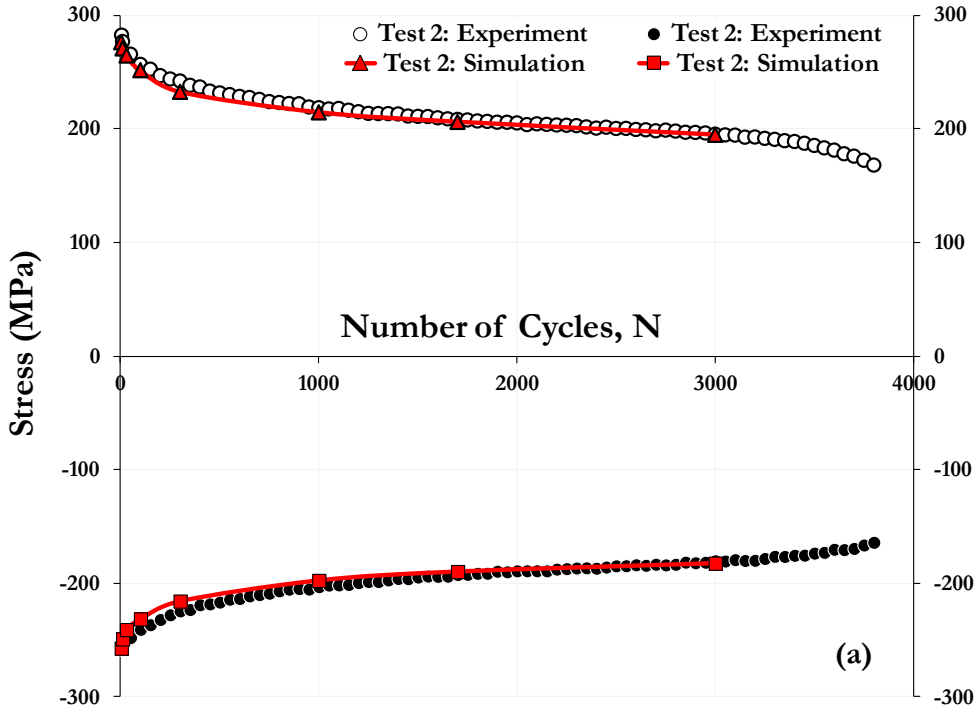

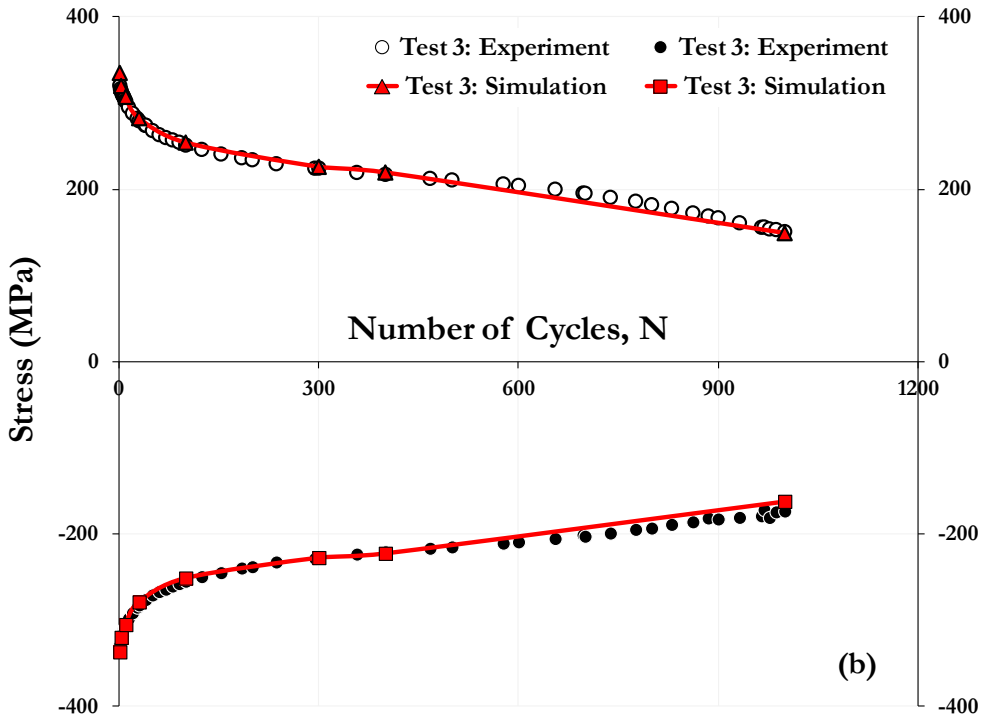

Figure 7.28. The simulated (continuous line with markers) and experimental (markers) variation of maximum (peak tensile) and minimum (peak compressive) stresses with loading cycles, N for (a) Test 2 ($\Delta\varepsilon = 0.5\%$) and (b) Test 3 ($\Delta\varepsilon = 1\%$).

The observed macroscopic cyclic softening correlates with an increasing frequency of discrete long-range dislocation avalanches (as indicated earlier by increasing a values) with each loading cycle. In a thermodynamic drive to minimize the internal energy of the crystal, long-range dislocation density tends to reduce significantly during these numerous long-range dislocation excursions. Depinned long-range dislocations can also get activated much faster at elevated temperatures due to the increased dynamic heterogeneity of short-range dislocations along crystallographically active and non-active slip systems. Localized plasticity concurrently involves gradual expansion or coarsening of the CIZs like subgrain/lath boundaries, grain boundaries and precipitate-matrix interfaces. Expansion of CIZs into CPZs also accordingly corresponds to a decrease in the backstresses within CPZs. All these observations can be collectively termed as

dynamic recovery of the material's microstructure in existing literature. All of these dynamic recovery phenomena are due to the evolution and cumulative interactions of both types of dislocation densities with LCF cycles.

7.2.3.5. Predictive capabilities

By conducting short-term laboratory experiments on a test material with accelerated test conditions, analytical predictions at a particular loading condition are typically made without considering the stochastic nature of microstructural variability. Since individual specimens of nominally homogeneous materials differ in the nature and spatial distribution of internal defects, they are certainly expected to provide scatter in test results even under identical test conditions (refer Table 6.1). Any extrapolation of experimental data without proper consideration of microstructural variability will tend to offer disparate predictions. The proposed constitutive relations (Equations (6.5) and (6.6)) greatly assist in this regard by minimizing the experimental data required for characterizing the microstructural LCF response of a particular specimen. If predictive accuracy can be sacrificed, mere averaging of model inputs from other accelerated tests at identical testing conditions can also be done by disregarding microstructural variability between test specimens.

Since the proposed plasticity mechanism (or shape of hysteresis loops) is rather generalized, the obtained evolutionary trends of the model indices for grade P91 steel are expected to be qualitatively similar for any material. A material can however cyclically harden or soften or exhibit a combination of both under certain LCF loading conditions. Accordingly, few laboratory experiments need to be performed for a test material to particularize these trends. Once the trends are established, the LCF deformation response of a particular specimen at any testing condition can be accurately predicted by cyclically loading it for just few cycles at that condition. For example, the

evolutionary trends of the various model indices for grade P91 steel are already identified in the current modeling effort for lower strain amplitudes at 625°C. It can be easily concluded that *only* the first 2 loading cycles are needed – to numerically identify the coefficients and exponents of the evolutionary indices – to accurately predict the LCF response of any grade P91 steel specimen for any strain amplitude at 625°C (see Tables 7.8 and 7.9). Although only 2 cycles are ideally required to identify the two unknown quantities for each evolutionary index, it is practically preferred to have the first 10 cycles of test data to maximize accuracy during modeling. Figures 7.29(a) and (b) show the comparison between experimental and simulated hysteresis loops of grade P91 steel for the two ± 0.75% strain amplitude tests 5 and 6, respectively. The simulation loops are obtained with model indices estimated from the first 10 cycles of experimental data only to account for microstructural variability of the test specimen in consideration. The robustness of the constitutive relations in predicting the LCF response with very minimal experimental data is again clearly demonstrated.

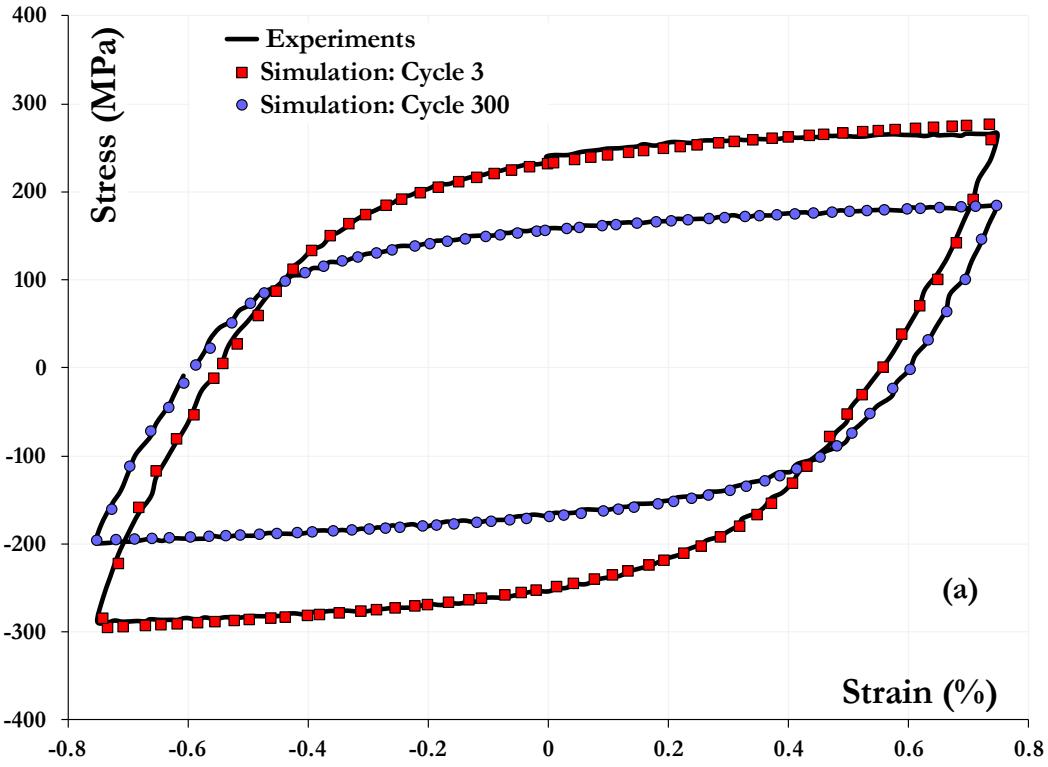

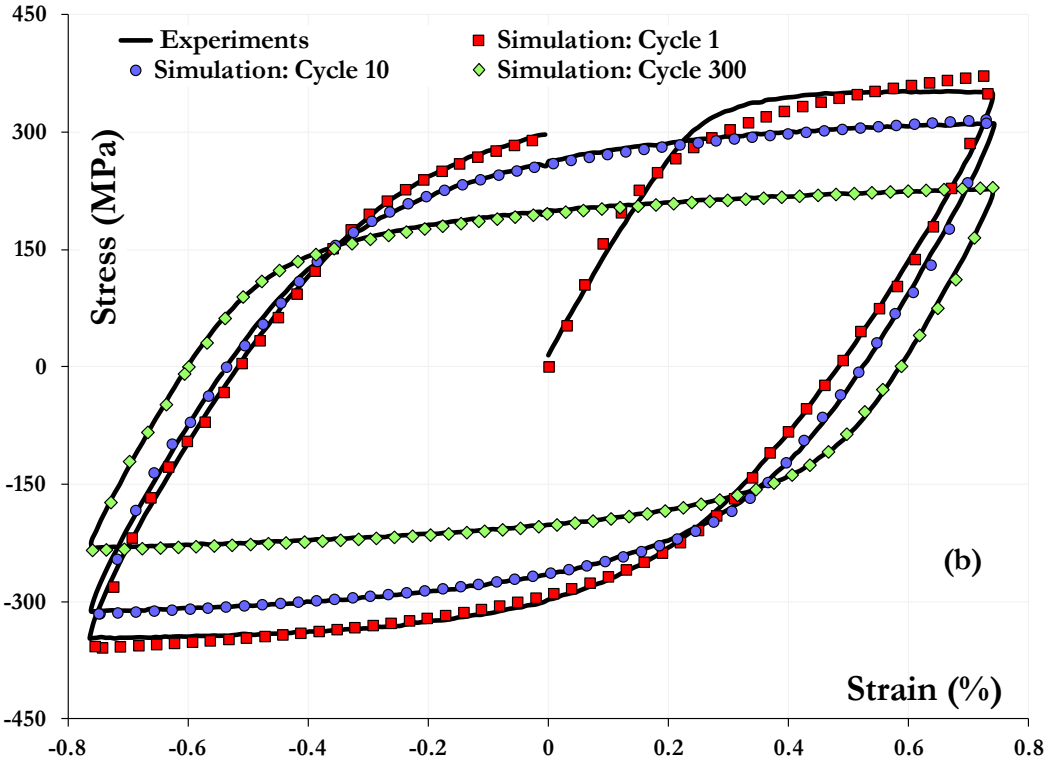

Figure 7.29. Comparison between the simulated (markers) and experimental (continuous) conventional hysteresis loops at different stages of the LCF life for (a) Test 5 ($\Delta\varepsilon = 1.5\%$) and (b) Test 6 ($\Delta\varepsilon = 1.5\%$).

When a macroscopic crack initiates on the test specimen's gage length, the system thereafter cannot be described as thermodynamically closed. In a physical sense, stresses can be relieved and consequently they do not uniquely correspond to the dislocation behavior within a material. Hence the formulated constitutive relations do not apply beyond macroscopic crack initiation in LCF test specimens. Due to the stochastic spatial distribution of defects within a material, the lifetime of a test specimen therefore cannot be predicted with this model alone. However, it can be combined with other life prediction approaches to aid in that regard.

7.2.4. Creep-fatigue behavior

From a qualitative perspective, the description of the various results as described in the previous section for LCF tests hold equally good for C-F results. Hence, to avoid repetition in this context, the results in this section will be supported by minimal text if they can be described using the same description(s) provided earlier for LCF behavior. Results that are unique to C-F behavior, however, are explained in detail in this section.

7.2.4.1. Parameter identification for cyclic loading components

The cyclic stress-strain loading data, obtained after executing the protocol for strain offset, is best-fit with Equations (6.5) and (6.6) for each cycle to adjust the values of the evolutionary indices a and c by Z minimization. If the first loading cycle starts at zero strain and continues under tension, the cyclic stress-strain data after strain offset will consist of an additional tensile loading component that can also be fit using Equation (6.5). This routine is initially performed only for the lower hold time tests (600 seconds) to identify the evolution trends for indices a and c. On careful analysis of the experimental data, it is observed that inelastic strain accumulated at both these strain amplitudes exhibits a power-law relationship with loading cycles (see Figure 7.30(a)). The coefficient of regression (R^2) of such a fit for each of these 4 tests varies between 0.9621 and 0.9925. As expected, the macroscopic plasticity index a also demonstrates a power-law relationship with loading cycles similar to that of macroscopic plasticity (see Figures 7.30(b) and (c)). Table 7.10 provides the numerical quantities for both these parameters for tests numbered 7 to 10. It is further noticed that the localized plasticity index c exhibits a logarithmic dependence on loading cycles (see Figures 7.30(b) and (c)). This table also provides the numerical values of the index c for tests numbered 7 to 10, along with the maximum Z value obtained after minimization for *any* loading

cycle of a given test. The robustness of the constitutive relation in predicting cyclic loading data is hereby clearly illustrated with minimal scatter indicated by these maximum Z values.

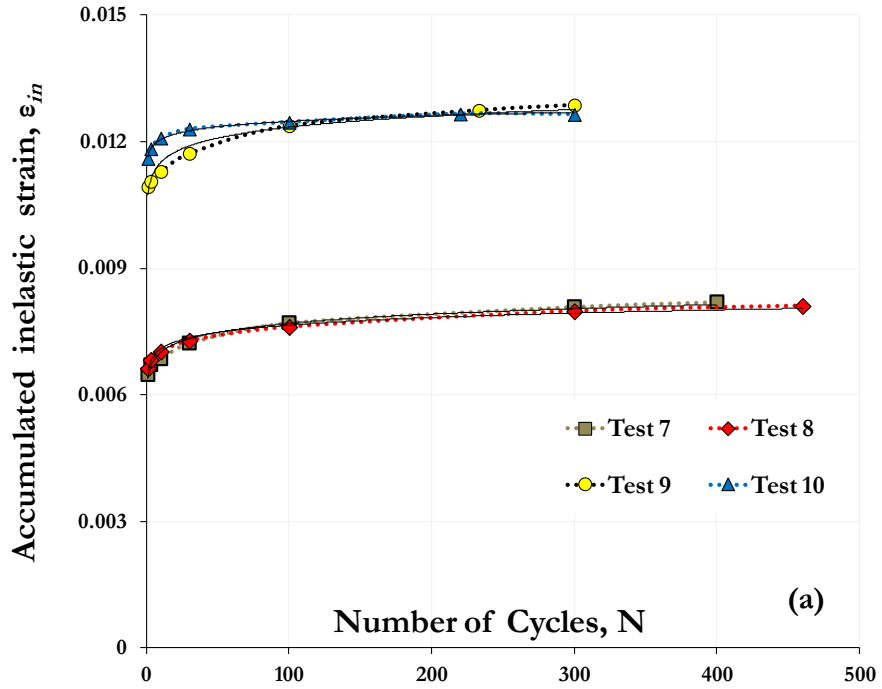

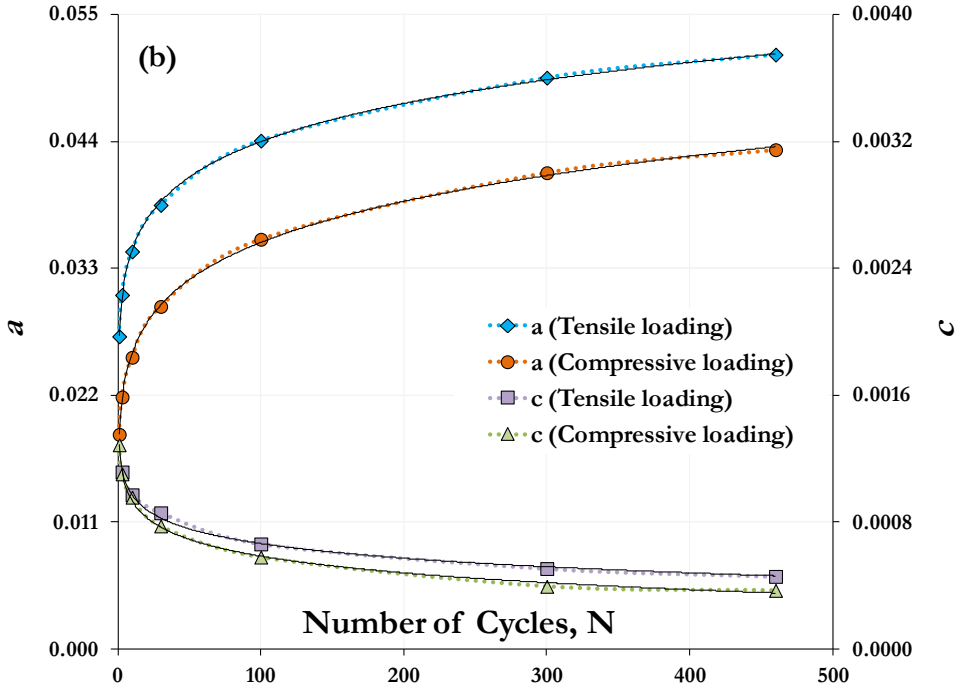

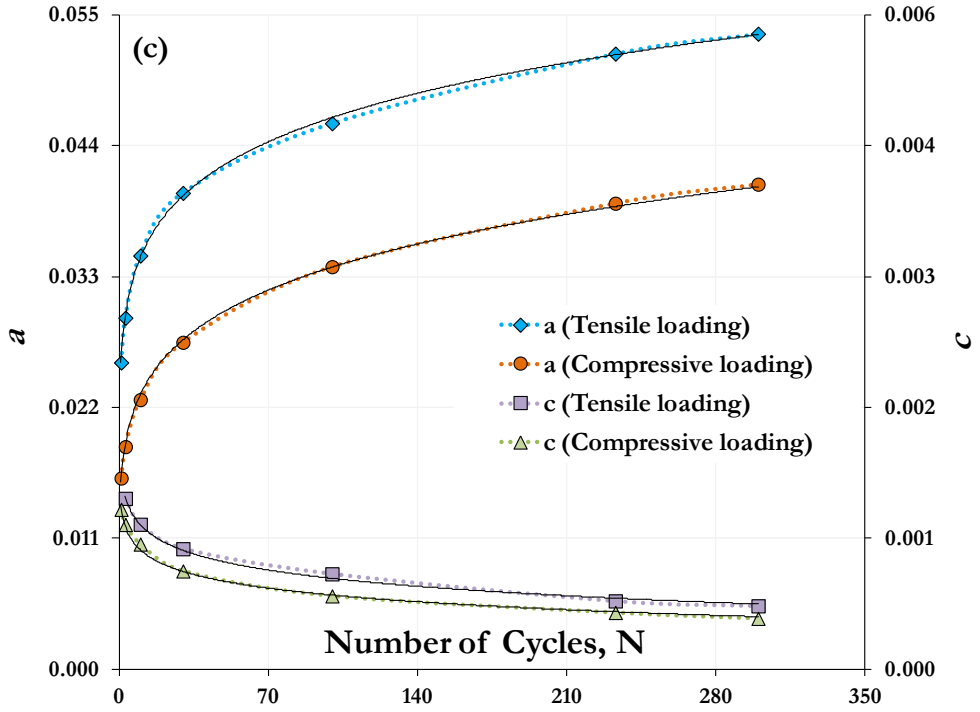

Figure 7.30. Relationship between accumulated inelastic strain, evolutionary indices a and c, and the number of loading cycles N is presented for the 4 C-F tests under consideration (a) and for Test 8 (b) and Test 9 (c). The continuous black line in all the plots refers to the trendline for the involved relationship.

Table 7.10. Accumulated inelastic strain and evolutionary indices identified for tensile and compressive loading components for any C-F cycle N where N = 1, 2,…..till failure. The maximum scatter factor obtained after minimization for a given test is also provided.

Test number	Accumulated inelastic strain, ε_{in} $(\varepsilon_{in})_N = (\varepsilon_{in})_0 . N^m$	Tensile loading		Compressive loading		Max. Z
		a $a_N = a_0 . N^n$	c $c_N = c_0 + p . ln(N)$	a $a_N = a_0 . N^n$	c $c_N = c_0 + p . ln(N)$	
7	$(\varepsilon_{in})_0$: 0.006385 m : 0.040428	a_0: 0.0261 n : 0.1199	c_0: 0.001525 p : -0.000155	a_0: 0.0102 n : 0.2153	c_0: 0.001656 p : -0.000202	1.099
8	$(\varepsilon_{in})_0$: 0.006567 m : 0.033178	a_0: 0.0272 n : 0.1047	c_0: 0.001279 p : -0.000133	a_0: 0.0186 n : 0.1388	c_0: 0.001287 p : -0.000152	1.075
9	$(\varepsilon_{in})_0$: 0.010732 m : 0.030381	a_0: 0.0258 n : 0.1273	c_0: 0.001670 p : -0.000197	a_0: 0.0158 n : 0.1659	c_0: 0.001385 p : -0.000165	1.065
10	$(\varepsilon_{in})_0$: 0.011638 m : 0.015232	a_0: 0.0286 n : 0.1098	c_0: 0.001109 p : -0.000088	a_0: 0.0218 n : 0.1307	c_0: 0.001034 p : -0.000108	1.079

Increasing values of macroscopic plasticity index a with C-F cycles indicate that the frequency of long-range dislocation avalanches increases with loading cycles. It also corresponds to the fact that long-range dislocation densities tend to gradually decrease from their initial values and consequently, the material is cyclically losing its strength. Decreasing values of localized plasticity index c with C-F cycles indicate that the expansion of CIZs into adjacent or nearby CPZs is gradually increasing and correlates to decreasing backstresses within CPZ interiors. It also corresponds to the fact that CIZs – like lath/subgrain boundaries, precipitate-matrix interfaces – gradually coarsen with C-F loading.

7.2.4.2. Parameter identification for cyclic unloading components

Since localized material response is always structural (or mechanical) and vibrational (or thermal), both the indices c and f are gradually adjusted for both the unloading components. Both the indices exhibit a logarithmic relationship with loading cycles N but their evolution is not identical (compared with LCF behavior) for both tensile and compressive unloading at a given strain amplitude (see Figures 7.31(a) and (b)). This might be due to the total inelastic strain accumulated and/or influence of environmental oxidation during the hold time that immediately precedes tensile unloading. The index f noticeably changes its sign from positive during loading to negative during unloading. This alludes to the observation that heat is locally absorbed during unloading in clear contrast to localized heat generation via plasticity during loading. Table 7.11 provides the numerical quantities of both these indices for tests numbered 7 to 10, along with the maximum Z values obtained after minimization. Although the maximum Z values for unloading data are still quite low, they are comparatively higher than cyclic loading component predictions.

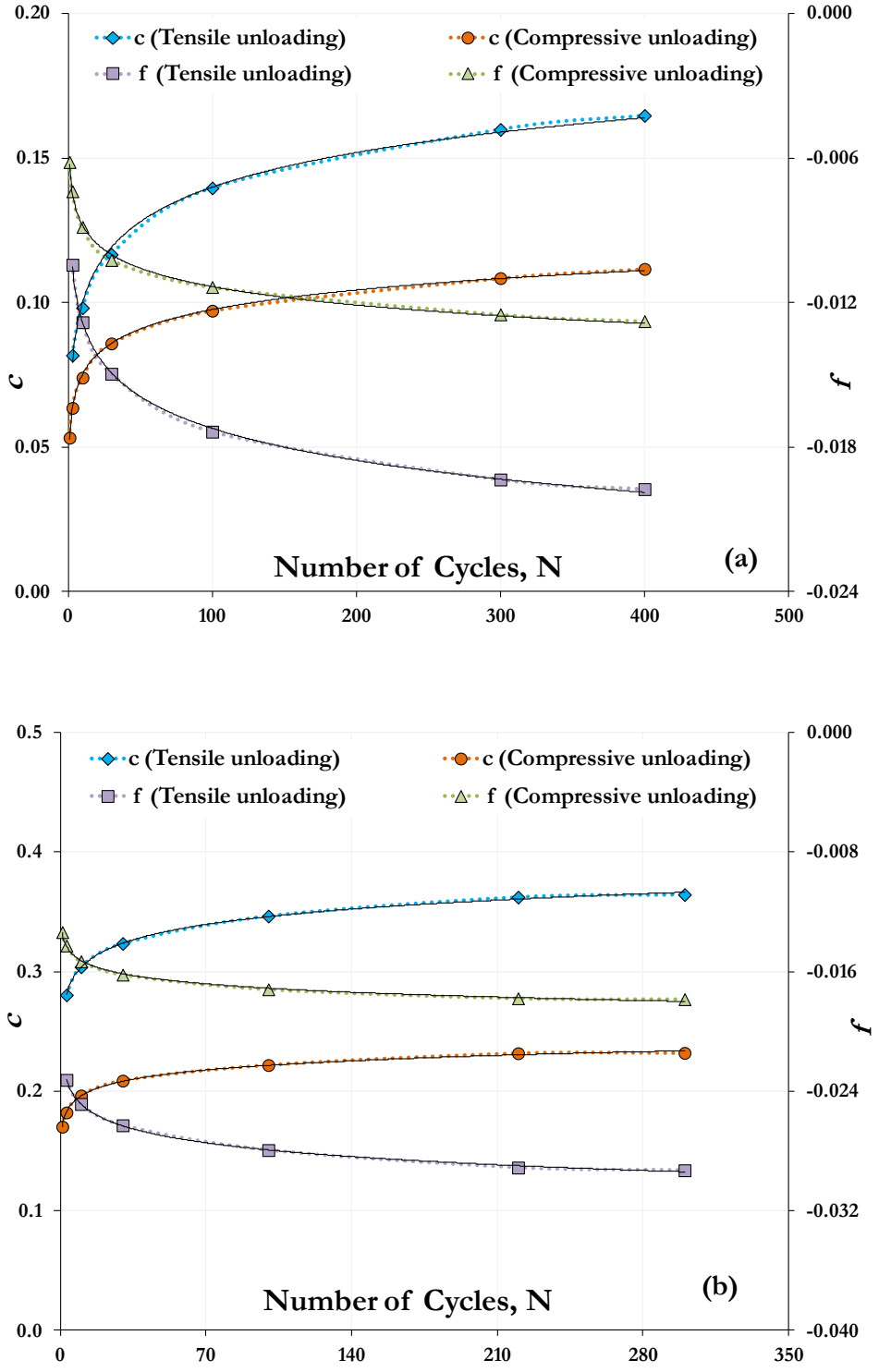

Figure 7.31. Relationship between the unloading evolutionary indices c and f, and the number of loading cycles N is presented for Test 7 (a) and Test 10 (b). The continuous black line in the plots refers to the trendline for the involved relationship.

Table 7.11. Evolutionary indices for the tensile and compressive unloading components for any C-F cycle N where N = 1, 2,…...till failure along with the maximum scatter factor obtained after minimization for a given test.

Test number	Tensile unloading		Compressive unloading		Max. Z
	c $c_N = c_0 + q.ln(N)$	f $f_N = f_0 + r.ln(N)$	c $c_N = c_0 + q.ln(N)$	f $f_N = f_0 + r.ln(N)$	
7	c_0: 0.0601 q : 0.0173	f_0: -0.00839 r : -0.00192	c_0: 0.0526 q : 0.0098	f_0: -0.00624 r : -0.00111	1.353
8	c_0: 0.0455 q : 0.0224	f_0: -0.00604 r : -0.00268	c_0: 0.0527 q : 0.0099	f_0: -0.00616 r : -0.00115	1.210
9	c_0: 0.1045 q : 0.0492	f_0: -0.00940 r : -0.00375	c_0: 0.1065 q : 0.0219	f_0: -0.00842 r : -0.00163	1.257
10	c_0: 0.2608 q : 0.0185	f_0: -0.02177 r : -0.00134	c_0: 0.1705 q : 0.0111	f_0: -0.01340 r : -0.00080	1.228

7.2.4.3. Stress relaxation and strain accumulation during hold time

As per the proposed constitutive model, the external strain-rate is the only test parameter that is gradually varied during the hold time of a C-F cycle. Rather interestingly, the strain-rate during hold is found to exhibit a power-law relation with hold time (t_h) wherein the power-law coefficient $(\dot{\varepsilon}_{hold})_0$ varies for a given C-F cycle and the exponent k quantifies the degree of stress relaxation with time. It is important to note that $(\dot{\varepsilon}_{hold})_0$ gradually increases from its initial value but never exceeds the applied (external) strain-rate. This corresponds to the observation that internal strain-rates at the start of hold ($0 < t_h \leq 0.5$ seconds) decrease rapidly in the first cycle (N = 1) and then increase gradually with C-F cycles, although they never exceed the external strain-rate at any stage before failure. It is also desired to keep k as a characteristic constant for a given material to facilitate in C-F model predictions at any hold time. For grade P91 steel, k is therefore kept a constant as -0.5897. Figures 7.32(a) and (b) show the comparison between experimental and simulated stress relaxation characteristics during the tensile hold at different stages of C-F lifetime

for Tests 7 and 10, respectively. As it can be seen, the degree of correlation is excellent indicating further the robustness of the model. In this context, the strain-rate at the end of a given hold period is expected to be the minimum creep rate for that particular C-F cycle. The total strain accumulated during the hold time of a given C-F cycle can thus be computed by multiplying t_h with the strain-rate at t_h = 600 seconds (for Tests 7 to 10) as per the power-law function. Figures 7.33(a) and (b) show plots obtained by plotting the total strain accumulated at the end of hold time of different C-F cycles for 600 seconds hold time tests at 1% and 1.5% strain range, respectively. Quite interestingly, these plots closely resemble conventional creep curves and can provide a numerical estimate of the strain accumulated just during the hold time of a C-F cycle. Further investigation can highlight the importance of this aspect of constitutive modeling and forms an interesting scope for future work.

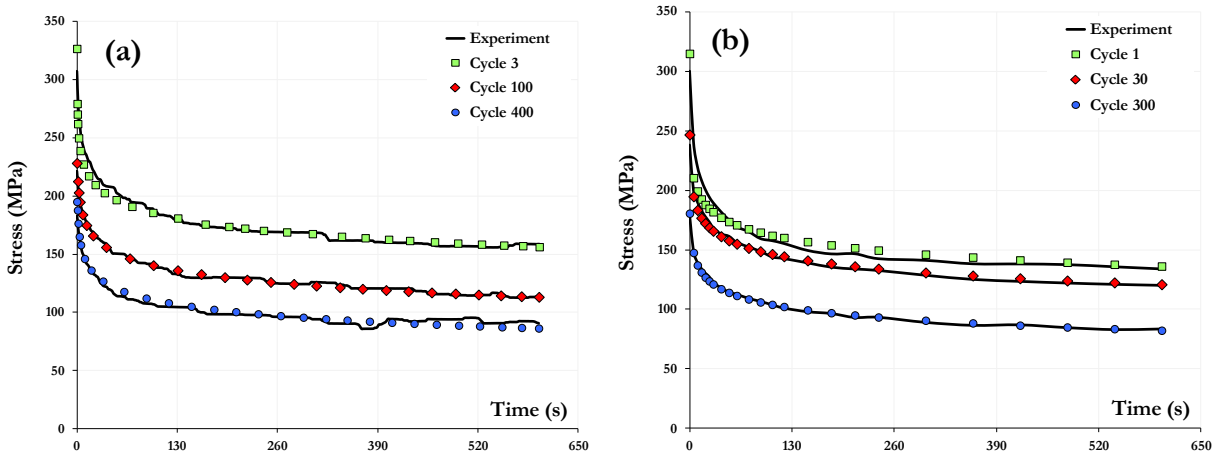

Figure 7.32. Comparison between experimental and simulated stress relaxation behavior during hold time at different stages of C-F lifetime for Test 7 (a) and Test 10 (b).

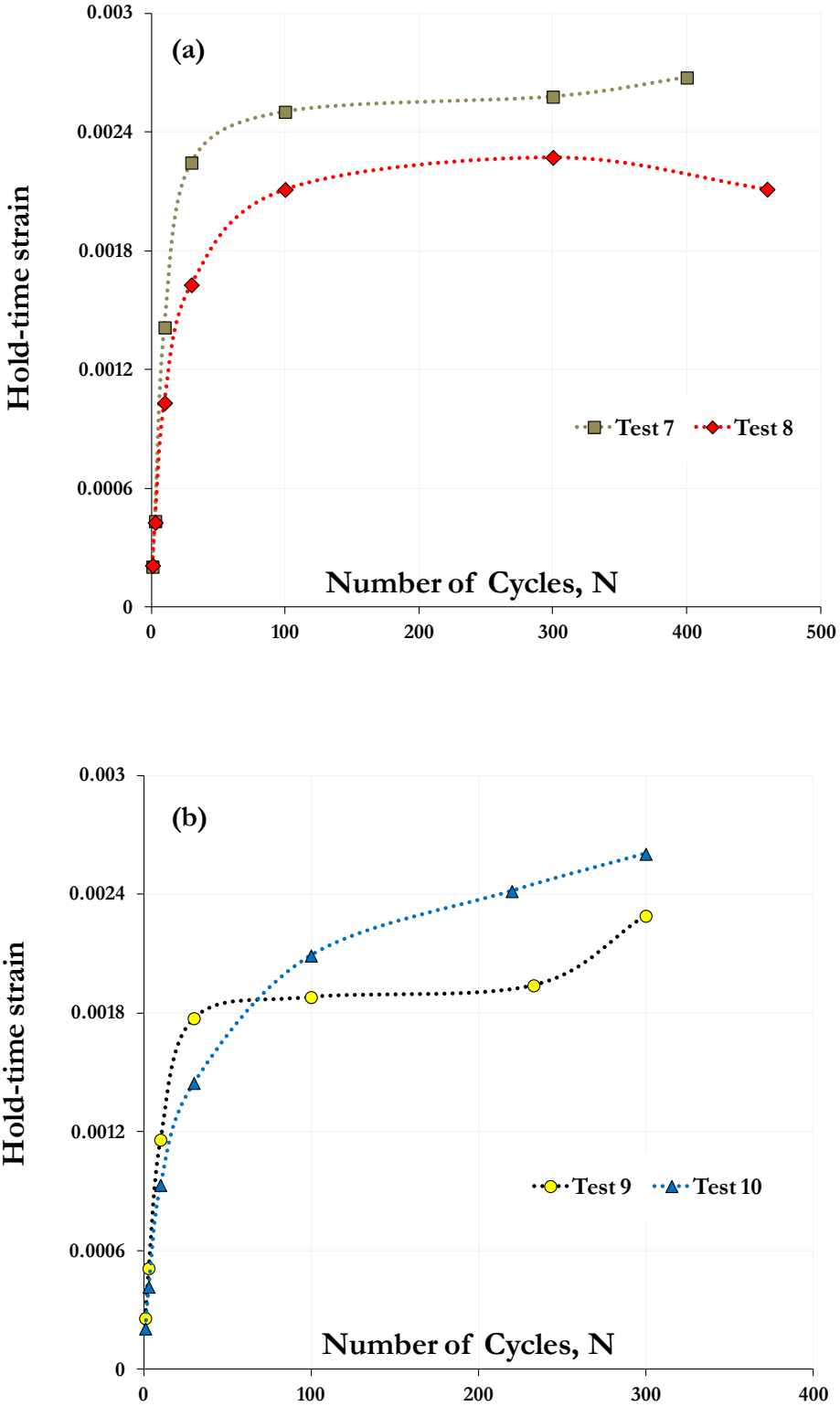

Figure 7.33. Total strain accumulated at the end of hold time (600 seconds) is plotted against C-F loading cycles *N* for 1% (a) and for 1.5% strain range (b).

7.2.4.4. Simulation of hysteresis loops

The cyclic stress-strain data obtained after Z minimization, in the form of conventional hysteresis loops, for tests numbered 7 to 10 are compared and presented in Figures 7.34(a)-(d). Although perfectly symmetrical hysteresis loops are expected for C-F tests, the evolutionary tendencies of inelastic strain along with indices a and c during loading and indices c and f during unloading indicate that slight deviations from this ideal behavior are expected (refer Tables 7.10 and 7.11). It is clearly observed that the general profile of the loops is accurately reproduced at different stages of C-F lives for all the lower hold time tests. Most importantly, the loading components that involve work-hardening behavior are better replicated in comparison to unloading components for these different tests. Such robust predictions also lend more credence to the analytical formulation of the proposed constitutive model and the presumed underlying dislocation mechanics.

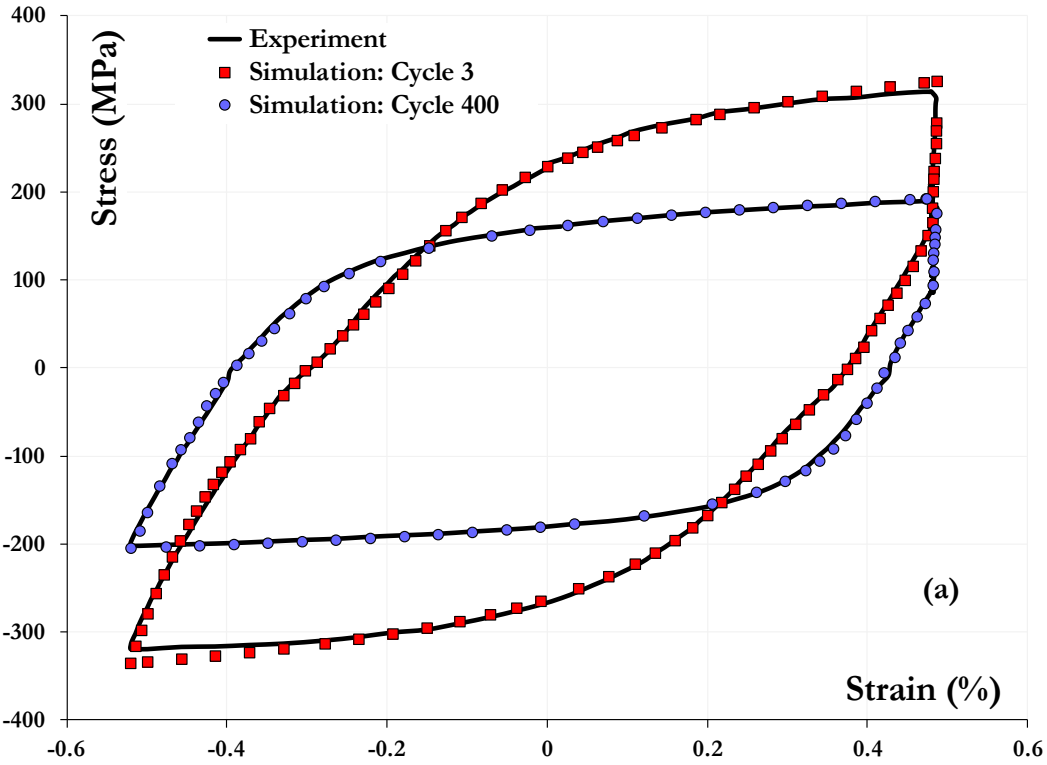

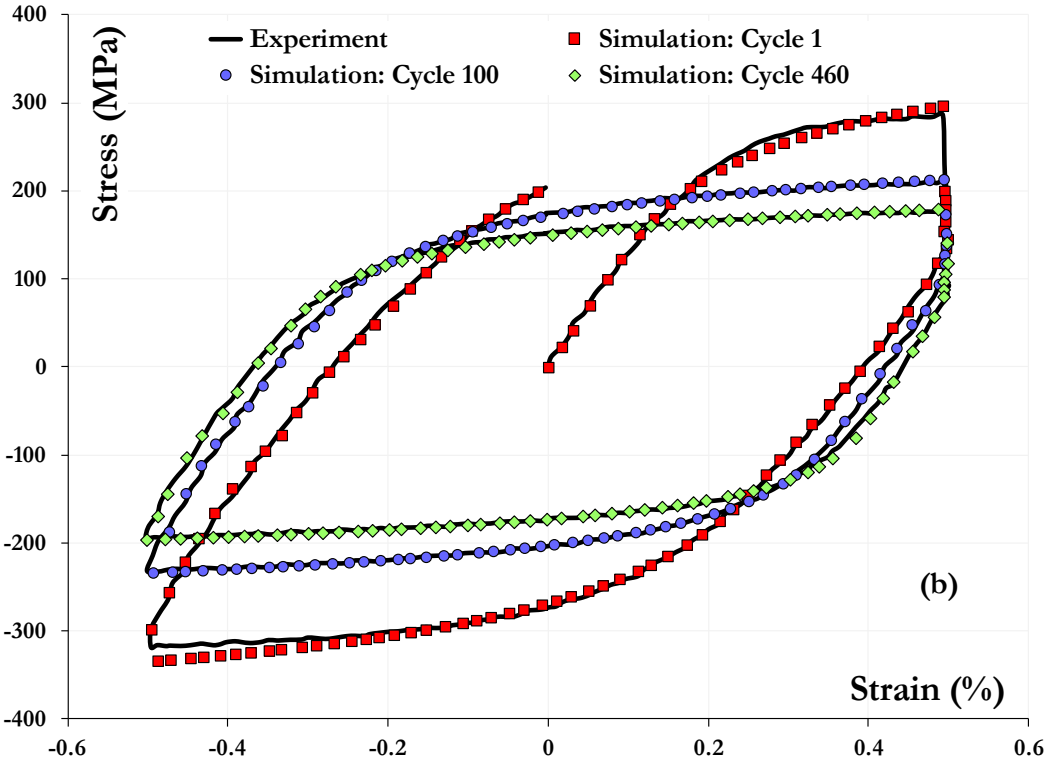
Experiment
Simulation: Cycle 1
Simulation: Cycle 100
Simulation: Cycle 460
Stress (MPa)
Strain (%)
(b)
400
300
200
100
0
-100
-200
-300
-400
-0.6
-0.4
-0.2
0
0.2
0.4
0.6

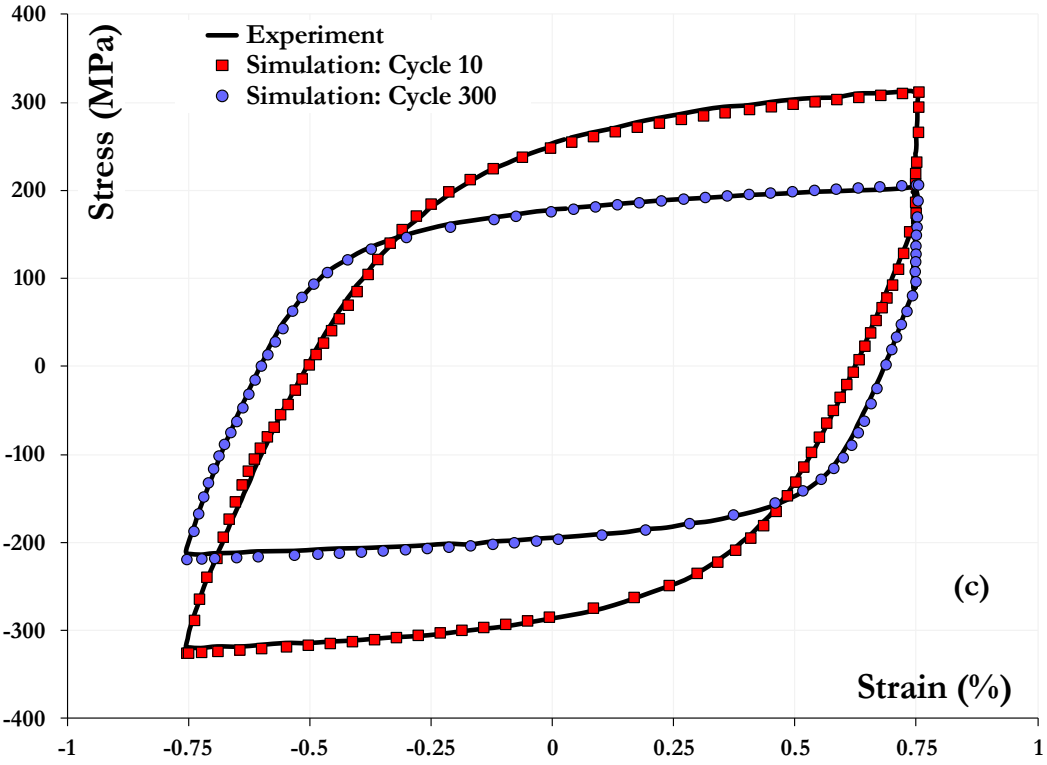
Experiment
Simulation: Cycle 10
Simulation: Cycle 300
Stress (MPa)
Strain (%)
(c)
400
300
200
100
0
-100
-200
-300
-400
-1
-0.75
-0.5
-0.25
0
0.25
0.5
0.75
1

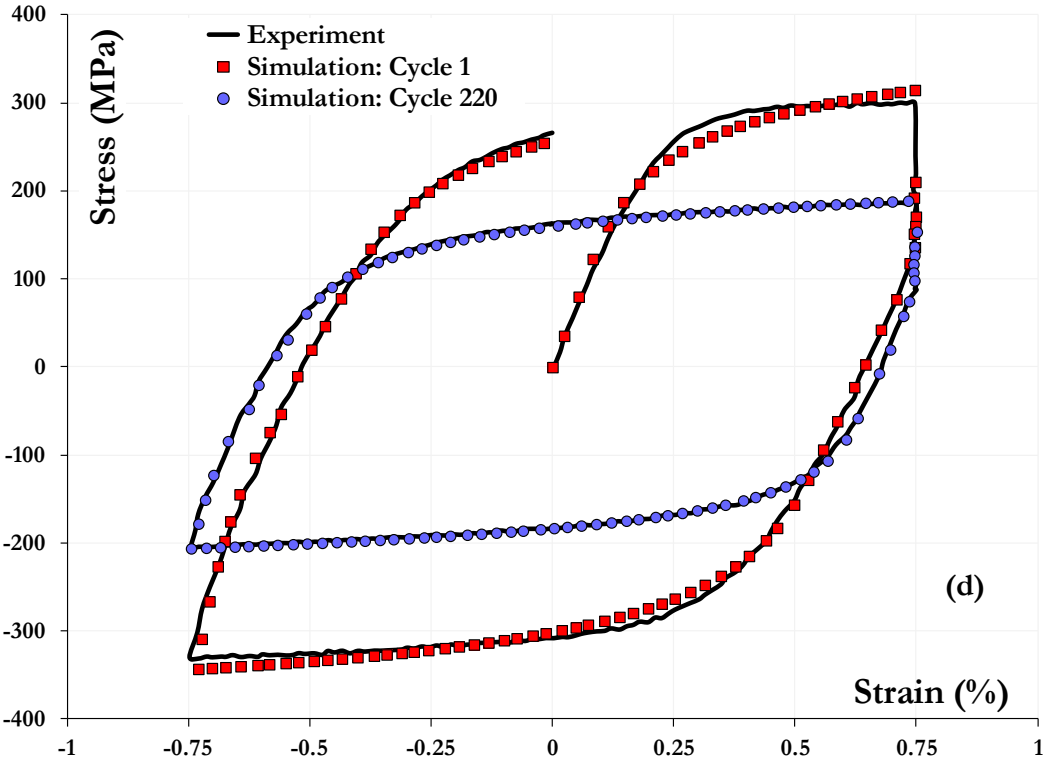

Figure 7.34. Comparison between simulated (markers) and experimental (continuous) conventional hysteresis loops at different stages of C-F life for (a) Test 7 ($\Delta\varepsilon = 1\%$), (b) Test 8 ($\Delta\varepsilon = 1\%$), (c) Test 9 ($\Delta\varepsilon = 1.5\%$) and (d) Test 10 ($\Delta\varepsilon = 1.5\%$) with 600 seconds tensile hold.

7.2.4.5. Simulation of cyclic softening

The most prominent feature of grade P91 steels under C-F loading at elevated temperatures is its cyclic softening behavior. Figures 7.35(a) and (b) present both the experimental and simulated peak stress curves for two different lower hold time tests. The model predictions closely represent the first two stages (till end-of-life) of the actual cyclic softening of grade P91 steels at 625°C. It can also be clearly seen that this effect does not depend on the applied strain amplitude, with higher strain amplitudes and hold times corresponding to a stronger degree of softening.

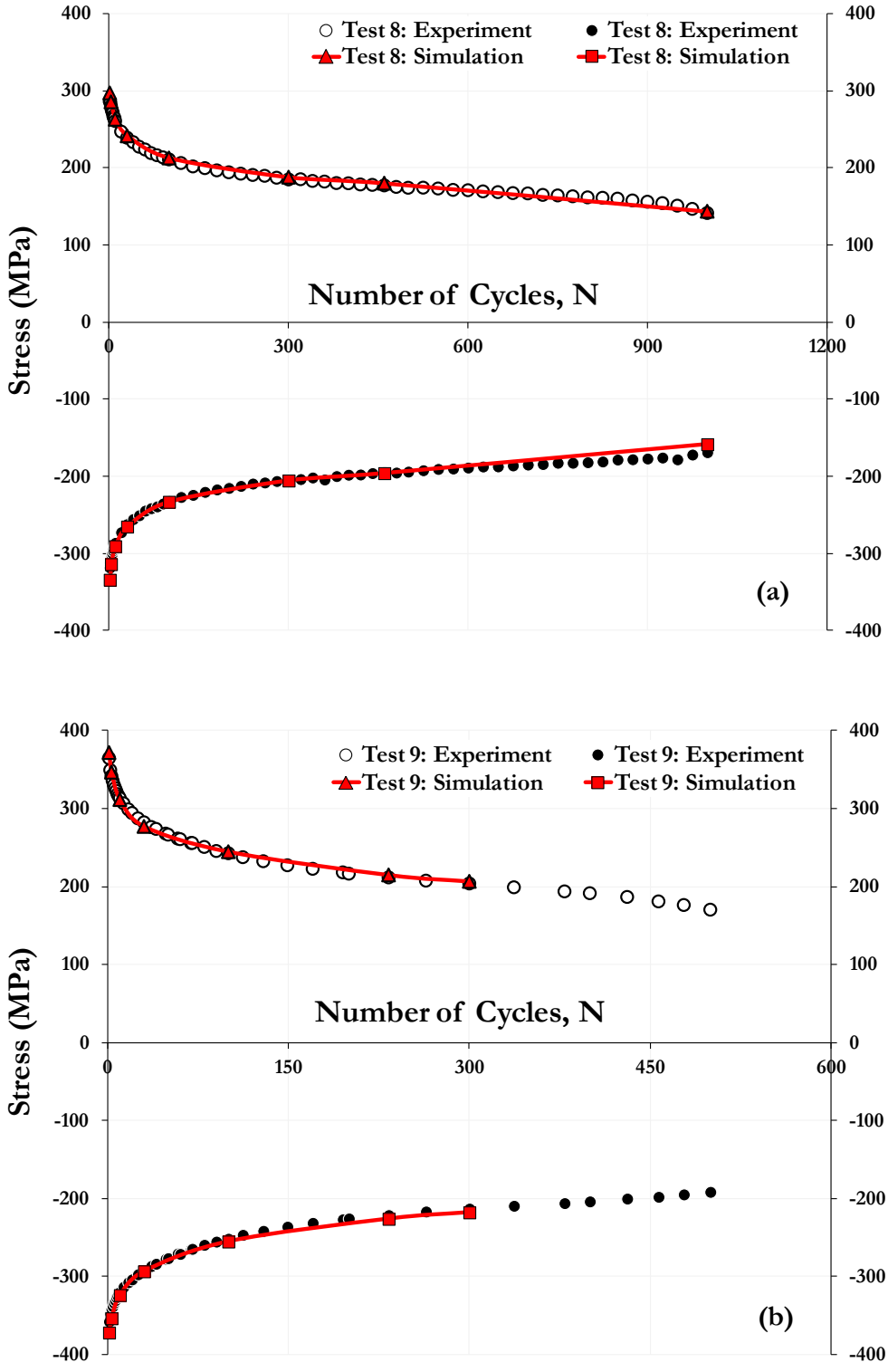

Figure 7.35. The simulated (continuous line with markers) and experimental (markers) variation of maximum (peak tensile) and minimum (peak compressive) stresses with loading cycles, N for (a) Test 8 ($\Delta\varepsilon = 1\%$) and (b) Test 9 ($\Delta\varepsilon = 1.5\%$).

7.2.4.6. Predictive capabilities

By conducting short-term laboratory experiments on a test material at accelerated test conditions, analytical predictions at a particular loading condition are typically made without considering the stochastic nature of microstructural variability. Since individual specimens of nominally homogeneous materials differ in the nature and spatial distribution of internal defects, they are certainly expected to provide scatter in test results even under identical test conditions (refer Table 6.2). Any extrapolation of experimental data without proper consideration of microstructural variability will tend to offer disparate predictions. The proposed constitutive relations (Equations (6.5) and (6.6)) greatly assist in this regard by minimizing the experimental data required for characterizing the microstructural C-F response of a particular specimen. If predictive accuracy can be sacrificed, mere averaging of model inputs from other accelerated tests at identical testing conditions can also be done by disregarding microstructural variability between test specimens.

Since the proposed plasticity mechanism (or shape of hysteresis loops) is rather generalized, the obtained evolutionary trends of the model indices for grade P91 steel are expected to be qualitatively similar for any material. A material can however cyclically harden or soften or exhibit a combination of both under certain C-F loading conditions. Accordingly, few laboratory experiments need to be performed for a test material to particularize these trends. Once the trends are established, the C-F deformation response of a particular specimen at any testing condition can be accurately predicted by cyclically loading it for just few cycles at that condition. For example, the evolutionary trends of the various model indices for grade P91 steel are already identified in the current modeling effort for lower hold times at 625°C. It can be easily concluded that *only* the first 2 loading cycles are needed – to numerically identify the coefficients and exponents of the

evolutionary indices – to accurately predict the C-F response of any grade P91 steel specimen for any strain amplitude at 625°C (see Tables 7.10 and 7.11). Although only 2 cycles are ideally required to identify the two unknown quantities for each evolutionary index, it is practically preferred to have the first 10 cycles of test data to maximize accuracy during modeling. Figures 7.36(a) and (b) show the comparison between experimental and simulated hysteresis loops of grade P91 steel for the two 1800 seconds hold time tests 11 and 12, respectively. The simulation loops are obtained with model indices estimated from the first 10 cycles of experimental data only to account for microstructural variability of the test specimen in consideration. The robustness of the constitutive relations in predicting the C-F response with very minimal experimental data is again clearly demonstrated.

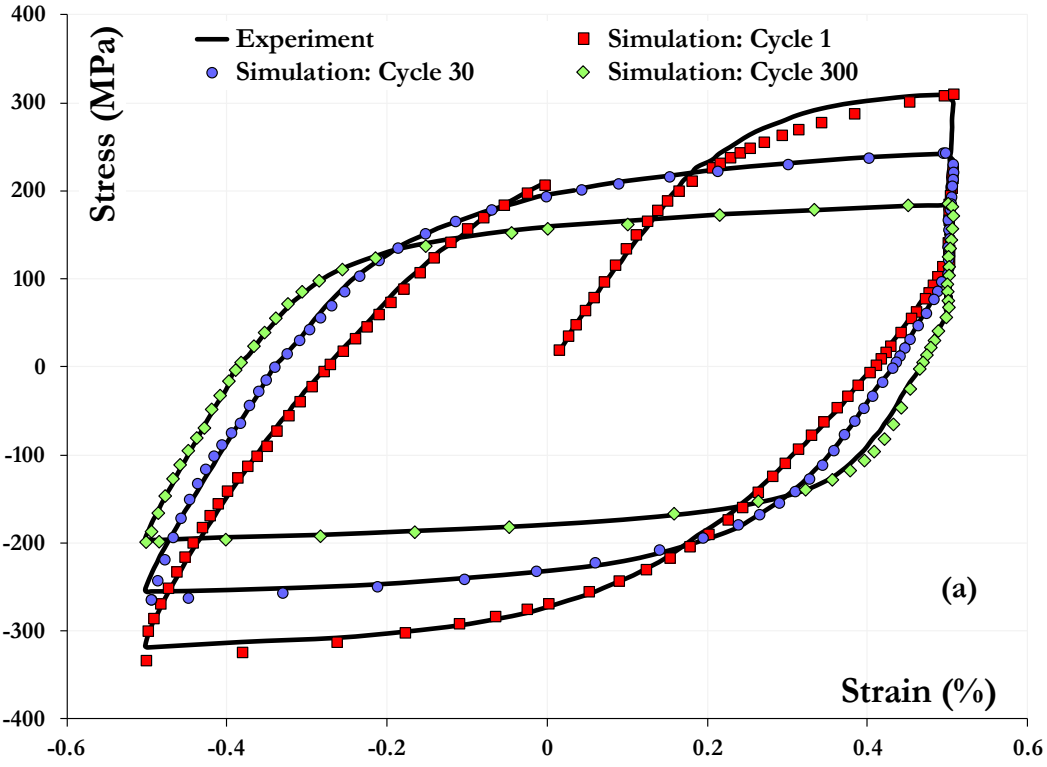

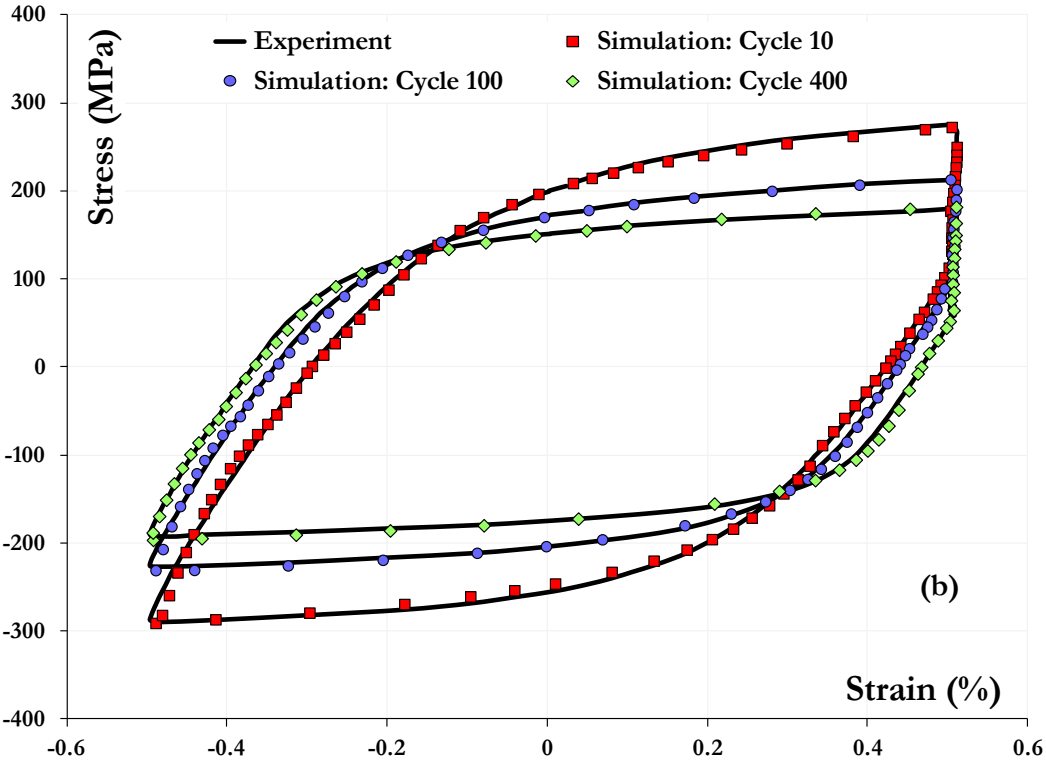

Figure 7.36. Comparison between the simulated (markers) and experimental (continuous) conventional hysteresis loops at different stages of the C-F life for (a) Test 11 ($\Delta\varepsilon = 1\%$) and (b) Test 12 ($\Delta\varepsilon = 1\%$) with 1800 seconds tensile hold.

When a macroscopic crack initiates on the test specimen's gage length, the system thereafter cannot be described as thermodynamically closed. In a physical sense, stresses can be relieved and consequently they do not uniquely correspond to the dislocation behavior within a material. Hence the formulated constitutive relations do not apply beyond macroscopic crack initiation in C-F test specimens. Due to the stochastic spatial distribution of defects within a material, the lifetime of a test specimen therefore cannot be predicted with this model alone. However, it can be combined with other life prediction approaches to aid in that regard.

Chapter 8: CONCLUSIONS AND RECOMMENDATIONS FOR FUTURE WORK

8.1. Conclusions

8.1.1. Experimental

The primary experimental conclusions from this dissertation work can be summarized as follows:

- The monotonic tensile and creep deformation and rupture behavior of grade P91 steels at 625°C reported in this work agrees quite well with existing literature, and metallographic studies on creep ruptured specimens show *predominantly* transgranular mode of deformation.

- On average and as expected specimen LCF and C-F lives, as measured by the 2% load drop criterion recommended in the ASTM E2714-09 standard, seem to decrease with increasing strain ranges and increasing hold times at 625°C.

- Resistance furnace based heating systems seem to offer the least C-F endurance for a given strain range as compared to radiation and induction heating, based on the limited RR data.

- Specimens from pipe subsection 2-4 seem to offer comparatively higher C-F endurances for the different RR test conditions. The reasons for this difference in C-F lives in pipe subsections are not yet clear; therefore, they are treated as material variability for the purposes of this work.

- Metallographic assessment of the tested specimens is performed to determine the extent of fatigue and creep damage under each test condition:

- The damage mode in tests conducted under the conditions of no hold time and with 600 seconds of tensile hold time is *predominantly* transgranular fatigue with some presence of oxidation spikes.
- The damage mode in tests conducted under the condition of 1800 seconds tensile hold time consists of an *interaction* of transgranular fatigue with dominant oxide spikes and creep cavitation.

- When an improved analytical method, not currently prescribed in the standard, is utilized to determine the cycles for crack formation, the mean C-F endurance and its standard deviation and reproducibility do not significantly change, but the repeatability in tests involving higher hold times is better.

- The overall variability in C-F endurances varied with the strain range and hold times as follows (*not including test results that failed to meet the criteria for valid tests*):
  - For tests with no hold times, the variability factor (ratio of maximum to minimum life) for the 95% confidence interval bands is 3, 3 and 2 for strain amplitudes of ± 0.25%, ± 0.5% and ± 0.75%, respectively.
  - For tests conducted with a hold time of 600 seconds, the variability factor for the 95% confidence interval bands is 3 and 2 for strain amplitudes of ± 0.5% and ± 0.75%, respectively.
  - For tests conducted with a hold time of 1800 seconds, the variability factor for the 95% confidence interval bands is 5 for a strain amplitude of ± 0.5%.

- Following recommendations are made for changes in the current ASTM standard E2714-09 based on the RR testing:

- It is observed that when induction heating method is used for testing magnetic ferritic materials like grade P91 steel, unusually high C-F lives are obtained in comparison with that from resistance heating method for comparable tests. This brings to question whether induction heating method should be permitted for testing magnetic materials.

8.1.2. Constitutive modeling

A modified version of an existing model (LCSP) is proposed in this work and shown to closely simulate the creep deformation and rupture response of grade P91 steel under various stress levels at 625°C. A thermodynamically consistent atomistic scale framework on crystal plasticity is also discussed in this work by considering the thermodynamic plastic instabilities due to localized entropy fluctuations. Specifically a probabilistic interatomic shearing process – founded on statistical thermodynamics – is proposed based on transitory structural ordering events that result in localized entropy fluctuations. Such localized entropy losses drive the system towards global entropy gains in the form of enhanced plastic deformation during loading. Global plasticity for crystalline materials is proposed to be mediated by the cumulative interaction tendencies of two different types of dislocation densities that nucleate and operate at two different length scales. Short-range dislocation densities grow exponentially and induce continuous heterogeneous localized plasticity whereas long-range dislocation densities grow as per a power-law distribution characterizing time and scale invariance. Moreover, the latter induces nominally homogeneous macroscopic plasticity in the form of temporospatially intermittent dynamic avalanches or bursts. The proposed framework also has the potential to describe the deformation behavior of nanostructured materials and the influence of temperature and strain-rate on crystal plasticity is also elucidated. A constitutive relation based on

the proposed dislocation mechanics is formulated and shown to closely simulate the uniaxial monotonic tensile behavior of grade P91 steel, along with a qualitative demonstration of other predictive capabilities. Since dislocations mediate plasticity under any loading condition, the formulated constitutive relation is also extended to simulate and predict the uniaxial cyclic behavior without hold time effects in this work.

The complex LCF and C-F response of grade P91 steels at 625°C is accurately predicted by just considering the evolution and cumulative interaction characteristics of two different types of dislocation densities that induce plasticity at two distinct microstructural states. By employing just 2 evolutionary indices each for describing the loading and unloading components of a typical LCF cycle and gradually varying strain-rate for describing C-F hold time effects, the proposed constitutive relation has demonstrated excellent robustness with very minimal degrees of freedom. Once the evolutionary trends of these indices are established, the model can be conveniently employed for extrapolation with experimental data from just 10 LCF or C-F cycles to account for microstructural variability among nominally homogeneous materials. Successful implementation and demonstration of the proposed model has also ensured that the presumed underlying mechanics of dislocation behavior and its analytical formulation are valid. Most importantly, this work has shown that macroscopic plasticity is characterized by a power-law relation with loading cycles indicating its time and scale invariance during deformation.

8.2. Recommendations for future work

8.2.1. Experimental

There are several aspects of experimental investigations that can be pursued in more depth as part of future work. An experimental research program could be initiated to complement the work conducted as part of this RR on the creep, LCF and C-F behavior of grade P91 steels:

- The scientific rationale behind the observed preferential creep deformation along secondary-phase precipitates needs further detailed microscopic investigation.
- The current RR tests are limited to three strain ranges, single temperature and hold times of 0, 600 and 1800 seconds. The data should be expanded to include additional strain ranges, temperatures and longer hold times.
- The results of this RR indicate that LCF and C-F crack formation lives of specimens tested seem to vary with specimen location and heating method employed for laboratory testing. Consideration should be accordingly given in this regard to understand variability in LCF and C-F lives in grade P91 steel with nominally same microstructures. Comprehensive test programs focusing individually on each of these aspects can throw more light on their specific influence towards LCF and C-F crack formation.

8.2.2. Constitutive modeling

There are several aspects of constitutive modeling efforts that can be pursued in more depth as part of future work to further the demonstrated capabilities of models described in this work for simulating/predicting the creep, LCF and C-F behavior of grade P91 steels:

- The modified LCSP model should be tested for robustness under different non-isothermal loading conditions not only for grade P91 steels but also for other elevated temperature materials.
- Similarly, the applicability of the novel constitutive relation for predicting/simulating the response of grade P91 steels under various multiaxial, non-isothermal and non-proportional loading conditions should be checked to enable it as a well-rounded analytical model.
- Specifically, the numerical estimate of strain accumulated during the hold time of a C-F cycle needs to be verified with further experimental input and/or microscopic examination.

Chapter 9: REFERENCES

1. World Energy Outlook Executive Summary IEA Paris, pp. 1-10, 2011.

2. Muramatsu, K., *Advanced Heat Resistant Steel For Power Generation* (The University Press, Cambridge, Great Britain, 1999).

3. Staubli, M. *et al.*, in *Proceedings of the 6th International Charles Parsons Turbine Conference*, edited by Strang, A. *et al.* (Maney, Dublin, 2003), pp. 305-324.

4. Jara, D. R., *9-12% Cr Heat Resistant Steels: Alloy Design, TEM Characterization of Microstructure Evolution and Creep Response at 650 ℃* (der Ruhr-Universitat Bochum, Ph.D. Dissertation, 2011).

5. Scheu, C. *et al.*, Requirements For Microstructural Investigations of Steels Used in Modern Power Plants. *Zeitschrift fur Metallkunde* **96**, 653-659 (2005).

6. Fujita, T., Advanced High-Chromium Ferritic Steels For High-Temperatures. *Metal Progress* **130**, 33-40 (1986).

7. Hald, J., Microstructure and Long-term Creep Properties of 9-12% Cr Steels. *International Journal of Pressure Vessels and Piping* **85**, 30-37 (2008).

8. Yoshizawa, M. & Igarashi, M., Long-term Creep Deformation Characteristics of Advanced Ferritic Steels For USC Power Plants. *International Journal of Pressure Vessels and Piping* **84**, 37-43 (2007).

9. Klueh, R. L., Elevated Temperature Ferritic and Martensitic Steels and Their Application to Future Nuclear Reactors. *International Materials Review* **50**, 287-310 (2005).

10. Eggeler, G., Nilsvang, N. & Ilschner, B., Microstructural Changes in a 12% Chromium Steel During Creep. *Steel Research* **58**, 97-103 (1987).

11. Eggeler, G., Earthman, J. C., Nilsvang, N. & Ilschner, B., Microstructural Study of Creep-Rupture in a 12% Chromium Ferritic Steel. *Acta Metallurgica* **37**, 49-60 (1989).

12. Fujita, T., Heat-resistant Steels For Advanced Power-Plants. *Advanced Materials & Processes* **141**, 42-47 (1992).

13. Masuyama, F., History of Power Plants and Progress in Heat Resistant Steels. *ISIJ International* **41**, 612-625 (2001).

14. Buschow, K. H. J., *Encyclopedia of Materials: Science and Technology* (Elsevier, Amsterdam, Netherlands, 2001).

15. Diehl, H. & Granacher, J., Results of Creep-rupture Tests at 500°C with Loading Times up to more than 300000 h. *Archiv fur Das Eisenhuttenwesen* **50**, 299-303 (1979).

16. Dubey, J. S. *et al.*, Effects of Cyclic Deformation on Subgrain Evolution and Creep in 9-12% Cr Steels. *Materials Science and Engineering A* **406**, 152-159 (2005).

17. Kadoya, Y. *et al.*, Assessment of Remaining Life of Fossil Power-plant Parts by means of a Miniature Creep-rupture Test. *ISIJ International* **30**, 854-861 (1990).

18. Kimura, A. *et al.*, Recent Progress in US-Japan Collaborative Research on Ferritic Steels R&D. *Journal of Nuclear Materials* **367**, 60-67 (2007).

19. Knezevic, V., Balun, J., Sauthoff, G., Inden, G. & Schneider, A., Design of Martensitic/Ferritic Heat-resistant Steels for Application at 650°C with Supporting Thermodynamic Modelling. *Materials Science and Engineering A* **477**, 334-343 (2008).

20. Gandy, D., *X20CrMoV12-1 Steel Handbook* (Electric Power Research Institute (EPRI), Palo Alto, USA, 2006).

21. Abe, F., Kern, T. U. & Viswanathan, R., *Creep-resistant Steels* (Woodhead Publishing, CRC Press, Cambridge, England, 2008).

22. Shibli, A. & Starr, F., Some Aspects of Plant and Research Experience in the use of New High Strength Martensitic Steel P91. *International Journal of Pressure Vessels and Piping* **84**, 114-122 (2007).

23. Vigneron, G., Vanderschaeghe, A. & Lecoq, J., A Metallurgical Contribution to the Industrial-Development of 12% Chromium Martensitic Steels for Pressure-vessels. *International Journal of Pressure Vessels and Piping* **32**, 389-413 (1988).

24. Swindeman, R. W., Santella, M. L., Maziasz, P. J., Roberts, B. W. & Coleman, K., Issues in Replacing Cr-Mo Steels and Stainless Steels with 9Cr-1Mo-V Steel. *International Journal of Pressure Vessels and Piping* **81**, 507-512 (2004).

25. Yao, M. X., Wu, J. B. C., Yick, S., Xie, Y. & Liu, R., High Temperature Wear and Corrosion Resistance of a Laves phase Strengthened Co-Mo-Cr-Si alloy. *Materials Science and Engineering A* **435-436**, 78-83 (2006).

26. Fin, Y. F. & Faulkner, R. G., Creep Damage and Grain Boundary Precipitation in Power Plant

Metals. *Materials Science and Technology A* **21**, 1239-1246 (2005).

27. Cahn, R. W. & Haasen, P., *Physical Metallurgy* (North-Holland Physics Publication: Elsevier Science Publishing Company, New York, USA, 1983).

28. Janovec, J., Svoboda, M., Kroupa, A. & Vyrostkova, A., Thermal-induced Evolution of Secondary Phases in Cr-Mo-V Low Alloy Steels. *Journal of Materials Science* **41**, 3425-3433 (2006).

29. Shtansky, D. V. & Inden, G., Phase Transformation in Fe-Mo-C and Fe-W-C steels. 1. The Structural Evolution during Tempering at 700°C. *Acta Materialia* **45**, 2861-2878 (1997).

30. Shtansky, D. V. & Inden, G., Phase transformation in Fe-Mo-C and Fe-W-C steels. 2. Eutectoid reaction of M23C6 Carbide Decomposition during Austenitization. *Acta Materialia* **45**, 2879-2895 (1997).

31. ASTM E2714-09, Standard Test Method for Creep-Fatigue Testing, Annual Book of ASTM Standards, Vol. 03.01, ASTM International, West Conshohocken, PA, 2009.

32. Armor, A. F. & Viswanathan, R., in *4th International Conference in Advances in Materials Technology for Fossil Power Plants* (ASM International, Hilton Head Island, 2005).

33. Cerjak, H., Hofer, P. & Schaffernak, B., The Influence of Microstructural Aspects on the Service Behavior of Advanced Power Plant Steels. *ISIJ International* **39** (9), 874-888 (1999).

34. M.E. Kassner, M. T. P.-P., *Fundamentals of Creep in Metals and Alloys* (Elsevier, Amsterdam, Netherlands, 2004).

35. Evans, R. W. & Wilshire, B., *Introduction to Creep* (Institute of Materials, London, England, 1993).

36. Evans, R. W. & Wilshire, B., *Creep of Metals and Alloys* (Institute of Metals, London, England, 1985).

37. Ashby, M., Shercliff, H. & Cebon, D., *Materials: Engineering, Science, Processing and Design* (Elsevier, New York, USA, 2007).

38. Ashby, M. F. & Jones, D. R. H., *Engineering Materials 1: An Introduction to Their Properties and Applications*, 2nd ed. (Butterworth Heinemann, Oxford, UK, 1996).

39. ASTM E139–06, Standard Test Methods for Conducting Creep, Creep-Rupture, and Stress-Rupture Tests of Metallic Materials, Annual Book of ASTM Standards, Vol. 03.01, ASTM International, West Conshohocken, PA, 2006.

40. Callister Jr., W. D. ., in *Materials Science and Engineering, an Introduction* (1996, Fourth edition), pp. 220-227.

41. Cadek, J., *Creep in Metallic Material* (Elsevier, Amsterdam, Netherlands, 1988).

42. Nabarro, F. R. N. & Villiers, H. L. D., *The Physics Of Creep: Creep and Creep-resistant Alloys* (Taylor & Francis, London, UK, 1995).

43. Naumenko, K. & Altenbach, H., *Modelling of Creep for Structural Analysis* (Springer-Verlag, Berlin, Germany, 2007).

44. Rosler, J., Harders, H. & Baker, M., *Mechanical Behaviour of Engineering Materials* (Springer-Verlag, Berlin, Germany, 2007).

45. Andrade, E. N. D. C., On the Viscous Flow of Metals, and Allied Phenomena. *Proceedings of the Royal Society of London* **ALXXXIV**, 1-12 (1910).

46. Yawny, A. & Eggeler, G., Assessment of Back Stress and Load Transfer Approaches for Rationalizing Creep of Short Fiber Reinforced Aluminium Alloys. *Metallurgical and Materials Transactions A* **387-389**, 905-909 (2004).

47. Viswanathan, R., *Damage Mechanisms and Life Assessment of High-Temperature Components* (ASM International, Metals Park, Ohio, USA, 1989).

48. Neubauer, B. & Wedel, U., in *Advances in Life Prediction Methods: Proceedings of the ASME International Conference*, edited by Woodford, D. A. & Whitehead, J. R. (New York, USA, 1983), pp. 307-314.

49. Frost, H. J. & Ashby, M. F., *Deformation Mechanism Maps* (Pergamon Press, Oxford, UK, 1982).

50. Graham, A. & Walles, K. F. A., NGTE Report, 1961 Report No. R247, On the Extrapolation of Creep Data.

51. Penny, R. K. & Mariott, D. L., *Design for Creep* (Chapman & Hall, London, UK, 1995).

52. Riedel, H., *Fracture at High Temperatures* (Springer-Verlag, New York, USA, 1987).

53. ASTM E1823-11, Standard Terminology Relating to Fatigue and Fracture Testing, ASTM International, West Conshohocken, PA, 2011.

54. MacNeal Schwendler Corporation, L. A. (. U., MSC Fatigue, Encyclopedia, 2003.

55. ASTM E606, Standard Practice for Strain-Controlled Fatigue Testing, Annual Book of ASTM Standards, 2007.

56. Holdsworth, S. R., Mazza, E., Binda, L. & Ripamonti, L., Development of thermal fatigue damage in 1CrMoV rotor steel. *Nuclear Engineering and Design* **237**, 2292-2301 (2007).

57. Miller, D. A. & Priest, R. H., in *Materials Response to Thermal-Mechanical Strain Cycling, High Temperature Fatigue: Properties and Prediction*, edited by Skelton, R. P. (Elsevier Applied Science Publication Limited, 1987), p. 113.

58. Kofstad, P., *High-temperature oxidation of metals* (John Wiley & Sons, Inc., New York, 1966).

59. Briggs, Z. & Parker, T. D., The Super 12% Cr Steels, Climax Molybdenum Company, New York, USA, 1965.

60. Anon, Super 12% Cr Steels-An Update, Climax Molybdenum Company, New York, USA, 1983.

61. Hayashi, T., Takamoto, M., Ito, K. & Tanaka, K., The Effect of Nb and W Alloying Additions to the Thermal Expansion Anisotropy and Elastic Properties of Mo5Si3. *Metallurgical and Materials Transactions A* **36**, 533-538 (2005).

62. Blum, R., Vanstone, R. W. & Messelier-Gouze, C., in *4th International Conference in Advances in Materials Technology for Fossil Power Plants* (ASM International, Hilton Head Island, 2005).

63. Staubli, M., Bendick, W., Orr, J., Deshayes, F. & Henry, C., in *International Conference in Materials for Advanced Power Engineering 1998* (Forschungszentrum Jülich, Liege, 1998).

64. Blum, R. & Hald, J., in *Benefit Of Advanced Steam Power Plants, Materials Of Advanced Power Engineering*, edited by Lacomte-Becker (European Commission And University Of Liége 21 Part II, 2002), pp. 1007-1015.

65. Ennis, P. J. & Czyrska-Filemonowicz, A., Recent Advances In Creep-Resistant Steels For Power Plant Applications. *Sādhanā* **28** (3&4), 709-730 (2003).

66. Abe, F., Analysis Of Creep Rates Of Tempered Martensitic 9% Cr Based On Microstructure Evolution. *Materials Science and Engineering A* **510-511**, 64-69 (2009).

67. Abe, F., Precipitate Design for Creep Strengthening of 9% Cr Tempered Martensitic Steels for Ultra-supercritical Power Plants. *Science and Technology of Advanced Materials* **9**, 013002 (1-15) (2008).

68. Abe, F., Effect of Boron on Creep Deformation Behavior and Microstructure Evolution in 9% Cr Steel at 650°C. *International Journal of Materials Research* **99**, 387-394 (2008).

69. Andren, H. O., Combining TEM and APFIM Techniques to Study the Microstructure of Steels and Hardmetals. *Micron* **32**, 713-719 (2001).

70. Eggeler, G. & Dlouhy, A., Boron Segregation and Creep in Ultra-fine Grained Tempered Martensite Ferritic Steel. *Zeitschrift fur Metallkunde* **96**, 743-748 (2005).

71. Hattestrand, M., Schwind, M. & Andren, H. O., Microanalysis of Two Creep Resistant 9-12% Chromium Steels. *Metallurgical and Materials Transactions A* **250**, 27-36 (1998).

72. Hattestrand, M. & Andren, H. O., Boron Distribution in 9-12% Chromium Steels. *Metallurgical and Materials Transactions A* **270**, 33-37 (1999).

73. Klueh, R. L., in *Elevated – Temperature Ferritic and Martensitic Steels and Their Application to Future Nuclear Reactors* (Oak Ridge National Laboratory, Tennessee for the US Department of Energy), Vol. 37831-6285.

74. Vaillant, J. C., Vandenberghe, B., Hahn, B., Heuser, H. & Jochum, C., T/P23, 24, 911 and 92: New Grades for Advanced Coal-fired Power Plants: Properties and Experience. *International Journal of Pressure Vessels and Piping* **85**, 38-46 (2008).

75. Albert, S. K. *et al.*, Improving the Creep Properties Of 9Cr-3W-3Co-NbV Steels and Their Weld Joints by the Addition of Boron. *Metallurgical and Materials Transactions A* **36**, 333-343 (2005).

76. Eggeler, G. *et al.*, Analysis of Creep in a Welded P91 Pressure Vessel. *International Journal of Pressure Vessels and Piping* **60**, 237-257 (1994).

77. Tuma, J. V. & Kosec, G., Effect of Microstructure on the Accelerated Creep of 20CrMoV12-1 and P91 Steels. *Steel Research International* **78**, 643-647 (2007).

78. Spigarelli, S. & Quadrini, E., Analysis of the Creep Behavior of Modified P91 (9Cr-1Mo-NbV) Welds. *Materials & Design* **23**, 547-552 (2002).

79. Viswanathan, R. *et al.*, in *4th International Conference in Advances in Materials Technology for Fossil Power Plants* (ASM International, Hilton Head Island, 2005).

80. Kern, T. U., Wieghardt, K. & Kirchner, H., in *4th International Conference in Advances in Materials Technology for Fossil Power Plants* (ASM International, Hilton Head Island, 2005).

81. Masuyama, F., in *4th International Conference in Advances in Materials Technology for Fossil Power Plants* (ASM International, Hilton Head Island, 2005).

82. Hald, J., in *Proceedings of the 9th Liege Conference in Materials For Advanced Power Engineering*, edited by Lecomte-Beckers, J., Contrepois, Q., Beck, T. & Kuhn, B. (Liege, Belgium, 2010), pp. 55-66.

83. Jia, X. & Dai, Y., Microstructure in Martensitic Steels T91 and F82H after Irradiation in SINQ Target-3. *Journal of Nuclear Materials* **318**, 207-214 (2003).

84. Dai, Y., Jia, X. J. & Farrell, K., Mechanical Properties of Modified 9Cr-1Mo (T91) irradiated at ≤300℃ in SINQ Target-3. *Journal of Nuclear Materials* **318**, 192-199 (2003).

85. Sikka, V. K., Ward, C. T. & Thomas, K. C., in *Ferritic steels for High Temperature Applications*, edited by Khare, A. K. (ASM, Metals Park, Ohio, USA, 1983), pp. 65-84.

86. Booker, M. K., Sikka, V. K. & Booker, B. L. P., in *Comparison of the Mechanical Strength Properties of Several High-Chromium Ferritic Steels* (op. cit. (63)), pp. 257-273.

87. Bodine, G. C. & McDonald, R. E., in *Laboratory and Pilot Commercial Process/Product Development of Modified 9Cr1Mo Ferritic Alloy* (op. cit. (63)), pp. 9-19.

88. Sikka, V. K., Advanced Alloy Technology Program - Semiannual Progress Report for period ending March 1983 pp. 1-49 Report No. ORNL/MSP/1.7-83/2, 1983.

89. Swindeman, R. W., in *Cyclic Stress-Strain-Time Response of a 9Cr1MoVNb Pressure Vessel Steel at High Temperature* (op. cit. (21)), pp. 107-122.

90. Clarke, P. D., Morris, P. F., Cardinal, N. & Worral, M. J., in *Proceedings of the 6th International Charles Parsons Turbine Conference* , edited by Strang, A. *et al.* (Maney, Dublin, 2003), pp. 333-345.

91. Blum, R. & Vanstone, R. W., in *Proceedings of the 8th Liege Conference in Materials For Advanced Power Engineering*, edited by Lecomte-Beckers, J., Carton, M., Schubert, F. & Ennis, P. J. (Liege, Belgium, 2006), pp. 41-60.

92. Hanus, R., Casting, COST Summer School, Lanzarote, 2008.

93. Cahn, R. W., Haasen, P., Kramer, E. J. & Meijer, H. E. H., *Materials Science and Technology: A Comprehensive Treatment* (Wiley-VCH, Weinheim, Germany, 1998).

94. Abe, F., Horiuchi, T., Taneike, M. & Sawada, K., Stabilization of Martensitic Microstructure in Advanced 9Cr Steels during Creep at High Temperature. *Materials Science and Engineering A* **378**, 299-303 (2004).

95. Available at http://www.materialsengineer.com/E-Alloying-Steels.htm (Accessed on December 3, 2011).

96. Ennis, P. J., Wouters, Y. & Quadakker, W. J., in *Proceedings of the Advanced Heat Resistant Steels For Power Generation*, edited by Viswanathan, R. & Nutting, J. (San Sebastian, Spain, 1998), pp. 457-467.

97. Klotz, U. E., Solenthaler, C. & Uggowitzer, P., Martensitic-Austenitic 9-12% Cr Steels-Alloy Design, Microstructural Stability and Mechanical Properties. *Materials Science and Engineering A* **476**, 186-194 (2008).

98. Abe, F., Coarsening Behavior of Lath and its Effect on Creep Rates in Tempered Martensitic 9Cr-W Steels. *Materials Science and Engineering A* **387-389**, 565-569 (2004).

99. Abe, F., Creep Rates and Strengthening Mechanisms in Tungsten-Strengthened 9Cr Steels. *Materials Science and Engineering A* **319-321**, 770-773 (2001).

100. Sawada, K. *et al.*, Effect of W on the Recovery of Lath Structure during Creep of High Chromium Martensitic Steels. *Metallurgical and Materials Transactions A* **267**, 19-25 (1999).

101. Baker, R. G. & Nutting, J., The Tempering of 2.25Cr1Mo Steel after Quenching and Normalizing. *The Journal of the Iron and Steel Institute* **192**, 257-268 (1959).

102. Miyata, K. & Sawaragi, Y., Effect of Mo and W on the Phase Stability of Precipitates in Low Cr Heat Resistant Steels. *ISIJ International* **41**, 281-289 (2001).

103. Onizawa, T., Wakai, T., Ando, M. & Aoto, K., Effect of V and Nb on Precipitation Behavior and Mechanical Properties of High Cr Steels. *Nuclear Engineering and Design* **232**, 408-416 (2008).

104. Taneike, M., Abe, F. & Sawada, K., Creep-Strengthening of Steel at High Temperatures using Nano-sized Carbonitride Dispersions. *Nature* **424**, 294-296 (2003).

105. Huntz, A. M. *et al.*, Effect of Silicon on the Oxidation Resistance of 9% Cr Steels. *Applied Surface Science* **207** (1-4), 255-275 (2003).

106. Fujitsuna, N., Igarashi, M. & Abe, F., Acceleration of Fe2W Precipitation and its Effects on Creep Deformation Behavior of 8.5Cr-2W-VNb Steels with Si. *Key Enginering Materials* **171-174**, 469-476 (2000).

107. Aghajani, A. *et al.*, On the Formation and Growth of Mo-rich Laves phase Particles during Long-term Creep of a 12% Chromium Tempered Martensite Ferritic Steel. *Scripta Materialia* **61**, 1068-1071 (2009).

108. Woodhead, J. H. & Quarrel, A. G., Role of Carbides in Low-alloy Creep Resisting Steels. *The Journal of the Iron and Steel Institute* **203**, 605-620 (1965).

109. Abe, F. *et al.*, in *Proceedings of the 7th Liege Conference on Materials for Advanced Power Engineering*, edited by Lecomte-Beckers, J., Carton, M., Schubert, F. & Ennis, P. J. (Liege, Belgium, 2002), pp. 1397-1406.

110. Miyata, K., Igarashi, M. & Sawaragi, Y., Effect of Trace Elements on Creep Properties of 0.06C-2.25Cr-1.6W-0.1Mo-0.25V-0.05Nb Steel. *ISIJ International* **39**, 947-954 (1999).

111. Tsuchida, Y. *et al.*, Internal Report, Nippon Steel Corporation, 1990.

112. Fujita, T. & Takahashi, N., The Effects of V and Nb on the Long Creep Rupture Strength of 12% Cr Heat-resisting Steels Containing Mo And B. *Transactions of the Iron and Steel Institute of Japan* **18**, 269-278 (1979).

113. Fujita, T., Asakura, K., Sawada, T., Takamatsu, T. & Otoguro, Y., Creep Rupture Strength and Microstructure of Low C-10Cr-2Mo Heat-resisting Steels with V and Nb. *Metallurgical Transactions A* **12A**, 1071-1079 (1981).

114. Ku, B. S. & Yu, J., Effect of Cu Additions on the Creep Rupture Properties of 12%Cr Steels. *Scripta Materialia* **45**, 205-211 (2001).

115. Taneike, M., Kondo, M. & Morimoto, T., Accelerated Coarsening of MX Carbonitrides in 12% Cr Steels during Creep Deformation. *ISIJ International* **41**, S111-S115 (2001).

116. Fujita, T., Development of High Chromium Ferritic Heat Resistant Steels for Power Plant. *Journal of Thermal Nuclear Power* **42**, 1485-1496 (1991).

117. Helis, L., Toda, Y., Hara, T., Miyazaki, H. & Abe, F., Effect of Cobalt on the Microstructure of Tempered Martensitic 9Cr Steels for Ultra-Supercritical Power Plants. *Materials Science and Engineering A* **510-511**, 88-94 (2009).

118. Yamada, K., Igarashi, M., Muneki, S. & Abe, F., Creep Properties Affected by Morphology of MX in High-Cr Ferritic Steels. *ISIJ International* **41**, S116-S120 (2001).

119. Perrin, J. & Fishburn, J. D., *A Perspective on the Design of High Temperature Boiler Components*, presented at ECCC Creep Conference, London, UK, 2005 (unpublished).

120. Abe, F., Bainitic and Martensitic Creep-resistant Steels. *Current Opinions in Solid State Materials* **8**, 305-311 (2004).

121. Jemian, P. R., Weertman, J. R., Long, G. G. & Spal, R. D., Characterization of 9Cr-1MoVNb Steel by Anomalous Small-angle X-ray Scattering. *Acta Metallurgica Materialia* **39**, 2477-2487 (1991).

122. Maziasz, P. J. & Sikka, V. K., The effects of 25,000 h Aging at 480 to 700℃ on Precipitation and Microstructural Stability in Several Heats of Tempered 9Cr-1MoVNb Steel, Alloy Development for Irradiation Performance, Semiannual progress report Report No. DOE/ER-0045/15, ORNL, pp. 102-116, 1985.

123. Paul, V. T., Saroja, S. & Vijayalakshmi, M., Microstructural Stability of Modified 9Cr-1Mo Steel during Long Term Exposures at Elevated Temperatures. *Journal of Nuclear Materials* **378**, 273-281 (2008).

124. Hätteststrand, M., Schwing, M. & Andrén, H.-O., Microanalysis of Two Creep Resistant 9-12% Chromium Steels. *Materials Science and Engineering A* **250**, 27-36 (1998).

125. Bazazi, A. A., Evolution of Microstructure during Long-term Creep of a Tempered Martensite Ferritic Steel, der Ruhr-Universität Bochum, Ph.D. Dissertation, 2009.

126. Hätteststrand, M. & Andrén, H.-O., Evaluation of Particle Size Distribution of Precipitates in a 9 Chromium Steels using Energy Filtered Transmission Electron Microscopy. *Micron* **32**, 789-797 (2001).

127. Hald, J. & Korcakova, L., Precipitate Stability in Creep Resistant Ferritic Steels – Experimental Investigations and Modelling. *ISIJ International* **43**, 420-427 (2003).

128. Gustafson, A. & Hattestrand, M., Coarsening of Precipitates in an Advanced Creep Resistant 9% Chromium Steel – Quantitative Microscopy and Simulations. *Metallurgical and Materials Transactions A* **333**, 279-286 (2002).

129. Hattestrand, M. & Andren, H. O., Microstructural Development during Ageing of an 11% Chromium Steel Alloyed with Copper. *Materials Science and Engineering A* **318**, 94-101 (2001).

130. Janovec, J., Vyrostkova, A., Svoboda, M., Kroupa, A. & Grabke, H. J., Evolution of Secondary Phases in Cr-V Low-alloy Steels during Aging. *Metallurgical and Materials Transactions A* **35A**, 751-759 (2004).

131. Sawada, K., Kubo, K. & Abe, F., Creep Behavior and Stability of MX Precipitates at High Temperature in 9Cr-0.5Mo-1.8W-VNb Steel. *Materials Science and Engineering A* **319-321**, 784-787 (2001).

132. Sawada, K., Kubo, K. & Abe, F., Contribution of Coarsening of MX Carbonitrides to Creep Strength Degradation in High Chromium Ferritic Steel. *Materials Science and Technology* **19**, 732-

738 (2003).

133. Skobir, D. A., Vodopivec, F., Spaic, S. & Markoli, B., Effect of Tempering on the Chemical and Phase Composition of MxCy Precipitates in Low Carbon Chromium-Molybdenum-Vanadium Steel. *Zeitschrift fur Metallkunde* **95**, 1020-1024 (2004).

134. Taneike, M., Sawada, K. & Abe, F., Effect of Carbon Concentration on Precipitation Behavior of M23C6 Carbides and MX Carbonitrides in Martensitic 9Cr Steel during Heat Treatment. *Metallurgical and Materials Transactions A* **35A**, 1255-1262 (2004).

135. Ennis, P. J. & Czyrska-Filemonowicz, A., Recent Advances in Creep-resistant Steels for Power Plant Applications. *OMMI* **1** (1) (2002).

136. Korcakova, L., Hald, J. & Somers, M. A. J., Quantification of Laves phase Particle Size in 9CrW Steel. *Materials Characterization* **47**, 111-117 (2001).

137. Li, Q. A., Precipitation of Fe2W Laves phase and Modeling of its Direct Influence on the Strength of a 12Cr-2W Steel. *Metallurgical and Materials Transactions A* **37A**, 89-97 (2006).

138. Murata, Y., Koyama, T., Morinaga, M. & Miyazaki, T., Prediction of the Laves phase Morphology in Fe-Cr-W-C Quaternary Steels with the Aid of System Free Energy Concept. *ISIJ International* **42**, 1423-1429 (2002).

139. Prat, O., Garcia, J., Rojas, D., Carrasco, C. & Inden, G., Investigations on the Growth Kinetics of Laves phase Precipitates in 12% Cr Creep-resistant Steels: Experimental and DICTRA Calculations. *Acta Materialia* **58**, 6142-6153 (2010).

140. Danielsen, H. K. & Hald, J., A Thermodynamic Model of the Z-phase Cr(V,Nb)N. *Computer Coupling of Phase Diagrams and Thermochemistry* **31**, 505-514 (2007).

141. Jack, D. H. & Jack, K. H., Carbide and Nitrides in Steels. *Materials Science and Engineering* **11**, 386-405 (1973).

142. Danielsen, H. K., Hald, J., Grumsen, F. B. & Somers, M. A. J., On the Crystal Structure of Z-Phase Cr(V,Nb)N. *Metallurgical and Materials Transactions A* **37A**, 2633-2640 (2006).

143. Danielsen, H. K. & Hald, J., Tantalum-containing Z-phase in 12% Cr Martensitic Steels. *Scripta Materialia* **60**, 811-813 (2009).

144. Danielsen, H. K. & Hald, J., On the Nucleation and Dissolution Process of Z-Phase Cr(V,Nb)N in Martensitic 12% Cr Steels. *Materials Science and Engineering A* **505**, 169-177 (2009).

145. Vodarek, V., Danielsen, H. K., Grumsen, F. B., Hald, J. & Strang, A., in *Proceedings of the 8th Liege Conference in Materials For Advanced Power Engineering*, edited by Lecomte-Beckers, J., Carton, M., Schubert, F. & Ennis, P. J. (Liege, Belgium, 2006), pp. 1251-1266.

146. Cipolla, L. *et al.*, Conversion of MX Nitrides to Z-phase in Martensitic 12% Cr Steels. *Acta Materialia* **58**, 669-679 (2010).

147. Letofsky-Papst, I., Warbichler, P., Hofer, F., Letofsky, E. & Cerjak, H., On the Occurrence of Z-phase in a Creep-tested 10% Cr Steel. *Zeitschrift fur Metallkunde* **95**, 18-21 (2004).

148. Sawada, K., Suzuki, K., Kushima, H., Tabuchi, M. & Kimura, K., Effect of Tempering Temperature on Z-phase Formation and Creep Strength in 9Cr-1Mo-V-Nb-N Steel. *Materials Science and Engineering A* **480**, 558-563 (2008).

149. Hald, J., Metallurgy and Creep Properties of New 9-12% Cr Steels. *Steel Research* **67**, 369-374 (1996).

150. Tchizhik, T. A., Tchizhik, T. A. & Tchizhik, A. A., Optimization of the Heat Treatment for Steam and Gas Turbine Parts Manufactured from 9-12% Cr Steels. *Journal of Materials Processing Technology* **77**, 226-232 (1998).

151. Bhadeshia, H. K. D. H., Design Of Ferritic Creep-Resistant Steels. *ISIJ International* **41**, 626-640 (2001).

152. Bhadeshia, H. K. D. H., Strang, A. & Gooch, D. J., Ferritic Power Plant Steels: Remanent Life Assessment and Approach to Equilibrium. *International Materials Reviews* **43**, 45-69 (1998).

153. Tawancy, H. M. & Al-Hdhrami, L., Failure of Refurbished Turbine Blades in a Power Station by Improper Heat Treatment. *Engineering Failure Analysis* **16** (3), 810-815 (2009).

154. Ennis, P. J. & Quadakkers, W. J., High chromium martensitic steels - microstructure properties and potential for further development. *VGB PowerTech* **8**, 87-90 (2001).

155. Czyrska-Filemonowicz, A., Zielińska-Lipiec, A. & Ennis, P. J., Modified 9% Cr steels for advanced power generation: microstructure and properties. *Journal of Achievements in Materials and Manufacturing Engineering* **19** (2), 43-48 (2006).

156. Jones, W. B., Effects of Mechanical Cycling on the Substructure of Modified 9Cr1Mo Ferritic Steel, op. cit. (63), 221-235.

157. Pickering, F. B. & Vassilou, A. D., Effect of Austenitizing Temperature on Constitution, Transformation and Tempering of 9Cr-1Mo Steels. *Metals Technology* **7**, 409-413 (1980).

158. Thomson, R. C. & Bhadeshia, H. K. D. H., Changes in Chemical-composition of Carbides in 2.25Cr-1Mo Power-plant Steel. 2. Mixed Microstructure. *Materials Science and Technology* **10**, 205-208 (1994).

159. Tsai, M. C., Chiou, C. S. & Yang, J. R., Microstructural Evolution of Simulated Heat-affected Zone in Modified 2.25Cr-1Mo Steel during High Temperature Exposure. *Journal of Materials Science* **38**, 2373-2391 (2003).

160. Brozda, J. & Zeman, M., Weldability of 9Cr-1Mo-Nb, V P91 steel intended for service in the power industry. *Welding International* **10** (5), 370-380 (1996).

161. Fournier, B. *et al.*, Creep-Fatigue Interactions in a 9%Cr-1%Mo Martensitic Steel: Part II. Microstructural Evolutions. *Metallurgical and Materials Transactions A* **40A**, 330-341 (2009a).

162. Kitahara, H., Ueji, R., Tsuji, N. & Minamino, Y., Crystallographic features of lath martensite in low-carbon steel. *Acta Materialia* **54**, 1279-1288 (2006).

163. Vitek, J. M. & Klueh, R. L., Precipitation Reactions During the Heat Treatment of Ferritic Steels. *Metallurgical Transactions A* **14A**, 1047-1055 (1983).

164. Orr, J., Beckitt, F. R. & Fawkes, G. D., in *Ferritic steels for fast reactor steam generators*, edited by Pugh, S. F. & Little, E. A. (British Nuclear Energy Society, London, UK, 1978), pp. 99-109.

165. Hald, J., *Microstructure and long-term creep properties of 9-12%Cr steels*, presented at ECCC Creep Conference on creep and fracture in high temperature components - design & life assessment issues, pp. 20-30, London, U.K., 2005 (unpublished).

166. Orlova, A., Bursik, J., Kucharova, K. & Sklenicka, V., Microstructural Development during High Temperature Creep of 9%Cr Steel. *Materials Science and Engineering* **A245**, 39-48 (1998).

167. Tokuno, K., Hamada, K., Uemori, R., Takeda, T. & Itoh, K., A Complex Carbonitride of Niobium and Vanadium in 9% Cr Ferritic Steels. *Scripta Metallurgica Materialia* **25**, 871-876 (1991).

168. Tokuno, K., Hamada, K., Uemori, R., Takeda, T. & Itoh, K., Role of a Complex Carbonitride of Niobium and Vanadium in Creep Strength of 9% Cr Ferritic Steels. *Scripta Metallurgica Materialia* **25**, 1763-1768 (1991).

169. Maruyama, K., Sawada, K. & Koike, J., Strengthening Mechanisms of Creep Resistant Tempered Martensitic Steel P92 for Advanced Power Plant. *ISIJ International* **41**, 641-653 (2001).

170. Reed-Hill, R. E., *Physical Metallurgy Principles* (D. Van Nostrand Company, New Jersey, USA,

1964).

171. Thomson, R. C. & Bhadeshia, H. K. D. H., Carbide Precipitation in 12Cr1MoV Power Plant Steel. *Metallurgical Transactions A* **23**, 1171-1179 (1992).

172. Ennis, P. J., ZielinskaLipiec, A., Wachter, O. & Czvrska, F. A., Microstructural Stability and Creep Rupture Strength of the Martensitic Steel P92 for Advanced Power Plant. *Acta Materialia* **45**, 4901-4907 (1997).

173. Ridley, N., Maropoulos, S. & Paul, J. D. H., Effects of Heat Treatment on Microstructure and Mechanical Properties of Cr-Mo-3.5Ni-V Steel. *Materials Science and Technology* **10**, 239-249 (1994).

174. Takeuchi, S. & Argon, A. S., Steady State Creep of Single Phase Crystalline Matter at High Temperature. *Journal of Materials Science* **11**, 1542-1566 (1976).

175. Masuyama, F., Creep Degradation in Welds of Modified 9Cr-1Mo Steel. *International Journal of Pressure Vessels and Piping* **83**, 819-825 (2006).

176. Giroux, P. F. *et al.*, Mechanical and Microstructural Stability of P92 Steel under Uniaxial Tension at High Temperature. *Materials Science and Engineering A* **527**, 3984-3993 (2010).

177. Hu, Z. F. & Yang, Z. G., Identification of the Precipitates by TEM and EDS in X20CrMoV12-1 after Long-term Service at Elevated Temperature. *Journal of Materials Engineering and Performance* **12**, 106-111 (2003).

178. Straub, S., Hennige, T., Polcik, P. & Blum, W., Microstructure and Deformation Rate during Long-term Cyclic Creep of the Martensitic Steel X22CrMoV12-1. *Steel Research* **66**, 394-401 (1995).

179. Blum, W. & Straub, S., Subgrain Growth during Creep of a Tempered Martensitic 12% Cr steel. *Steel Research* **62**, 72-74 (1991).

180. Chung, Y. K., Park, J. J., Joo, C. H. & Park, I. M., Characteristics of Material Degradation for Thermal Aged X20CrMoV12-1 steel. *Designing, Processing and Properties of Advanced Engineering Materials* **449-454 (Pts 1 and 2)**, 537-540 (2004).

181. Hu, Z. F. & Yang, Z. G., An Investigation of the Embrittlement in X20CrMoV12-1 Power Plant Steel after Long-term Service Exposure at Elevated Temperature. *Metallurgical and Materials Transactions A* **383**, 224-228 (2004).

182. Skobir, D. A., Jenko, M. & Mandrino, D., The Characterization of Various Chromium Carbide

Compounds in X20CrMoV121 steel. *Surface and Interface Analysis* **36**, 941-944 (2004).

183. Skobir, D. A., Godec, M., Jenko, M. & Markoli, B., Characterization of the Carbides in the Steel X20CrMoV12-1 used in Thermal Power Plants. *Surface and Interface Analysis* **40**, 512-517 (2008).

184. Storesund, J., Borggreen, K. & Zang, W. L., Creep Behavior and Lifetime of Large Welds in X20CrMoV 12 1 – Results Based on Simulation and Inspection. *International Journal of Pressure Vessels and Piping* **83**, 875-883 (2006).

185. Straub, S. *et al.*, Microstructural Evolution of the Martensitic Cast Steel GX12CrMoVNbN9-1 during Long-term Annealing and Creep. *Steel Research* **66**, 402-408 (1995).

186. Straub, S. *et al.*, Microstructural Stability of the Martensitic Steel X20CrMoV12-1 After 130000 h of Service at 530°C. *Steel Research* **68**, 368-373 (1997).

187. Rojas, D. *et al.*, Design and Characterization of Microstructure Evolution during Creep of 12% Cr Heat Resistant Steels. *Materials Science and Engineering A* **527**, 3864-3876 (2010).

188. Sklenicka, V. *et al.*, Long-term Creep Behavior of 9-12% Cr Power Plant Steels. *Materials Characterization* **51**, 35-48 (2003).

189. Kadoya, Y., Dyson, B. E. & McLean, M., Microstructural Stability during Creep of Mo- or W-bearing 12Cr Steels. *Metallurgical and Materials Transactions A* **33**, 2549-2557 (2002).

190. Qin, Y., Gotz, G. & Blum, W., Subgrain Structure during Annealing and Creep of the Cast Martensitic Cr-steel G-X12CrMoWVNbN 10-1-1. *Metallurgical and Materials Transactions A* **341**, 211-215 (2003).

191. Rojas, D. *et al.*, Effect of Processing Parameters on the Evolution of Dislocation Density and Sub-grain Size of a 12% Cr Heat Resistant Steel during Creep at 650°C. *Materials Science and Engineering A* **528**, 1372-1381 (2011).

192. Mayr, P. T. & Holzer, I., Microstructure Evolution During Production – General Principles, Cost Summer School, Lanzarote, 2008.

193. Eggeler, G., The Effect of Long-term Creep on Particle Coarsening in Tempered Martensite Ferritic Steels. *Acta Metallurgica* **37**, 3225-3234 (1989).

194. Voorhees, P. W., The Theory of Ostwald Ripening. *Journal of Statistical Physics* **38**, 231-252 (1985).

195. Bladan, A., Review Progress in Ostwald Ripening Theories and their Applications to Nickel-Base Superalloys – Part I: Ostwald Ripening Theories. *Journal of Materials Science* **37**, 2171-2202

(2002).

196. Wey, M. Y., Sakuma, T. & Nishizawa, T., Growth of Alloy Carbide Particles in Austenite. *Transactions of the Japanese Institute of Metals* **22**, 733-742 (1981).

197. Abe, F., Araki, H. & Noda, T., Microstructural Evolution in Bainite, Martensite and delta-Ferrite of Low Activation Cr-2W Ferritic Steels. *Materials Science and Technology* **6**, 714-723 (1990).

198. Dronhofer, A. H., Pešička, J., Dlouhy, A. & Eggeler, G., On the Nature of Internal Interfaces in Tempered Martensite Ferritic Steels. *Zeitschrift fur Metallkunde* **94**, 511-520 (2003).

199. Blum, W. & Götz, G., Evolution of Dislocation Structure in Martensitic CrMoV Steels: The Subgrain Size as Sensor for Creep Strain and Residual Creep Life. *Steel Research* **70**, 274-278 (1999).

200. Blum, W. & Eisenlohr, P., Dislocation Mechanics of Creep. *Materials Science and Engineering A* **510-511**, 7-13 (2009).

201. Sikka, V. K., Ward, C. T. & Thomas, K. C., *Technical Program and data package for use of modified 9%Cr-1%Mo steel*, presented at ASME Sections I and VIII, 1982 (unpublished).

202. Brinkman, C. R., Alexander, D. J. & Maziasz, P. J., presented at Proceedings in the Joint ASME/IEEE power generation Conference, Boston, 1990 (unpublished).

203. ECCC Datasheets, ETD, 2005.

204. Bendick, W., Cipolla, L., Gabrel, J. & Hald, J., New ECCC assessment of creep rupture strength for steel grade X10CrMoVNb9-1 (Grade 91). *International Journal of Pressure Vessels and Piping* **87** (6), 304-309 (2010).

205. Gaffard, V., Besson, J. & Gourgues-Lorenzon, A. F., Creep Failure Model of a Tempered Martensitic Stainless Steel Integraiting Multiple Deformation and Damage Mechanisms. *International Journal of Fracture* **133**, 139-166 (2005).

206. Gaffard, V., Gourgues-Lorenzon, A. F. & Besson, J., High Temperature Creep Flow and Damage Properties of the Weakest Area of 9Cr1Mo-NbW Martensitic Steel Weldments. *ISIJ International* **45** (12), 1915-1924 (2005).

207. Kloc, L. & Fiala, J., On Creep Behaviour of Several Metallic Materials at Low Stresses and Elevated Temperatures. *Chemical Papers* **53** (3), 155-164 (1999).

208. Kloc, L. & Fiala, J., Viscous Creep in Metals at Intermediate Temperatures. *Kovove Materialy* **43**

(2), 105-112 (2005).

209. Kloc, L. & Sklenicka, V., Transition from Power-law to Viscous Creep Behaviour of P91 Type Heat-resistant Steel. *Materials Science and Engineering* **A234-A236**, 962-965 (1997).

210. Kloc, L. & Sklenicka, V., Confirmation of Low Stress Creep Regime in 9% Chromium Steel by Stress Change Creep Experiments. *Materials Science and Engineering* **A387-A389**, 633-638 (2004).

211. Kloc, L., Sklenicka, V., Dlouhy, A. A. & Kucharova, K., in *Microstructural Stability of Creep Resistant Alloys for High Temperature Plant Applications*, edited by Strang, A., Cawley, J. & Greenwood, G. W. (Cambridge University Press, Cambridge, UK, 1998), pp. 445-455.

212. Kloc, L., Sklenicka, V. & Ventruba, J., Comparison of Low Creep Properties of Ferritic and Austenitic Creep Resistant Steels. *Materials Science and Engineering* **A319-A321**, 774-778 (2001).

213. Sklenicka, V., Kucharova, K., Kloc, L. & Svoboda, M., in *Advances in Materials Technology for Fossil Power Plants: Proceedings of the 4th International Conference* , edited by Viswanathan, R., Gandy, D. & Coleman, K. (ASM International, Materials Park, Ohio, USA, 2004), pp. 1086-1100.

214. Sklenicka, V., Kucharova, K., Kloc, L., Svoboda, M. & Staubli, M., in *Materials for Advances Power Engineering 2002: Proceedings of the 7th Liege Conference*, edited by Lecomte-Beckers, J., Carton, M., Schubert, F. & Ennis, P. J. (Institut fur Werkstoffe und Verfahren der Energietechnik, Forschungszentrum, Julich, Germany, 2002), pp. 1189-1200.

215. Sklenicka, V., Kucharova, K., Kudrman, J., Svoboda, M. & Kloc, L., Microstructure Stability and Creep Behaviour of Advanced High Chromium Ferritic Steels. *Kovove Materialy* **43** (1), 20-33 (2005).

216. Hagen, I. V. & Bendick, W., *Creep resistant ferritic steels for power plants*, presented at International Symposium on Niobium 2001, 2001 (unpublished).

217. Sklenicka, V., Kucharova, K., Svoboda, M. & Cmakal, J., *Creep behavior and microstructural changes in 9-12% Cr steels under nonsteady loading*, presented at New developments on Metallurgy and applications of high strength steels, Buenos Aires, 2008 (unpublished).

218. Gianfrancesco, D., Matera, A. & Tassa, O., Properties and microstructure of modified 9%Cr steels. *La Revue de Metallurgie-CIT* **98** (1), 117-123 (2001).

219. Holdsworth, S. R. *et al.*, Factors influencing creep model equation selection. *International Journal of Pressure Vessels and Piping* **85**, 80-88 (2008).

220. Holmström, S., Engineering Tools for Robust Creep Modeling, The Aalto University School of

Science and Technology, Espoo, Finland, Ph.D. Dissertation, 2010.

221. Wells, C. H., in *High-temperature fatigue, in Fatigue and Microstructure*, edited by Meshii, M. (American Society for Metals, Metals Park, 1979), pp. 307-331.

222. Suresh, S., *Fatigue of Materials*, 2nd ed. (Cambridge University Press, Cambridge,UK, 1998).

223. Kunz, L. & Lukas, P., in *High temperature fatigue and cyclic creep of P91 steel, in Temperature-Fatigue Interaction*, edited by Rémy, L. & Petit, J. (Elsevier Science Ltd. and ESIS, 2002), pp. 37-44.

224. Fournier, B., Sauzay, M., Caës, C., Noblecourt, M. & Mottot, M., Analysis of the hysteresis loops of a martensitic steel. Part I: Study of the influence of strain amplitude and temperature under pure fatigue loadings using an enhanced stress partitioning method. *Materials Science and Engineering A* **437**, 183-196 (2006).

225. Fournier, B. *et al.*, Analysis of the hysteresis loops of a martensitic steel: Part II: Study of the influence of creep and stress relaxation holding times on cyclic behavior. *Materials Science and Engineering: A* **437** (2), 197-211 (2006).

226. Choudhary, B. K., Bhanu Sankara Rao, K. & Mannan, S. L., High-temperature low cycle fatigue properties of a thick-section 9wt.%Cr-1wt.%Mo ferritic steel forging. *Materials Science and Engineering A* **148**, 267-278 (1991).

227. Mannan, S. L. & Valsan, M., High-temperature low cycle fatigue, creep-fatigue and thermomechanical fatigue of steels and their welds. *International Journal of Mechanical Sciences* **48**, 160-175 (2006).

228. Ebi, G. & McEvily, A. J., Effect of Processing on the High Temperature Low Cycle Fatigue Properties of Modified 9Cr-1Mo Ferritic Steel. *Fatigue & Fracture of Engineering Materials & Structures* **7** (4), 299-314 (1984).

229. Kim, S. & Weertman, J. R., Investigation of microstructural changes in a ferritic steel caused by high temperature fatigue. *Metallurgical Transactions A* **19**, 999-1007 (1988).

230. Fournier, B. *et al.*, Creep-Fatigue Interactions in a 9 Pct Cr-1 Mo Martensitic Steel: Part I. Mechanical Test Results. *Metallurgical and Materials Transactions A* **40A**, 321-329 (2009).

231. Wood, D. S., Baldwin, A. B. & Williamson, K., *The creep/fatigue behaviour of 9%Cr steel at 525C*, presented at Proceedings of the IAEA Meeting on Time and Load Dependent Degradation of Pressure boundary Materials, Innsbruck, 1979 (unpublished).

232. Gieseke, B. G., Brinkman, C. R. & Maziasz, P. J., in *The influence of thermal aging on the microstructure and fatigue properties of modified 9Cr-1Mo steel, in Microstructures and mechanical properties of*

aging material, edited by Liaw, P. K., Viswanathan, R., Murty, K. L., Simonen, E. P. & Frear, D. (The Minerals, Metals & Materials Society, Warrendale, 1993).

233. Holdsworth, S. R., Creep-fatigue properties of high temperature turbine steels. *Materials at High Temperatures* **18**, 261-265 (2001).

234. Aoto, K., Komine, R., Ueno, F., Kawasaki, H. & Wada, Y., Creep–fatigue evaluation of normalized and tempered modified 9Cr-1Mo. *Nuclear Engineering Design* **153**, 97-110 (1994).

235. Tavassoli, A. A., Mottot, M., Bretherton, I. & Wareing, J., Fatigue and creep-fatigue failure in wrought modified 9Cr–1Mo ferritic steel, AEA Technology - AEAT-0539, 1997.

236. Fournier, B. *et al.*, Creep-fatigue-oxidation interactions in a 9Cr-1Mo martensitic steel. Part I: Effect of tensile holding period on fatigue lifetime. *International Journal of Fatigue* **30**, 649-662 (2008).

237. Fournier, B. *et al.*, Creep-fatigue-oxidation interactions in a 9Cr-1Mo martensitic steel. Part II: Effect of compressive holding period on fatigue lifetime. *International Journal of Fatigue* **30**, 663-676 (2008).

238. Fournier, B. *et al.*, Creep–fatigue–oxidation interactions in a 9Cr–1Mo martensitic steel. Part III: Lifetime prediction. *International Journal of Fatigue* **30** (10-11), 1797-1812 (2008).

239. Shankar, V. *et al.*, Low cycle fatigue behavior and microstructural evolution of modified 9Cr–1Mo ferritic steel. *Materials Science and Engineering: A* **437** (2), 413-422 (2006).

240. Sugiura, T., Ishikawa, A., Nakamura, T. & Asada, Y., Formulation of air environmental effect on creep–fatigue interaction. *Nuclear Engineeering Design* **153**, 87-95 (1994).

241. Kannan, R., Sandhya, R., Ganesan, V., Valsan, M. & Rao, K. B. S., Effect of sodium environment on the low cycle fatigue properties of modified 9Cr–1Mo ferritic martensitic steel. *Journal of Nuclear Materials* **384** (3), 286-291 (2009).

242. Asayama, T., JAEA Task 10 Final Report, 2009.

243. Tanaka, K. & Mura, T., A Dislocation Model for Fatigue Crack Initiation. *Journal of Applied Mechanics* **48** (1), 97-103 (1981).

244. DOE/ASME, Generation IV Materials Project Task 5 Report, 2005.

245. Takahashi, Y., Study on creep-fatigue evaluation procedures for high-chromium steels – Part I: Test results and life prediction based on measured stress relaxation. *International Journal of Pressure*

Vessels and Piping **85**, 406-422 (2008).

246. Hoffelner, W., A Strain Range Partitioning type approach for the determination of creep-fatigue (cyclic creep) in modified 9Cr-1Mo steel, RWH, Oberrohrdorf , 2008.

247. Prager, M., Extended Low Chrome Steel Fatigue Rules: An approach for pressure vessel applications of 2 1/4 Cr-1Mo-V and similar materials, BPVC #2- RFP-ASME ST-07-04, ASME ST-LLC Research Project, 2004.

248. HPIS C107 TR 2005, Creep-Fatigue Life Evaluation Scheme for Ferritic Component at Elevated Temperature, High Pressure Institute of Japan, 2005.

249. Jetter, R., An Alternate Approach to Evaluation of Creep-Fatigue Damage for High Temperature Structural Design Criteria, PVP- Vol 5, H01146-1998, Fatigue, Fracture and High Temperature Design Methods in Pressure Vessel and Piping, 1998.

250. Chaboche, J. L., A review of some plasticity and viscoplasticity constitutive theories. *International Journal of Plasticity* **24**, 1642–1693 (2008).

251. Déprés, C., Fivel, M. & Tabourot, L., A dislocation-based model for low-amplitude fatigue behavior of face-centred cubic single crystals. *Scripta Materialia* **58** (12), 1086-1089 (2008).

252. Gomez, J. & Basaran, C., A thermodynamics based damage mechanics constitutive model for low cycle fatigue analysis of microelectronics solder joints incorporating size effects. *International Journal of Solids and Structures* **42**, 3744–3772 (2005).

253. Kubin, L. P. & Estrin, Y., Evolution of dislocation densities and the critical conditions for the Portevin-Lechatelier effect. *Acta Metallurgica et Materialia* **38** (5), 697-708 (1990).

254. Ma, A. & Roters, F., A constitutive model for fcc single crystals based on dislocation densities and its application to uniaxial compression of aluminium single crystals. *Acta Materialia* **52**, 3603-3612 (2004).

255. Mayama, T., Sasaki, K. & Ishikawa, H., A constitutive model of cyclic viscoplasticity considering changes in subsequent viscoplastic deformation due to the evolution of dislocation structures. *International Journal of Plasticity* **23** (5), 915-930 (2007).

256. Mayer, T., Balogh, L., Solenthaler, C., Müller, E. & Holdsworth, S. R., Dislocation density and sub-grain size evolution of 2CrMoNiWV during low cycle fatigue at elevated temperatures. *Acta Materialia* **6**, 2485-2496 (2012).

257. Pham, M. S. & Holdsworth, S. R., Dynamic strain ageing of AISI 316L during cyclic loading at

300 °C: Mechanism, evolution, and its effects. *Materials Science & Engineering A*, In Press (2012).

258. Saï, K., Multi-mechanism models: Present state and future trends. *International Journal of Plasticity* **27** (2), 250–281 (2011).

259. Staroselsky, A. & Cassenti, B. N., Creep, plasticity, and fatigue of single crystal superalloy. *International Journal of Solids and Structures* **48**, 2060–2075 (2011).

260. Voyiadjis, G. Z. & Abed, F. H., Effect of dislocation density evolution on the thermomechanical response of metals with different crystal structures at low and high strain rates and temperatures. *Archives of Mechanics* **57** (4), 299-343 (2005a).

261. Wang, A.-J., Kumar, R. S., Shenoy, M. M. & McDowell, D. L., Microstructure-based multiscale constitutive modeling of γ-γ' Nickel-base superalloys. *International Journal for Multiscale Computational Engineering* **4** (5&6), 663-692 (2006).

262. Lemaitre, J. & Chaboche, J.-L., *Mechanics of Solid Materials* (Cambridge University Press, Cambridge, 1994).

263. Beyerlein, I. J. & Tomé, C. N., A dislocation-based constitutive law for pure Zr including temperature effects. *International Journal of Plasticity* **24** (5), 867-895 (2008).

264. Khan, A. S. & Baig, M., Anisotropic responses, constitutive modeling and the effects of strain-rate and temperature on the formability of an aluminum alloy. *International Journal of Plasticity* **27**, 522-538 (2011).

265. Khan, A. S. & Liang, R. Q., Behaviors of three BCC metal over a wide range of strain rates and temperatures: experiments and modelling. *International Journal of Plasticity* **15**, 1089-1109 (1999).

266. Sung, J. H., Kim, J. H. & Wagoner, R. H., A plastic constitutive equation incorporating strain, strain-rate, and temperature. *International Journal of Plasticity* **26**, 1746-1771 (2010).

267. Uenishi, A. & Teodosiu, C., Constitutive modeling of the high strain rate behavior of interstitial-free steel. *International Journal of Plasticity* **20**, 915-936 (2004).

268. Voyiadjis, G. Z. & Abed, F. H., Microstructural based models for BCC and FCC metals with temperature and strain rate dependency. *Mechanics of Materials* **37** (2-3), 355-378 (2005b).

269. Zerilli, F. J. & Armstrong, R. W., Dislocation mechanics-based constitutive relations for material dynamics calculation. *Journal of Applied Physics* **5**, 1816-1825 (1987).

270. Okrajni, J., Junak, G. & Marek, A., Modelling of the deformation process under thermo-

mechanical fatigue conditions. *International Journal of Fatigue* **30**, 324–329 (2008).

271. Aktaa, J. & Petersen, C., Challenges in the constitutive modeling of the thermo-mechanical deformation and damage behavior of Eurofer 97. *Engineering Fracture Mechanics* **76**, 1474–1484 (2009).

272. Aktaa, J. & Petersen, C., Modeling the constitutive behavior of RAFM steels under irradiation conditions. *Journal of Nuclear Materials* **417** (1-3), 1123-1126 (2011).

273. Aktaa, J. & Schmitt, R., High temperature deformation and damage behavior of RAFM steels under low cycle fatigue loading: Experiments and modeling. *Fusion Engineering and Design* **81** (19), 2221–2231 (2006).

274. Koo, G.-H.. & Kwon, J.-H.., Identification of inelastic material parameters for modified 9Cr-1Mo steel applicable to the plastic and viscoplastic constitutive equations. *International Journal of Pressure Vessels and Piping* **88**, 26-33 (2011).

275. Koo, G.-H. & Lee, J.-H., Investigation of ratcheting characteristics of modified 9Cr-1Mo steel by using the Chaboche constitutive model. *International Journal of Pressure Vessels and Piping* **84**, 284–292 (2007).

276. Saad, A. A., Sun, W., Hyde, T. H. & Tanner, D. W. J., Cyclic softening behaviour of a P91 steel under low cycle fatigue at high temperature. *Procedia Engineering* **10**, 1103–1108 (2011).

277. Taguchi, K., Kanno, E., Ozaki, S. & Uno, T., Application of the overstress concept to inelastic behavior and evaluation of creep-fatigue damage for modified 9Cr-1Mo steel. *International Journal of Pressure Vessels and Piping* **44** (1), 99-115 (1990).

278. Yaguchi, M. & Takahashi, Y., A viscoplastic constitutive model incorporating dynamic strain aging effect during cyclic deformation conditions. *International Journal of Plasticity* **16** (3-4), 241-262 (2000).

279. Fournier, B., Sauzay, M. & Pineau, A., Micromechanical model of the high temperature cyclic behavior of 9–12%Cr martensitic steels. *International Journal of Plasticity* **27**, 1803-1816 (2011).

280. Fournier, B. *et al.*, in *Creep and Fracture in High Temperature Components – Design and Life Assessment Issues* (Destech Publications Inc., Pennsylvania, USA, 2005).

281. Sauzay, M., Fournier, B., Mottot, M., Pineau, A. & Monnet, I., Cyclic softening of martensitic steels at high temperature – Experiments and physically based modelling. *Materials Science and Engineering A* **483–484**, 410–414 (2008).

282. Sauzay, M. *et al.*, Cyclically induced softening due to low-angle boundary annihilation in a martensitic steel. *Materials Science and Engineering A* **400-401**, 241–244 (2005).

283. Giroux, P.-F. *et al.*, Influence of strain rate on P92 microstructural stability during fatigue tests at high temperature. *Procedia Engineering* **2** (1), 2141–2150 (2010).

284. ASTM E8-06, Standard Test Methods for Tension Testing of Metallic Materials, Annual Book of ASTM Standards, ASTM International, West Conshohocken, PA, 2006.

285. Thomas, G. B. & Varma, R. K., in *Review of BCR/VAMAS Low Cycle Fatigue Intercomparison Programme", Chapter 8, Harmonization of Testing Practice for High Temperature Materials*, edited by Loveday, M. S. & Gibbons, T. B. (Elsevier Applied Science, London, UK, 1992), pp. 155-185.

286. Kalyanasundaram, V., Saxena, A., Narasimhachary, S. & Dogan, B., ASTM round-robin on creep-fatigue and creep behavior of P91 steel. *Journal of ASTM International* **8** (4), 1-10 (2011a).

287. Parker, J., (P91 material offered by Kent K. Coleman, EPRI) private communication to Ashok Saxena, 2009.

288. Kalyanasundaram, V., Saxena, A., Holdsworth, S. R. & Dogan, B., Report Work Item Number: WK 20360, 2012.

289. ASTM E691 – 09, Standard Practice for Conducting an Interlaboratory Study to Determine the Precision of a Test Method, ASTM International, West Conshohocken, PA.

290. Gold, M., Tanzosh, J., Swindeman, R. W., Maziasz, P. J. & Santella, M. L., Safe use limits for advanced ferritic steels in Ultra-supercritical power boilers, CRADA Final Report Report No. ORNL00-0598.

291. Hirth, J. P. & Lothe, J., *Theory of Dislocations* (Wiley Interscience, New York, 1982).

292. Schuh, C. A., Mason, J. K. & Lund, A. C., Quantitative insight into dislocation nucleation from high-temperature nanoindentation experiments. *Nature Materials* **4**, 617-621 (2005).

293. Weiss, J. & Marsan, D., Three-Dimensional Mapping of Dislocation Avalanches: Clustering and Space/Time Coupling. *Science* **299** (5603), 89-92 (2003).

294. Sun, L., Krasheninnikov, A. V., Ahlgren, T., Nordlund, K. & Banhart, F., Plastic Deformation of Single Nanometer-Sized Crystals. *Physical Review Letters* **101**, 156101 (2008).

295. Minor, A. M. *et al.*, A new view of the onset of plasticity during the nanoindentation of aluminium. *Nature Materials* **5**, 697-702 (2006).

296. Sammonds, P., Plasticity goes supercritical. *Nature Materials* **4**, 425-426 (2005).

297. Schwaiger, R., Moser, B., Dao, M., Chollacoop, N. & Suresh, S., Some critical experiments on the strain-rate sensitivity of nanocrystalline nickel. *Acta Materialia* **51**, 5159-5172 (2003).

298. Uchic, M. D., Dimiduk, D. M., Florando, J. N. & Nix, W. D., Sample Dimensions Influence Strength and Crystal Plasticity. *Science* **305** (5686), 986-989 (2004).

299. Kumar, K. S., Suresh, S., Chisholm, M. F., Horton, J. A. & Wang, P., Deformation of electrodeposited nanocrystalline nickel. *Acta Materialia* **51**, 387-405 (2003).

300. Li, J., Vliet, K. J. V., Zhu, T., Yip, S. & Suresh, S., Atomistic mechanisms governing elastic limit and incipient plasticity in crystals. *Nature* **418**, 307-310 (2002).

301. Shan, Z. W., Mishra, R. K., Syed Asif, S. A., Warren, O. L. & Minor, A. M., Mechanical annealing and source-limited deformation in submicrometre-diameter Ni crystals. *Nature Materials* **7**, 115-119 (2008).

302. Ziegenhain, G. & Urbassek, H. M., Reversible plasticity under nanoindentation of atomically flat and stepped surfaces of fcc metals. *Philosophical Magazine Letters* **89** (11), 717-723 (2009).

303. Kuhlmann-Wilsdorf, D., The theory of dislocation-based crystal plasticity. *Philosophical Magazine A* **79** (4), 955-1008 (1999).

304. Cottrell, A. H., *Dislocations in Solids, Nabarro, F.N.R.; Duesbery, M.S. Eds. Vol. 11, page vii* (Elsevier, Amsterdam, 2002).

305. Boyer, H. W., *Atlas of Stress Strain Curves* (American Society of Metals, Metals Park, OH, 1987).

306. Nadgorny, E., *Dislocation Dynamics and Mechanical Properties of Crystals* (Pergamon Press, Oxford, 1988).

307. Tanaka, H., Kawasaki, T., Shintani, H. & Watanabe, K., Critical-like behaviour of glass-forming liquids. *Nature Materials* **9**, 324-331 (2010).

308. Fultz, B. ., Vibrational thermodynamics of materials. *Progress in Materials Science* **55** (4), 247-352 (2010).

309. Saha, A., Lahiri, S. & Jayannavar, A. M., Entropy production theorems and some consequences. *Physical Review E* **80** (1), 011117 (1-10) (2009).

310. Kondepudi, D. & Prigogine, I., *Modern Thermodynamics. From Heat Engines to Dissipative Structures*

(Wiley, Chichester, 1998).

311. Sun, S., Adams, B. L. & King, W. E., Observations of lattice curvature near the interface of a deformed aluminium bicrystal. *Philosophical Magazine* **80**, 9-25 (2000).

312. Alsayed, A. M., Islam, M. F., Zhang, J., Collings, P. J. & Yodh, A. G., Premelting at Defects Within Bulk Colloidal Crystals. *Science* **309**, 1207-1210 (2005).

313. Li, Z. Y. *et al.*, Three-dimensional atomic-scale structure of size-selected gold nanoclusters. *Nature* **451**, 46-48 (2008).

314. Zhang, H., Srolovitz, D. J., Douglas, J. F. & Warren, J. A., Characterization of atomic motion governing grain boundary migration. *Physical Review B* **74**, 115404 (2006).

315. Knap, J. & Ortiz, M., Effect of Indenter-Radius Size on Au(001) Nanoindentation. *Physical Review Letters* **90** (22), 226102 (2003).

316. Nicolis, G. & Prigogine, I., *Self-Organization in Nonequilibrium Systems: From Dissipative Structures to Order through Fluctuations* (Wiley, New York, 1977).

317. Kardar, M., Parisi, G. & Zhang, Y.-C., Dynamic scaling of growing interfaces. *Physical Review Letters* **56**, 889-892 (1986).

318. Legros, M., Gianola, D. S. & Hemker, K. J., In situ TEM observations of fast grain-boundary motion in stressed nanocrystalline aluminum films. *Acta Materialia* **56**, 3380-3393 (2008).

319. Mompiou, F., Caillard, D. & Legros, M., Grain boundary shear-migration coupling – I. In situ TEM straining experiments in Al polycrystals. *Acta Materialia* **57**, 2198-2209 (2009).

320. Rupert, T. J., Gianola, D. S., Gan, Y. & Hemker, K. J., Experimental Observations of Stress-Driven Grain Boundary Migration. *Science* **326**, 1686-1690 (2009).

321. Wang, Y. B., Sui, M. L. & Ma, E., In situ observation of twin boundary migration in copper with nanoscale twins during tensile deformation. *Philosophical Magazine Letters* **87** (12), 935-942 (2007).

322. Puglisi, G. & Truskinovsky, L., Thermodynamics of rate-independent plasticity. *Journal of Mechanics and Physics of solids* **53**, 655–679 (2005).

323. Gerberich, W. W. *et al.*, Superhard silicon nanospheres. *Journal of the Mechanics and Physics of Solids* **51** (6), 979-992 (2003).

324. Gleiter, H., Nanocrystalline materials. *Progress in Materials Science* **33** (4), 223-315 (1989).

325. Khalfallah, O., Condat, M. & Priester, L., Image force on a lattice dislocation due to a grain boundary in b.c.c. metals. *Philosophical Magazine A* **67** (1), 231-250 (1993).

326. Koning, M. d. *et al.*, Modeling of dislocation–grain boundary interactions in FCC metals. *Journal of Nuclear Materials* **323**, 281-289 (2003).

327. Furukawa, A. & Tanaka, H., Inhomogeneous flow and fracture of glassy materials. *Nature Materials* **8**, 601-609 (2009).

328. Bulatov, V. V. *et al.*, Dislocation multi-junctions and strain hardening. *Nature* **440**, 1174-1178 (2006).

329. Moretti, P., Miguel, M.-C., Zaiser, M. & Zapperi, S., Depinning transition of dislocation assemblies: Pileups and low-angle grain boundaries. *Physical Review B* **69**, 214103 (2004).

330. Koslowski, M., LeSar, R. & Thomson, R., Avalanches and Scaling in Plastic Deformation. *Physical Review Letters* **93** (12), 125502 (1-4) (2004).

331. Richeton, T., Weiss, J. & Louchet, F., Breakdown of avalanche critical behaviour in polycrystalline plasticity. *Nature Materials* **4**, 465-469 (2005).

332. Bulatov, V. V., Tang, M. & Zbib, H. M., Crystal Plasticity from Dislocation Dynamics. *MRS Bulletin*, 191-195 (2001).

333. Marian, J., Cai, W. & Bulatov, V. V., Dynamic transitions from smooth to rough to twinning in dislocation motion. *Nature Materials* **3**, 158-163 (2004).

334. Chandler, D., *Introduction to Modern Statistical Mechanics*, 1st ed. (Oxford University Press, USA, 1987).

335. Armstrong, R. W. & Walley, S. M., High strain rate properties of metals and alloys. *International Materials Reviews* **53** (3), 105-128 (2008).

336. Asaro, R. J. & Suresh, S., Mechanistic models for the activation volume and rate sensitivity in metals with nanocrystalline grains and nano-scale twins. *Acta Materialia* **53**, 3369-3382 (2005).

337. Suresh, S. & Li, J., Deformation of the ultra-strong. *Nature* **456**, 716-717 (2008).

338. Bruce, D., Dynamic tensile testing of sheet steels and influence of strain rate in strengthening mechanisms in sheet steels, Colorado School of Mines, Ph.D. Dissertation, 2003.

339. Ramberg, W. & Osgood, W. R., Description of Stress-strain Curves by Three Parameters. *Technical Note No. 902, NACA* (1943).

340. Levine, L. E. *et al.*, X-ray microbeam measurements of individual dislocation cell elastic strains in deformed single-crystal copper. *Nature Materials* **5**, 619-622 (2006).

341. Mughrabi, H., Dislocation wall and cell structures and long-range internal stresses in deformed metal crystals. *Acta Metallurgica* **31** (9), 1367-1379 (1983).

342. Luenberger, D. G., *Linear and Nonlinear Programming*, 2nd ed. (Addison-Wesley, Reading, MA, USA, 1984).

343. Holdsworth, S. R. & Merckling, G., *Engineering issues in turbine machinery, power plant and renewables, IOM*, presented at 6th International Charles Parsons Conference , Trinity College, Dublin, Ireland, 2003 (unpublished).

344. Spigarelli, S., Cerri, E., Bianchi, P. & Evangelista, E., Interpretation of creep behavior of a 9Cr-Mo-Nb-V-N (T91) steel using threshold stress concept. *Materials Science and Technology* **15**, 1433–1440 (1999).

345. Orlova, A. & Cadek, J., Dislocation structure in high temperature creep of metals and solid solution. *Materials Science and Engineering* **77**, 1–18 (1986).

346. Holdsworth, S. R., Developments in the assessment of creep strain and ductility data. *Materials at High Temperatures* **21** (1), 125-132 (2004).

347. Ho, K. & Krempl, E., The Modeling of Unusual Rate Sensitivities Inside and Outside the Dynamic Strain Aging Regime. *Transactions of the ASME: Journal of Engineering Materials and Technology* **123**, 28-35 (2001).

348. Roy, A. K., Kumar, P. & Maitra, D., Dynamic strain ageing of P91 grade steels of varied silicon content. *Materials Science and Engineering A* **499**, 379–386 (2009).

349. Samuel, E. I., Choudhary, B. K. & Rao, K. B. S., Influence of post-weld heat treatment on tensile properties of modified 9Cr–1Mo ferritic steel base metal. *Materials Science and Technology* **23** (8), 992-999 (2007).